Polarisation Dependence on Aplanarity in the Near-Planar Ring Laser

A THESIS

SUBMITTED IN PARTIAL FULFILMENT

OF THE REQUIREMENTS FOR THE DEGREE

OF

DOCTOR OF PHILOSOPHY IN PHYSICS

IN THE

UNIVERSITY OF CANTERBURY

by

Peter V Wells

University of Canterbury

1997

Acknowledgements

Sincere thanks goes to my supervisor Professor Geoff Stedman for his guidance and patience and to Professor Hans Bilger for his collaboration over publications.

Special thanks goes to the following staff and students:

Dr R G T Bennett whose wisdom and timely council avoided much wasted time and effort;

Clive Rowe for his help with experimental work;

Bruce Bradshaw, Stephen Hemmingsen, Morrie Poulton and Ron Culley for their time, effort and fine craftsmanship in making experimental apparatus;

Ross Ritchie and Geoff Graham for their work and help with electronics;

Dr C Hooker and Dr T Seed for their advice and encouragement;

Mark Aitchison, Roger Govind, Andrew Richards and Andrew McGregor for their direction on matters to do with computing;

the office staff who have been kind and helpful at all times;

other students in the department who have made my time at Canterbury enjoyable and pleasant.

Contents

Figures

Abstract

Polarisation of the beam in a near-planar skew-rhombus ring laser is dependent on the aplanarity of the geometrical ray-path and the defects of its cavity mirrors. With reduction in the anisotropy of birefringence in state-of-the-art multilayer dielectric-stack cavity mirrors it is shown that the polarisation measurements for a ring laser employing them would have picoradian sensitivity to the dihedral (fold) angle of the geometrical ray-path. Correction of the residual anisotropy of birefringence in multilayer dielectric-stack mirrors without a substantial increase in the reflectance losses is shown to be possible through reduction in the thickness of the top protective layer. The fundamental limits of the reflectance loss for multilayer mirrors is of the order of 1 part in 10^9 for mirrors employing SiO_2 and TiO_2 and these limits are shown to be set by the associated losses in the internal materials due to the Urbach tail near the band gap and to the thermodynamic density fluctuations in fabrication. Theoretical expressions have been found which predict the polarisation dependence on the dihedral angle of the geometrical ray-path for three types of near-planar skew-rhombus ring laser. An expression has been found which predicts the tilts required for the mirrors in a symmetric near-planar ring laser to produce a given closed geometrical ray-path. As a special case it is shown that for a near-planar square ring laser which employs pairs of planar and spherical mirrors the dihedral angle is equal to the sum of the tilts of the planar mirrors. A computer program has been prepared which calculates the power reflectances in the s- and p-directions, the coefficients of power transmission into the substrate in the same respective directions, and the anisotropy of birefringence for a multilayer dielectric-stack mirror design. We use the measurements of the amplitude transmission coefficients into the substrate for a given multilayer mirror design and the multilayer mirror program to show that the (real) refractive indices of the layer materials can be determined uniquely and that they can be determined with a fractional uncertainty which is one order of magnitude lower than the greatest fractional uncertainty of the measured amplitude transmission coefficients into the substrate. An experimental 1m×1m square ring laser which has been constructed and made operational is described. A review is made of polarimeter designs and it is shown that the measurement accuracy can be improved for each by accounting for the anisotropic attenuation of their optical components. A polarimeter which has been constructed is also described.

Chapter 1

Introduction

The nature of the beam polarisation in a ring laser is dependent on the mirror defects and the degree of aplanarity of the geometrical ray-path. Although the ring laser is more well known through the exploitation of the Sagnac effect[73] to create the inertial rotation sensor or gyroscope for aircraft (for example the Airbus 320), the polarisation dependence on the aplanarity of the geometrical ray-path can also be exploited to create an optical lever of picosecond resolution[14].

The polarisation modes of the beam internal to a non-planar ring laser are largely defined by the resonant modes of the mirror cavity containing them. The mirror cavity of a non-planar ring laser belongs to the class of nonorthogonal resonators which were investigated even before the advent of the ring laser. Nonorthogonal resonators possess no meridional plane of symmetry[3]. Arnaud along with Luneberg[48] investigated such optical systems and they in turn referenced those who had worked in the field before them. Arnaud and Kogelnik[6] developed a formalism for treating the orientation, but not the phase, of Gaussian beams propagating in nonorthogonal systems. Popov[66][65] and Kahn and Nemit[40] used the phase in their analysis. Their work was enlarged upon by Arnaud[3][4][5] and Bergmann[10] with their introductory studies of nonorthogonal resonators and in particular non-planar ring resonators. A number of other authors[21][20][29][62][2][92] have since contributed to work in the non-planar ring laser field. Yelland *et al.*[92] and Nilsson *et al.*[62] are of particular interest in that they specifically calculate the eigenmodes for the polarisation in non-planar ring lasers. Other work on ring lasers[76][75][91][59] is also mentioned. Work on fibre-optic ring lasers and the polarisation in fibre-optics may also be of interest[36][45][1].

With the advent of the first working ring laser[49] came the problem of lock-in. One of the proposed solutions to the problem was the multioscillator ring laser, first proposed by de Lang[26]. The type which used an aplanar mirror cavity design was thought to split the polarisation modes in frequency, however this was only true for modes of the opposite handedness. The reason for this was later pointed out by Arnaud[5, p 137]. Use of a nonreciprocal polarisation rotation element in the beam path removed the degeneracy and so the four frequency multioscillator laser gyroscope was made possible[30][31]. The investigations have continued with the basic theory

on polarisation set out by Martin[52] and Statz *et al.*[81], being that used to calculate polarisation modes for the non-planar ring laser in Section (2.2).

Investigation into the polarisation in ring lasers at the University of Canterbury has been motivated by the need to understand their operation so that the behaviour of the beating between the counterpropagating beams can be predicted. The successful operation of Canterbury 'C-I' ring laser without the need of any biasing methods raised expectations that such a device had the potential for making very sensitive tests of nonreciprocal phenomena. A review made of the types of test possible [85] includes, for example, the creation of a linear seismometer exploiting the polarisation sensitivity of the ring laser to changes in the aplanarity of the geometrical ray-path[14]; an increase in the precision of the classic experiments of Zeeman[93] which have already been improved upon by Bilger and Stowell[15]. and Sanders and Ezekiel[74]; a search for violations of special relativity in a conjugate ring geometry[67][84] by postulating a parity-violating preferred-frame test theory (detection is gained when diurnal variations in the beat frequency are found); nonlinear optical effects in gases associated with the chiral effects of electric and magnetic fields should give absolute phase shifts of 10^{-10} rad. which should be detectable[83][82][69][86]; a search for pseudoscalar particles like axions may be possible as a result of their interaction with one the counterpropagating linearly polarised beams rotated to align with a magnetic field and the other beam rotated to be orthogonal to the first[24].

The Canterbury 'C-I' ring laser has a nominally planar geometrical ray-path. To actually achieve planarity and maintain it is impossible in practice due to, among other things, thermal vibrations. Aplanarity of the geometrical ray-path of the beam internal to a ring laser causes a net rotation of the image plane of the beam after making a circuit of the mirror cavity.

Statz *et al.*[81, p259] investigated image rotation for non-planar mirror cavities by synthesis of dihedral rotators i.e. calculating the image rotation which results from reflection of the beam from successive pairs of mirrors. On investigating this we concluded that the results for some parts of their work were incorrect. The calculations are reworked and are presented.

Rotation of the image plane due to the aplanarity of the ray-path results in the beam being linearly polarised when the geometrical ray-path is in-plane and elliptically polarised when the ray-path is non-planar. It is because of the vector nature of the electric field of the beam that when the image plane of the beam is rotated the electric field vector must also rotate to satisfy the cavity resonance condition so as to produce a sustained oscillation, namely, lasing. Prediction of the polarisation of the beam in a ring laser enables one to calculate the beat frequencies between the counterpropagating beams. A number of groups had investigated the factors controlling the polarisation and therefore the beat frequencies of the non-planar ring laser[21][31][52][81][20][29] before the advent of the Canterbury 'C-I' ring laser, however, none made it clear how the polarisation changed from being linear when the

geometrical ray-path was in-plane[76, p742] to being nearly circular when the ray-path was out-of-plane[81, p267]. Our work[14] makes this clear for the near-planar square ring laser. Our investigation also shows that the rate at which the polarisation changes is dependent on the scale parameter $\beta_0 = \sqrt{(\delta^2 + \chi^2)/2}$ for each of the ring mirrors, assuming they are identical and where the differential reflectivity $\delta = r_p - r_s$ is the difference in the reflectivities between the p- (parallel to the plane of incidence) and s- (perpendicular to the plane of incidence) directions; the anisotropy of birefringence $\chi = \chi_p - \chi_s$ is the phase difference on reflection between the components of the beam in the p- and s-directions. Our calculations show that the smaller this parameter is the more rapid is the transition from linear to nearly circular polarisation with the change in aplanarity of the geometrical ray-path. For example, for a near-planar square ring laser whose mirrors have a differential reflectivity of $\delta \sim 10^{-9}$ and an anisotropy of birefringence of $\chi \sim 10^{-3}$ rad. the polarisation measurements of the beam exiting the back of one of the cavity mirrors has picoradian sensitivity to the change in the aplanarity of the geometrical ray-path. Our calculation of the ratio of the beam polarisations $A = E_p/E_s$, where E_p, E_s are the magnitude of the electric field vectors of the beam in the p- and s-directions, assumes that the discharge in the laser has linear gain independent of the direction of the electric field in the projective plane perpendicular to the propagation vector.

The great sensitivity of the polarisation to change in the aplanarity of the geometrical ray-path stimulated a search by the author for other topologically equivalent near-planar skew-rhombus ring lasers whose sensitivity were greater than that for the near-planar square one. In the process of investigation the author has extended the polarisation ratio expression and the scale parameter definition to cover all skew-rhombus near-planar ring laser designs. The eigen-equation for the skew-rhombus ring laser makes it possible to calculate the gain required by the discharge to obtain lasing for each of the eigenmodes, so placing on a more mathematical basis the selection of the eigenmodes which are excited given the gain of the discharge. Also derived from the eigen-equation is the frequency of operation dependence on the dihedral (fold) angle of the geometrical ray-path of the beam. It must be pointed out that the gain of the discharge and frequency of operation expressions are only applicable in the approximation that the ring laser is non-rotating, the gain produced by the discharge is linear and non-gyrotropic, and the back-scatter from the cavity mirrors coupling the counterpropagating beams is ignored.

To show the type of polarisation modes produced, sets of ellipses are plotted where for one cycle of oscillation of the beam the tip of the polarisation vector is projected onto the plane orthogonal to the propagation vector at the point at which the ratio of the polarisations was calculated. The curves plotted are for the mode requiring the least gain produced by the discharge. Also included in the plots is the set of vector amplitudes for the linearly polarised mode which results when the beam internal to the ring laser is compensated and $\delta/\chi = 0.1$.

The same set of calculations and graphs were prepared for the other near-planar

ring lasers investigated, namely, the ones which we have given the names 'folded' ring laser (a design in which the geometrical ray-path of the skew-rhombus ring has been folded over) and the 'Wünschelrute' ('Wishbone') ring laser (one in which all the angles of incidence of the beam on all the cavity mirrors are the same and small). This work on polarisation is presented in Chapter (2).

The precision of the ring laser as a tool for research and its accuracy as a gyroscope is dependent to a large degree on the quality of its cavity mirrors. It was because of this that the multilayer dielectric-stack mirror was developed and are almost standard in the ring laser industry. Metal coated mirrors can never approach the performance of multilayer ones because of the ohmic losses in the metal film. The accuracy of the ring laser gyro is not just dependent on the back-scatter but also on the 'Q' of the mirror cavity which, in turn, ultimately depends on the total losses of its mirrors. Apart from the shape and smoothness of its surface and the back-scatter there are two other characteristics which define the performance of the multilayer dielectric-stack mirror.

The first is its loss upon reflection which is in general greater for the p-direction than for the s-direction. The second is the phase-shift upon reflection of the components of the beam in the same respective directions. In general these are different as well. Since the cavity mirrors have a decisive influence on the polarisation of the internal beam of the ring laser they come in for special study in Chapter (3).

The performance of multilayer dielectric-stack mirrors can be calculated using Jones matrices. Based on the work by H. A. MacLeod[51] we show[14] that the residual anisotropy of birefringence in such mirrors can be reduced to $\chi = 3 \times 10^{-3}$ rad. without substantial loss in reflectance by reduction in thickness of the top protective $\lambda/2-SiO_2$ layer by etching. We also show that there is a fundamental limit for reflectance loss in multilayer mirrors, that this limit has not yet been reached, and we give mirror manufacturers encouragement and direction on how to achieve this limit[16].

Mirror losses can be categorised into three types: loss by absorption in the layer materials, loss by scattering, and loss by transmission into the substrate of the mirror. The number of layers on the mirror can always be increased so that transmission into the substrate is reduced below the absorption losses. We show that it is possible for mirror manufacturing techniques to improve so that loss by scattering will be reduced below that for absorption. Absorption at the present is set by impurities in the layer materials, particularly the high refractive index material, and purification will result in these losses being reduced to that determined by the Urbach edge. We show that an ultimate limit on reflectance losses in multilayer dielectric-stack mirrors is at the parts in 10^9, i.e. parts per billion (ppb) level.

The author has extended the work on multilayer mirrors by creating a computer program (the Turbo Pascal program on the disk accompanying this work), based on

the work by MacLeod, which calculates the reflectance and anisotropy of birefringence of multilayer dielectric-stack mirrors. In the development of the program the author noticed that previous calculations performed on multilayer dielectric-stack designs had not taken into account the need to use complex angles in Snell's law when the refractive indices are complex for waves in lossy materials. This was subsequently incorporated into the computer program. In using the program the author discovered that the coefficients of amplitude transmission into the substrate are independent of the losses of the dielectric-stack materials to first order and that this can be exploited to determine, uniquely, the refractive indices of the multilayer film materials. This investigation also shows that there is a great sensitivity of the coefficients of amplitude transmission to the refractive indices of the layer materials. Mathematical investigation shows that the fractional change in the refractive index of one of the layer materials produces an order of magnitude greater fractional change in the coefficient of amplitude transmission. The result of this is that the refractive indices of the layer materials can be calculated with a fractional uncertainty which is an order of magnitude smaller than the largest fractional uncertainty of the measured coefficients of amplitude transmission used in determining them.

It was the intention of the author to measure the change in polarisation of the beam internal to an experimental ring laser as a function of the dihedral (fold) angle of the geometrical ray-path. Beam stability in the mirror cavity is dependent on the geometry of the ray-path and the curvature of the mirrors. Considerable work has already been done on this[44][37][33][79][13][78]. The work of Bilger and Stedman[13] was used to check the beam stability for the mirror cavity design of the near-planar experimental ring laser. Control of the geometrical ray-path of the beam to set up a given dihedral (fold) angle has not, as such, been covered in the literature. By inverting the beam stability equations of Bilger and Stedman[13] the author derives expressions for calculating the mirror tilts required to set up a given closed geometrical ray-path for the beam in a near-planar ring laser with a mirror cavity having N mirrors symmetrically arranged. As a special case the dihedral angle of the near-planar square ring laser with pairs of planar and spherical mirrors is shown to be given by the sum of the tilts of the diametrically opposed planar cavity mirrors. The work on beam stability and control is covered in Chapter (4).

The author has constructed an experimental ring laser in which preliminary qualitative tests have shown that for one configuration of the geometrical ray-path the polarisation was reduced to being linear as tested by observation of the extinction by eye using a Glan-Thompson prism. For another configuration of the ray-path it was estimated that the maximum reduction in intensity of the beam under all rotations of the Glan-Thompson was of the order of 20%, hence it would seem from these preliminary observations that the limits of our theoretical analysis are correct.

The base of the 1m $\times$ 1m square ring laser was constructed from steel. Further details of the construction are given in Chapter (5).

In order measure the polarisation of the beam in the experimental ring laser it was necessary to construct a polarimeter. Collett[22] reviews several methods possible and these are investigated. In each case Collett makes the approximation that the optical devices used in making the measurements are ideal. The author reworks the theory behind the methods quoted to take account of the anisotropy in absorption of the optical components. Also discussed is the photo elastic modulator as a possible candidate for a polarimeter. A discussion ends Chapter (6) as to which methods the author is to use in making polarisation measurements.

Chapter(7) shows the mechanical construction of the polarimeter built.

Chapter 2

Polarisation in Near-Planar Ring Lasers

Dorschner[31] and Martin[52] provide the following main features for calculating the polarisation eigenmodes in the non-planar ring laser, namely, that the cavity resonance condition demanded that the E-M field reproduce itself in phase, intensity and polarisation; out-of-plane mirror geometries rotated the image plane of the beam; real mirrors have defects, being loss in reflectance and anisotropy of birefringence which when reduced make the polarisation modes in the non-planar ring laser more closely circular. Statz *et al.*[81], following these authors, drew on their work and provided a comprehensive treatise showing nearly all that is necessary to calculate the polarisation modes in the non-planar ring laser. In addition to the work of Dorschner and Martin, Statz *et al.* treated Gaussian beams in non-planar resonators. It must also be mentioned that the work of Aronowitz[7] drew attention to the difference between resonance condition for a linear cavity and that for a ring mirror cavity.

Our contribution to the work[14] on polarisation in non-planar ring lasers provides a mathematical treatment which describes how the polarisation of the beam in a near-planar square ring laser changes as the geometrical ray-path becomes progressively aplanar, having started in the in-plane condition. We show that the smaller the cavity mirror defects are, the more rapid is the change in the polarisation of the internal beam from being linear when in-plane to being closely circular for a fold angle $\beta \sim 0.1$ rad. for mirrors of the sort that we have in our possession with the birefringence appropriately reduced by etching the top protective layer. Later in this chapter the expression describing the ratio of the polarisation vectors for the near-planar square ring laser is derived and extended by calculating the polarisation ratio for two other near-planar ring laser types. The work by Statz *et al.*[81, p266] is the source of most of the basic theory for the calculations.

Since the beam in a ring laser can be considered fully polarised, one can use Jones algebra to calculate the polarisation modes. Each of the elements in the ring laser which has an optical effect on the beam can be represented by a 2×2 complex Jones matrix with the electric field of the beam being represented by a 2×1 complex Jones vector.

Real mirrors, being non ideal, can be represented by a Jones matrix of the form[81. p270]

$$\mathbf{F} = \begin{bmatrix} \rho_p e^{i\phi_p} & 0 \\ 0 & -\rho_s e^{i\phi_s} \end{bmatrix}, \tag{2.1}$$

where ρ_s, ρ_p, ϕ_s and ϕ_p are, respectively, the reflectivities in the s- and p-directions and the associated changes in phase on reflection for the same respective directions. Chapter (3) discusses how these parameters may be obtained for multilayer mirrors, being those most commonly used for ring lasers.

In a non-planar ring laser geometrical rotation of the image plane results from the beam being successively reflected from pairs of mirrors whose normals do not lie in the same plane. These rotations can be followed if one considers a coordinate system which moves along with the beam. We shall use the approach taken by Statz *et al.*[81, p255] who have in turn base their work on that by Berkowitz[11] and Arnaud[5].

Since we want to calculate only the geometrical effects which produce beam rotation we shall assume that the mirrors are ideal. Further we make the approximation that the effect of image rotation on the whole beam is the same as that on the adjacent part of the beam near the geometric ray-path. We shall also assume that the beam is a plane wave perpendicular to the axis as it is possible to consider a Gaussian beam as a superposition of plane waves for each surface of constant phase with the plane wave on the axis being perpendicular to it. If the region representing the beam is small then the part of a curved mirror which the representative beam intercepts can be regarded as planar. Hence, to the accuracy stated above, it is enough to consider a cavity of planar ideal mirrors in which a plane wave propagates along the closed geometrical ray-path forming the cavity.

Figure (2.1) shows a diagram representing the successive reflections of a light beam by a pair of ideal planar mirrors M_1 and M_2 whose respective normals $\mathbf{n}_1$ and $\mathbf{n}_2$ are not parallel to a common plane.

For each point along the geometrical ray-path considered, a triad of mutually orthogonal unit vectors is set up. The binormals $\mathbf{s}_1$ and $\mathbf{s}_2$ are defined as the unit vectors normal to the planes of incidence of the corresponding mirrors where $\mathbf{n}_i \times \mathbf{s}_i$ has a positive projection along the wave vector $\mathbf{k}_i$.

The mutually orthogonal vectors $\mathbf{s}_1$ and $\mathbf{q}_1$ span the projective plane P_1 which is the object plane for mirror M_1. P_2, spanned by either $\mathbf{s}_1', \mathbf{q}_1'$ or $\mathbf{s}_2, \mathbf{q}_2$, is the image plane for M_1 and the object plane for M_2.

To follow the progress of the electromagnetic field of a light beam let us choose its unit polarisation vector $\hat{\mathbf{e}}$ to lie in the object plane of mirror M_1 so that it makes an angle $-\alpha$ with the vector $\mathbf{q}_1$. Reflection in M_1 transforms this to $\hat{\mathbf{e}}'$ which makes an angle α with $\mathbf{q}_1'$ in the image plane of M_1. We may assume this because the

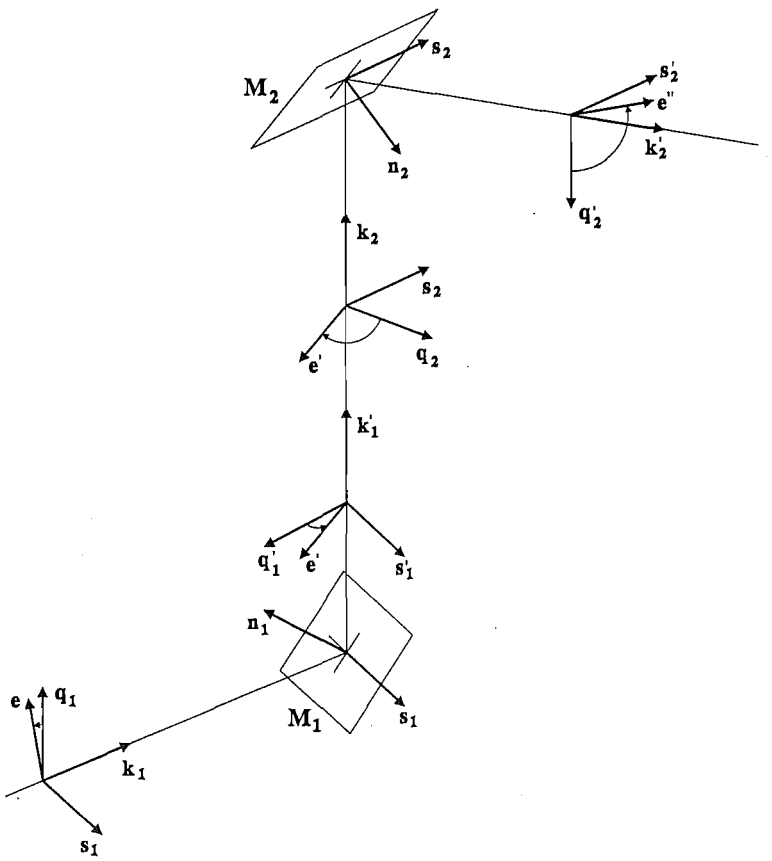

Figure 2.1: Coordinate systems and their rotation for calculation of the image rotation past a pair of mirrors.

boundary conditions at the surface of a perfectly conductive mirror demand that no electric field be present in it. Hence the component of the electric field of the reflected wave tangential to the surface is equal and opposite to that for the incident wave[18, p39]. To find the reflection of $\hat{\mathbf{e}}'$ in mirror M_2 requires that it be expressed in terms of the vectors spanning the object plane of M_2. It will be observed that the object plane of M_2 is rotated with respect to the image plane of mirror M_1. If a rotation through angle θ_{12} takes the basis vectors of the image plane for M_1 into the corresponding ones for the object plane of mirror M_2 then the vector $\hat{\mathbf{e}}'$ makes an angle $\theta_{12} - \alpha$ with $\mathbf{q}_2$ in the object plane of M_2. Reflection in mirror M_2 transforms vector $\hat{\mathbf{e}}'$ into vector $\hat{\mathbf{e}}''$ which makes an angle $\alpha - \theta_{12}$ with $\mathbf{q}_2'$ in the image plane of M_2.

If a geometrical ray-path is closed by reflections in the four planar mirrors M_1, M_2, M_3 and M_4 then the net image rotation ρ is $\rho = \theta_{12} - \theta_{23} + \theta_{34} - \theta_{41}$. For a mirror cavity with an even number of mirrors $2J$ we get[81, p256]

$$\rho = \theta_{12} - \theta_{23} + \theta_{34} - \cdots + \theta_{2J-1\,J} - \theta_{2J\,1}.$$

For a particular example showing this the reader could consult Statz *et al.*[81. p257]

2.1 Dihedral Rotator

It is possible to calculate the image rotation for a non-planar mirror cavity by synthesis from dihedral rotators. An optical system in which a beam is reflected from two mirrors in succession can be considered a dihedral rotator. We have already seen such a system in Figure (2.1) above. Statz *et al.* have considered this approach in finding image rotations in their work[81, p259]. In order to understand, use and extend their work we attempted to duplicate their results. There were, however, significant differences between their sets of results and ours and we look this now

Let us suppose that $\widehat{\mathbf{p}}_i$ and $\widehat{\mathbf{k}}_i$ are the respective unit polarisation and propagation vectors for the electromagnetic field of a light beam in the object plane of a mirror M_i. The propagation vector $\widehat{\mathbf{k}}_{i+1}$ of the reflected beam is found in terms of that for the incident beam by considering Maxwell's equations, the boundary conditions at the mirror surface[18, p39] and the transversality of the electric and magnetic fields for an isotropic medium[18, p23]. From this

$$\widehat{\mathbf{k}}_{i+1} = \mathbf{k}_i^{\perp} - \mathbf{k}_i^{\parallel} = \widehat{\mathbf{k}}_i - 2\widehat{\mathbf{n}}_i(\widehat{\mathbf{k}}_i \cdot \widehat{\mathbf{n}}_i) = -\mathbf{F}_i\widehat{\mathbf{k}}_i,$$

where $\mathbf{k}_i^{\parallel}$, $\mathbf{k}_i^{\perp}$ are, respectively, the components of the propagation vector parallel with and perpendicular to the unit normal vector $\widehat{\mathbf{n}}_i$ at the point where the ray intercepts mirror M_i. The reflection is also represented by the matrix $\mathbf{F}_i$ where, dropping the subscript i,

$$\mathbf{F} = [F_{\alpha\beta}] = 2n_\alpha n_\beta - \delta_{\alpha\beta},$$

where $\alpha = 1, 2, 3$. It is easy to show that $\mathbf{F}\mathbf{F}^{\top} = \mathbf{I}$ and $\det(\mathbf{F}) = -1$, demonstrating that $\mathbf{F}$ represents a reflection matrix. The polarisation $\widehat{\mathbf{p}}_{i+1}$ of the reflected ray in

terms of that of the incident ray $\widehat{\mathbf{p}}_i$ are obtained, using the Fresnel formulae[18, p39], as

$$\widehat{\mathbf{p}}_{i+1} = -\mathbf{p}_i^{\perp} + \mathbf{p}_i^{\parallel} = \mathbf{F}\widehat{\mathbf{p}}_i.$$

The rotation of the image plane produced by the successive reflections $\mathbf{F}_1$ and $\mathbf{F}_2$ in the respective mirrors M_1 and M_2 is given by

$$\mathbf{R} = \mathbf{F}_2\mathbf{F}_1 = \delta_{\alpha\beta} + 4n_{2\alpha}n_{1\beta}(\widehat{\mathbf{n}}_1 \cdot \widehat{\mathbf{n}}_2) - 2(n_{2\alpha}n_{2\beta} + n_{1\alpha}n_{1\beta}). \tag{2.2}$$

From this result it is easy to show $\mathbf{R}$ is a rotation matrix as $\mathbf{R}\mathbf{R}^{\top} = \mathbf{I}$ and $\det(\mathbf{R}) = 1$.

Mayer[53, p108] shows that

$$\mathrm{Tr}(\mathbf{R}) = 2\cos\theta' + 1,$$

where θ' is the effective rotation produced by matrix $\mathbf{R}$. From equation(2.2) we have

$$\mathrm{Tr}(\mathbf{R}) = 4\cos^2\gamma - 1 = 2\cos 2\gamma + 1$$

hence the effective rotation produced by $\mathbf{R}$ is 2γ.

The first point of departure between the work by Statz *et al.* and ours was in the denominator of the right hand side of their equation (3.2.18). From the definition of the dot product

$$\cos 2\gamma = \frac{(\widehat{\mathbf{k}}_1 \times \widehat{\Gamma})}{\left|\widehat{\mathbf{k}}_1 \times \widehat{\Gamma}\right|} \cdot \frac{(\widehat{\mathbf{k}}_3 \times \widehat{\Gamma})}{\left|\widehat{\mathbf{k}}_3 \times \widehat{\Gamma}\right|},$$

where $\widehat{\mathbf{k}}_1$ is the unit propagation vector of a ray incident on the first mirror M_1 of the dihedral rotator. The reflected ray, in the direction $\widehat{\mathbf{k}}_2$, becomes the incident ray for the second mirror M_2. From mirror M_2 the reflected ray finally exits the system in the direction $\widehat{\mathbf{k}}_3$. Angle γ is the dihedral angle between the two mirror planes. The unit vector $\widehat{\Gamma}$, defined by Statz *et al.* in their equation (3.2.17), is collinear with the line of intersection of the planes of reflection of the two mirrors and is the axis about which an effective dihedral rotation of 2γ transforms $\widehat{\mathbf{k}}_1$ into $\widehat{\mathbf{k}}_3$ (angle 2γ is that subtended by the projections of $-\widehat{\mathbf{k}}_1$ and $\widehat{\mathbf{k}}_3$ onto the plane perpendicular to $\widehat{\Gamma}$).

Equation (3.2.19) of Statz *et al.*, $\cos\gamma = \pm\sin\theta\cos(\rho/2)$, was of particular interest to us as it appeared to provide a simple relationship between the dihedral angle γ, the corner angle θ (one-half the angle subtended by $-\widehat{\mathbf{k}}_1$ and $\widehat{\mathbf{k}}_3$), and the image rotation angle ρ for a ray transformed by such a dihedral rotator.

Although equation (3.2.19) holds for the special cases treated in their work we contend that it is not valid in general. To show this, we follow the authors by first defining a cartesian coordinate system so that the origin is located where the incident beam intercepts the first mirror. The x-axis is aligned so that $\widehat{\mathbf{k}}_1$ points along it towards the origin and $\widehat{\mathbf{k}}_3$ is oriented so that it is parallel to the xy-plane (see Figure (2.2)).

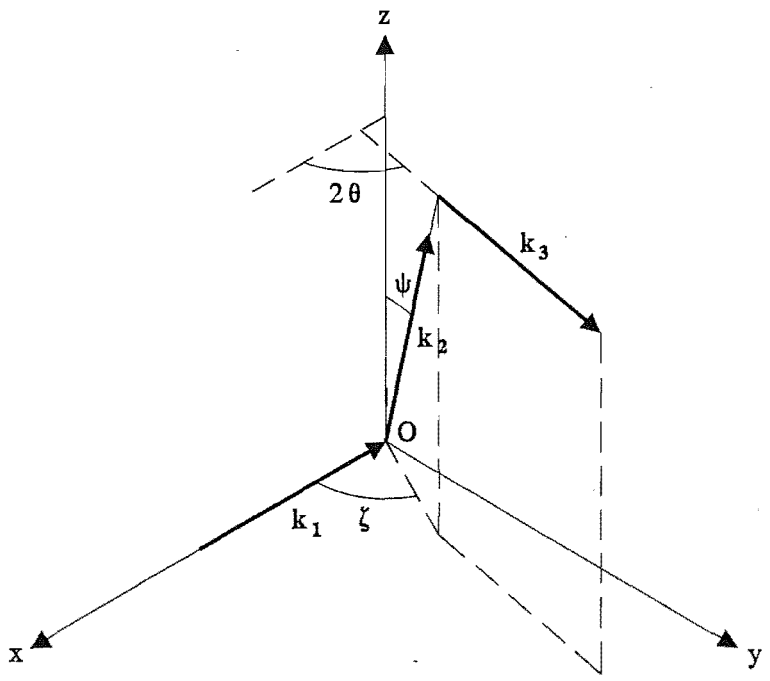

Figure 2.2: Propagation vectors at points along the geometrical ray-path of a beam reflected from a system of two mirrors synthesizing a dihedral rotator.

Although Statz *et al.* did not define the propagation vector $\widehat{\mathbf{k}}_2$ for the beam reflected from the first mirror M_1 our analysis demanded it, hence in polar coordinates $\widehat{\mathbf{k}}_2^{\top} = (1, \zeta, \psi)$. In cartesian coordinates the propagation vectors for all the beams involved in the dihedral rotator are $\widehat{\mathbf{k}}_1^{\top} = (-1, 0, 0)$, $\widehat{\mathbf{k}}_2^{\top} = (\sin\psi\cos\zeta, \sin\psi\sin\zeta, \cos\psi)$ and $\widehat{\mathbf{k}}_3^{\top} = (\cos 2\theta, \sin 2\theta, 0)$.

The unit normals $\widehat{\mathbf{n}}_1$, $\widehat{\mathbf{n}}_2$ to the mirrors M_1 and M_2, respectively, can now be found as

$$\begin{aligned}
\widehat{\mathbf{n}}_1 &= (\widehat{\mathbf{k}}_2 - \widehat{\mathbf{k}}_1)/\left|\widehat{\mathbf{k}}_2 - \widehat{\mathbf{k}}_1\right| = (\cos\zeta\sin\psi + 1, \sin\zeta\sin\psi, \cos\psi)^{\top}/N_1, \\
\widehat{\mathbf{n}}_2 &= (\widehat{\mathbf{k}}_3 - \widehat{\mathbf{k}}_2)/\left|\widehat{\mathbf{k}}_3 - \widehat{\mathbf{k}}_2\right| = (\cos 2\theta - \cos\zeta\sin\psi, \sin 2\theta - \sin\zeta\sin\psi, -\cos\psi)^{\top}/N_2,
\end{aligned}$$

where $N_1 = \sqrt{2(1+\cos\zeta\sin\psi)}$ and $N_2 = \sqrt{2[1-\sin\psi\cos(2\theta-\zeta)]}$. The dihedral angle γ between the normals of mirrors M_1 and M_2 can be found by using the definition of the dot product and the corresponding normal vectors to the mirrors

$$\cos\gamma = \widehat{\mathbf{n}}_1 \cdot \widehat{\mathbf{n}}_2 = \frac{\sin\theta[\sin\psi\sin(\zeta-\theta) - \sin\theta]}{\sqrt{(1+\sin\psi\cos\zeta)(1-\sin\psi\cos(2\theta-\zeta))}}. \tag{2.3}$$

From vectors $\widehat{\mathbf{n}}_1$, $\widehat{\mathbf{n}}_2$ we have

$$\begin{aligned}
\widehat{\Gamma} &= (\widehat{\mathbf{n}}_1 \times \widehat{\mathbf{n}}_2)/\left|\widehat{\mathbf{n}}_1 \times \widehat{\mathbf{n}}_2\right| = (\widehat{\mathbf{n}}_1 \times \widehat{\mathbf{n}}_2)/\sin\gamma \\
&= (-\cos\psi\sin\theta, \cos\psi\cos\theta, \sin(\theta-\zeta)\sin\psi + \sin\theta)^{\top}/G,
\end{aligned} \tag{2.4}$$

where the dihedral angle γ between the mirror planes is also that subtended by their normals and

$$G = \sin\gamma\sqrt{(1+\sin\psi\cos\zeta)(1-\sin\psi\cos(2\theta-\zeta))}/\cos\theta.$$

An expression for $\cos(\rho/2)$ can be found from $\cos(\rho) = \widehat{\mathbf{s}}_1 \cdot \widehat{\mathbf{s}}_2$ where $\widehat{\mathbf{s}}_1$ and $\widehat{\mathbf{s}}_2$ are the binormals to the first and second mirrors respectively. Statz *et al.* define the binormal to a mirror[81, p255] as $\widehat{\mathbf{s}}_i = \left(\widehat{\mathbf{k}}_i \times \widehat{\mathbf{n}}_i\right) / \left|\widehat{\mathbf{k}}_i \times \widehat{\mathbf{n}}_i\right|$. This expression is equivalent to

$$\widehat{\mathbf{s}}_i = \left(\widehat{\mathbf{k}}_i \times \widehat{\mathbf{k}}_{i+1}\right) / \left|\widehat{\mathbf{k}}_i \times \widehat{\mathbf{k}}_{i+1}\right| \tag{2.5}$$

as $\widehat{\mathbf{k}}_i$, $\widehat{\mathbf{k}}_{i+1}$ and $\widehat{\mathbf{n}}_i$ all lie in the same plane. We use the latter expression as it is more convenient. Substitution for the appropriate unit propagation vectors in equation (2.5) give

$$\begin{aligned}\widehat{\mathbf{s}}_1^{\top} &= (0, \cos\psi, -\sin\psi\sin\zeta)/S_1 \\ \widehat{\mathbf{s}}_2^{\top} &= (-\cos\psi\sin 2\theta, \cos\psi\cos 2\theta, \sin\psi\sin(2\theta-\zeta))/S_2\end{aligned}$$

where $S_1 = \sqrt{1-\cos^2\zeta\sin^2\psi}$ and $S_2 = \sqrt{1-\sin^2\psi\cos^2(2\theta-\zeta)}$. The image rotation angle ρ can be found from

$$\cos\rho = \widehat{\mathbf{s}}_1 \cdot \widehat{\mathbf{s}}_2 = \left(\cos^2\psi\cos 2\theta - \sin^2\psi\sin\zeta\sin(2\theta-\zeta)\right)/S, \tag{2.6}$$

where $S = \sqrt{(1-\sin^2\psi\cos^2\zeta)(1-\sin^2\psi\cos^2(2\theta-\zeta))}$. The sign of ρ is considered positive if a counter-clockwise rotation carries the image plane of M_1 into the object plane of M_2 as seen by an observer facing into the propagation vector of the beam. Substitution of equation (2.6) in the trigonometric identity $\cos(\rho/2) = \sqrt{(1+\cos\rho)/2}$ gives $\cos(\rho/2) = \sqrt{[1+(\cos^2\psi\cos 2\theta - \sin^2\psi\sin\zeta\sin(2\theta-\zeta))/S]/2}$ where S is the same quantity defined in equation (2.6). It is now easy to show that equation (3.2.19) of Statz *et al.* does not hold for example where $\theta = \pi/6$, $\zeta = \psi = \pi/4$ when the values for γ and $\rho/2$, as derived from equations (2.3) and (2.6), are used. Comparison between components of $\widehat{\mathbf{\Gamma}}$ of equation (3.2.20) of Statz *et al.* and our equation (2.4) show that these also differ.

We haver attempted to reverse engineer Statz *et al.* in the hopes of tracing the reasons for these disagreements, but have been unsuccessful. Statz *et al.* simply quote their erroneous formulae.

2.2 Calculation of the Beam Polarisation

The polarisation of the beam can be determined by considering the conditions for cavity resonance[7, p1][81, p266], namely, when the electromagnetic field propagating in the mirror cavity reproduces itself in phase, intensity and polarisation after one circuit. The following will only consider ring lasers which have an even number of

mirrors. We shall also assume that the only surfaces which the beam encounters on making a circuit of the mirror cavity are the mirrors themselves (we assume that the mirrors are immersed in the gain medium, but the discharge producing the gain is not near the mirrors, and the refractive index of the discharge is not significantly different from the rest of the gain medium).

2.2.1 Polarisation States for a Non-Planar Ring Laser

Let us consider a non-planar ring laser where the ith side has length l_i and where the mirror cavity is composed of an even number N of mirrors. We shall assume that the discharge is non-gyrotropic and provides a linear gain g which is independent of the direction of the electric field in the plane perpendicular to the propagation vector of the beam passing through it. Rotation matrices are included in the eigen-equation to account for the image rotations which result from the normals of successive pairs of cavity mirrors not being parallel. It is assumed that the ring is in a non-rotating frame and we are ignoring the effects of lock-in produced by back-scattering off the faces of the mirrors. The polarisation eigenvalue problem for the electric field in the first leg of the mirror cavity (between mirrors M_N and M_1) takes the form[81, Section 3.4].

$$g\left(\mathbf{T}_N\mathbf{R}_N\mathbf{F}_N\cdots\mathbf{R}_2\mathbf{F}_2\mathbf{T}_1\mathbf{R}_1\mathbf{F}_1\right)\mathbf{E} = ge^{ikL}\left(\mathbf{R}_N\mathbf{F}_N\mathbf{R}_{N-1}\cdots\mathbf{R}_2\mathbf{F}_2\mathbf{R}_1\mathbf{F}_1\right)\mathbf{E} = h\mathbf{E}, \tag{2.7}$$

where the $\mathbf{F}_i$ operator represents the reflection in the mirror M_i; the translation $\mathbf{T}_i$ operator is a diagonal matrix where both non-zero elements are $\exp(ikl_i)$, kl_i is the phase advance in traversing the distance between mirrors M_i and M_{i+1}, and where k is the wave number $2\pi/\lambda$; $\mathbf{E}$ is the complex electric field vector for the beam incident on mirror M_1; h takes the value unity so as to satisfy the conditions for cavity resonance. Since the translation matrices are unit matrices multiplied by a phase factor it is possible to combine the phase factors as e^{ikL}, where $L = \sum_i l_i$, and to absorb the unit matrices by multiplying each of them into an adjacent reflection matrix. We shall assume that the mirrors are not ideal and that equation (2.1) above can be used to model each of them. The operator $\mathbf{R}_i$, associated with the geometrical image rotation in transforming from the image plane of mirror M_i to the object plane of mirror M_{i+1}, has the form

$$\mathbf{R}_i = \begin{bmatrix} \cos\theta_{ii+1} & -\sin\theta_{ii+1} \\ \sin\theta_{ii+1} & \cos\theta_{ii+1} \end{bmatrix},$$

where θ_{ii+1} is the associated rotation angle. In general the matrices $\mathbf{R}_i$ and $\mathbf{F}_j$ do not commute so it is not possible regroup the factors in equation (2.7).

2.2.2 Polarisation in the Near-Planar Skew Rhombus Ring Laser

Figure (2.3) is the diagram of a near-planar skew rhombus ring laser with sides of length l.

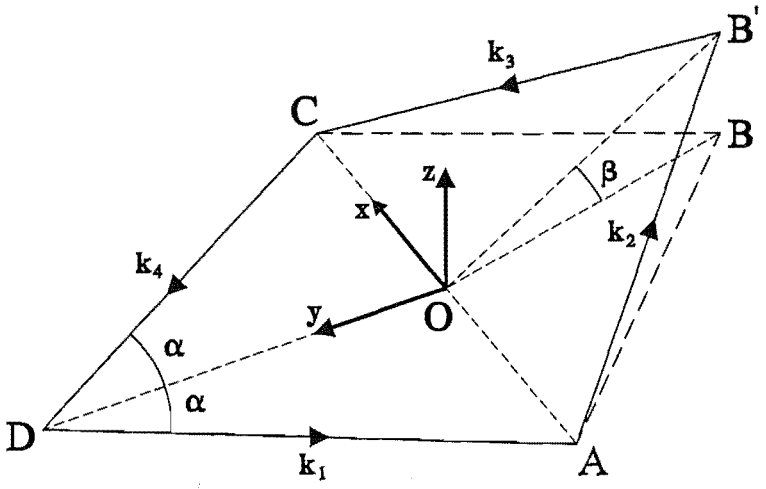

Figure 2.3: The closed geometrical ray-path for a beam propagating in the mirror cavity of a near-planar skew-rhombus ring laser. The beam is reflected from the mirrors at points $A, B^{'}, C$ and D. The dihedral (fold) angle for the ray-path is β.

The poles of the mirrors are located at the vertices of the rhombus and are labelled, respectively, $ABCD$. We assume that the mirrors are given appropriate small tilts so that the closed geometrical ray-path forms the skew rhombus $AB^{'}CD$. One can view the ray-path $AB^{'}CD$ as being that for the planar rhombus labelled $ABCD$ folded along the diagonal AC. The planarity of the geometrical ray-path is defined by the dihedral angle β between the planes defined by $AB^{'}C$ and ADC. Let 2α be the size of each of the two angles $\angle ADC$ and $\angle AB^{'}C$.

The image rotation matrices take the form

$$\mathbf{R}_1 = \mathbf{R}_3 = \frac{1}{R}\begin{bmatrix} \cos(\beta/2)\sin\alpha & \sin(\beta/2) \\ -\sin(\beta/2) & \cos(\beta/2)\sin\alpha \end{bmatrix}, \tag{2.8}$$

where $R = \sqrt{1-\cos^2\alpha\cos^2(\beta/2)}$. The matrices $\mathbf{R}_2$ and $\mathbf{R}_4$ are the same as the matrices $\mathbf{R}_1$ and $\mathbf{R}_3$ except for a sign change on the off diagonal elements.

We assume that the mirrors are non ideal and the losses in reflectivity in the s- and p-directions are, respectively, δ_s, δ_p, and the corresponding phase shifts on reflection are χ_s, χ_p. All four of the mirror parameters are treated as being small. Hence the reflection matrix (2.1) becomes

$$\mathbf{F}_i = \begin{bmatrix} 1-\delta_p+i\chi_p & 0 \\ 0 & -(1-\delta_s+i\chi_s) \end{bmatrix}, \tag{2.9}$$

where $\delta_p = 1-\rho_p$, $\delta_s = 1-\rho_s$, $\phi_p \to \chi_p$ and $\phi_s \to \chi_s$.

The eigen-equation for the ring laser takes the form

$$ge^{ikL}\left(\mathbf{R}_4\mathbf{F}_4\mathbf{R}_3\mathbf{F}_3\mathbf{R}_2\mathbf{F}_2\mathbf{R}_1\mathbf{F}_1\right)\mathbf{E} = h\mathbf{E}, \tag{2.10}$$

where h takes the value unity to satisfy the conditions for cavity resonance. If we assume that the dihedral (fold) angle β is small and substitute for the appropriate matrices from (2.8) and (2.9) in equation (2.10) then

$$ge^{ikL}\begin{bmatrix} 1-4\delta_p+i4\chi_p & 2\beta/\sin\alpha \\ -2\beta/\sin\alpha & 1-4\delta_s+i4\chi_s \end{bmatrix}\begin{pmatrix} E_p \\ E_s \end{pmatrix} = h\begin{bmatrix} 1 & 0 \\ 0 & 1 \end{bmatrix}\begin{pmatrix} E_p \\ E_s \end{pmatrix}, \tag{2.11}$$

where E_p and E_s are the components of the electric field $\mathbf{E}$ of the beam in the p- and s-directions, respectively; $k = 2\pi/\lambda$, where λ is the wavelength of the beam in the gas within the mirror cavity; L is the total physical geometrical path-length of the beam. The associated characteristic equation is

$$h^2 - 2hge^{ikL}\left(1-2\left(c_p+c_s\right)\right) + g^2e^{i2kL}\left(1-4c_p\right)\left(1-4c_s\right) + \frac{4\beta^2g^2e^{i2kL}}{\sin^2\alpha} = 0,$$

where $c_s = \delta_s - i\chi_s$, $c_p = \delta_p - i\chi_p$. The eigenvalues are found to be

$$h = ge^{ikL}\left[1-2\left(c_p+c_s\right) \pm 2\sqrt{\left(c_p-c_s\right)^2 - \beta^2/\sin^2\alpha}\right]. \tag{2.12}$$

Substitution for the eigenvalues of (2.12) in the bottom equation of matrix expression (2.11) gives the expression

$$A = \frac{\gamma \pm \sqrt{\gamma^2-\beta^2}}{\beta}, \tag{2.13}$$

where $A = E_p/E_s$ and $\gamma = (c_p - c_s)\sin\alpha$. Substitution of $\alpha = \pi/4$ in equation (2.13) gives our published result[14] which is the same equation as given in (2.13), but with $\gamma = (c_p - c_s)/\sqrt{2}$.

The $\pm$ sign in equation (2.13) shows that two polarisation modes are possible. We shall see presently that the gain of the discharge required to excite each of the modes is different and so it is possible to excite only one of them. It is easy to decide what sign must be chosen for such a case if one considers the polarisation as the aplanarity of the geometrical ray-path approaches the limiting case $\beta = 0$. The ratio of the polarisations A approaches either infinity or zero, depending on the sign chosen in equation (2.13). Since the losses in the cavity mirrors are greater in the p- than in the s-direction the beam will be linear polarised in the s-direction. Hence, if the real part of $\sqrt{\gamma^2-\beta^2}$ in equation (2.13) is chosen to be positive then the negative sign must be chosen to correspond.

We can extend the published work by calculating both the gain required of the discharge to produce lasing and the frequency of oscillation dependence on planarity for a near-planar ring laser, assuming as stated above that the device is in a non rotating frame and that we are ignoring the effects of back scatter with its associated lock-in effects.

If we set h to unity we may rewrite equation (2.12) as $ge^{ikL}(a+ib)=1$ where

$$a+ib=1-2(c_p+c_s)\pm 2\sqrt{(c_p-c_s)^2-\beta^2/\sin^2\alpha}, \tag{2.14}$$

and where a and b are real quantities. Since c_p, c_s and β are small we can write $a=1-\Delta$ so that to first order $a+ib\simeq(1-\Delta)(1+ib)\simeq(1-\Delta)e^{ib}$. Hence equation (2.12) becomes

$$g(1-\Delta)e^{i(kL+b)}=1. \tag{2.15}$$

Invoking the conditions for cavity resonance gives

$$kL+b=2\pi q, \tag{2.16}$$

where q is a positive integer. Substitution of $\lambda=c/(nf)$ in equation (2.16) and rearrangement gives an expression for the lasing frequency f as a function of the dihedral angle β as

$$f=\frac{c}{nL}\left(q-\frac{1}{2\pi}\operatorname{Im}\left(1-2(c_p+c_s)\pm 2\sqrt{(c_p-c_s)^2-\beta^2/\sin^2\alpha}\right)\right), \tag{2.17}$$

where n and c are, respectively, the refractive index of the gas within the laser and the speed of light in vacuum.

Substitution of equation (2.16) in equation (2.15) and rearrangement obtains the gain g required by the discharge to produce lasing as

$$g=\frac{1}{\operatorname{Re}\left(1-2(c_p+c_s)\pm 2\sqrt{(c_p-c_s)^2-\beta^2/\sin^2\alpha}\right)}. \tag{2.18}$$

In general, for the two polarisation modes of the beam there is a difference in their frequency of operation and also a difference in the gain required of the discharge to excite them. If the ratio of polarisations A is calculated for the counter-propagating beam incident on the mirror at the point labelled A in Figure (2.3) then the result is identical to that obtained in equation (2.13). This may have important consequences for the Canterbury ring lasers in that if the gain of the discharge is allowed to grow large enough then it is possible that both the polarisation modes in each direction will be excited and depending on whether the two polarisations are orthogonal or not beating may be produced between them. Further, if beating is produced then it will now have a dependence on the planarity of the ring laser.

2.2.3 Polarisation Characteristics for the Near-Planar Skew Rhombus Ring Laser

The characteristics of the mirror defects have a large influence on how the polarisation changes with the aplanarity of the geometrical ray-path of the beam. The value for

$A = E_p/E_s$ is very sensitive to the difference $\gamma^2 - \beta^2$ in equation (2.13). As a measure of the sensitivity we defined[14] $\beta_0 = \sqrt{\delta^2 + \chi^2}/\sqrt{2}$ being the modulus of γ for the near-planar square ring laser. We may extend this definition to include all types of near planar skew rhombus ring lasers by redefining the scale parameter as

$$\beta_{0p} = \sqrt{\delta^2 + \chi^2}\sin\alpha.$$

The type of polarisation produced is dependent on the ratio δ/χ of the differential reflectivity to the anisotropy of birefringence for the cavity mirrors, assuming they are all the same. This is illustrated in Figure (2.4) where the three sets of diagrams on the left show the path traced out by the tip of the polarisation vector during one period for the ratio $\delta/\chi = \infty, 10$ and 0.1.

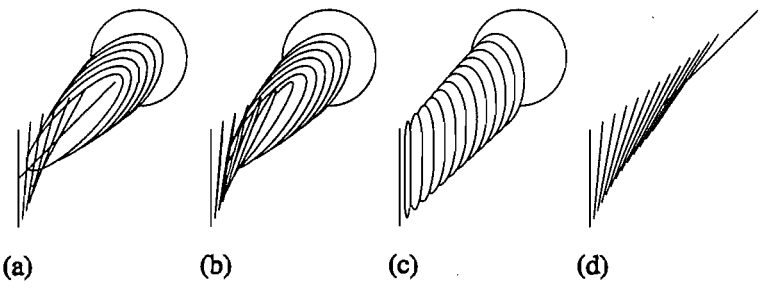

Figure 2.4: Polarisation modes for a skew-rhombus near-planar ring laser as a function of the relative nonplanarity β/β_{0p} where the ratio δ/χ of differential reflectivity to differential birefringence has the values $\infty, 10, 0.1$ for (a), (b), (c), respectively. In (d), $\delta/\chi = 0.1$ as for (c), but the ellipticity has been compensated by an $s-p$ phase shift (approximately $\pi/2$). In each case β/β_{0p} ranges from 0 to 2 in 12 steps, and the limiting case ($\beta = \infty$) of circular polarisation is included.

For each of the sets of diagrams the vertical linearly polarised mode in front is that for the case where the geometrical ray-path is planar. The dihedral angle β then increases in 12 equal steps of $\beta_{0p}/6$ where the choice of step size has made it possible to show for the case where δ dominates χ that $\beta = \beta_{0p}$ is the transition value for which the beam polarisation changes from linear to elliptical, that the angle of orientation of the electric field of the linearly polarised mode at the transition value is $\pi/4$ to the p-direction (the horizontal direction for the diagram), and that this is also the angle of orientation of the major axes of the ellipses where $\beta > \beta_{0p}$.

One method for measuring the polarisation ratio A is to compensate it and measure the orientation of the electric field of the resultant linearly polarised beam. The diagram to the extreme right of Figure (2.4) shows the orientation of the electric field for such a compensated beam when $\delta/\chi = 0.1$ rad^{-1}.

Figure (2.5) shows the polarisation characteristics for the experimental near-planar ring laser using the mirrors we have in our possession whose characteristics will be quoted as being those for 'our mirrors' in Section (3.2.1). The characteristics which are relevant to this work are the anisotropy of birefringence $\chi \sim 0.1$ radian and the differential reflectivity is $\delta = 165$ ppm so that $\delta/\chi = 1.65 \times 10^{-3}$.

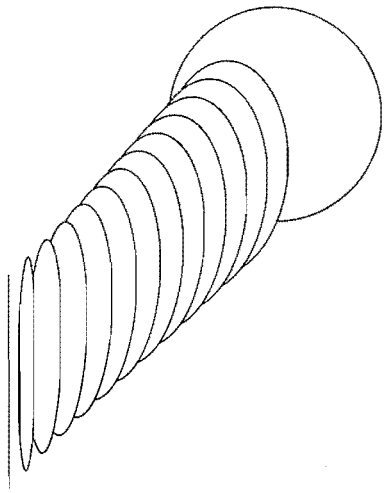

Figure 2.5: Polarisation modes of the skew-square near-planar ring laser as a function of the relative nonplanarity β/β_{0p} where the ratio δ/χ of differential reflectivity to differential birefringence has the value 1.65×10^{-3} which is that for 'our' mirrors. β/β_{0p} ranges from 0 to 2 in 12 steps, and the limiting case ($\beta = \infty$) of circular polarisation.

2.2.4 Detector Sensitivity to Aplanarity Change in the Geometrical Ray-Path

Since we have obtained an expression which predicts the polarisation in the beam given the aplanarity of the geometrical ray-path for a near-planar square ring laser we are in a position to calculate the change in a detector measuring the ratio of the polarisations of the beam exiting the back of the mirror at A in Figure (2.3).

In our work[14, p136] a split-field analyser and a compensator were used as the detector in calculating the ellipticity of the beam from the back of one of the cavity mirrors for a near-planar square ring laser. It was also assumed that the detector performance was enhanced with the use of synchronous detection to obtain the best performance possible. It must be pointed out that the split-field analyser and compensator is by no means the only apparatus which can be used and Chapter (6) gives a review of some of the main methods used for beam polarisation measurement and also shows how the losses in the optical elements of these devices can be taken into account to improve the accuracy of the results. Since we are interested in the order of magnitude limits of sensitivity of the detector to aplanarity change in a ring laser we will not take into account the losses in these optical elements as they are small.

2.2.5 The Detector and its Angular Resolution

The compensated linearly polarised beam exiting the back of one of the cavity mirrors of the ring laser falls on two adjacent identical detectors whose shared common edge

is positioned so that each detector 'sees' half the power of the beam. Polarisation detection is achieved by placing polarisers in front of each detector so that their transmission axes are inclined at an angle of 2α to each other and the combination is oriented so that it is bilaterally symmetric with respect to the common edge of the detectors (see Figure (2.6)).

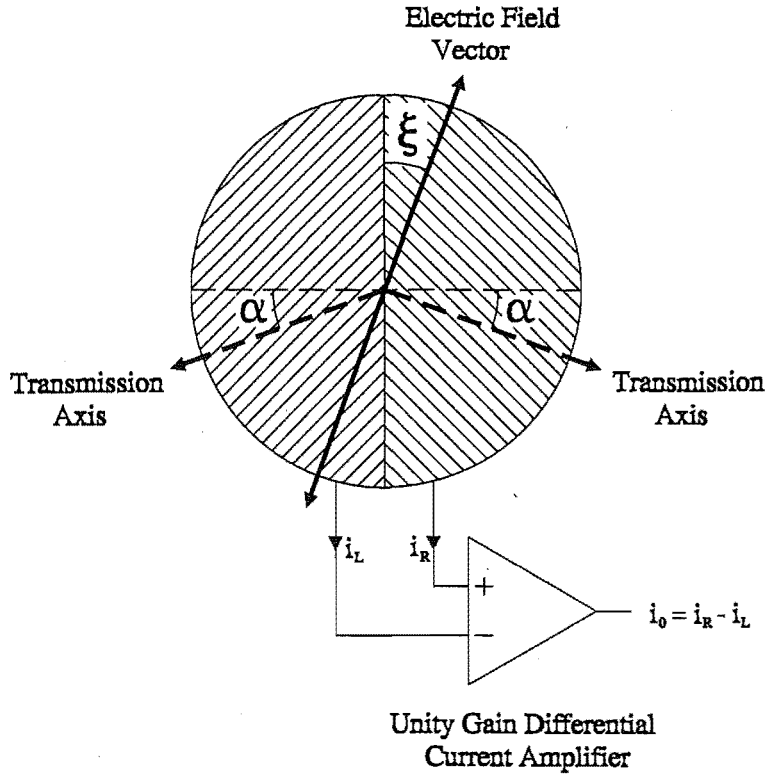

Figure 2.6: Schematic diagram for a split-field analyser for measuring the orientation of the electric field vector for a beam of light incident upon it. Semicircular photo detectors are covered by linear polarisers oriented so that their transmission axes are at an angle of 2α to each other.

The electric field of the beam is assumed to make an angle ξ with the common edge between the detectors and the current output from each detector is assumed to be proportional to the energy deposited on it per unit time. Hence

$$\begin{aligned} i_L &= I_0 \cos^2(\pi/2 + (\alpha - \xi)), \\ i_R &= I_0 \cos^2(\pi/2 + (\alpha + \xi)). \end{aligned}$$

The output from the unity gain differential current amplifier is

$$\Delta i = i_R - i_L = I_0 \sin 2\xi,$$

where it is assumed that the differential output is maximum when $\alpha = \pi/4$ (this condition only holds when the incident power on the detectors is large compared to the noise of the system; when the power of the incident beam is near that for the noise, α will require a value somewhat nearer zero radian for a maximum signal to noise ratio).

The angular resolution of the detector can be calculated using beam power considerations only. To obtain numerical results we shall first makes some assumptions about operational conditions under which the measurements are to be made. Let us suppose that the circulating power inside the mirror cavity of the ring is $P_c = 1$ W (the total for both counter-propagating beams). The geometrical ray-path is considered to be so close to planar that the beam is essentially linearly polarised in the s-direction hence the power of one of the beams exiting the back of a cavity mirror is $P = P_c T_s/2 \simeq 2 \times 10^{-6}$ W, where the value of $T_s \simeq 4$ ppm (close to the value we measured for one of our mirrors[14, p134]). A full analysis would require the sum of the weighted components in the s- and p-directions of the power of the circulating beam internal to the laser cavity).

Let us now calculate the angular resolution for the detector for the case where it is quantum noise limited. Since we are assuming the polarisers are ideal the average number of photons striking each detector during time interval T is $N_L = PT\sin^2(\alpha - \xi)/2\hbar\omega$ and $N_R = PT\sin^2(\alpha + \xi)/2\hbar\omega$. The signal power obtained is therefore

$$\begin{aligned} P_S &= \frac{(N_R - N_L)\,\hbar\omega}{T} \\ &\simeq P\xi, \end{aligned}$$

where it is assumed that $\alpha = \pi/4$ and ξ is small.

Because of the stochastic nature of the arrival of photons at the detector the signal generated in each has a random variation around some mean value and this variation appears as noise superimposed on the signal, being the mean difference between the numbers of photons arriving at the two detectors during time interval T. Since the arrival times of the photons in each of the detectors are independent of each other we can calculate the noise in the output signal from the square root of the sum of the variances in the number of photons arriving at each of the detectors during the time interval T. The arrival times of photons at each of the detectors follow a Poisson distribution for which the variance is the same as the mean. Hence the variance in the signal is given by

$$\sigma^2 = \frac{PT}{2\hbar\omega}\left[\sin^2(\alpha + \xi) + \sin^2(\alpha - \xi)\right] \simeq \frac{PT}{2\hbar\omega},$$

where again the final result assumes that $\alpha = \pi/4$ and ξ is small. The noise equivalent power P_N in the signal is therefore

$$P_N = \frac{\sigma\hbar\omega}{T} = \sqrt{\frac{P\hbar\omega}{2T}}.$$

If we assume a measurement duration of 10^2 seconds then $P_N \simeq 5 \times 10^{-14}$ W. If we suppose the limit of signal detection is when $P_N \sim P_S$ then for the quantum noise limited system

$$\xi = \sqrt{\frac{\hbar\omega}{2PT}} \simeq 10^{-8}\text{rad}.$$

For a system which is detector noise limited (for a modern detector the noise power is $N_d \sim 10^{-16}$ W) the noise power in the output signal is the sum of the noise powers of the detectors. Again, let us assume that the limit of signal detection is when $P_N \sim P_S$ then

$$\xi = \frac{2N_d}{P} \simeq 10^{-10}\text{rad}.$$

For the case we had treated the resolution with which the split-field analyser can measure the orientation of the electric field in a linearly polarised beam is limited by quantum noise to be $\xi \simeq 10^{-8}$ rad.

We now require the relationship between the aplanarity of the geometrical ray-path of the ring laser and the orientation of the electric field in the compensated beam exiting the back of the cavity mirror. We will assume that we are using our present day multilayer dielectric-stack mirrors with 11 pairs of $\lambda/4 - \lambda/4$ layers that have been improved to the point where the anisotropy of birefringence is $\chi \simeq 4 \times 10^{-3}$ rad (see Section (3.2.1) for a discussion of this). We assume the differential reflectivity is ~ 150 ppm[14, p134]. Since $\chi \gg \delta$ in equation (2.13) we can make the approximation

$$A \simeq \frac{-i\beta}{\sqrt{2}\chi}.$$

The ratio of the amplitude transmission coefficients has been measured for one of our mirrors[14, p136] (and is independent of the layer material losses) as $t_p/t_s = \sqrt{T_p/T_s} \simeq 8.8$. Hence the ratio $A' = E'_p/E'_s$ of the beam transmitted by the mirrors is

$$A' = 8.8A = \frac{8.8\beta}{\sqrt{2}\chi} \simeq 1500\beta. \tag{2.19}$$

If the geometrical ray-path of the ring laser is very nearly planar then the angle ϕ between the electric field vector of the linearly polarised compensated beam exiting the back of the mirror and the s-direction will be small so that

$$A' = \tan\phi \simeq \phi. \tag{2.20}$$

Hence for the detector considered above $\phi \sim 10^{-8}$ rad and so if equation (2.20) is substituted in equation (2.19) then the angular resolution with which the aplanarity of the geometrical ray-path for the near-planar square ring laser can be determined is $\beta \simeq 6 \times 10^{-12}$ rad!

Not only do we have a system that is extremely sensitive to angular changes in the geometrical ray-path and hence the angular changes of the tilts of the mirrors but we have uncovered an extremely sensitive optical lever using present day technology, but with the requirement that the birefringence be corrected using a proven technique.

It may seem tthat when picoradians of ring folding are being discussed many larger effects would dominate, such as angular variations in the polarisation of the beams under diffraction, birefringence of the discharge tube windows and of the atomic

vapour, spatial uniformity of the analysers, polarisation sensitivity and dark current of the detectors etc.

The last-mentioned problems certainly required careful checking in practise. However this quoted sensitivity of picoradians translates into a much larger figure (of order nanoradians) for polarisation angular sensitivity. The Gaussian beams under discussion have finite radius of curvature, of order several metres (the radius of the mirrors used) means that over their beam diameter (typically 0.6 mm) the angular variation of the polarisation of the beam across its diameter, which might influence our quoted sensitivity , do not accompany such effects, but vanish in the same model approximation. While no model has been proposed to our knowledge for their possible analysis, they are likely to arise only from mirror defects which already are at the 10^{-4} level or less. Hence we expect such to be 4 orders of magnitude less than the beam divergence figure, i.e. in the nanoradian regime.

With the near-planar square ring laser being such a sensitive optical lever when used in conjunction with a polarimeter it natural to ask whether there is a way to further improve its performance. One possibility of course is to improve the quality of the detector, but the margin for this is small. The other avenue of investigation is to change the topology of the geometrical ray-path of the ring laser. Rapid change in polarisation only occurs when the geometrical ray-path is in the near-planar configuration. We look at other near-planar configurations next.

2.2.6 The Folded Ring Laser

Instead of folding the geometrical ray-path of the skew rhombus ring laser along the diagonal through a small angle we can fold it over so that one half is nearly coincident with the other (see Figure (2.7)).

The topology of the new ray-path is also near-planar. As before we shall assume that the physical distance along the ray-path between successive pairs of mirrors has length l. The dihedral angle β is that between the planes defined by ABC and ADC. The size of angles $\angle ABC$ and $\angle ADC$ are 2α.

The image rotation matrices for this ring laser are given by

$$R_1 = R_3 = \frac{1}{R}\begin{bmatrix} \sin\alpha\sin(\beta/2) & \cos(\beta/2) \\ -\cos(\beta/2) & \sin\alpha\sin(\beta/2) \end{bmatrix}, \tag{2.21}$$

where $R = \sqrt{1-\cos^2\alpha\cos^2(\beta/2)}$. Matrices R_2 and R_4 are the same as R_1 and R_3 except that the signs on the off diagonal elements are interchanged.

The angles of incidence for mirrors at B and D are α as in the near-planar skew rhombus ring laser, however, the angles of incidence for mirrors A and C are near

mastpol.tex

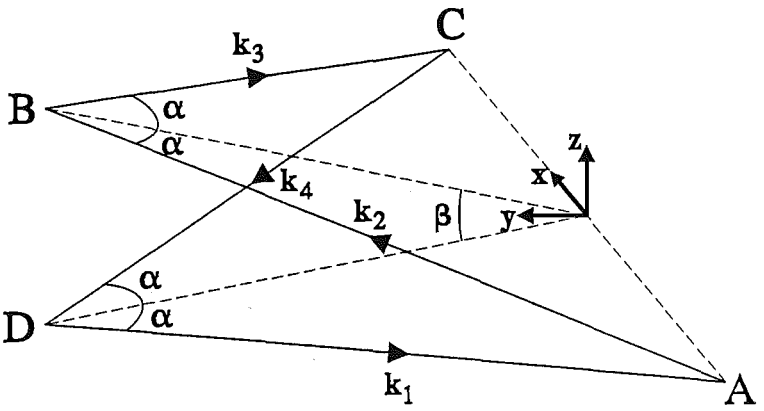

Figure 2.7: The closed geometrical ray-path for a beam propagating in the mirror cavity of a near-planar folded ring laser. The beam is reflected from the mirrors at A, B, C and D. The dihedral (fold) angle for the ray-path is β.

zero radians and this means that we require two sets of reflection matrices instead of the one for the previous ring laser. Hence, using equation (2.1) and assuming the differential reflectivity and anisotropy of birefringence for each are small, we define

$$\begin{aligned} F_1 &= F_3 = \begin{bmatrix} 1-\delta_p^{'}+i\chi_p^{'} & 0 \\ 0 & -\left(1-\delta_s^{'}+i\chi_s^{'}\right) \end{bmatrix}, \\ F_2 &= F_4 = \begin{bmatrix} 1-\delta_p+i\chi_p & 0 \\ 0 & -\left(1-\delta_s+i\chi_s\right) \end{bmatrix}, \end{aligned} \tag{2.22}$$

where $\delta_p, \delta_s, \chi_p$ and χ_s are, respectively, the differential reflectivities in the p- and s-directions and the anisotropy of birefringence for the same respective directions for the $\pi/4$ incidence mirrors. The zero incidence mirrors have the same corresponding labels except they are primed.

The form given by eigen-equation (2.10) also describes the behaviour of the electric field vector for the beam in this ring. If we assume β is small then substitution of the appropriate matrices from the sets given in (2.21) and (2.22) we get the explicit eigen-equation

$$\begin{aligned} & ge^{ikL} \begin{bmatrix} 1-2\left(\delta_s+\delta_p^{'}\right)+2i\left(\chi_s+\chi_p^{'}\right) & 2\beta\sin\alpha \\ -2\beta\sin\alpha & 1-2\left(\delta_p+\delta_s^{'}\right)+2i\left(\chi_p+\chi_s^{'}\right) \end{bmatrix} \begin{pmatrix} E_p \\ E_s \end{pmatrix} \\ = \; & h \begin{bmatrix} 1 & 0 \\ 0 & 1 \end{bmatrix} \begin{pmatrix} E_p \\ E_s \end{pmatrix}, \end{aligned} \tag{2.23}$$

where $L = 4l$ is the perimeter length of the geometrical ray-path, h is the eigenvalue for the equation and takes the value unity to satisfy the cavity resonance condition. The associated characteristic equation is

$$h^2 - 2h\left[1-(G_1+G_2)\right]ge^{ikL} - \left[1-2\left(G_1+G_2\right)+4G_1G_2-4\beta^2\sin^2\alpha\right]g^2e^{i2kL} = 0,$$

where $G_1 = \delta_p + \delta_s^{'} - i\left(\chi_p + \chi_s^{'}\right), G_2 = \delta_s + \delta_p^{'} - i\left(\chi_s + \chi_p^{'}\right)$. The possible eigenvalues for h are given by

$$h = \left\{ [1 - (G_1 + G_2)] \pm \sqrt{(G_1 - G_2)^2 - 4\beta^2 \sin^2 \alpha} \right\} g e^{ikL}. \tag{2.24}$$

Substitution of h given by equation (2.24) into the bottom equation of the matrix expression (2.23) gives the ratio of the polarisations as

$$A = \frac{E_p}{E_s} = \frac{-\gamma \pm \sqrt{\gamma^2 - \beta^2}}{\beta}, \tag{2.25}$$

where $\gamma = (\tau - i\kappa)/2 \sin \alpha$, and where $\tau = (\delta_p - \delta_s) - \left(\delta_p^{'} - \delta_s^{'}\right)$ and $\kappa = \left(\chi_p - \chi_s\right) - \left(\chi_p^{'} - \chi_s^{'}\right)$. Although it appears there is some similarity between equation (2.25) and equation (2.13) the expressions for the differential reflectivities τ and the anisotropies of birefringence κ of the folded ring laser are different from the corresponding δ and χ for the skew rhombus ring laser.

The discharge gain and frequency of operation of this laser configuration are respectively

$$\begin{aligned} g_f &= \left\{ \mathrm{Re}\left[1 - (G_1 + G_2) \pm \sqrt{(G_1 - G_2)^2 - 4\beta^2 \sin^2 \alpha} \right] \right\}^{-1}, \\ f_f &= \frac{c}{nL} \left\{ u - \frac{1}{2\pi} \mathrm{Im}\left[1 - (G_1 + G_2) \pm \sqrt{(G_1 - G_2)^2 - 4\beta^2 \sin^2 \alpha} \right] \right\}, \end{aligned}$$

where u is a positive integer. As for the near planar skew rhombus ring laser in general the gain required of the discharge to produce lasing is different for the two polarisation modes. The frequencies of operation of the two modes are also different.

The choice of the sign in equation (2.25) for single mode operation can again be assigned by considering the case where the aplanarity approaches the limit $\beta = 0$. If the value for $\sqrt{\gamma^2 - \beta^2}$ is chosen so that the real part is positive then the positive sign must be chosen because the losses in the p-direction are greater than those in the s-direction for the mirrors.

2.2.7 Polarisation Characteristics of the Near-Planar Folded Ring Laser

The scale parameter β_{0f} is defined in a way similar to that for the skew rhombus ring laser above, namely,

$$\beta_{0f} = \frac{\sqrt{\tau^2 + \kappa^2}}{2 \sin \alpha}.$$

The type of polarisation produced depends on the ratio τ/κ. Figure (2.8) shows a corresponding set of polarisation diagrams to those in Figure (2.4).

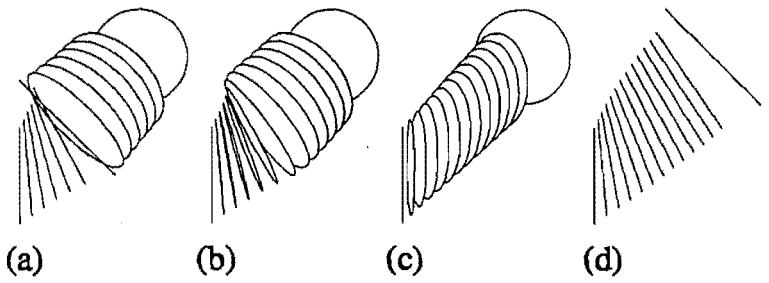

Figure 2.8: Polarisation modes for a near-planar folded ring laser as a function of the relative nonplanarity β/β_{0f} where the ratio τ/κ of differential reflectivity to differential birefringence has the values $\infty, 10, 0.1$ for (a), (b), (c), respectively. In (d), $\tau/\kappa = 0.1$ as for (c), but the ellipticity has been compensated by an $s-p$ phase shift (approximately $\pi/2$). In each case β/β_{0f} ranges from 0 to 2 in 12 steps, and the limiting case ($\beta = \infty$) of circular polarisation is included.

It can be seen that the two sets of diagrams are the same except that the change in orientation is in the anticlockwise direction. An order of magnitude comparison between the scale factors β_{0p} and β_{0f} can be made by choosing $\alpha = \pi/4$ in each case. Now since $\tau = \delta - \left(\delta_p^{'} - \delta_s^{'}\right)$, $\kappa = \chi - \left(\chi_p^{'} - \chi_s^{'}\right)$ and $\left(\delta_p^{'} - \delta_s^{'}\right) \ll \delta$, $\left(\chi_p^{'} - \chi_s^{'}\right) \ll \chi$ we can see that $\beta_{0p} \sim \beta_{0f}$, hence there is no real advantage of one topological configuration over the other.

2.2.8 Wünschelrute (Wishbone) Ring Laser

Another near-planar ring laser is created if we set $\alpha = \beta$, where α is considered small, for the folded ring laser (see Figure (2.9)).

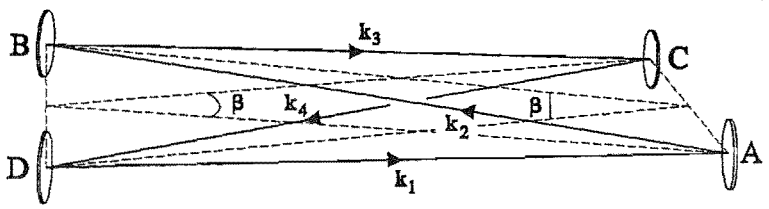

Figure 2.9: The closed geometrical ray-path for a beam propagating in the mirror cavity of a near-planar Wünschelrute ring laser. The beam is reflected from the mirrors at A, B, C and D. The horizontal and vertical dihedral (fold) angles are both β.

Because $\alpha = \beta$ the angle of incidence for all the mirrors is the same and this has consequences for the types of polarisation modes produced.

Because the configuration of the ring laser is a special case of the folded ring laser it is not necessary to recalculate the equation for the ratio of the polarisations A, the equation for the eigenvalue h or the gain of the discharge g required for lasing in the various modes, but requires making the appropriate adjustments which result

from setting $\alpha = \beta$ and being considered small. If we consider the defects for all the mirrors to be identical then we can write $G = G_1 = G_2 = (\delta_p + \delta_s) - i(\chi_p + \chi_s)$. The equation (2.25) for the folded ring laser becomes

$$A = \pm i,$$

that is, both the polarisation modes are circular, but of opposite handedness. We see that there is no dependence of the polarisation on β, hence there can no longer be the rapid change of polarisation we have seen in the above two configurations.

The eigenvalue equation becomes

$$h = g_w e^{ikL}\left\{1 - 2G \pm 2i\beta^2\right\}.$$

If we now invoke the conditions for cavity resonance we can obtain equations for the gain of the discharge g_w required to sustain oscillation for each mode and their frequency of operation f_w

$$\begin{aligned} g_w &= \frac{1}{1-2G}, \\ f_w &= \frac{c}{n\pi L}\left\{v\pi \mp \beta^2\right\}, \end{aligned}$$

where the negative sign is that associated with the right circularly polarised mode. It will be observed that the gain for both polarisation modes are the same which is what we should suspect from the topological symmetry of the geometrical ray-path for this ring laser design. This result also means that both polarisation modes are present at the same time. The degeneracy in the frequency of the modes is raised when $\beta \neq 0$ so that the frequency difference between the right and left circularly polarised modes is $\Delta f = 2c\beta^2/n\pi L$. It should be noted that now the dependence of Δf on β is quadratic.

If however we can pair the mirrors for their defects and makes the characteristics for one pair slightly different from the other pair in a controlled way then there is the possibility of producing a different outcome in the polarisation of the internal beam to the parameter β.

The scale parameter β_{0w} is defined this time by

$$\beta_{0w} = \frac{\sqrt[4]{\tau^2 + \kappa^2}}{\sqrt{2}}.$$

The polarisation ratio equation (2.25) for the folded ring laser now becomes

$$A = \frac{-\gamma \pm \sqrt{\gamma^2 - \beta^4}}{\beta^2},$$

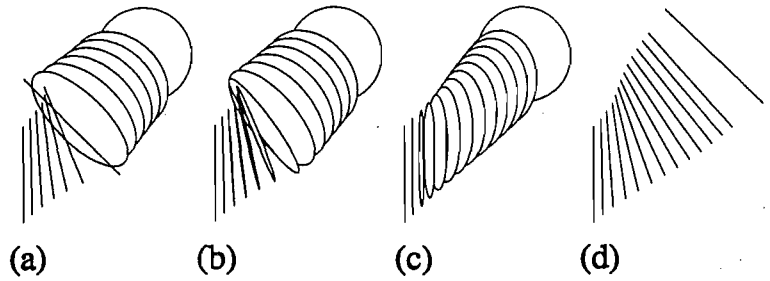

Figure 2.10: Polarisation modes for a near-planar Wünschelrute ring laser as a function of the relative nonplanarity β/β_{0w} where the ratio τ/κ of differential reflectivity to differential birefringence has the values $\infty, 10, 0.1$ for (a), (b), (c), respectively. In (d), $\tau/\kappa = 0.1$ as for (c), but the ellipticity has been compensated by an $s-p$ phase shift (approximately $\pi/2$). In each case β/β_{0w} ranges from 0 to 2 in 12 steps, and the limiting case ($\beta = \infty$) of circular polarisation is included.

where $\gamma = (\tau - i\kappa)/2$, and where $\tau = (\delta_p - \delta_s) - \left(\delta_p^{'} - \delta_s^{'}\right)$ and $\kappa = \left(\chi_p - \chi_s\right) - \left(\chi_p^{'} - \chi_s^{'}\right)$. The polarisation ellipses which result as β is varied are shown in Figure (2.10).

The potential sensitivity of this ring laser to change in planarity is much greater than for the previous two, however it will depend on how well the differential reflectivity and anisotropy of birefringence can be controlled in the two pairs of matched mirrors.

Chapter 3

Ring Laser Mirrors

The ability of a ring laser to unlock, the degree of frequency pulling when unlocked, and the polarisation of the final beam depend on the quality of its cavity mirrors. Metal coated mirrors will not be adequate for this application because their losses are too great. Multilayer dielectric-stack mirrors provide the necessary low loss, with state-of-the-art mirrors boasting power reflectances of better than 99.99997% and with further improvement possible. The means of improvement is discussed below in Section(3.3). Aside from the imperfections in the surface shape and scattering due to the roughness of the mirror surface there are two other types of defect which affect the performance of mirrors.

The first type is the loss in amplitude of the electric field vector of a beam on reflection from a mirror. In general the reflectivities in the p-(parallel) and s-(perpendicular) directions are different; this must be taken into consideration if a full treatment is required. The second type of defect is the anisotropy in birefringence, that is the change in relative phase between the p and s components of a beam on reflection. We shall see that both the power loss on reflection and anisotropy in birefringence can be controlled in the mirror manufacturing process and that both these defects can be minimised.

In order to investigate the above questions and others the author has constructed a computer program which calculates the power reflectance and the anisotropy in birefringence for a given mirror design, including angular effects and fluctuations in layer thickness. This program does not however take into account scattering as measured by the *TIS* (Total Integrated Scattering) parameter. A brief introduction to the theory on which the program is based follows.

3.1 Multilayer Dielectric-Stack Mirrors

Multilayer dielectric-stack mirrors are constructed by depositing alternate layers of high and low refractive index materials on a prefigured substrate. For example, state-

of-the-art gyro mirrors used by the author have a substrate of Zerodur upon which is deposited a $\lambda/4$-thick layer of TiO_2. Above this are stacked pairs of $\lambda/4$-thick layers where the top one is TiO_2 (high refractive index) and the bottom one is SiO_2 (low refractive index). To make the mirror surface more robust the stack is completed with a $\lambda/2$-thick layer of SiO_2 which is more chemically and physically resistant to damage than TiO_2. Figure (3.1) shows the typical construction of a dielectric-stack mirror.

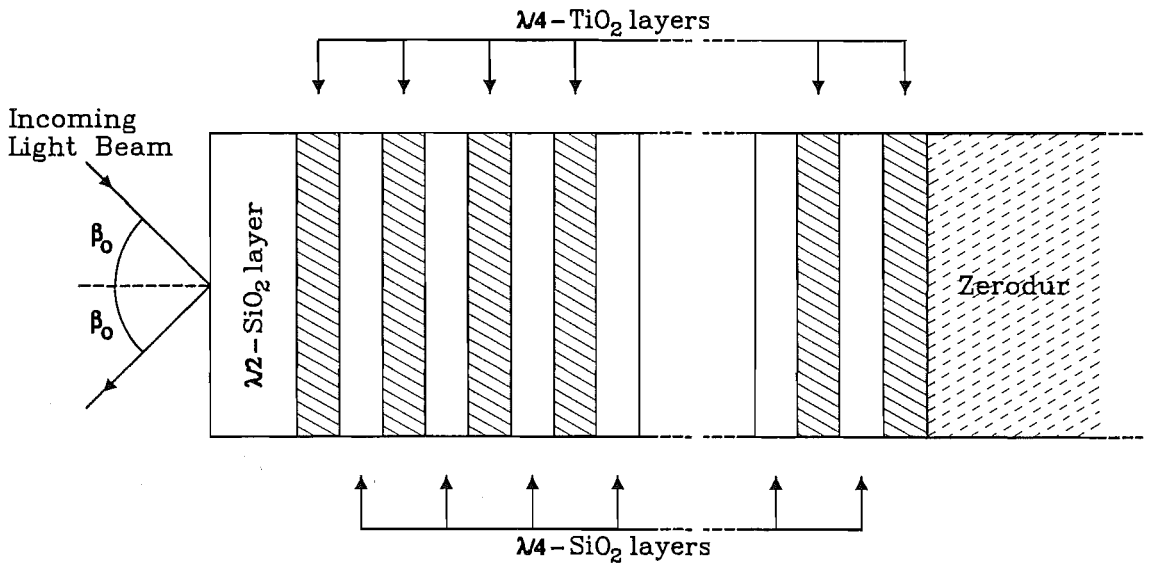

Figure 3.1: Construction of a dielectric-stack multilayer mirror.

3.1.1 The Thin-Film Layer Matrix

MacLeod[50] presents a matrix method which enables one to calculate the reflectance, the transmittance into the substrate, and the anisotropy in birefringence for a dielectric-stack mirror. Each layer of the stack is represented by a 2×2 complex matrix where it is assumed that: A harmonic plane-polarised wave is incident on a thin-film layer at oblique incidence; the layer material is treated as being isotropic (a good approximation for a nearly amorphous layer in state-of-the-art gyro mirrors) with the optical properties being represented by the complex refractive index $N = n - ik$. n is referred to as simply the refractive index and k is the extinction coefficient.

From the fact that the total tangential components of the electric and magnetic field vectors, respectively **E** and **H**, are continuous across an interface between adjacent layers MacLeod derives a relationship which connects the tangential components of **E** and **H** at the top interface (boundary a, see Figure(3.2)) with the tangential components of **E** and **H** at the bottom interface (boundary b). namely.

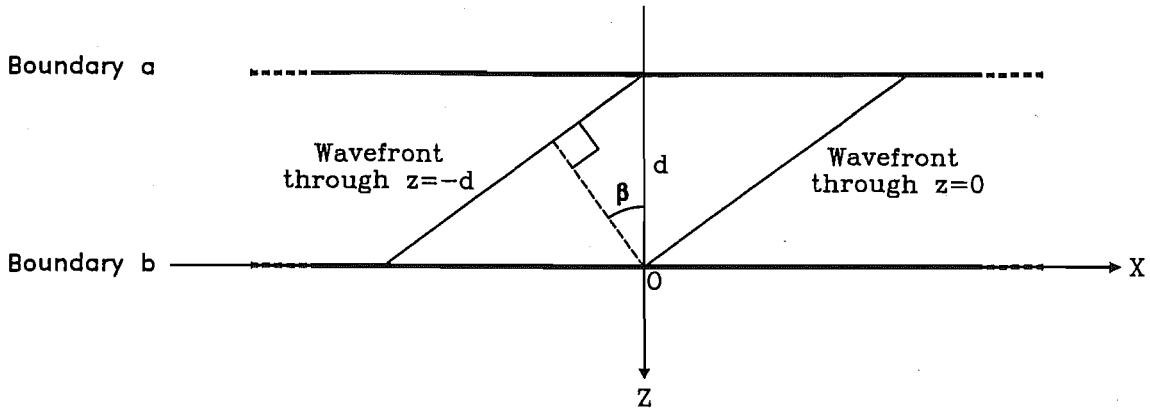

Figure 3.2: The phase difference δ is related to the physical distance $d\cos\beta$ between the wave fronts by $\delta = 2\pi N\,(d\cos\beta)\,/\lambda$

$$\begin{pmatrix} E_a \\ H_a \end{pmatrix} = \begin{bmatrix} \cos\delta & i\,(\sin\delta)\,/\eta \\ i\eta\sin\delta & \cos\delta \end{bmatrix} \begin{pmatrix} E_b \\ H_b \end{pmatrix}, \tag{3.1}$$

where δ is the difference in phase between the wave front at the top interface, a, and the one at the bottom interface, b, at the same instant and for the same x and y coordinates. The phase factor δ allows for the shift in z-coordinate the beam traversed from 0 to $-d$ and is given by

$$\delta = \frac{2\pi N d\cos\beta}{\lambda}. \tag{3.2}$$

The parameter η is the complex admittance and is defined by one of the two expressions

$$\eta_s = Ny_0\cos\beta,\ \ \eta_p = Ny_0/\cos\beta, \tag{3.3}$$

depending on, respectively, whether it is the s- or p- component of the harmonic plane-polarised wave which is being considered. The constant $y_0 = \sqrt{\varepsilon_0/\mu_0}$ is the free space admittance; ε_0 and μ_0 are the permittivity and permeability of free space, respectively. The factor $\cos\beta$ makes allowance for the use of the components of the waves parallel to the boundary and the energy flow normal to it.

Since the layer material has loss, the angle β takes on a complex value. Born and Wolf[18, p 611] define substances for which σ the specific conductivity is negligibly small as being insulators or dielectrics. Electrical conduction implies the evolution of Joule heat and therefore loss of electromagnetic energy. Hence, we may model loss in a dielectric layer by the introduction of a non-zero conductivity.

To demonstrate the need for this expanded law of refraction let us consider the propagation of a plane wave from vacuum into a conductor. Both the vacuum and the conductor assumed to be of infinite extent, the surface contact between them being the plane $z = 0$. Since the refractive index for vacuum has a value unity Snell's law can be written in the form

$$\sin\theta_t = \frac{1}{N}\sin\theta_i,$$

where θ_i is the angle of incidence: $N = n - ik$, the complex refractive index of the conductor, replaces the $\hat{n}$ defined by Born and Wolf. Since both k and n are real, in general, θ_t is complex and can no longer have the simple significance of an angle of refraction. This is reflected in the nature of a wave propagating in the conductive medium. Born and Wolf define such a wave to be inhomogeneous as the surfaces of constant amplitude and the surfaces of constant phase do not, in general, coincide with each other. In our work on the geometric dependence of polarisation in near-planar ring lasers[14] we assumed the 'angle of refraction' in a layer was a real quantity. As we have seen it is complex and to treat it as being real has a significant effect on the results when calculating the reflectance, transmittance into the substrate, and anisotropy in birefringence in multilayer dielectric-stack mirrors.

3.1.2 The Multilayer Mirror

The matrix equation describing a multilayer mirror is simply a development of the one layer matrix already given in equation (3.1). To accommodate more layers requires the layer matrices to be cascaded and multiplied together.

For example a two layer mirror has the equation

$$\begin{pmatrix} E_a \\ H_a \end{pmatrix} = \begin{bmatrix} \cos\delta_2 & (i\sin\delta_2)/\eta_2 \\ i\eta_2\sin\delta_2 & \cos\delta_2 \end{bmatrix} \begin{bmatrix} \cos\delta_1 & (i\sin\delta_1)/\eta_1 \\ i\eta_1\sin\delta_1 & \cos\delta_1 \end{bmatrix} \begin{pmatrix} E_c \\ H_c \end{pmatrix}.$$

The indexed parameters within each matrix show that the value appropriate to that layer must be used to replace it when the equation is evaluated.

For a dielectric-stack mirror with n layers we can use the extended form of Snell's law

$$\sin\beta_0 = N_1\sin\beta_1 = \cdots = N_j\sin\beta_j = \cdots = N_n\sin\beta_n, \tag{3.4}$$

where β_0 is the angle of incidence for the beam in the external medium and N_j, β_j are, respectively, the complex refractive index and the complex 'angle of refraction' in the jth layer. Since the extinction coefficients for all the materials in a mirror are small, first order approximations can be used in all expressions involving them. Hence from equation (3.4) we can write for the jth layer

$$\sin\beta_j = \sin\beta_0/(n_j + ik_j). \tag{3.5}$$

Use of the trigonometric identity $\cos^2\beta_j + \sin^2\beta_j = 1$ with equation (3.5) gives

$$\cos\beta_j = (1/n_j)\sqrt{{n_j}^2 - \sin^2\beta_0} - i\left(k_j\sin^2\beta_0\right) / \left({n_j}^2\sqrt{{n_j}^2 - \sin^2\beta_0}\right), \tag{3.6}$$

where the positive sign is chosen for the square root factors because the incident angle, β_0, is always in the first quadrant. We can now find an expression for the

complex phase factor, δ_j, by substituting equation (3.6) in equation (3.2) with the appropriate parameters and constants changed for the jth layer to get

$$\delta_j = n_j^{'} - ik_j^{'}, \tag{3.7}$$

where

$$n_j^{'} = (2\pi d/\lambda)\sqrt{{n_j}^2 - \sin^2\beta_0}, \quad k_j^{'} = (2\pi d n_j k_j/\lambda)\,/\sqrt{{n_j}^2 - \sin^2\beta_0}. \tag{3.8}$$

Hence

$$\cos\delta_j = \cos n_j^{'} + ik_j^{'}\sin n_j^{'}, \ \sin\delta_j = \sin n_j^{'} - ik_j^{'}\cos n_j^{'}.$$

To obtain the reflectance, the transmittance into the substrate, and anisotropy in birefringence for a mirror it is necessary to calculate its effective input optical admittance. The optical admittance, y, of a medium[50, p 25] is defined by

$$\mathbf{H} = y\,(\hat{\mathbf{s}} \times \mathbf{E})\,.$$

For a wave at oblique incidence to an interface within a given medium the optical admittance is defined as $\eta = H/E$ where H and E are, respectively, the magnetic and electric field components tangential to the interface. By analogy the input optical admittance of a whole mirror assembly at oblique incidence is defined by MacLeod to be

$$Y = H_a/E_a, \tag{3.9}$$

where E_a and H_a are the total tangential electric and magnetic fields either side of the top interface. By considering the contributions of the incident and reflected waves at the top interface MacLeod derives an expression for the reflectivity ρ in terms of the admittance η_0 of the incident medium (usually air or vacuum which is considered to be lossless) and the input optical admittance Y of the mirror itself, where

$$\rho = \frac{\eta_0 - Y}{\eta_0 + Y}. \tag{3.10}$$

The power reflectance R is given by

$$R = \rho\rho^* = \left(\frac{\eta_0 - Y}{\eta_0 + Y}\right)\left(\frac{\eta_0 - Y}{\eta_0 + Y}\right)^*,$$

where $*$ denotes complex conjugation. The phase-shift ϕ between the beam reflected from the mirror and the beam incident upon it can be obtained from MacLeod's equation (2.61)

$$\tan\phi = \frac{(-2b\eta_0)}{(\eta_0^2 - a^2 - b^2)},$$

where $Y \equiv a + ib$. An equivalent method, used in the computer program, is to find the phase difference between the complex expressions in the numerator and the denominator of the expression used to calculate the reflectivity. It remains to find an expression for Y from the matrix equation representing a mirror.

Let us suppose that a mirror has n layers then the electric and magnetic field components E_a and H_a, respectively, tangential to the interface of the mirror with the external medium are given by

$$\begin{pmatrix} E_a \\ H_a \end{pmatrix} = \begin{bmatrix} \cos\delta_n & (i\sin\delta_n)/\eta_n \\ i\eta_n \sin\delta_n & \cos\delta_n \end{bmatrix} \cdots \begin{bmatrix} \cos\delta_1 & (i\sin\delta_1)/\eta_1 \\ i\eta_1 \sin\delta_1 & \cos\delta_1 \end{bmatrix} \begin{pmatrix} E_z \\ H_z \end{pmatrix} \tag{3.11}$$

In this treatment the substrate is assumed to be of infinite thickness and so there is no wave within it reflected back towards the interface with the layer above, hence the components E_z and H_z are, respectively, the electric and magnetic field components tangential to the interface of the wave transmitted into the substrate from the multilayer stack. These components are related to the complex admittance η_z of the substrate by

$$H_z = \eta_z E_z. \tag{3.12}$$

From equations (3.9) and (3.11)

$$\begin{aligned} \begin{pmatrix} B \\ C \end{pmatrix} &\equiv \begin{pmatrix} E_a/E_z \\ E_a Y/E_z \end{pmatrix} \\ &= \begin{bmatrix} \cos\delta_n & (i\sin\delta_n)/\eta_n \\ i\eta_n \sin\delta_n & \cos\delta_n \end{bmatrix} \cdots \begin{bmatrix} \cos\delta_1 & (i\sin\delta_1)/\eta_1 \\ i\eta_1 \sin\delta_1 & \cos\delta_1 \end{bmatrix} \begin{pmatrix} 1 \\ \eta_z \end{pmatrix} \end{aligned} \tag{3.13}$$

so that $Y = C/B$. Hence from equations (3.13) and (3.10)

$$\rho = \frac{A}{Q}, \tag{3.14}$$

where $A \equiv B\eta_0 - C, Q \equiv B\eta_0 + C$ so that

$$\begin{pmatrix} A \\ Q \end{pmatrix} = \begin{bmatrix} \eta_0 & -1 \\ \eta_0 & 1 \end{bmatrix} \begin{bmatrix} \cos\delta_n & (i\sin\delta_n)/\eta_n \\ i\eta_n \sin\delta_n & \cos\delta_n \end{bmatrix} \cdots \begin{bmatrix} \cos\delta_1 & (i\sin\delta_1)/\eta_1 \\ i\eta_1 \sin\delta_1 & \cos\delta_1 \end{bmatrix} \begin{pmatrix} 1 \\ \eta_z \end{pmatrix}$$

The reflectance is given by

$$R = \rho\rho^* = \frac{AA^*}{QQ^*}. \tag{3.15}$$

The anisotropy in birefringence is found by calculating the phase difference between the complex quantities A and Q in equation (3.14)

The power transmittance into the substrate can also be calculated for the mirror assembly. MacLeod finds[50, p39]

$$T = \frac{I_z}{I_i} = \frac{\mathrm{Re}\,(\eta_z)\,(1-R)}{\mathrm{Re}\,(BC^*)}, \tag{3.16}$$

where I_z and I_i are, respectively, the intensities of the beam entering the substrate and the top layer of the mirror.

It may be observed in the computer program that the free space admittance, y_0, does not appear in any of the calculations. All layer matrices are of the form

$$\begin{bmatrix} a & b/y_0 \\ cy_0 & d \end{bmatrix}. \tag{3.17}$$

It is easy to show that all products of layer matrices are also of this form. The vector representing the properties of the substrate is of the form

$$\begin{bmatrix} e \\ fy_0 \end{bmatrix}. \tag{3.18}$$

Hence the equation representing the external medium in which the mirror is immersed, the layers and the substrate is of the form

$$\begin{aligned} \begin{pmatrix} A \\ Q \end{pmatrix} &= \begin{bmatrix} my_0 & -1 \\ my_0 & 1 \end{bmatrix} \begin{bmatrix} a & b/y_0 \\ cy_0 & d \end{bmatrix} \begin{bmatrix} e \\ fy_0 \end{bmatrix} \\ &= \begin{pmatrix} y_0\left((ma-c)\,e+(mb-d)\,f\right) \\ y_0\left((ma+c)\,e+(mb+d)\,f\right) \end{pmatrix}. \end{aligned}$$

From equation (3.14) we have

$$\rho = \frac{A}{Q} = \frac{(ma-c)\,e+(mb-d)\,f}{(ma+c)\,e+(mb+d)\,f},$$

where we see that the factor y_0 common to both the numerator and denominator has been eliminated from the expression.

The transmittance into the substrate can be treated in a similar manner. We start with equation (3.13) for just the substrate and the layers above. If we use (3.17) and (3.18) we can write the following vector equation to represent all the layers and the substrate of a mirror assembly as

$$\begin{pmatrix} B \\ C \end{pmatrix} = \begin{bmatrix} a & b/y_0 \\ cy_0 & d \end{bmatrix} \begin{bmatrix} e \\ fy_0 \end{bmatrix} = \begin{pmatrix} ae+bf \\ y_0\,(ce+df) \end{pmatrix} \tag{3.19}$$

The refractive index of the substrate, η_z, can be written in the form

$$\eta_z = N_z y_0 \cos^{\pm}\beta = y_0 M^{\pm}, \tag{3.20}$$

where $\cos^{+}\beta = \cos\beta$ and $\cos^{-}\beta = 1/\cos\beta$ account for the difference in the admittances in the s- and p-directions. If we use the expressions (3.14), (3.20) and the components of matrix equation (3.19) in equation (3.16) we get

$$T = \frac{\mathrm{Re}\,(M^{\pm})\left(1-\left|\frac{A}{Q}\right|^2\right)}{\mathrm{Re}\,\left((ae+bf)\,(ce+df)^{*}\right)},$$

where, as in the calculation for the reflectivity, the factor y_0 in common with both the numerator and denominator has been eliminated from the expression.

It can now be seen that the vast majority of the calculations determining the optical characteristics of a mirror are complex matrix multiplications, tasks which are easily implemented using a computer program.

3.2 Implementation of the Multilayer Mirror Calculation

The disk accompanying this work contains a Turbo Pascal program to calculate the reflectances and the birefringence of multilayer dielectric-stack mirrors. It was developed for the Borland Turbo Pascal 5.0 environment and actually consists of the main program called Mirror.pas and three Turbo Pascal Units called Cmatmul.pas, Mircalc.pas and Head.pas. Since the subprograms are interdependent the suite must be compiled in the order Cmatmul.pas, Mircalc.pas, Head.pas and finally Mirror.pas.

The program is divided up as follows. The subprogram Mirror.pas contains the primary interface with the user, the main menu. Although the program can be used to calculate the characteristics for a single mirror design the options presented allow the user to create a mirror design and vary one or more of the parameters to see its effect on the optical performance of a mirror. A mirror design requires the following data to complete its task: the angle of incidence of the incoming beam in degrees, its wavelength in nanometres, the number of $\lambda/4$-layer pairs, the refractive indices of the layer materials and the substrate, and the losses of the layer materials and the substrate. The high and low refractive index layers are referred to as 'Hi-Ref' and 'Low-Ref', respectively. The user is given the option of stepping one of the parameters over a given range of his or her choice. The layer depths can also be set to a fixed percentage of the ideal layer depth or given a percentage which is a random normal value chosen from a Gaussian distribution where the 3σ limit is chosen by the user. The purpose of this last selection is to run a Monte Carlo simulation of the optical characteristics of mirrors produced by a manufacturer where the depths of the layers randomly vary from a nominal value because of the tolerances in the manufacturing process. The user is able to choose the number of mirrors for the simulation. This subprogram also contains code to store and retrieve a design calculation option selected from the main menu.

The unit Mircalc generates the numerical values for the elements of the matrices used in the calculations. It also manages the actual mirror calculation and arranges for the results of the calculations to be sent to the output devices selected by the user. The results of any calculation consist of the loss in reflectance and the transmittance into the substrate for each of the p- and s- directions and the anisotropy in birefringence (labelled 'birefringence' on the monitor). The output is always presented on the monitor but the user can also select to send it to either the disk drive, the printer, or both.

The procedure Gap generates the random normal changes in the depth of the layers. The random normal (Gaussian) deviates were obtained by transforming random numbers generated by the computer whose values are uniformly distributed from 0 to 1 using the 'Box-Muller' method. Press et al.[68, p 288] describe this in their book 'Numerical Recipes in C'. The procedure was adapted for use with Pascal.

The actual matrix multiplications are performed by the Unit Cmatmul. The 2×2 complex matrices are stored in 3-dimensional arrays. At the conception of the matrix multiplication routine it was thought that the complex numbers should be stored in two parts, zero-order quantities and first-order quantities.

For the arrays used to store the 2×2 complex numbers the first two dimensions can be viewed as, respectively, the row and column of the 2×4 matrices with columns 1 and 2 holding the zero order quantities and columns 3 and 4 the first order quantities. The third dimension of the array is set to 1 to access the real part of the element and to 2 for the complex part. The routine accepts arrays in this form and returns the results in the same form after multiplication.

3.2.1 Results from using the Multilayer Mirror Program

One of the original reasons the multilayer mirror program was written was to test the hypothesis that the variations in anisotropy of birefringence could be attributed to the random variations in the depth of layers in multilayer dielectric-stack mirrors. In our work on the geometrical dependence of polarisation in near-planar ring lasers[14] we mention that the birefringence of a ring laser mirror has been measured to have a value of $\chi \sim 0.1$ rad. The physical construction of this mirror and the ones we possess is that shown in Figure (3.1), with each mirror having 11 pairs of $\lambda/4 - \lambda/4$ SiO_2-TiO_2 layer-pairs. We assigned the values of the material properties as follows: The refractive index for Zerodur was calculated to be $n_Z = 1.54$ from data given in the Schott catalogue[77]. The refractive index for SiO_2 (fused silica) $n_s = 1.46$ is that given by Kalb[41] which is also the same as that given by Kaye and Laby[42] rounded to two decimal places. The refractive index of TiO_2 given by Kalb as 2.40 was modified to 2.33 in view of our investigations[14]. There is further discussion about the values assigned to both SiO_2 and TiO_2 later in this section. The extinction coefficient for Zerodur was calculated to be 0.4 ppm and was also obtained from the data given in the Schott Catalogue. The extinction coefficients for TiO_2 and SiO_2 were nominally set to 2 ppm and 0.5 ppm, respectively. There is also discussion about the values which can be assigned to these last two material parameters later in this section. Unless otherwise stated the angle of incidence is 45° and the wavelength at which the measurements are taken is 633 nm. For convenience, mirrors with the above design will be referred to as 'our' mirrors.

Figure (3.3) shows the results of using the Monte Carlo method to simulate the effects of layer depth variation on the birefringence of 10000 of our mirrors.

For each mirror the depths of all the layers were given a random normal percentage variation from their ideal value with the values being selected from a distribution having a 3σ value of 5%. This $5\% - 3\sigma$ value was selected because the manufacturer claimed he could control the layer depths of mirrors to this accuracy.

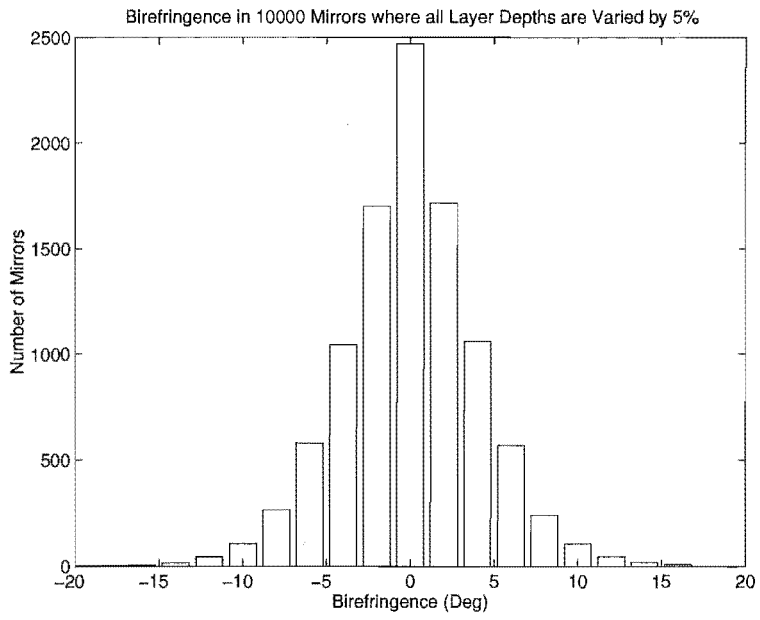

Figure 3.3: Distribution produced by using the Monte Carlo method to simulate the effects of layer depth variations on birefringence for 11 layer-pair real mirrors where the angle of incidence is 45°.

The distribution shown in Figure (3.3) has a standard deviation of 4.05° and a mean of 0.012°, hence the birefringence of the tested mirror is within 2 standard deviations of the mean. The fact that a distribution of birefringence values is produced as a result of layer depth changes and the fact that the measured birefringence of the mirror tested lies within 2 standard deviations of the mean makes a strong case for our original hypothesis.

In the same article[14] we also reported that the birefringence in mirrors could be adjusted after manufacture by etching the top protective $\lambda/2-SiO_2$ layer. The multilayer mirror program has since been used to demonstrate the principles of this. Figure (3.4) shows the resulting calculated birefringence of mirrors with our basic design, but where the top layer depth has been varied and all the other layers are of ideal depth.

It can be seen that the dependence is almost linear and that residual birefringence can be corrected with at most a 40% change in the top layer depth for nearly all mirrors produced by a manufacturer whose mirror deposition processes can be controlled so that all layers depths are within 5% of the ideal value. Naturally the manufacturer must ensure that the top layer is made at least 20% too thick in order to cater for the whole range of birefringence correction required. It also requires him to add another step in his manufacturing process.

Next we look at how the reflectance in both the s- and p-directions change with the number of $\lambda/4-\lambda/4$ layer-pairs for mirrors with our basic design. Multilayer mirrors

Figure 3.4: Birefringence produced when only the top protective SiO_2 layer is varied.

with lossless materials have the ultimate capability of being perfectly reflective. In Figures (3.5) and (3.6) (see the points labelled 'o') this is demonstrated by the loss in reflectance approaching the asymptotic limit of zero in both the s- and p-directions. Real mirrors have losses so one would expect that the loss in reflectance would never reach zero, no matter how many layer-pairs were applied. Figures(3.5) and (3.6) confirm this (see the points labelled '+') with the loss in reflectance in the s- and p-directions approaching finite limits.

A feature of dielectric-stack mirrors at non-zero incidence is that the loss in reflectance in the p-direction is greater than that in the s-direction. For mirrors with our design (11 $\lambda/4 - \lambda/4$ layer-pairs) it can be seen that this ratio is $\sim 37 : 1$. This has important consequences for the type of polarisation present in a near planar ring laser.

In our work 'Origin of fundamental limits for reflection losses at multilayer dielectric mirrors'[16] we discussed the sources of loss in dielectric-stack mirrors. They fall into three categories. The first is non-specular reflection from surface effects which is measured using a scatterometer where the measurements have units defined by the dimensionless parameter *TIS*. This type of loss is not taken into account directly by the multilayer mirror program. The second type of loss is from absorption by the mirror materials. The extinction coefficient k, being the imaginary part of the complex refractive index of the layer material, takes account of this in the mirror program. The last type of loss results from transmission of light into the substrate. This type of loss can be controlled by mirror design and we look at this next.

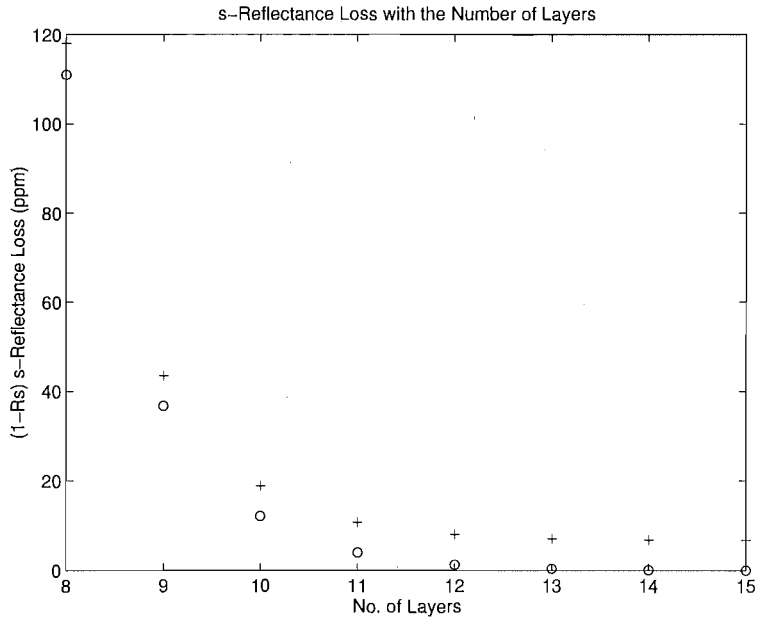

Figure 3.5: The reflectance loss in the s-direction for a mirror at 45° incidence whose basic design is the same as those we obtained, but where the number of $\lambda/4 - \lambda/4$ layer-pairs are stepped ('o' - no material losses, '+' - material losses which are the same as for our mirrors).

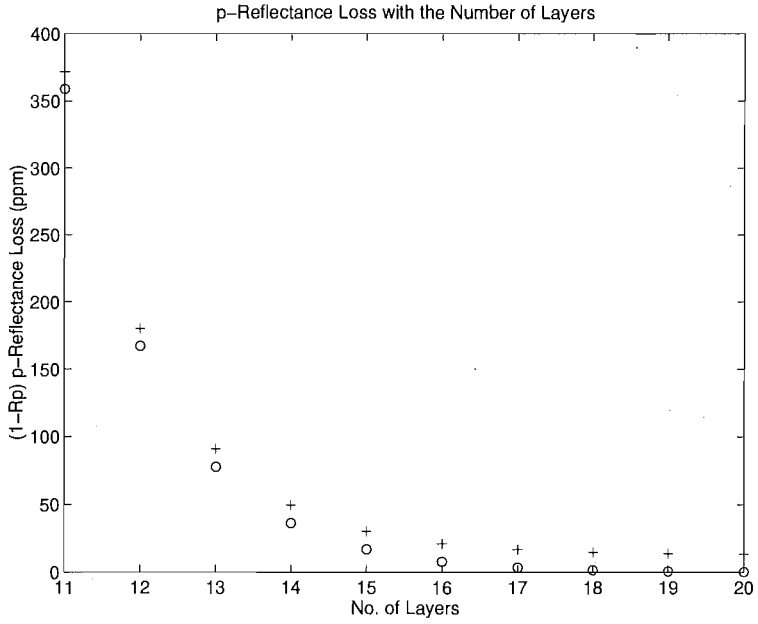

Figure 3.6: The reflectance loss in the p-direction for a mirror at 45° incidence whose basic design is the same as those we obtained and where the number of $\lambda/4 - \lambda/4$ layer-pairs are stepped ('o' - no material losses, '+' - material losses which are the same as for our mirrors).

Figures (3.7) and (3.8) show how the transmittance into the substrate changes with the number of $\lambda/4 - \lambda/4$ layer-pairs for mirrors of our design.

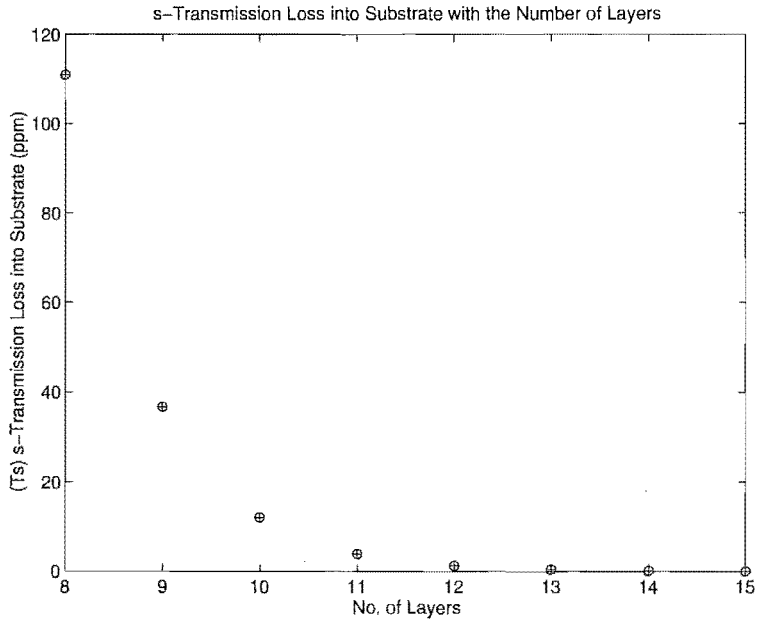

Figure 3.7: The transmittance into the substrate in the s-direction for a mirror at 45° incidence where the number of $\lambda/4 - \lambda/4$ layer-pairs are stepped ('o' - no material losses, '+' - material losses which are the same as those for our mirrors).

For comparison, at each point of the abscissa for which the transmittance has been calculated for mirrors of our basic design the transmittance has also been calculated for a mirror with the same design, but where the material losses are zero.

It is plain that absorption by the mirror materials at the ppm level has no part to play in limiting transmission into the substrate as the transmittance is the same for mirrors with and without losses. The very small absorption of the layer materials reduces both the reflected and transmitted beams by a very small fraction. However this is not visible for transmission, being directly plotted, but is for the reflectance since it is $1 - R$ that is being plotted and the fractional change is much greater.

It is easy to prove that absorption by the mirror materials at the ppm level has no part to play in limiting transmission into the substrate for normal incidence. In our work[16, p7393] we found the following complex matrix equation representing a dielectric-stack mirror with N $\lambda/4 - \lambda/4$ layer-pairs of ideal layer depth, but with no top $\lambda/2$ layer. With typographical corrections the equation is

$$\begin{pmatrix} a \\ b \end{pmatrix} = \gamma \begin{pmatrix} c \\ d \end{pmatrix} = \frac{(-1)^N j}{x^{N-1} y n_H} \begin{pmatrix} n_s x^{2N-1} y + \epsilon_1 {n_H}^2 \\ {n_H}^2 y/x + \epsilon_2 n_s z \end{pmatrix}, \tag{3.21}$$

where $x = n_L/n_H$, $y \equiv 1 - x^2, z \equiv 1 - x^{2N}, \epsilon_1 = \pi\left(k_H + k_L\right)/\left(2 n_H n_L\right), \epsilon_2 =$

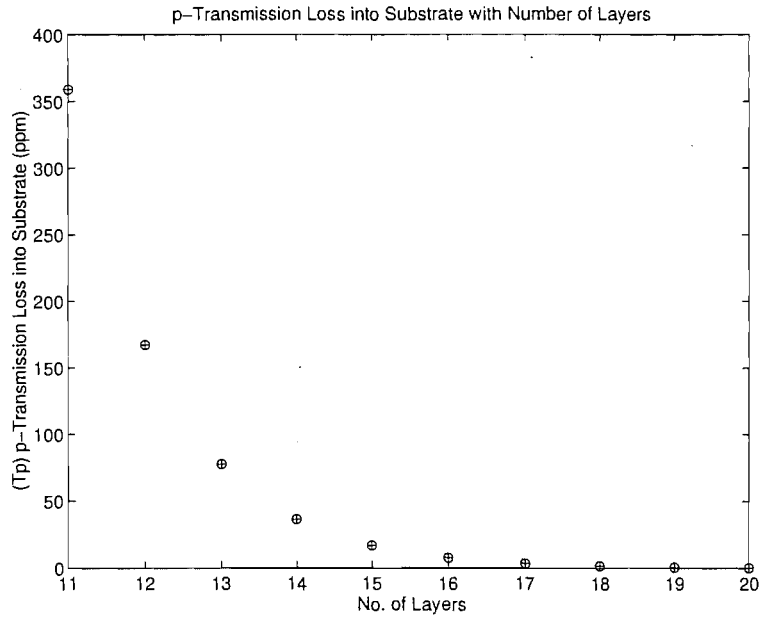

Figure 3.8: The transmittance into the substrate in the p-direction for a mirror at 45° incidence where the number of $\lambda/4 - \lambda/4$ layer-pairs are stepped ('o' - no material losses, '+' - material losses which are the same as for our mirrors).

$(\pi/2)\left[(n_H/n_L)\,k_L + (n_L/n_H)\,k_H\right], \gamma = \left[(-1)^N j\right] / \left[x^{N-1} y n_H\right]$; n_H, n_L are, respectively, the refractive indices for the high and low refractive index layer materials; k_H, k_L are the corresponding extinction coefficients. If we make the identification

$$\begin{pmatrix} a \\ b \end{pmatrix} \equiv \begin{pmatrix} B \\ C \end{pmatrix} \tag{3.22}$$

then we can use equation (3.15) to calculate the reflectance for the mirror in vacuum, i.e.

$$R = \frac{(c-d)^2}{(c+d)^2}.$$

The loss in reflectance is

$$1 - R = \frac{4cd}{(c+d)^2}. \tag{3.23}$$

Substitution in equation (3.16) using the appropriate factors from equations (3.21) and (3.23) in conjunction with definition (3.22) gives

$$T = \frac{4n_Z}{(c+d)^2\,|\gamma|^2},$$

where n_Z is the refractive index of the substrate material. To first order $c + d = n_H\left({n_H}^2 - {n_L}^2\right)/n_L$, hence we may write

$$T = \frac{4n_Z}{{n_H}^2}\left(\frac{n_L}{n_H}\right)^{2N}. \tag{3.24}$$

Equation (3.24) confirms at normal incidence what our observations on the graphs in Figures (3.7) and (3.8) had suggested, i.e. that for small extinction coefficients and to first order the transmittance into the substrate is independent of the losses of the materials of the mirror. It is reasonable to assume, and there is good evidence in the graphs in Figures (3.7) and (3.8), that the transmittance into the substrate is also independent of the material losses at non-zero incidence. This knowledge can be used to determine the indices of refraction for the SiO_2 and TiO_2 layer materials for a mirror whose layer depths are ideal.

A value for the refractive index of Zerodur calculated from data given in the Schott catalogue[77] is $n_Z = 1.540\,(\pm 0.003)$. We obtained measurements of the transmittance into air behind one of our mirror in the s- and p-directions of $T_s' = 3.9\,(\pm 0.1)$ ppm and $T_p' = 304\,(\pm 2)$ ppm[14, p134]. If we take account of the extinction in the Zerodur substrate and the loss in reflectance from the Zerodur-air interface at the back of the mirror the transmittance into the substrate in the s- and p-directions are, respectively, $T_s = 4.6\,(\pm 0.1)$ ppm and $T_p = 328\,(\pm 2)$ ppm. By using the mirror program with the value of the refractive index of Zerodur above and optimising the transmittances by adjusting the refractive indices for TiO_2 and SiO_2 the following respective values were obtained $n_H = 2.3854\,(\pm 0.001)$ and $n_L = 1.498\,(\pm 0.001)$. It may seem extraordinary that this type of accuracy can be obtained from values of the transmittance whose accuracy is one order of magnitude less, but consideration of the sensitivity of the transmittance to the change in refractive indices for normal incidence will explain this.

Ghausi[34, p363] defines sensitivity S_k^A as a measure of the degree of dependence of one quantity upon the value of another quantity where

$$S_k^A = \frac{k}{A} \cdot \frac{\partial A}{\partial k} = \frac{\partial \ln A}{\partial \ln k}. \tag{3.25}$$

For small Δk we can write

$$\frac{\Delta k}{k} = \frac{\Delta A}{A} \cdot \frac{1}{S_k^A} \tag{3.26}$$

The sensitivity of the transmittance to both the refractive indices n_L and n_H are found by substituting equation (3.24) in equation (3.25) and replacing A by T and k by either n_L or n_H. Hence

$$\begin{aligned} S_{n_L}^T &= \frac{\partial T}{\partial n_L} \cdot \frac{n_L}{T} = 2N \\ S_{n_H}^T &= \frac{\partial T}{\partial n_H} \cdot \frac{n_H}{T} = -\,(2N+2)\,. \end{aligned}$$

We can substitute these in equation (3.26) to get

$$\begin{aligned} \frac{\Delta n_L}{n_L} &= \frac{\Delta T}{T} \cdot \frac{1}{2N} \\ \frac{\Delta n_H}{n_H} &= -\frac{\Delta T}{T} \cdot \frac{1}{2N+2}. \end{aligned}$$

If Δn_L, Δn_H and ΔT are, respectively, the uncertainties in the refractive indices of the high and low refractive index layers and the transmittance then for an 11 layer-pair mirror it becomes apparent that the fractional uncertainty in the refractive indices is approximately one order of magnitude smaller than the fractional uncertainty in the transmittance, assuming that we are adjusting the refractive indices to optimise for the transmittance value. The negative sign for $S^T_{n_H}$ indicates that the direction of the fractional change in T is opposite that for the fractional change in n_H.

As we have seen it is possible to use the measured components of transmittance to determine the independent unknown components of refractive index for the high and low refractive index materials by optimisation using the multilayer mirror program. It must be pointed out that the accuracy with which the refractive indices can be found is dependent on the accuracy with which the transmittances can be determined for a mirror with ideal layer depths. Figure (3.9) shows distributions of transmittance in the s- and p-directions where the Monte Carlo method has been used to simulate the changes in all the layer depths expected from the tolerances involved in the manufacturing process. As with the distribution of birefringence above we assume that the layer depths change by a random normal percentage of their ideal depth where the percentage was selected from a distribution in which $3\sigma = 5\%$.

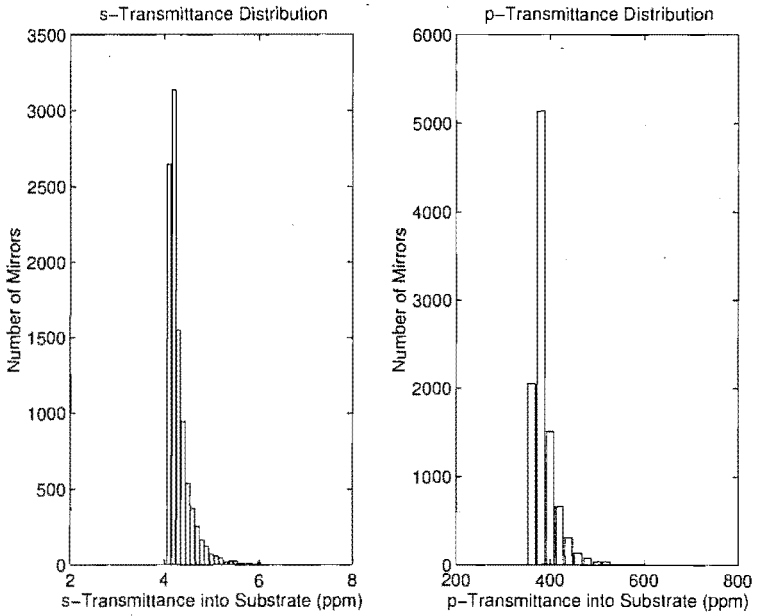

Figure 3.9: The distribution of s- and p-transmittances for mirrors at 45° incidence whose design is the same as ours, but where all the layer depths have been changed by a random normal percentage selected from a distribution where $3\sigma = 5\%$.

For a mirror whose design is the same as ours and whose layer depths are ideal the transmittance into the substrate in the s- and p-directions are, respectively, $T_s = 4.11$ ppm and $T_p = 366$ ppm. It will be observed that these values lie at the smallest extreme of the abscissa for the distributions in Figure (3.9). It might be thought that the mirror with ideal layer depths would have transmittances which lie at the mean or mode of the distributions. The ability of a mirror to limit transmission into

the substrate relies on the interference between the incident beam and the reflected beams within the mirror layers. It is only when ideal interference occurs that the transmittances are a minimum. Hence it is the mirror with least transmittance, all other parameters being constant, which has layer depths which are nearest ideal. This is confirmed when we observe where in the distributions shown in Figure (3.9) that the transmittances lie for the mirror whose layer depths are ideal, taking into account the way in which a histogram is prepared. Hence the mirror manufacturer who wished to know the refractive indices of the materials in the mirrors he makes will measure the transmittances of a batch of them and select the mirror with the lowest values and use them to estimate the refractive indices of the layer materials.

Once the refractive indices for the layer materials have been obtained it is possible to place upper limits on their extinction coefficients. If we suppose that the refractive indices for SiO_2 and TiO_2 are those we calculated earlier being, respectively, 2.3854 and 1.498 (we shall ignore the uncertainties as a principle is being explored here) and the s-reflectance loss has been measured to be $1 - Rs = 10.7\,(\pm 3)$ ppm (as measured for one of our mirrors[14]) then we can optimise for this value using the multilayer mirror program by adjusting the extinction coefficients. For this example if we attribute all the losses to TiO_2 then the maximum value for its extinction coefficient is $k_H = 4.5\,(\pm 1.8)$ ppm. Similarly if we attribute all the losses to SiO_2 then the maximum value for its extinction coefficient is $k_L = 0.8\,(\pm 0.4)$ ppm. In practice a mirror manufacturer would obtain the best value for the s-reflectance loss from a batch of mirrors and use this measurement to make estimates on the upper bounds of the extinction coefficients for the layer materials.

Figures (3.10) -(3.13) show the optical response of our mirrors to variations in some of the other mirror parameters. These have been added to give the reader a broad picture of the optical response of our multilayer mirrors.

3.3 The Origin of Losses in Multilayer Dielectric-Stack Mirrors

In our work 'Origin of fundamental limits for reflection losses at multilayer dielectric mirrors'[16] presented here towards the degree material we group the losses of beam intensity in multilayer dielectric-stack mirrors into three areas, light scatter as measured by *TIS* (totally integrated scattering), light absorbed by the mirror materials and transmission of light into the substrate with its subsequent loss out the back of the mirror.

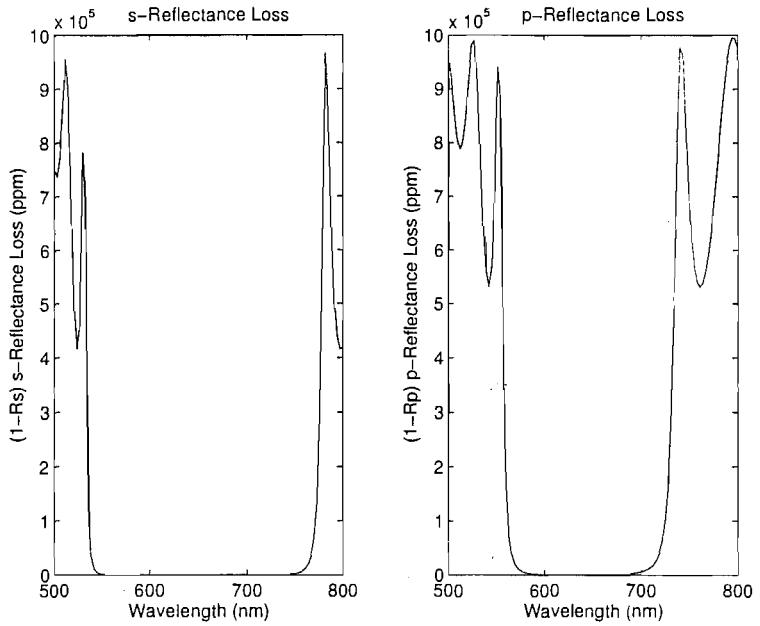

Figure 3.10: The reflectance loss in the s- and p-directions as a function of wavelength at 45° incidence for our mirrors.

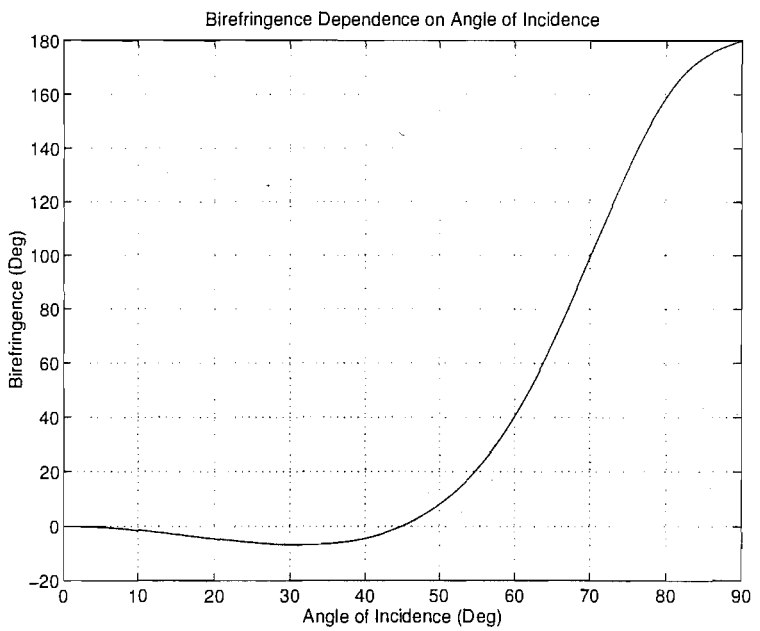

Figure 3.11: The anisotropy in birefringence as a function of the angle of incidence at a wavelength of 633 nm for our mirrors.

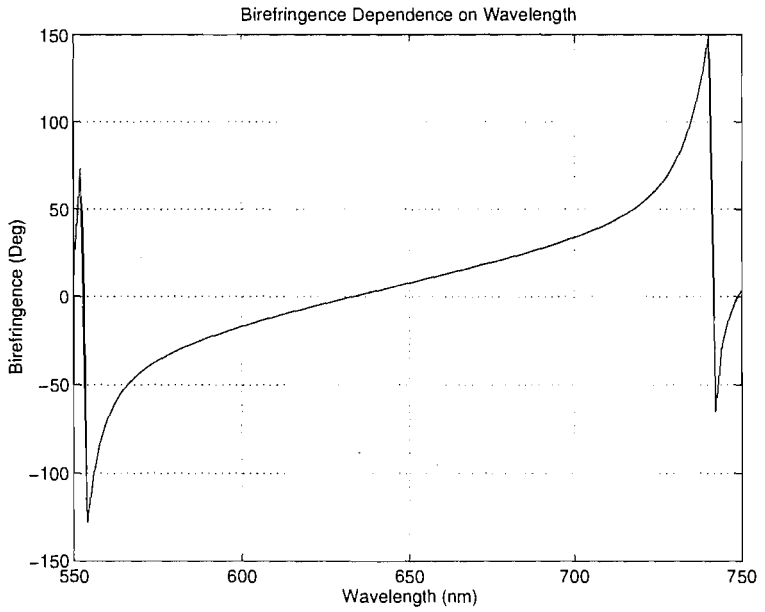

Figure 3.12: The anisotropy in birefringence as a function of the wavelength calculated at 45° incidence for our mirrors.

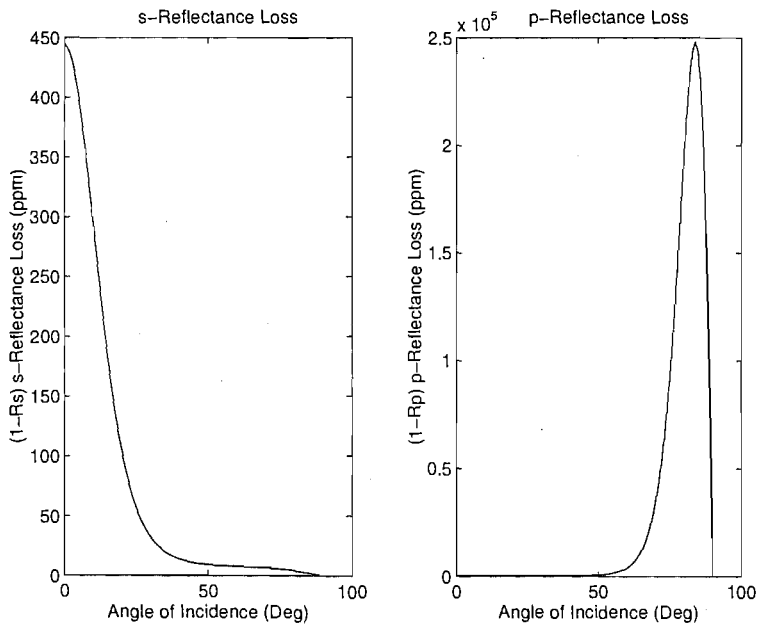

Figure 3.13: The reflectance loss in the s- and p-directions as a function of the angle of incidence at a wavelength of 633 nm for our mirrors.

3.3.1 Scattering as Measured by Total Integrated Scattering

The roughness of the top surface of a multilayer mirror is to a large degree controlled by the topography of the layers below it which in turn are dependent on the topography of the substrate on which they are deposited[89]. For a multilayer mirror at zero incidence the dependence of the coefficient of amplitude transmission T on the number of pairs of layers N has been found in equation (3.24). Since, in general, $n_L < n_H$ then $T \to 0$ as $N \to \infty$. Hence one can reduce the transmission into the substrate to being negligible compared to the incident beam on a mirror by applying enough $\lambda/4 - \lambda/4$ layer pairs. Figures (3.7) and (3.8) show that this is also true for mirrors at non-zero incidence. By this means it is possible to create a mirror for which the light reflected from the substrate is negligible and so the manufacturer is free to choose a substrate material for its other qualities, e.g. its surface smoothness, expansion coefficient and compatibility with the layer materials above.

For a flat mirror a clean cleaved surface might make an ideal substrate. The regularity of the molecular spacing on the cleaved surface of the substrate might, by itself, produce a diffraction pattern in a beam reflected from it however with ion-sputtered dielectric material deposited on it to a depth of several molecular diameters the new top surface will lose its crystalline regularity and follow the amorphous character which the method of deposition promotes. The surface roughness of optical materials have been estimated by measuring their *TIS*, using the following empirical relation

$$\sigma = \frac{\lambda}{4\pi}\sqrt{TIS}. \tag{3.27}$$

where λ is the wavelength of the light used in making the measurement. State-of-the-art methods now produce surfaces whose *TIS* is so low that the derived values of rms roughness parameter σ, using expression (3.27), has a value much less than the lattice constant. For example $\sigma = 0.05$ nm for a well prepared silicon surface[87] where the lattice constant for silicon is 0.54 nm. Also a roughness of $\sigma = 0.0188$ nm has been measured in SiO_2[16] and in another case one mirror has been measured to have $\sigma = 0.0166$ nm[16]. Equation (3.27) was derived assuming a random Gaussian distribution of surface roughness. This theory has been extended by the addition of lateral covariance functions to account for nonrandom or correlated surface features[32]. Improvement of the surface of the substrate, including the use of a cleaved surface, may produce scattering which is nonrandom, being not unlike that produced by a molecular grating. A better theoretical development which links *TIS* with surface roughness σ should take into account the local potential changes at the atomic scale having their maximum value at the surface. It should also be reasonable to assume that the bulk material is both homogeneous and isotropic. With the lattice spacing being much less than the wavelength of light used it is expected that interference will reduce the scattering much below that from isolated individual scattering centres whose distance apart is much greater than the lattice constant. Such theoretical development would require extension to the theory of scattering from rough surfaces based on a Fresnel-Huygens-Kirchhoff approach where the boundary conditions are dependent on the surface features being small compared to the wavelength

of light[46].

Currently available surface scans universally indicate that the principal contribution to nonspecular scattering is that of isolated individual scattering centres. Scanning tunnelling microscopes are now making a contributions in this area[71]. For future substrates we anticipate a decrease of the density of such isolated scattering centres to negligible magnitudes; the scattered power off the resulting surfaces should then be negligible even at the parts in 10^9 (ppb) level.

Surface effects, such as scattering losses along interface boundaries caused by the density fluctuations of two blending species and their stoichiometric differences, might be argued to play a much more important role in mirror coatings as opposed to optical fibres, and so might be expected to distinguish their fundamental limits, disallowing the parallel we draw. However, the use of a graded refractive index is a critical feature of both systems and over similar linear dimensions, and itself raises related issues concerning stoichiometry, homogeneity, extra absorption losses, and vitrification in the transition regions. The success of optical fiber technology in approaching the fundamental loss limits of the bulk materials therefore is evidence that such concerns are not insurmountable at the ppb level, and it is relevant to our interest in the ppb loss regime in the context of surface effects as well as of volume effects.

3.3.2 Absorption near the Band Gap

For SiO_2 and TiO_2 material which has been purified of absorbing paramagnetic ions there is an empirical relation called Urbach's Rule which predicts the absorption α. It is defined by

$$\alpha = A \exp\left(\sigma\hbar\left(\omega - \omega_0\right)/k_B T\right),$$

where k_B is Boltzmann's constant, T is the temperature and A, σ, and ω_0 are fitted to the data. The relationship between the absorption α and the extinction coefficient k is given by

$$\alpha = \frac{4\pi k}{\lambda},$$

where λ is the wavelength at which the measurement is being made. Present estimates for k for TiO_2[41] suggest that its extinction coefficient gives the fundamental limit on absorption A and hence on the reflectance in multilayer mirrors.

The estimate of k has been reduced over the years with its magnitude lowering by one order per 2 years over the last 10 years (see Figure (3.14)).

Wei[90] documents an order of magnitude per 6 years over the last 20 years. We consider that there is a possibility for further dramatic reduction and look at the fundamental mechanisms contributing to the value of k in TiO_2. This material is a

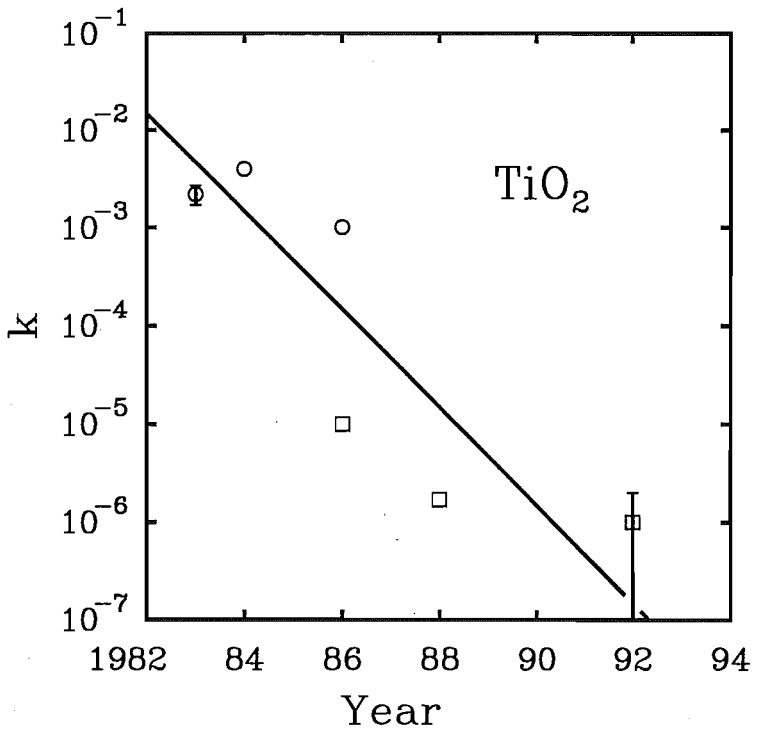

Figure 3.14: Progress in lowering the exctinction coefficient k for TiO_2 over recent decades as evaluated for data, mostly in the literature, on finished mirrors. Circles denote data taken at 500 nm: 1983,[27]; 1984,[72]; 1986,[80]. Squares denote data taken at 633 nm: 1986,[41]; 1988 our estimate by difference from measurements of R, S, T on a 1988 set of supermirrors:[14]; 1992, as for our 1988 measurements, but using more recent supermirrors (unpublished). Here k is either taken directly from the literature cited above or is evaluated from R after subtraction of TIS and transmission losses. The line has a slope of $-1/2$ and indicates 1 order of magnitude improvement per 2-yr period.

dielectric and an insulator which exhibits a large band gap of 3.05 eV (neglecting the fine detail due to anisotropic band structure of the various crystalline forms). As a consequence there is a nominal limit on the transparency at 407 nm. The visible part of the spectrum is at present limited by impurities and in the infrared it is opaque due to phonon resonances (see Figure (3.15)).

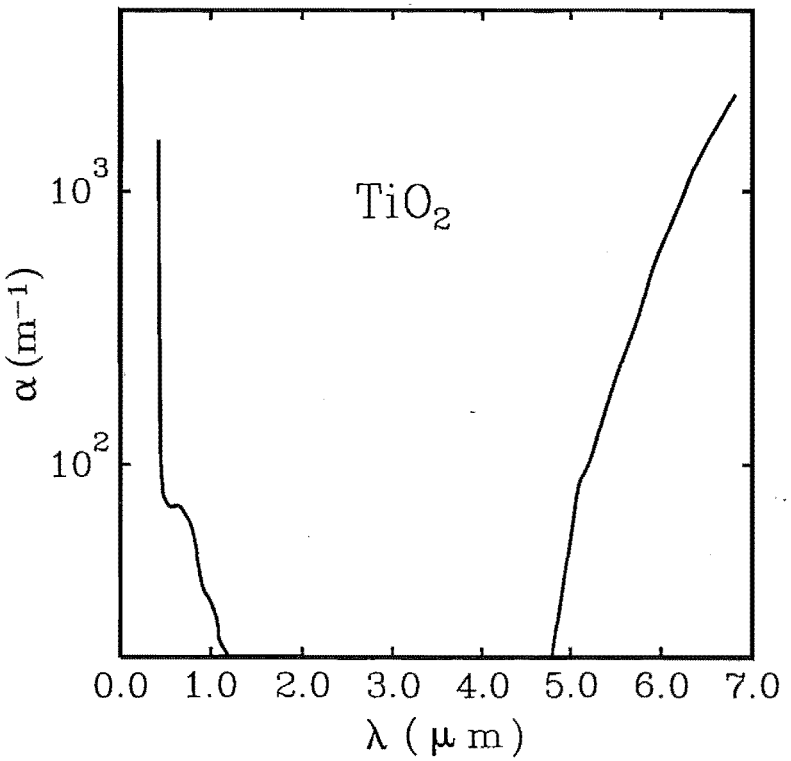

Figure 3.15: Plot of absorption coefficient α of a slab of bulk TiO_2 after subtraction of the surface reflection (after Cronemeyer[25]).

Between the limits produced by the band gap and the phonon resonances is a usable window. The Urbach tail from the band gap in the UV is the most obvious limitation. An equivalent tail from the IR phonon resonances produces much less absorption than from the band gap as it starts at $\lambda \geq 5$ μm.

The data on absorption is contradictory with DeVore[28] proposing a single oscillator model for the index of refraction of TiO_2 from the band gap to 15 μm. The extinction coefficient would vary as with an inverse power law according to the Kramers-Kronig relations. This would make the extinction coefficient vary as the inverse of the wavelength. This is clearly not the case for the direct measurements from Cronemeyer[25]. Figure (3.16) shows an essentially linear relationship between $\log \alpha$ and λ^{-1} which transforms to $k \propto \lambda \exp(-a/\lambda)$.

We attribute the nonlinearity of the graph in Figure (3.16) to impurities. This means that the extinction coefficient of clean TiO_2 at 500 nm would be less than 10^{-11}, a value similar to that for the cleanest fused SiO_2. Decades of work in the

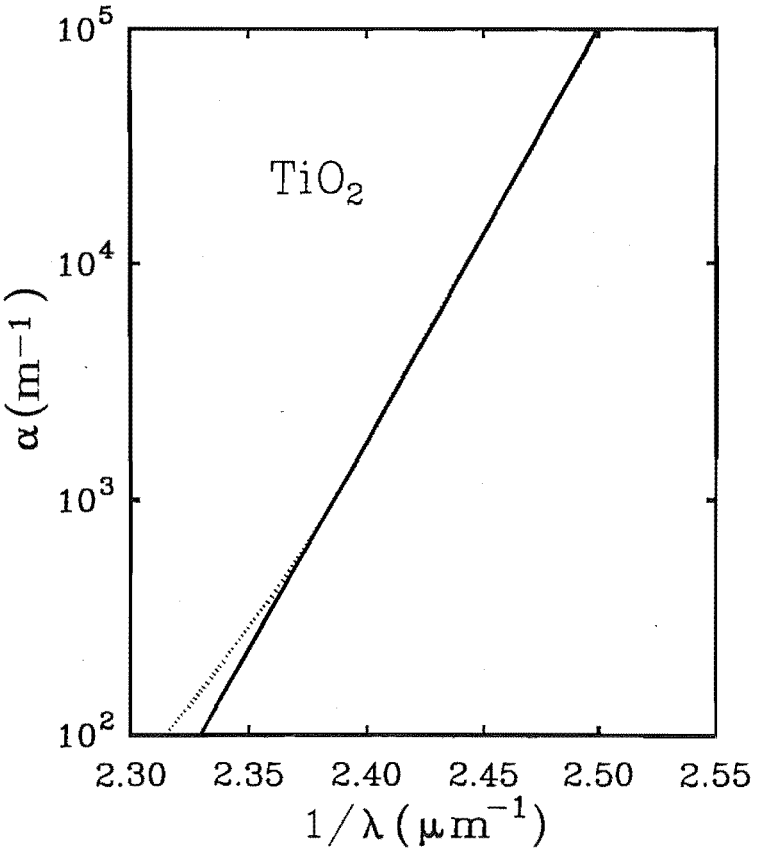

Figure 3.16: Urbach tail for TiO_2 in the visible (400–430 nm), after Cronemeyer[25]. The deviation from linearity is attributed to impurities; a linear fit to this tail (solid line) gives on extrapolation to 500 nm an extinction coefficient of less than 10^{-11}.

optical fibre industry has resulted in the best fibres (fused silica) having a loss of only 0.15 dB/km at $\lambda = 1.55\ \mu$m. This corresponds to $k = 4 \times 10^{-12}$[38]. This figure includes Rayleigh scattering from density fluctuations and residual phonon absorption as well as the Urbach tail in silica.

The data for TiO_2 from Cronemeyer is for crystalline material. In multilayer mirrors TiO_2 is deposited in an amorphous form to avoid the crystallite scattering. The crystal data shows exciton peaks at low temperature but such exciton activity in amorphous materials is questionable. The slope of the semilog plot for the Urbach tail can decrease when the material becomes amorphous[60, p 240].

In summary, currently available measurements of absorption in TiO_2 have extinction coefficients several orders of magnitude greater than the extrapolated values given above. This is presumed to be due to impurities like paramagnetic ions[63]. It is an extrapolation from current measurements to suggest that TiO_2 will be as amenable as SiO_2 to high purification, but the above evidence does not support a significant distinction between TiO_2 and SiO_2 in this regard. The extrapolation deserves to be investigated.

3.3.3 Rayleigh Scattering from Density Variations in the Layer Volume

Another loss process which removes power from a coherent beam reflected from a multilayer mirror is due to Rayleigh scattering from density variations within the layers. This may be treated more like an absorption process than one which produces scattering measured by *TIS*. Reduction of loss from this source requires that crystallisation be avoided at all costs. The modern technique of creating multilayer mirrors by ion-beam sputtering[51] results in more energy being given to the vapour being deposited on the surface of a mirror during the creation of a layer. The greater impact of the molecules in the vapour with the surface results in greater disorder in the material deposited. This, combined with the lower temperature of the surface on which the material is being deposited causing a high quench rate, results in the disorder being frozen into the surface as there is no time for grain boundaries to form. The admixture of a few percent of SiO_2 in the TiO_2 layer material also helps by suppressing crystallisation in the TiO_2[80]. The density fluctuations are then thermodynamically determined and this dominates the Rayleigh scattering[51][63].

The mean square density fluctuations $\langle \delta\rho^2/\rho^2 \rangle = k_B T_f \bar{k}/V$ are given by Oster[64] and Becker[9], where T_f is the absolute temperature at which the fluctuations are established, $\bar{k}$ is the bulk compressibility, and V is the layer volume.

The extinction coefficient which results from this scattering process is[63]

$$k_r = 2\pi^2 \left({n_r}^2 - 1\right)^2 k_B T_f \bar{k}/3{\lambda_0}^3.$$

Comparison of the Rayleigh limits for SiO_2 and TiO_2 show that they are of similar magnitude ($T_f \sim 1800 - 2000$ K, $n \sim 1.5 - 2.33$, $\bar{k} \sim 2.7 - 1.5 \times 10^{-11}$ Pa^{-1}, $\lambda_0 = 500$ μm) with the extinction coefficients being $k_r \simeq 1.0 \times 10^{-10}$. This limit is 4 orders of magnitude better than the current value (see Figure(3.14)). As mentioned above thermodynamic fluctuations in the interface may also cause loss due to nonspecular reflections[46], but it should be of the same level as for Rayleigh scattering discussed above.

Chapter 4

Beam Control and Beam Stability with Offsets

Experimental measurement of the polarisation of the beam in a near-planar square ring laser as a function of the aplanarity of the geometrical ray-path of the beam requires that one must be able to control the aplanarity. A related topic is the stability of the geometrical ray-path for the beam in a ring laser and this has already been studied[37][33][13], but controlling the beam so as to position the point at which the geometrical ray-path intercepts each mirror has not. Bilger and Stedman[13] show that, in general, given the displacement and tilt of cavity mirrors in a symmetric near-planar ring laser the position at which the geometrical ray-path of the beam intercepts each of the mirrors can be predicted. By inverting their equations it is shown below that given the positions at which the geometrical ray-path of the beam intercepts the mirrors and the displacements of the poles of the mirrors it is possible to predict the necessary tilt and displacement of the mirrors to achieve this.

For the experiment it was proposed that the mirror cavity be composed of pairs of spherical and planar mirrors placed opposite each other. It is shown below that for this case the tilt of the planar mirrors determines the aplanarity of the ray-path. However, for the ray-path to close in the mirror cavity it is shown that one of the curved mirrors must also be tilted. To familiarise the reader with the definitions used by Bilger and Stedman a derivation of their main equations is given.

4.1 Beam Control in the Symmetric Ring Laser

Let a planar ring laser mirror cavity consist of N mirrors, each having a spherical surface with radius of curvature R_i, i=1,$\cdots$, N. Let the poles of the mirrors lie at the vertices, $I_1 - I_N$, of a symmetric N-polygon with side length l; itself the design ray-path for the ring. Consider a general reflection.

Local cartesian axes at the poles of each of the mirrors are chosen so that x is normal to the surface of the mirror at the pole, y is orthogonal to this and lies in the plane of the design ray-path and z is in the out-of-plane direction. The coordinate

system for the whole ring is aligned with that of the ith mirror, but has its origin at the centre of the ring (see Figure 4.1). Let $\mathbf{r}_i = (0, \beta_i, \gamma_i)^T$ be the point at which

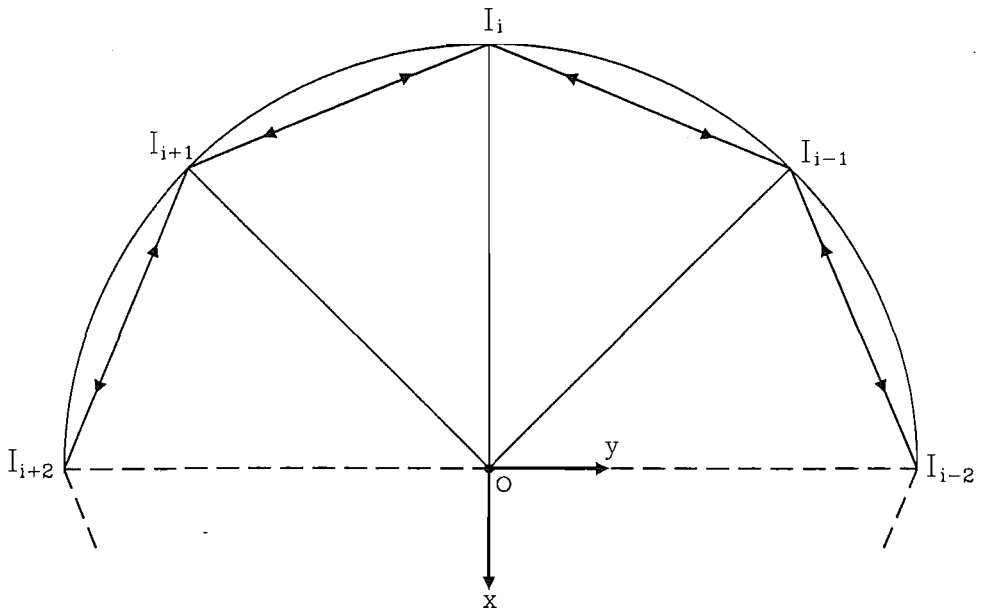

Figure 4.1: Ray-path of the beam internal to a ring laser where the mirror cavity is formed with N mirrors symmetrically arranged at the vertices of an N-sided polygon.

the laser beam internal to the cavity intercepts the ith mirror. where β_i and γ_i are first-order displacements from the pole along the local y-and z-axes, respectively.

Now let the mirrors of the initially planar and ideally adjusted ring laser be misadjusted so that the pole of the ith mirror is displaced by $(\xi_i, \eta_i, \zeta_i)^T$ parallel to the local coordinate system and the mirror itself is tilted about the local y- and z-axes through angles θ_i, φ_i, respectively. All misadjustments are assumed to be small and their effects considered only to first order.

Under small mirror tilts only, the point, $(0, \beta_i, \gamma_i)^T$, at which the beam intercepts the ith mirror does not change, but the normal to the mirror is transformed from $\mathbf{n}_i' = (1, -\beta_i/R_i, -\gamma_i/R_i)^T$ to

$$\mathbf{n}_i = \begin{pmatrix} 1 \\ \varphi_i - \beta_i/R_i \\ -\theta_i - \gamma_i/R_i \end{pmatrix}. \tag{4.1}$$

Under combined displacement and tilt, when evaluated in the local coordinate system, the point at which the beam hits the mirror is

$$\mathbf{s}_i = \begin{pmatrix} \xi_i \\ \beta_i + \eta_i \\ \gamma_i + \zeta_i \end{pmatrix}, \tag{4.2}$$

with the normal to the mirror at this point being still given by equation (4.1) .

If we define $\mathbf{s}_{k,l} \equiv \mathbf{s}_l - \mathbf{s}_k$ then the direction with which incident ray hits the ith mirror is given by $\mathbf{s}_{i-1,i} = D(\pi/N + \pi/2)\mathbf{s}'_{I-1}$ where

$$\mathbf{s}'_{I-1} = \begin{pmatrix} l - (\beta_i - \beta_{i-1})\, c - (\xi_i + \xi_{i-1})\, s - (\eta_i - \eta_{i-1})\, c \\ -(\beta_i + \beta_{i-1})\, s + (\xi_i - \xi_{i-1})\, c - (\eta_i + \eta_{i-1})\, s \\ (\gamma_i - \gamma_{i-1}) + (\zeta_i - \zeta_{i-1}) \end{pmatrix},$$

defined for a right handed coordinate system where the origin is located at $(1/2)\,\mathbf{I}_{i-1}\mathbf{I}_i$, the midpoint between the vertices I_{i-1} and I_i of the design ray-path, the x-axis is directed along, $\mathbf{I}_{i-1}\mathbf{I}_i$, the y-axis is orthogonal to this and lies in the plane of the design ray-path and the z-axis is in the out-of-plane direction; $D\,(\pi/N + \pi/2)$ is the rotation matrix transforming the coordinate system just defined into the ring's coordinate system; $c \equiv \cos(\pi/N)$ and $s \equiv \sin(\pi/N)$. A unit vector parallel to $\mathbf{s}'_{I-1}$ is

$$\widehat{\mathbf{s}}'_{I-1} = \begin{pmatrix} 1 \\ -(\beta_i + \beta_{i-1})\, s/l + (\xi_i - \xi_{i-1})\, c/l - (\eta_i + \eta_{i-1})\, s/l \\ (\gamma_i - \gamma_{i-1})\, /l + (\zeta_i - \zeta_{i-1})\, /l \end{pmatrix}$$

so that in the coordinate system of the ring

$$\widehat{\mathbf{s}}_{i-1,i} = D\,(\pi/N + \pi/2)\,\widehat{\mathbf{s}}'_{I-1}. \tag{4.3}$$

By similar reasoning a unit vector in the direction of the reflected ray at the ith mirror is

$$\widehat{\mathbf{s}}_{i,i+1} = D\,(\pi/2 - \pi/N)\,\widehat{\mathbf{s}}'_{I+1}, \tag{4.4}$$

where $\widehat{\mathbf{s}}'_{I+1} = \begin{pmatrix} 1 \\ -(\beta_{i+1} + \beta_i)\, s/l - (\eta_{i+1} + \eta_i)\, s/l - (\xi_{i+1} - \xi_i)\, c/l \\ (\gamma_{i+1} - \gamma_i)\, /l + (\zeta_{i+1} - \zeta_i)\, /l \end{pmatrix}.$

By specular reflection, the incident and reflected rays and the normal to the mirror at the point of reflection are coplanar: represented by

$$(\widehat{\mathbf{s}}_{i,i-1} + \widehat{\mathbf{s}}_{i,i+1}) \times \mathbf{n}_i = \mathbf{0}. \tag{4.5}$$

If we define

$$\widehat{\mathbf{s}}_{i,i-1} + \widehat{\mathbf{s}}_{i,i+1} \equiv (p, q, r)^T \tag{4.6}$$

then by substitution from equations (4.3) and (4.4) we get

$$\begin{gathered} p = 2s - (\beta_{i+1} - \beta_{i-1})\, sc/l - (\eta_{i+1} - \eta_{i-1})\, sc/l + (\xi_{i+1} - 2\xi_i + \xi_{i-1})\, c^2/l, \\ q = -(\beta_{i+1} + 2\beta_i + \beta_{i-1})\, s^2/l - (\eta_{i+1} + 2\eta_i + \eta_{i-1})\, s^2/l + (\xi_{i+1} - \xi_{i-1})\, sc/l, \\ r = (\gamma_{i+1} - 2\gamma_i + \gamma_{i-1})\, /l + (\zeta_{i+1} - 2\zeta_i + \zeta_{i-1})\, /l. \end{gathered}$$

Use of the definition (4.6) and substitution of (4.1) in equation (4.5) gives

$$q\,(-\theta_i - \gamma_i/R_i) = r\,(\varphi_i - \beta_i/R_i) \tag{4.7}$$

$$r = p\,(-\theta_i - \gamma_i/R_i) \tag{4.8}$$

$$q = p\,(\varphi_i - \beta_i/R_i) \tag{4.9}$$

If we substitute for p, q, and r in equations (4.8) and (4.9) and then collect on one side of each equation the variables representing the displacements of interception point of the ray-path from the poles of the mirrors and on the other the variables representing tilts and displacements of mirrors we get

$$\gamma_{i+1} - \Gamma_i \gamma_i + \gamma_{i-1} = -2sl\theta_i - \left(\zeta_{i+1} - 2\zeta_i + \zeta_{i-1}\right), \tag{4.10}$$

$$\beta_{i+1} - B_i \beta_i + \beta_{i-1} = -2l\varphi_i/s + (c/s)\left(\xi_{i+1} - \xi_{i-1}\right) - \left(\eta_{i+1} + 2\eta_i + \eta_{i-1}\right), \tag{4.11}$$

where $\Gamma_i = 2\left[1 - (sl/R_i)\right]$ and $B_i = 2\left[(l/(sR_i)) - 1\right]$. We can make the identification

$$\begin{aligned} \mathcal{G}_i &= -2sl\theta_i - \left(\zeta_{i+1} - 2\zeta_i + \zeta_{i-1}\right), \\ \mathcal{B}_i &= -2l\varphi_i/s + (c/s)\left(\xi_{i+1} - \xi_{i-1}\right) - \left(\eta_{i+1} + 2\eta_i + \eta_{i-1}\right) \end{aligned}$$

which are Bilger and Stedman's equations (20).

We now extended the work of Bilger and Stedman[13]. First we cast their equation (18) into full matrix form. Associated with each mirror of the ring are the two equations represented by (4.10), (4.11) with the subscripts appropriately adjusted. These pairs of equations can be collected into the pair of matrix equations

$$[D_N]\,\boldsymbol{\gamma} = -(2sl)\,[I_N]\,\boldsymbol{\theta} - [Z_N]\,\boldsymbol{\zeta}, \tag{4.12}$$

$$[B_N]\,\boldsymbol{\beta} = -(2s/l)\,\boldsymbol{\varphi} + (c/s)\,[X_N]\,\boldsymbol{\xi} - [Y_N]\,\boldsymbol{\eta}. \tag{4.13}$$

where

$$[D_N] = \begin{bmatrix} -\Gamma_1 & 1 & 0 & 0 & \cdots & 0 & 0 & 0 & 1 \\ 1 & -\Gamma_2 & 1 & 0 & \cdots & 0 & 0 & 0 & 0 \\ 0 & 1 & -\Gamma_3 & 1 & \cdots & 0 & 0 & 0 & 0 \\ 0 & 0 & 1 & -\Gamma_4 & \cdots & 0 & 0 & 0 & 0 \\ \cdot & \cdot & \cdot & \cdot & \cdots & \cdot & \cdot & \cdot & \cdot \\ \cdot & \cdot & \cdot & \cdot & \cdots & \cdot & \cdot & \cdot & \cdot \\ 0 & 0 & 0 & 0 & \cdots & 1 & -\Gamma_{N-2} & 1 & 0 \\ 0 & 0 & 0 & 0 & \cdots & 0 & 1 & -\Gamma_{N-1} & 1 \\ 1 & 0 & 0 & 0 & \cdots & 0 & 0 & 1 & -\Gamma_N \end{bmatrix},$$

$[I_N]$ is the $N \times N$ unit matrix, $[Z_N]$ is the same as matrix $[D_N]$ with $\Gamma_i \longrightarrow 2$; $[B_N]$ is the same as $[D_N]$ with $\Gamma_i \longrightarrow B_i$, $[Y_N]$ is the same as $[D_N]$ with $-\Gamma_i \longrightarrow 2$, and

$$[X_N] = \begin{bmatrix} 0 & 1 & 0 & \cdots & 0 & 0 & 0 & -1 \\ -1 & 0 & 1 & \cdots & 0 & 0 & 0 & 0 \\ 0 & -1 & 0 & 1 \cdots & 0 & 0 & 0 & 0 \\ \cdot & \cdot & \cdot & \cdots & \cdot & \cdot & \cdot & \cdot \\ \cdot & \cdot & \cdot & \cdots & \cdot & \cdot & \cdot & \cdot \\ \cdot & \cdot & \cdot & \cdots & \cdot & \cdot & \cdot & \cdot \\ 0 & 0 & 0 & 0 \cdots & -1 & 0 & 1 & 0 \\ 0 & 0 & 0 & 0 \cdots & 0 & -1 & 0 & 1 \\ 1 & 0 & 0 & 0 \cdots & 0 & 0 & -1 & 0 \end{bmatrix}.$$

Equations (4.12) and (4.13) can be rewritten so that $\boldsymbol{\theta}$ and $\boldsymbol{\varphi}$ are made the subject of the respective equations. We get [13]

$$\boldsymbol{\theta} = \frac{-1}{2sl}\{[Z_N]\boldsymbol{\zeta} + [D_N]\boldsymbol{\gamma}\}, \tag{4.14}$$

$$\boldsymbol{\varphi} = -\left(\frac{l}{2s}\right)\left\{[B_N]\boldsymbol{\beta} - \left(\frac{c}{s}\right)[X_N]\boldsymbol{\xi} + [Y_N]\boldsymbol{\eta}\right\}. \tag{4.15}$$

We shall assume, as Bilger and Stedman[13], that for the ith mirror the tilt axes are coplanar, orthogonal and cross at the pole of the mirror, but that the pole is displaced from its ideal position at the ith vertex of the symmetric polygon by $(\xi_i, \eta_i, \zeta_i)^T$ and that for each mirror this displacement is fixed. This means that for equations (4.14) and (4.15) the vectors $\boldsymbol{\xi}, \boldsymbol{\eta}$ and $\boldsymbol{\zeta}$ are constant so that the dependent $\boldsymbol{\theta}$ and $\boldsymbol{\varphi}$ are entirely controlled by the respective independent $\boldsymbol{\gamma}$ and $\boldsymbol{\beta}$. Hence given the geometry of the ideal symmetric ray-path for the ring mirror cavity, the radius R_i of each mirror and the displacement, $(0, \beta_i, \gamma_i)^T$, of the point where the ray-path intercepts each mirror we can predict the mirror tilts, θ_i, φ_i required about the respective local y- and z-axes.

4.2 Aplanarity Control in the Near-Planar Square Ring Laser

We are now in a position to calculate what factors control the aplanarity of the experimental near-planar square ring laser. For such a ring laser the number of mirrors, N, is four. Let us suppose that the side length of the ring is l and that the mirrors have radii of curvature $R_1 = R_3 = \infty, R_2 = R_4 = R$, hence

$$\begin{aligned} \Gamma_1 = \Gamma_3 = 2, \\ \Gamma_2 = \Gamma_4 = \Gamma = 2 - 2ls/R. \end{aligned} \tag{4.16}$$

Figure (4.2) shows a diagram of the ideal ray-path for the ring laser.

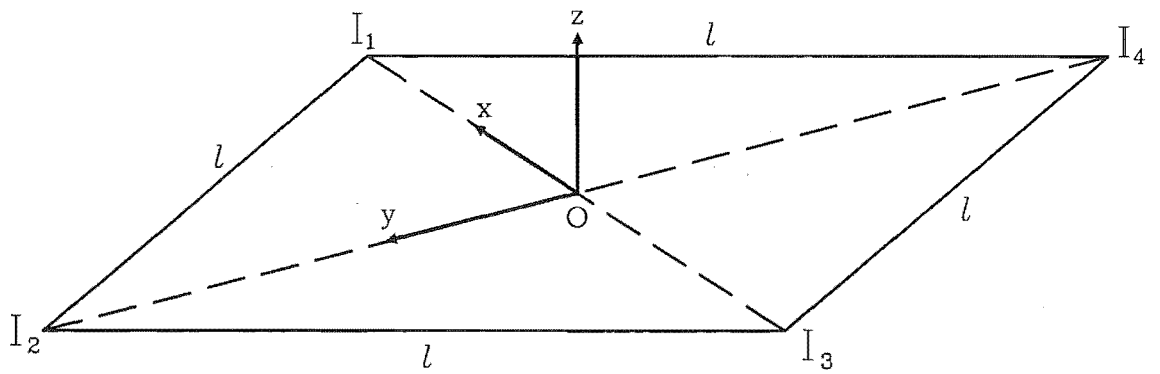

Figure 4.2: Ideal ray-path of the beam internal to the mirror cavity of a near-planar square ring laser.

The cartesian coordinate system is located at the center of the ring laser where the x- and y-axes point towards the poles, I_1, I_2, of the first and second mirrors and

the z-axis points out of plane. As we saw in Section (4.1) that for a ring laser with misadjusted mirrors the displacement of the point at which the ray-path intercepts the i-th mirror relative to the local coordinate system is given by equation (4.2). This is illustrated in Figure (4.3). We may now write the position vectors of the points at

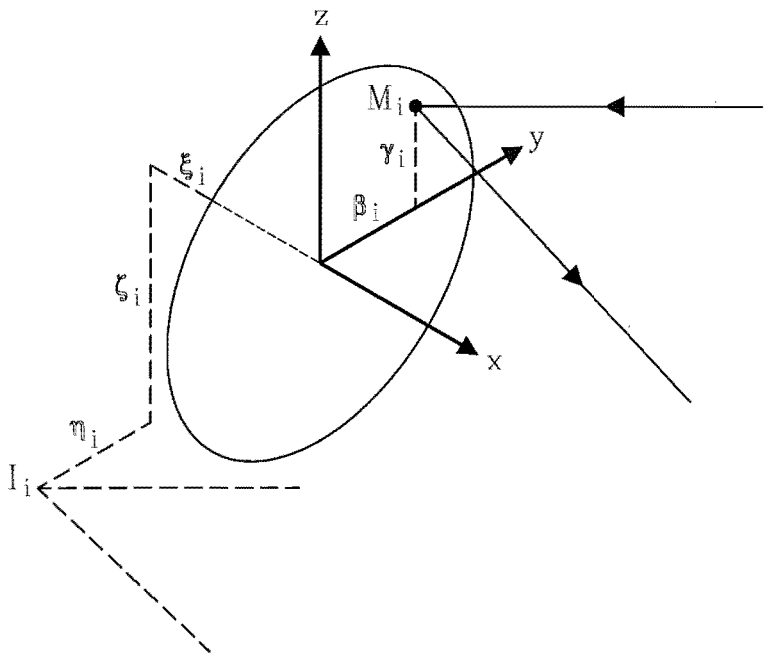

Figure 4.3: Beam offset from the ideal ray-path due to the displacement of the mirror from its ideal location and the point of interception of the beam with the mirror relative to the pole.

which the ray-path intercepts all the mirrors in the coordinate system at the center of the ring as

$$\begin{aligned} \mathbf{OM}_1 &= \begin{pmatrix} l/\sqrt{2} - \xi_1 \\ -(\beta_1 + \eta_1) \\ \zeta_1 + \gamma_1 \end{pmatrix}, \quad \mathbf{OM}_2 = \begin{pmatrix} \beta_2 + \eta_2 \\ l/\sqrt{2} - \xi_2 \\ \zeta_2 + \gamma_2 \end{pmatrix}, \\ \mathbf{OM}_3 &= \begin{pmatrix} -l/\sqrt{2} + \xi_3 \\ \beta_3 + \eta_3 \\ \zeta_3 + \gamma_3 \end{pmatrix}, \quad \mathbf{OM}_4 = \begin{pmatrix} -(\beta_4 + \eta_4) \\ -l\sqrt{2} + \xi_4 \\ \zeta_4 + \gamma_4 \end{pmatrix}. \end{aligned} \tag{4.17}$$

Figure (4.4) shows the ray-path for such an aplanar ring laser. A measure of the aplanarity of the ray-path is the displacement between the midpoints of M_1M_3 and M_2M_4, the diagonal lines joining the interception points of the ray-path on opposite mirrors in the ring laser. This is directly related to the dihedral angle $\beta(= \beta_1 + \beta_2)$ which is the usual parameter used to define the aplanarity. For a near-planar ring laser we can write

$$\sin\beta_1 \simeq \beta_1 = \frac{[\mathbf{MM}_2]_z}{|\mathbf{MM}_2|}, \quad \sin\beta_2 \simeq \beta_2 = \frac{[\mathbf{MM}_4]_z}{|\mathbf{MM}_4|}. \tag{4.18}$$

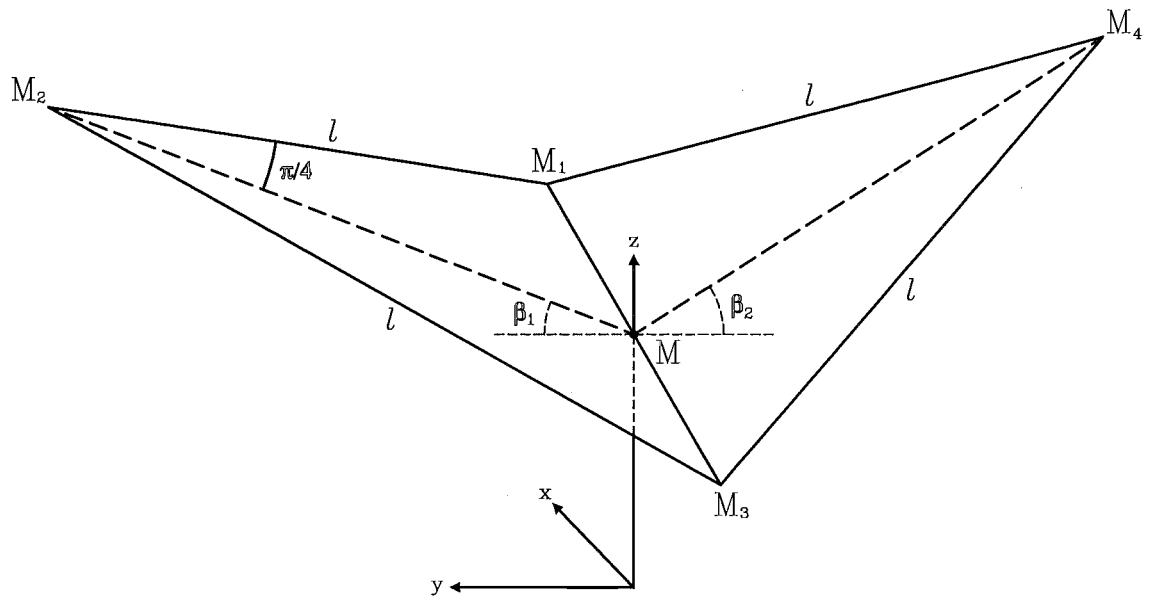

Figure 4.4: Tilt angles for the planes defined by ray-path of the beam in an aplanar ring laser

The point labelled, M, the midpoint of the line M_1M_3, has the position vector

$$\mathbf{OM} = \frac{1}{2}\left(\mathbf{OM}_1 + \mathbf{OM}_3\right) = \frac{1}{2}\begin{pmatrix} \xi_3 - \xi_1 \\ (\beta_3 - \beta_1) + (\eta_3 - \eta_1) \\ (\zeta_3 + \zeta_1) + (\gamma_3 + \gamma_1) \end{pmatrix}. \tag{4.19}$$

Use of this vector and the vectors of (4.17) in the equations (4.18) gives the result

$$\beta = \sqrt{2}\frac{[(\zeta_2 + \zeta_4) - (\zeta_1 + \zeta_3) + (\gamma_2 + \gamma_4) - (\gamma_1 + \gamma_3)]}{l} \tag{4.20}$$

To find β in terms of the mirror tilts we make $\boldsymbol{\gamma}$ the subject of matrix equation (4.12) by multiplying through on the left by, $[D_N]^{-1}$, the inverse of matrix $[D_N]$. Hence we get

$$\boldsymbol{\gamma} = -(2sl)\,[D_N]^{-1}\,\boldsymbol{\theta} - [D_N]^{-1}\,[Z_N]\,\boldsymbol{\zeta}. \tag{4.21}$$

For the experimental ring laser the Γ values are given by (4.16). Substitution of these in the matrices in equation (4.21) gives

$$\boldsymbol{\gamma} = \frac{sl}{(\Gamma - 2)}\begin{bmatrix} A & 1 & 1 & 1 \\ 1 & B & 1 & C \\ 1 & 1 & A & 1 \\ 1 & C & 1 & B \end{bmatrix}\boldsymbol{\theta} + \frac{1}{2}\begin{bmatrix} -2 & 1 & 0 & 1 \\ 0 & -C & 0 & C \\ 0 & 1 & -2 & 1 \\ 0 & C & 0 & -C \end{bmatrix}\boldsymbol{\zeta},$$

where $A = \Gamma - 1$, $B = 2\,(\Gamma - 1)\,/\Gamma$, $C = 2/\Gamma$ and $s = \sin(\pi/4)$ for the square ring laser. From the above equation we may obtain

$$\begin{aligned} \gamma_1 + \gamma_3 &= \frac{sl}{(\Gamma - 2)}\left\{\Gamma\,(\theta_1 + \theta_3) + 2\,(\theta_2 + \theta_4)\right\} + (\zeta_2 + \zeta_4) - (\zeta_1 + \zeta_3)\,, \\ \gamma_2 + \gamma_4 &= \frac{sl}{(\Gamma - 2)}\left\{2\,(\theta_1 + \theta_3) + 2\,(\theta_2 + \theta_4)\right\}. \end{aligned}$$

Substitution of these in equation (4.20) gives

$$\beta = -(\theta_1 + \theta_3)\,.$$

The negative sign is in keeping with the sign convention for positive rotations around the local y-axes for mirrors 1 and 2. It should be noted that this equation is completely independent of the γ and ζ offsets so that when $\theta_1 + \theta_3 = 0$ the ring is planar. This does not imply of course that this planar ring is parallel to the x-y plane.

Chapter 5

Ring Laser Construction

The base of the 1m × 1m square ring laser was constructed from steel. As the tests involved polarisation measurements covering a range of dihedral angles of the order of degrees the changes in aplanarity due to expansion from temperature changes would not be significant. The majority of the geometrical ray-path is in air. Multilayer dielectric-stack mirrors were used to create the mirror cavity with one pair being plane and the other pair having a radius of curvature of 6 m. The pairs of mirrors were mounted opposite each other. This combination of mirrors satisfied the criterion for beam stability. The fused silica discharge tube which provided gain to sustain laser oscillation was 0.7 m in length and had an internal diameter of 4 mm. Approximately 600 mm of discharge was required to maintain lasing, that is, create enough gain at the operating wavelength of 633 nm to offset the losses in the mirrors and the windows at the ends of the discharge tube. The gases for the discharge were supplied from bottles equipped with regulators. Measured volumes of the gases were valved off at approximately atmospheric pressure to supply the approximately 7 : 1 ratio of Helium to Neon (we have found the exact ratio was not critical to acheive lasing and was not closely monitored as it was not expected to play a significant role in determining the polarisation in the ring laser). On release into the discharge tube and auxiliary volume (the input port of a Hereaus Leak detector functioning as the vacuum pump) the gas mixed and the pressure was reduced to approximately 2.3 Torr by pumping (as for the gas mixture ratio the pressure was not closely monitored as it was not expected to play any significant role in the polarisation of the laser).

5.1 Ring Laser Support Framework

Oriel precision gimbal mirror mounts support the four multilayer dielectric-stack mirror. The mirror holders are placed on two parallel rectangular hollow-section steel beams 100 mm by 50 mm by 2 m long. Milled U-clamps are screwed to the beams to hold each of the mirror holders in place. Screws tapped into the U-clamps allow the mirror holders to be positioned so that the distance between the poles of the adjacent mirrors on the near-planar square ray-path is 1 m. Steel piers support each end of the rectangular hollow-section steel beams above steel U-beams 150 mm by 75 mm

by 2 m long. The U-beams are tied together with rectangular hollow-section steel beams 60 mm by 35 mm by 1.85 m long with brackets at each end to bolt to the U beams. Four tripod stands with screw height adjustment support the metal frame work of the ring laser.

The extra length of the U-beams are used to support the polarimeter and the alignment laser and its associated optics. The steel piers were required to raise the height of the ray-path of the beam exiting the back of one of the cavity mirrors to the same level as the centres of the rotating discs of the polarimeter. The discharge tube is mounted on adjustable V-blocks midway between the mirrors supported on one of the rectangular hollow-section beams. The support tray for the driver coils is mounted under the small diameter section of the discharge tube.

5.2 Discharge Tube Design

The Helium-Neon plasma in the discharge tube provides the necessary optical gain to offset the losses suffered by the beam internal to the ring laser as it makes a circuit of the mirror cavity. In the ring laser the plasma is formed by an oscillating electric field accelerating electrons which impact with the gas atoms at low pressure in the discharge tube. The oscillating electric field is created by an rf power oscillator driving three linked self-resonant solenoids arranged in a triangle around the discharge tube (see Section (5.5)). An idea of the order of magnitude of the gain possible from this sort of arrangement was obtained from work by Herziger et al[35]. For a dc driven plasma discharge they give the following approximate expression for the maximum optical gain, G,

$$G(l, D) \simeq \left[1 + 0.5\left(\frac{D_0}{D}\right)^{1.4}\right]^{l/l_0} \tag{5.1}$$

($l_0 = 1$ m, $D_0 = 1$ mm) and where D and l are the inside diameter of the discharge tube and the length of the discharge in the beam path, respectively. It can be seen that the maximum gain increases with a decrease in D and an increase in l. For example when $l = 0.7$ m and $D = 3$ mm the maximum gain is $G = 1.074$.

There are three main optical loss mechanisms in the experimental ring laser. The first occurs at the discharge tube end-window interfaces. The windows chosen were Melles Griot product number $02WLQ003/123$[54]; being 12.5 mm diameter fused silica discs with a *123* type multilayer antireflection coating on each of the optical surfaces. The *123* coatings are *V* type[55] (derived from the characteristic shape of their performance curve) and have 0.25 % maximum reflectance per surface; the total being 1 % for the two windows.

Loss also occurs when the skirts of the Gaussian beam are vignetted by the tube. The configuration of the optics in the experimental ring laser produces an astigmatic

beam profile with elliptical isophotes, and for the particular combination of mirrors chosen the waist spot size in the s direction is $w_{0,s} = 0.742$ mm and in the p direction it is $w_{0,p} = 0.602$ mm. To get an upper bound on the loss caused by vignetting, let us suppose that the beam is stigmatic and the waist spot size is $w_0 = w_{0,s}$. The profile of the intensity, I, for such a $0,0$ mode Gaussian beam[79] is

$$I = \frac{2P_0}{\pi w^2} \exp\left(\frac{-2r^2}{w^2}\right), \tag{5.2}$$

where P_0, r and w are, respectively, the total power of the beam, the radial distance from the axis of the beam and the spot size - the radius of the circular area perpendicular to the axis of the beam, centred on this axis, through which half the power of the beam passes. If we assume that the axis of the beam is perfectly aligned with the axis of the discharge tube then the tube approximates a circular aperture vignetting the beam thus causing power loss. If we assume the circular aperture has radius, a, then the power transmitted through it is

$$P = \frac{2P_0}{\pi w^2} \int_{\theta=0}^{\theta=2\pi} \int_{r=0}^{r=a} \exp\left(\frac{-2r^2}{w^2}\right) r\,dr\,d\theta.$$

Hence the relative loss is

$$1 - \frac{P}{P_0} = \exp\left(\frac{-2a^2}{w^2}\right). \tag{5.3}$$

For the experimental laser the waists of both the internal counterpropagating beams lie on the plane mirrors. Beam divergence causes the spot size to grow with the distance from the waist, hence the discharge tube intercepts the greatest amount of the beam at the end farthest from the waist. In the experimental laser this point is 0.85 m from the waist. The beam spot size, w, can be found using the Gaussian beam expressions[79]

$$w = w(z) = w_0\sqrt{1 + \left(\frac{z}{z_R}\right)^2}$$

$$z_R = \frac{\pi w_0^2}{\lambda},$$

where w_0, z, z_R and λ are, respectively, the waist spot size, the distance measured from the beam waist to the point at which the spot size is being calculated, the Rayleigh length for the beam and the wavelength of the beam in the medium. For example, when $z = 0.85$ m and $\lambda = 632.8$ nm the spot size is $w = 0.777$ mm. If the radius of the discharge tube is chosen so that the relative loss by vignetting is of the order of 0.01 % then the total loss is effectively set by sum of the losses in the end-window interfaces. Equation (5.3) can be used to show that this condition is met when $a \geq 1.67$ mm. The nearest conveniently available corresponding tube i.d. close to this size was 3 mm. Its calculated loss by vignetting is 0.06 % which was initially judged to be acceptable. However further loss by vignetting occurs if the axis of the beam is misaligned with respect to the axis of the discharge tube. Because of this, the 3 mm i.d. tube was later exchanged for a 4 mm i.d. one.

The length of the discharge tube was chosen to be as long as conveniently possible given the difficulty in aligning the mirrors adjacent to the discharge tube end-windows. This strategy was chosen because equation (5.1) was for a dc driven discharge and it was not obvious that an rf discharge would achieve the same maximum gain. In order to get laser action in the experimental ring laser at least 0.5 m of visible discharge was required, hence the choice on the length of discharge tube proved to be a wise one.

The fourth main optical loss was in the mirrors themselves. The power loss in each was ~ 370 *ppm* (see the characteristics for 'our' mirrors in Section (3.2.1)) hence the total loss from this source was insignificant compared to that in the end-windows.

5.3 Discharge Tube Construction

The discharge tube required a material which was transparent to an rf electromagnetic field, had a low outgassing rate, could stand the temperature required to outgas it as well as that generated by the plasma discharge within it when operating, and was optically transparent so that the spectrum of the plasma could be observed. Fused silica was chosen because it could stand the thermal stress induced by heating with an open flame and had all the other properties mentioned above. To allow the discharge tube to be swung aside during mirror alignment stainless steel bellows were used to connect the discharge tube to the pump and gas delivery system.

Figure(5.1) shows the construction of the discharge tube and the associated glass tubing connected to the gases and the vacuum system. Two different sizes of fused silica tube were used in making the discharge tube itself.

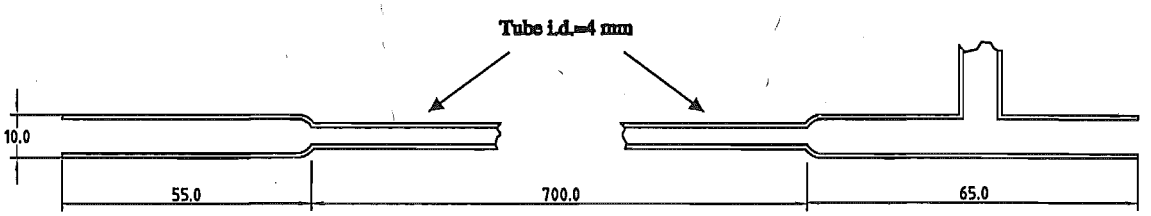

Figure 5.1: Design of the fused silica discharge tube. Wall thickness of large diameter section is 2 mm. Wall thickness of small diameter section is 1 mm.

The side arm was initially left short so that it would not foul the lathe in the operation of cutting the ends of the discharge tube. The o.d. of the larger tubing located at the ends of the discharge tube was chosen to be slightly smaller than the 12.5 mm diameter fused silica end-windows. This made the seats on which the windows rested more stable and also made it easier to cut, grind flat and polish the ends of the tube to the tolerances required. The tube ends were cut in a lathe using a carborundum cutting wheel. The planes containing the end faces were orthogonal

to the axis of the discharge tube within 1°. This type of accuracy was necessary to ensure that the window interfaces did not significantly influence the polarisation of the beam passing through them when the tube was in operation.

A split wooden cylinder 730 mm long and 43 mm in diameter was used to hold the discharge tube for cutting in the lathe. A hole 15 mm in diameter was drilled along the axis of the cylinder and the 10 mm diameter sections of tube at each end of the discharge tube were packed so that the ends ran centred in the lathe. Holes were drilled orthogonal to the axis of the cylinder at 50 mm intervals so that the smaller diameter section of the discharge tube could be viewed along its entire length to check whether it was bent when the cylinder halves were screwed together. Split metal collars were clamped around the wooden cylinder and discharge tube to hold the axis of tube accurately centred in the lathe at all times. They also provided a large area of contact with the wooden cylinder ensuring that minimum deformation would occur upon clamping. Mr Poulton judged the wood to be too soft for it to be placed in direct contact with the jaws of the lathe without the risk of nonuniform deformation putting the assembly out of true at some point during the cutting operations. To be extra sure that the discharge tube was rigidly held during cutting, a cardboard sleeve was clamped around each end of the wooden cylinder in turn and hot paraffin wax poured into the space between it and the discharge tube to a depth of about 15 mm and left to set. The bond between the wax, the cylinder and the discharge tube gave the necessary protection against any looseness of the tube in the wooden cylinder, should the fit not be perfect.

5.4 Gas Delivery System

There is an ideal pressure and gas mixture ratio which achieves the maximum lasing output for an rf discharge tube with a given i.d. This has been investigated by Mielenz et al[58] and they show that the lasing action of the $3s_2 - 2p_4$ transition of neon at 632.8 nm is maximised for a 3 mm i.d. discharge tube when the pressure is 2.3 Torr and the He:Ne molar ratio is 7 : 1. They used electrodes attached to the outside of the discharge tube to provide the electric field for driving the plasma whereas in the experimental laser this was provided by an rf power oscillator driving a triangular arrangement of self resonant solenoids whose axes lay parallel to the discharge tube (see Section (5.5)). Although there is a difference in the plasma driving arrangement there seemed to be no good reason to think that the results of Mielenz et al should not also apply for our set up. Experience with the Canterbury C-I ring laser has confirmed this expectation.

A schematic diagram of the gas delivery system is shown in Figure (5.2).

The helium and neon are each admitted to their own pre-evacuated line where valves A,B and C,D are used to close off and trap volumes of the respective gases

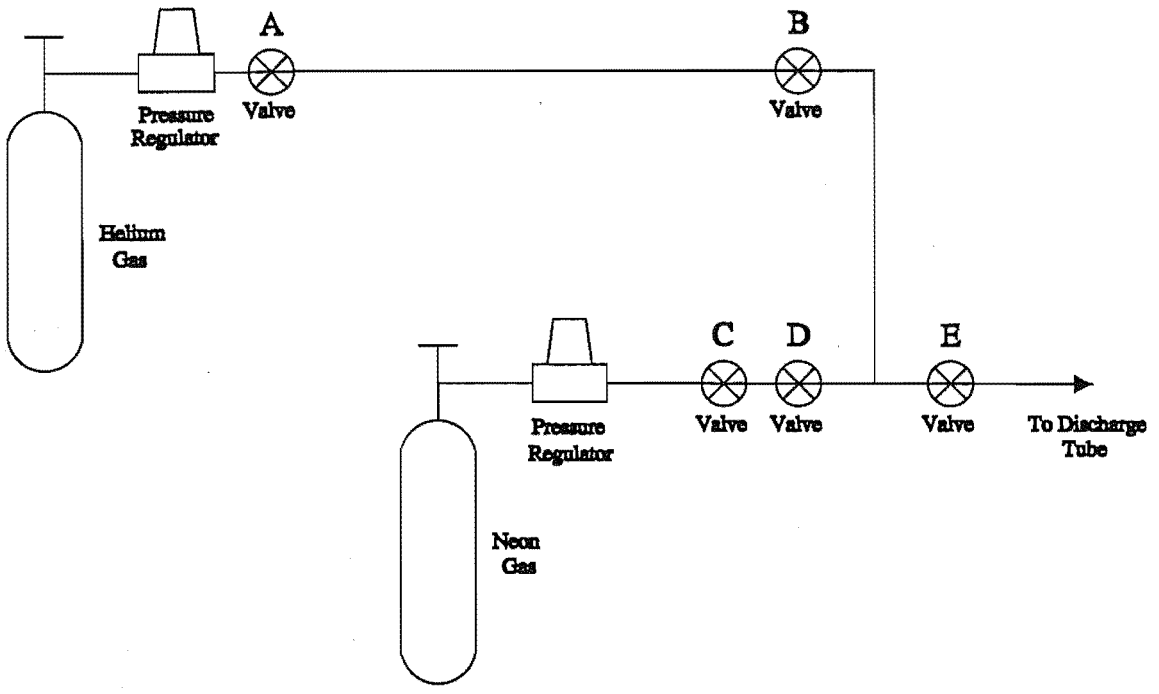

Figure 5.2: Design of the gas delivery system for the ring laser. The gases are trapped in the volumes between valves A and B and between valves C and D. Adjustment of the gas pressures to these two respective fixed volumes sets the ratio of the number of Helium to Neon atoms in the lasing mixture.

in the ratio of 7 : 1. The release of valves B and D to the pre-evacuated discharge tube and ballast volume allows the gases to mix in the required ratio. If quantities of helium and neon gas at the same pressure are each trapped in volumes in the ratio $7:1$, respectively, then the ratio of the number of helium to neon molecules is the same. This is the principle behind the gas delivery system design. It was not necessary to create these volumes to very high precision as the gas bottle pressure regulators could be adjusted to compensate for any imbalance in the gas mixture. This feature of the design proved to be useful when the i.d. of the discharge tube was changed from 3 mm to 4 mm as it required only a small re-adjustment of the regulators to obtain maximum lasing output. To get the correct pressure for the mixture of gases, the initial pressure was made slightly too high so that the excess could be pumped away to reach the desired figure

Previous experience with the C-I ring laser showed that the gas mixture in the laser must remain uncontaminated if the output power is to remain constant. Sealed off commercial lasers use getters to remove the last traces of impurities. Since supplies of high purity helium and neon were readily available and the contaminated gas could easily be pumped away, getters were not considered. For the gas mixture to remain uncontaminated requires that all the surfaces exposed to the low pressure gas be free of adsorbed molecules capable of being liberated easily. To get as close as possible to this ideal nearly all the parts whose internal surfaces were exposed to the laser mixture were made of materials that could be heated to outgas them. Stainless steel

was seen as the ideal material because it could be heated to red heat if necessary, it had a low outgassing rate, it was relatively cheap and was readily available.

The main contributor to outgassing in the whole of the low pressure gas system were the 'O'-rings. Viton *A* type were used to seal the gas delivery and pumping systems to the glassware leading to the discharge tube. The Whitey valves *B* and *D* also used this material for the 'O'-ring seals. The shaft and end seal 'O'-rings of the valves on the glassware were Teflon. Viton *A* and Teflon have approximately the same outgassing rates of ($\sim 10^{-6}$ Torr.Lit/sec.cm^2[70]) with teflon's rate being slightly lower. Stainless steel has an outgassing rate of $\sim 10^{-8}$ Torr.Lit/sec.cm^2[70]. The only other materials used were copper for the tubing connecting the vacuum pump, the cold trap and the discharge tube and brass in the form of hexagonal rod turned up to make the clamps holding the 'O'-rings which connect the glassware to the discharge tube and vacuum systems. Since brass is largely composed of copper I have assumed they have the same outgassing rate, namely $\sim 10^{-7}$ Torr.Lit/sec.cm^2[70].

The helium used was 99.998% pure 'Grade Zero High Purity' gas obtained from New Zealand Industrial Gases. The Neon was natural isotope composition 99.999% pure gas obtained from Spectra Gases Inc., Newark, New Jersey, USA. The gas bottle regulators were pumpable, high purity medical grade type with steel diaphragms. The metal tubing used was 3/16" i.d. made of 316 stainless steel. Swagelok connectors were used to join pipes together where this was required. Valves *C* and *D* were "1G" series Whitey toggle valves made from 316 stainless steel and use Viton *A* '*O*'-rings for seals. Although these were not considered to be 'high-vacuum' type they proved to be quite satisfactory in practice. Valve *E* was a high-vacuum Nupro "DL" series diaphragm valve with a metal-to-metal seal enclosed by metal bellows.

5.5 RF Discharge Driver Coils and Feed

Figure (5.3) shows the coil assembly used to generate the oscillating rf electric field to drive the plasma discharge.

The three long coils S_1, S_2 and S_3 are identical and are wound on 10 mm o.d. Borosilicate glass tubes 600 mm long. Borosilicate glass is a low loss material (dielectric loss factor $\sim 0.02m$[47]) at 27.88 MHz (the operating frequency of the power oscillator driving the discharge) and tubing of these dimensions is easily strong enough to support the coils. To ensure that each coil formed a close fit on the tubing it was wound on a metal rod with a diameter slightly less than the o.d. of the glass tubing. It was then expanded slightly by applying torque and slid onto the slightly larger glass tubing. When the torque was released the coil contracted to form the close fit required. The glass tubes are supported by 80 mm by 80 mm by 10 mm wooden cheeks at each end with holes drilled in an equilateral triangle pattern with the centres of the tubes 22 mm apart. A central 12 mm diameter hole with a slot 6 mm wide

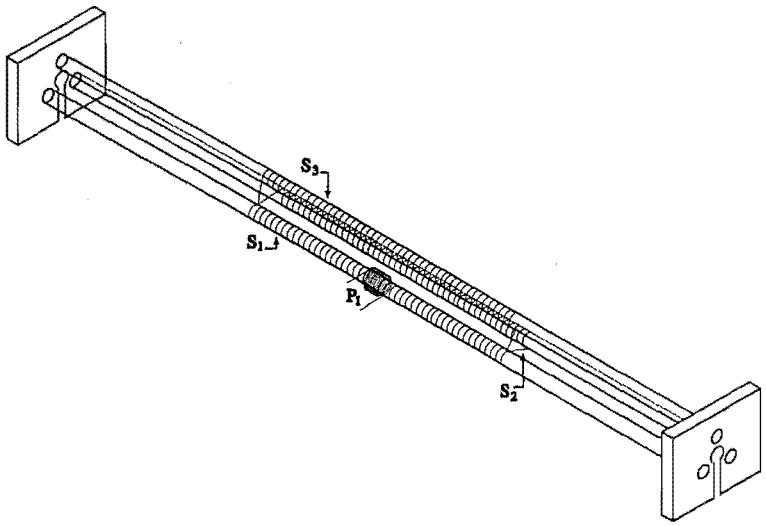

Figure 5.3: Coupled self-resonant coils S_1, S_2 and S_3 supply the alternating electric field to drive the Helium-Neon discharge. The magnetic coupling from coil P_1 to coil S_1 transfers rf power in the input coaxial cable from the power oscillator to the alternating electric field driving the Helium-Neon discharge.

allows the coils to be slid around the discharge tube without the need to dismount the discharge tube. The coils have $\sim$ 314 turns of copper wire of 22 gauge insulated with polyurethane. The coils are coupled by joining their corresponding ends together.. Electrically the coils appeared as a single secondary load on an air cored transformer. Power is fed to them by the coil, P_1, wound over S_1, which acted as the primary winding of the air cored transformer. The primary coil P_1 is self supporting, being 8.5 turns of 2.00 mm diameter shellac coated copper wire close wound. One end of the coil P_1 is earthed to the aluminium tray whose inside dimensions are 640 mm long, 80 mm wide and 40 mm deep which supports the coil assembly. A lid which is of identical inside dimensions to the tray covers the coil assembly so as to contain the radio frequency field. Semicircular cuts 24 mm in diameter in the ends of the tray and lid allow the discharge tube entry at each end. The non-earthed end of the primary winding P_1 was connected to a UHF connector.

A matching circuit (see Figure (5.4) was used to transform the impedance presented by the driver-coil assembly to that of the coaxial line connected to the power oscillator.

The 'matching-box', containing the matching circuitry, was connected to the primary coil P_1 by a short length of 50Ω coaxial cable. Although the coaxial cable did not match the impedance presented by the coil P_1 its length was substantially less than a wavelength and therefore did not substantially affect coupling.

Initially, before the discharge begins, the coil assembly appears to be a 'high-Q' system as the materials in the vicinity of the coils are low loss and so a potential difference of several thousand volts is able to develop between the middle of each coil

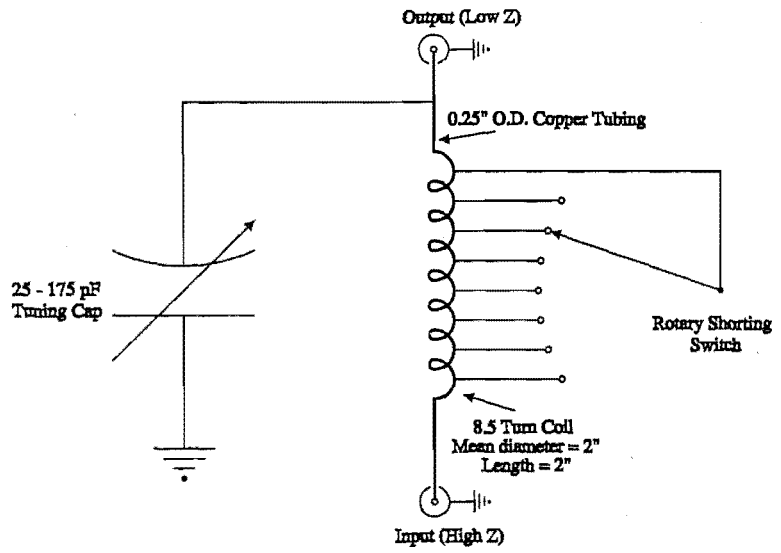

Figure 5.4: Schematic diagram for a circuit to match the impedance presented by the coil P_1 of the driving coils for the Helium-Neon discharge to the 50Ω impedance of the coaxial line to the power oscillator. The coaxial cable to the power oscillator is connected to the input side of the matching circuit.

and each of its ends. Because the coils S_1, S_2 and S_3 are coupled at the ends, there is a common potential for each coil at the point where it is intersected by a plane perpendicular to the axis of the discharge tube. This potential distribution along the coil assembly is the source of the electric field which first 'strikes' the plasma discharge and then maintains it.

The plasma, once created, becomes a source of loss which lowers the 'Q' of the system and so there is a corresponding decrease in the potential difference between the ends of the coils. The plasma changes not only the amplitude of the impedance, but also the phase, seen at the terminals of the primary of the transformer. In the experimental ring laser this change in impedance was detected as a change in the SWR measured in the line connecting the matching box to the power oscillator when the plasma struck. It was found that if the coil assembly was matched to the coaxial line initially then after plasma strike the matching box had to be readjusted for maximum lasing output, i.e. the SWR in the line between the matching box and power oscillator brought as close to unity as possible.

The design of coils S_1, S_2 and S_3 were circumscribed by the frequency of the power oscillator feeding them and the coil's length, being restricted to somewhere between one half and two thirds of the length of the discharge tube. This restriction in the length was to prevent the plasma impinging on the end-window antireflection coatings and destroying them. The power oscillator was originally designed for an early Helium-Neon 'Nelas' laser, one of the first purchased by the University of Canterbury. It is uses vacuum tubes and has a continuous output power slightly in excess of 60 W into a 50 Ω load. The original circuit design had already been modified to operate at 27.88 MHz when it was acquired.

As there was no easy way to calculate the precise dimensions for the single layer self-resonant coils at a given frequency a simpler approach was chosen. One can regard the length of wire used to make the coil as a self-resonant half-wavelength antenna with the wavelength being that in free space. It is well known that the self-resonant frequency of a single layer coil made using a given length of wire is not appreciably different from that when the same piece of wire is a free standing straight length. A length of 22 gauge polystyrene coated wire slightly in excess of the half-wavelength was chosen for each of the coils so that they could be trimmed to self-resonance, within a few megahertz or so, with the aid of a gate dip oscillator. The diameter of each of the coils was chosen so that when close wound as a single layer their length was within the specification mentioned above.

Chapter 6

Polarisation Measurement Methods

There are two purposes for which polarisation measurement is required. The first is to measure the polarisation characteristics of the beam internal to the ring laser as a function of the planarity of its geometrical ray-path. The second is to measure the anisotropy in birefringence and differential reflectance of the ring cavity mirrors by directing a linearly polarised beam at a mirror and measuring the polarisation characteristics of the reflected beam. In the first application the polarisation is expected to change from linear to nearly circular so that great sensitivity of the device is not required. In the second case the phase change in the beam is expected to be of the order of 0.1 radian [14], but the differential reflectance is of the order of 230 ppm. Hence the ellipticity angle will be of the order of 0.01° and greater sensitivity is required from the polarimeter. It will be seen that it is possible to construct a device which can function in two different modes. These correspond to two of the different methods for measuring polarisation which are reviewed below. First, however, we shall look at a number of polarimeter designs and explain the choice used in our design.

There are a number of ways in which the characteristics of polarised light can be measured. Collett[22, Chapter 6] presents five different methods which use as components a variable-wave-plate, a linear polariser and a detector. These will be discussed below together with another which uses rotation of a quarter-wave-plate and a polariser to measure the polarisation. There are several devices available which fall in the classes labelled variable-wave-plate, polariser and detector. The experimental work described here involves the use of the following devices: for the variable-wave-plate a Soleil-Babinet retarder (which can be manually adjusted over a range of phase shifts), for the linear polariser a Glan-Thompson polarising prism, and for the detector a photomultiplier tube.

A modern development of the variable-wave-plate is the photoelastic modulator. In this device a periodically changing phase-shift is introduced between orthogonal components of a beam passing through it. Once the range over which the phase-shift is scanned has been set the device requires no further manual adjustment to operate. By using two photoelastic modulators, an analyser, a detector and some ancillary equipment it is possible to obtain, automatically, the Stokes vectors, hence

the polarisation characteristics, for a beam entering the apparatus. It was because of the rapidity with which measurements can be obtained using this apparatus that its inclusion was warranted in the study below.

In most cases Collett[22] treats all the optical components as ideal. In an effort to make the methods analysed in this section more applicable to experimental work I have modified the results obtained by Collett and incorporated the losses for the optical components in all calculations. I also show how to eliminate the errors caused by these losses when using each of the methods.

Absorption in a variable-wave-plate can be represented by a separate matrix with the full behaviour being represented by a matrix formed from the product of the matrices representing its ideal behaviour and absorption. However, this approach may not work for all optical devices and so it is better to account for absorption in the equations which define the Mueller matrix modelling them.

6.1 The Diattenuator Matrix

If an optical device unequally absorbs the orthogonal components of a beam then it can be represented by a diattenuator Mueller matrix transforming the Stokes vector of the beam. Following Collett[22, p94], the orthogonal field components $E_x^{'}$ and $E_y^{'}$ of a beam emerging from such a device can be written in terms of the incident field components E_x and E_y as

$$E_x^{'} = E_x e^{-\alpha_x}, \tag{6.1}$$
$$E_y^{'} = E_y e^{-\alpha_y}, \tag{6.2}$$

where α_x and α_y are, respectively, the absorption coefficients in the OX- and OY-directions for a cartesian system fixed with respect to the device. These factors can also be expressed as

$$p_x = e^{-\alpha_x}, \tag{6.3}$$
$$p_y = e^{-\alpha_y}. \tag{6.4}$$

The diattenuator Mueller matrix becomes

$$D = \frac{1}{2}\begin{bmatrix} {p_x}^2 + {p_y}^2 & {p_x}^2 - {p_y}^2 & 0 & 0 \\ {p_x}^2 - {p_y}^2 & {p_x}^2 + {p_y}^2 & 0 & 0 \\ 0 & 0 & 2p_xp_y & 0 \\ 0 & 0 & 0 & 2p_xp_y \end{bmatrix}, \tag{6.5}$$

A more compact and easy to use form of the diattenuator matrix can be found if we let

$$p^2 = {p_x}^2 + {p_y}^2, \; p_x = p\cos\gamma, \; p_y = p\sin\gamma. \tag{6.6}$$

The matrix in (6.5) becomes

$$D_{p,\gamma} = \frac{p^2}{2}\begin{bmatrix} 1 & \cos 2\gamma & 0 & 0 \\ \cos 2\gamma & 1 & 0 & 0 \\ 0 & 0 & \sin 2\gamma & 0 \\ 0 & 0 & 0 & \sin 2\gamma \end{bmatrix}. \tag{6.7}$$

6.2 The Rotation Matrix

At every step in a calculation, the local axes must be related to those of the previous component by a suitable rotation matrix

$$M(2\theta) = \begin{bmatrix} 1 & 0 & 0 & 0 \\ 0 & \cos 2\theta & \sin 2\theta & 0 \\ 0 & -\sin 2\theta & \cos 2\theta & 0 \\ 0 & 0 & 0 & 1 \end{bmatrix}.$$

The following example illustrates its use. Suppose that the axes for the incident and output beams associated with some optical device are to be aligned and the axes associated with the optical device are rotated at an angle θ with respect to those of the beams. If the matrix, T, represents the optical component defined with respect to its own coordinate system then the equivalent matrix, T', defined with respect to the coordinate system associated with the beams is given by

$$T' = M(-2\theta)\,TM(2\theta).$$

6.3 The Linear Polariser Matrix

A linear polariser is an example of an anisotropic attenuator where the orthogonal components of the optical beam are attenuated unequally. It can be represented by a diattenuator Mueller matrix where $p_y \ll p_x$. As an example a Glan-Thompson prism manufactured by Melles Griot[56] has an extinction ratio ${p_y}^2/{p_x}^2 < 10^{-5}$ and the ratio of the total output to total unpolarised input is $({p_x}^2 + {p_y}^2)/2 = 0.36$. In most cases where analysis is carried out for a real optical system using a good polariser, i.e. where $p_y \ll p_x$, the approximation $p_y = 0$ is made and so the linear polariser matrix can be defined by

$$P = \frac{(p_p)^2}{2}\begin{bmatrix} 1 & 1 & 0 & 0 \\ 1 & 1 & 0 & 0 \\ 0 & 0 & 0 & 0 \\ 0 & 0 & 0 & 0 \end{bmatrix},$$

where p_x has been redefined as p_p, being the attenuation factor for the component of the beam parallel to the direction of the transmission axis. In the ideal polariser

$p_p = 1$. The matrix representing a linear polariser whose transmission axis has been rotated at an angle, θ, to the OX-axis is

$$P_\theta = M(-2\theta)\,PM(2\theta) = \frac{(p_p)^2}{2}\begin{bmatrix} 1 & \cos 2\theta & \sin 2\theta & 0 \\ \cos 2\theta & \cos^2 2\theta & \sin 2\theta \cos 2\theta & 0 \\ \sin 2\theta & \cos 2\theta \sin 2\theta & \sin^2 2\theta & 0 \\ 0 & 0 & 0 & 0 \end{bmatrix}.$$

6.4 The Variable-Wave-Plate Matrix

The Mueller matrix modelling a real variable-wave-plate with its fast and slow axes lying in the X-Y plane and with its fast axis oriented along OX is

$$W_\phi^{p,\gamma} = \frac{p^2}{2}\begin{bmatrix} 1 & \cos 2\gamma & 0 & 0 \\ \cos 2\gamma & 1 & 0 & 0 \\ 0 & 0 & \sin 2\gamma \cos\phi & \sin 2\gamma \sin\phi \\ 0 & 0 & -\sin 2\gamma \sin\phi & \sin 2\gamma \cos\phi \end{bmatrix}, \tag{6.8}$$

where p_x and p_y are, respectively the attenuation factors in the OX- and OY- directions and where $p^2 = {p_x}^2 + {p_y}^2$, $p_x = p\cos\gamma$, $p_y = p\sin\gamma$. The angle, ϕ, is the relative phase-shift introduced between the respective components of a beam transmitted by the variable-wave-plate. When Collett defines the retarder matrix it appears that he defines ϕ to be the retardance, that is, a negative phase-shift and then he uses this throughout his analysis. It is my preference to treat ϕ as a normal phase-shift along with all others in the course of analysing problems hence the change in sign of the components $W_\phi^{p,\gamma}(3,4)$ and $W_\phi^{p,\gamma}(4,3)$ from those defined by Collett.

It is easy to show that the real variable-wave-plate matrix, $W_\phi^{p,\gamma}$, can be written as the product of a diattenuator matrix, $D_{p,\gamma}$, and an ideal variable-wave-plate matrix $W_\phi\left(= W_\phi^{\sqrt{2},45^\circ}\right)$. Hence we can write

$$W_\phi^{p,\gamma} = D_{p,\gamma}W_\phi = W_\phi D_{p,\gamma}. \tag{6.9}$$

This property of $W_\phi^{p,\gamma}$ will be required later.

If the variable-wave-plate is rotated, the angle between the fast axis and the OX-axis being θ, and its phase shift ϕ then the variable-wave-plate is represented by

$$W_{\theta,\phi}^{p,\gamma} = M(-2\theta)\,W_\phi^{p,\gamma}M(2\theta) = \frac{p^2}{2}\begin{bmatrix} 1 & A & B & 0 \\ A & C & D & -E \\ B & D & F & G \\ 0 & E & -G & H \end{bmatrix}, \tag{6.10}$$

where

$$A = \cos 2\gamma \cos 2\theta,$$

$$
\begin{aligned}
B &= \cos 2\gamma \sin 2\theta, \\
C &= \cos^2 2\theta + \sin^2 2\theta \sin 2\gamma \cos\phi, \\
D &= \sin 2\theta \cos 2\theta (1 - \sin 2\gamma \cos\phi), \\
E &= \sin 2\gamma \sin 2\theta \sin\phi, \\
F &= \sin^2 2\theta + \cos^2 2\theta \sin 2\gamma \cos\phi, \\
G &= \sin 2\gamma \cos 2\theta \sin\phi, \\
H &= \sin 2\gamma \cos\phi.
\end{aligned}
$$

Now that we have defined the matrices representing the linear polariser and the variable-wave-plate and their rotated counterparts we should consider how the attenuation factors associated with them can be measured.

6.5 Measurement of the Attenuation Factors

Let us first consider how to find p_p, the attenuation factor for the component of the beam parallel to the transmission axes of the linear polariser. It may also be defined by

$$I = (p_p)^2 I_0,$$

where I_0 is the intensity of a beam of light whose electric field vector is parallel to the transmission axis of the polariser and is incident upon it; I is the intensity of the beam emergent from the polariser.

There are many ways in which p_p can be measured, but a particularly simple method uses another high quality Glan-Thompson prism. If this polariser is oriented so that its transmission axis is parallel to the OX-axis and the measured intensity of the transmitted beam is I_{0x} then the Stokes vector of the beam is $S = I_{0x}\,(1, 1, 0, 0)^T$. If the polariser whose attenuation factor is to be measured is introduced into the beam from the first polariser so that its transmission axis is also parallel to the OX-axis then the Stokes vector of the beam at the detector is now $S' = P_0 S = (p_p)^2 S$, with its intensity being $I = (p_p)^2 I_{0x}$. From both intensities we can calculate

$$p_p = \sqrt{\frac{I}{I_{0x}}}.$$

With modification the same method can be used for finding the attenuation factors for a variable-wave-plate. Two measurements are made, one with the extra polariser oriented along the OX-axis, the other at an angle of 90° to this. First, let the extra polariser be oriented so that its transmission axis is parallel to the OX-axis. If the intensity of the transmitted beam is measured to be I_{0x} then its Stokes vector is $S_x = I_{0x}\,(1, 1.0, 0)^T$. If the variable-wave-plate with its fast axis parallel to the

OX-axis is now introduced into the beam then the Stokes vector of the transmitted beam is given by $S_x' = W_\phi^{p,\gamma} S_x = {p_x}^2 S_x$, hence its intensity is $I_x = {p_x}^2 I_{0x}$. From the intensities we calculate

$$p_x = \sqrt{\frac{I_x}{I_{0x}}}. \tag{6.11}$$

The extra polariser is now rotated through 90°, with the source being adjusted if required (especially if a polarised laser has been used), and the intensity, I_{0y}, of the transmitted beam is measured. The Stokes vector of the beam is then $S_y = I_{0y}\,(1, -1, 0, 0)^T$. If the variable-wave-plate is replaced in the beam, oriented as before, then the Stokes vector of the transmitted beam is given by $S_y' = W_\phi^{p,\gamma} S_y = {p_y}^2 S_y$ and its intensity is given by $I_y = {p_y}^2 I_{0y}$. The intensity measurement allows us to calculate

$$p_y = \sqrt{\frac{I_y}{I_{0y}}}. \tag{6.12}$$

This completes the measurements. It can be seen that using the extra high quality Glan-Thompson makes the measurement of the attenuation factors very easy and direct.

We can now analyse all the methods mentioned as we can represent all the optical components used.

6.6 Intensity Measurement Method using an Oriented Quarter-Wave-Plate and an Analyser

It was in his work on polarisation that Stokes[88] gave us what we now call his classical method for measuring his parameters for any source of light. The arrangement of optical components for this is shown in Figure (6.1) below.

To begin the measurements, only the polariser is placed between the incoming beam and the detector; the three intensity measurements, $I(0°, 0°), I(45°, 0°)$, and $I(90°, 0°)$ are made, where $I(\theta, \phi)$ denotes the intensity of the beam falling on the detector after it passes through a wave-plate which introduces a phase shift ϕ between the components of the beam parallel to its fast and slow axes, respectively, and then through a polariser with its transmission axis at an angle θ to the OX-axis. A fourth measurement is taken where a quarter-wave-plate (QWP) with its fast axis along the OX direction is introduced between the incoming beam and the polariser and the measurement $I(45°, 90°)$ taken.

If the Stokes vector for the light source is $S = (S_0, S_1, S_2, S_3)^T$ then we may calculate the Stokes vectors and hence the intensities for the above four measurements. The symbol $S(\theta, \phi)$ denotes the Stokes vector of the beam falling on the detector

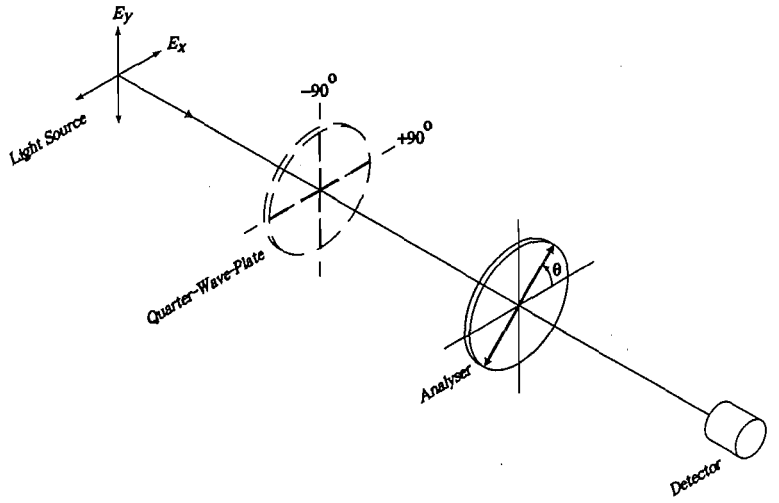

Figure 6.1: Polarisation characteristics determined from the measured intensity for three orientations of the analyser only and a fourth with a quarter-wave-plate introduced in addition.

after it has passed through a wave-plate which introduces a phase shift ϕ between the components of the beam parallel to its fast and slow axes, respectively, and then through a polariser whose transmission axis is at an angle θ to the OX-axis. For the first measurement the polariser transforms the Stokes vector of the incident beam, S, to $S(0°, 0°) = P_0 S$ and so

$$I(0°, 0°) = \frac{{p_p}^2}{2}(S_0 + S_1), \tag{6.13}$$

where p_p is the attenuation factor for the polariser. For the other two measurements we have $S(45°, 0°) = P_{45°} S$ and $S(90°, 0°) = P_{90°} S$ so that, respectively,

$$I(45°, 0°) = \frac{{p_p}^2}{2}(S_0 + S_2), \tag{6.14}$$

$$I(90°, 0°) = \frac{{p_p}^2}{2}(S_0 - S_1). \tag{6.15}$$

For the measurement with the quarter-wave-plate introduced into the optical train we have $S(45°, 90°) = P_{45°} W_{90°}^{p,\gamma} S$ so that

$$I(45°, 90°) = \frac{p^2 {p_p}^2}{4}(S_0 + S_1 \cos 2\gamma + S_3 \sin 2\gamma). \tag{6.16}$$

From the four equations (6.13), (6.14), (6.15) and (6.16) we can derive the four Stokes parameters in terms of the intensity measurements and the attenuation factors, i.e.

$$S_0 = \frac{I(0°, 0°) + I(90°, 0°)}{{p_p}^2},$$

$$S_1 = \frac{I(0°,0°) - I(90°,0°)}{{p_p}^2},$$
$$S_2 = \frac{2I(45°,0°) - I(0°,0°) - I(90°,0°)}{{p_p}^2}$$

$$S_3 = \frac{1}{p^2{p_p}^2 \sin 2\gamma}\left\{4I(45°,90°) - p^2\left[1+\cos 2\gamma\right]I(0°,0°) - p^2\left[1-\cos 2\gamma\right]I(90°,0°)\right\}$$

From the basic theory of polarisation[18, p31] we have

$$\sin 2\chi = \frac{S_3}{S_0} \tag{6.17}$$
$$= \frac{4I(45°,90°) - p^2\left[1+\cos 2\gamma\right]I(0°,0°) - p^2\left[1-\cos 2\gamma\right]I(90°,0°)}{p^2 \sin 2\gamma\left[I(0°,0°)+I(90°,0°)\right]}$$
(6.18)
$$\tan 2\psi = \frac{S_2}{S_1} = \frac{2I(45°,0°) - I(0°,0°) - I(90°,0°)}{I(0°,0°) - I(90°,0°)} \tag{6.19}$$

If the major and minor axis lengths for the polarisation ellipse for the beam are a and b, respectively, then the ellipticity is given by

$$\frac{\mp b}{a} = \tan\chi,$$

where $-\pi/4 \leq \chi \leq \pi/4$. If the sign of the ratio is negative (positive) then the polarisation is right-(left-) handed. The angle ψ is that which the major axis of the polarisation ellipse makes to the OX-axis where $0 \leq \psi < \pi$.

If the polariser and quarter-wave-plate were perfect devices ($p = \sqrt{2}$, $p_p = 1$ and $\gamma = 45°$) then the four measurements referred to in equations (6.13), (6.14), (6.15) and (6.16) would enable the four Stokes parameters to be found, so determining all the characteristics of the incident beam. However, as we have already seen, real devices have attenuation and so additional measurements are required to accomplish this. It was my purpose to obtain the ellipticity and orientation of the polarisation ellipse for a beam and equations (6.18) and (6.19) show that when the ratios of Stokes parameters are taken the attenuation factor for the polariser, p_p, is eliminated from the resultant expressions and so this parameter need not be measured.

In summary, inclusion of the anisotropic attenuation of the quarter-wave-plate will result in an improvement in accuracy for the ellipticity and orientation of the polarisation measured by Stokes classical method. The price to be paid for the increased accuracy is that the attenuation factors for the quarter-wave-plate must first be determined, however the attenuation factor for the polariser is not required.

6.7 Intensity Measurement Method using a Circular Polariser

The ellipticity and the orientation of the polarisation ellipse are found from the ratios S_3/S_0 and S_2/S_1, respectively. For Stokes classical method the polariser is used in the optical train for all the measurements hence its attenuation coefficient is a common factor in all the Stokes parameters and is eliminated when ratios are taken to determine the ellipticity and orientation of the polarisation ellipse.

Because the quarter-wave-plate is only included in the optical train for determining the Stokes parameter S_3 its attenuation coefficient p only appears in the expression for this parameter. When the expressions for the ratios S_3/S_0 and S_2/S_1 are obtained the factor p is not eliminated from the expression for S_3/S_0 and so it becomes a factor that must be measured in order to determine the ellipticity using Stokes classical method.

To eliminate the need to measure p Collett[22, p95] includes both the quarter-wave-plate and the linear polariser in all measurements by creating a circular polariser from the combination. In this way both the attenuation coefficient for the polariser p_p and the attenuation coefficient for the quarter-wave-plate p appear as common factors in all the Stokes parameters and are therefore eliminated by cancellation in the expressions for the ratios S_3/S_0 and S_2/S_1. To create the circular polariser the linear polariser and the quarter-wave-plate are cemented together so that the transmission axis of the polariser is fixed at an angle of 45° to the fast-axis of the quarter-wave-plate (see Figure(6.2)).

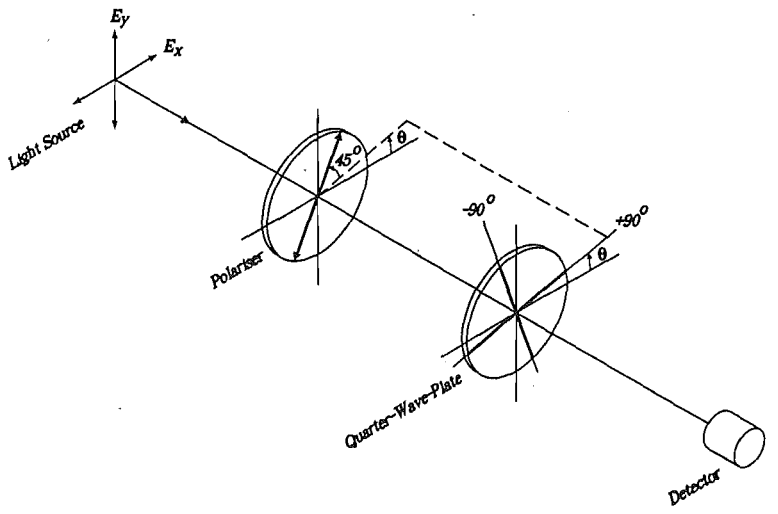

Figure 6.2: Polarisation characteristics determined from measured intensities for three orientations of the circular polariser and a fourth with the circular polariser reversed.

The strategy that Collett proposes will work provided the quarter-wave-plate has isotropic attenuation i.e. $p_x = p_y$ or $\gamma = 45°$. In general there will be some anisotropy in the attenuation of the quarter-wave-plate. We shall see that by following

the measurement methods proposed by Collett[22, p95] in finding the ellipticity and orientation of the polarisation ellipse for a beam of light we can accommodate the attenuation anisotropy of the quarter-wave-plate and make accurate measurements at the expense of first determining γ defined by

$$\tan\gamma = \frac{p_y}{p_x},$$

where p_x and p_y are defined in Section (6.1) and the method for measurements of p_x and p_y is discussed in Section (6.5).

Let us suppose that p_x and p_y have been measured for the quarter-wave-plate as mentioned above. Let us suppose that a beam of light is propagating along the z-axis so that its **k**-vector is collinear with it and points towards the origin and the beam has the Stokes vector $S = (S_0, S_1, S_2, S_3)^T$. If the polariser—quarter-wave-plate combination is placed at the origin so that the fast-axis of the quarter-wave-plate is inclined at an angle θ to the OX-axis and it lies in the XY-plane then the transformed beam leaving the combination will have a Stokes vector given by

$$S'_\theta = W^{p,\gamma}_{\theta,90^\circ} P_{(\theta+45^\circ)} S = \frac{{p_p}^2 p^2}{4}(S_0 - S_1\sin 2\theta + S_2\cos 2\theta)\begin{pmatrix} 1 \\ \cos 2\gamma\cos 2\theta \\ \cos 2\gamma\sin 2\theta \\ -\sin 2\gamma \end{pmatrix}.$$

Three measurements of the intensity of the beam transmitted by the combination are now made for $\theta = 0^\circ, \theta = 45^\circ$ and $\theta = 90^\circ$, respectively.

A fourth measurement is required. First the polariser—quarter-wave-plate combination is rotated about the OZ-axis so that the fast-axis of the quarter-wave-plate is along the OX-direction. Next the combination is rotated about the OX-axis through 180°. The reversed combination is now used to make a fourth intensity measurement. The Stokes vectors of the transmitted beam for the four sets of respective measurements are

$$S'_{0^\circ} = \frac{{p_p}^2 p^2}{4}(S_0 + S_2)\begin{pmatrix} 1 \\ \cos 2\gamma \\ 0 \\ -\sin 2\gamma \end{pmatrix}, \tag{6.20}$$

$$S'_{45^\circ} = \frac{{p_p}^2 p^2}{4}(S_0 - S_1)\begin{pmatrix} 1 \\ 0 \\ \cos 2\gamma \\ -\sin 2\gamma \end{pmatrix}, \tag{6.21}$$

$$S'_{90^\circ} = \frac{{p_p}^2 p^2}{4}(S_0 - S_2)\begin{pmatrix} 1 \\ -\cos 2\gamma \\ 0 \\ -\sin 2\gamma \end{pmatrix}, \tag{6.22}$$

$$S''_{R0^\circ} = P_{-45^\circ} W^{p,\gamma}_{0^\circ,90^\circ} S = \frac{{p_p}^2 p^2}{4} (S_0 + S_1 \cos 2\gamma - S_3 \sin 2\gamma) \begin{pmatrix} 1 \\ 0 \\ -1 \\ 0 \end{pmatrix}. \tag{6.23}$$

The intensity of the transmitted beam associated with each of the measurements is given by the first component of the respective Stokes vector. If these intensities are denoted $I(0°)$, $I(45°)$, $I(90°)$ and $I_R(0°)$, respectively, then solving these equations gives the Stokes parameters as

$$\begin{aligned}
S_0 &= \frac{2}{{p_p}^2 p^2} (I(0°) + I(90°)), \\
S_1 &= \frac{2}{{p_p}^2 p^2} (I(0°) + I(90°) - 2I(45°)), \\
S_2 &= \frac{2}{{p_p}^2 p^2} (I(0°) - I(90°)), \\
S_3 &= \frac{2}{{p_p}^2 p^2 \sin 2\gamma} ([1 + \cos 2\gamma] (I(0°) + I(90°)) - 2I_R(0°) - 2 (\cos 2\gamma) I(45°)).
\end{aligned}$$

The ellipticity and the orientation of the polarisation ellipse are obtained from

$$\begin{aligned}
\sin 2\chi &= \frac{S_3}{S_0} \\
&= \frac{([1 + \cos 2\gamma] (I(0°) + I(90°)) - 2I_R(0°) - 2 (\cos 2\gamma) I(45°))}{\sin 2\gamma (I(0°) + I(90°))}
\end{aligned} \tag{6.24}$$

$$\tan 2\psi = \frac{S_2}{S_1} = \frac{(I(0°) - I(90°))}{(I(0°) + I(90°) - 2I(45°))} \tag{6.25}$$

It will be seen that from equations (6.24) and (6.25) we can obtain the ellipticity and orientation of the polarisation ellipse, but that as they stand they are not independent of the attenuation factors as $\sin 2\gamma$ and $\cos 2\gamma$ appear. Both factors are functions of γ which is defined by

$$\tan \gamma = \frac{p_y}{p_x}. \tag{6.26}$$

If the attenuation of the quarter-wave-plate is isotropic, that is, $p_y = p_x$ then $\gamma = 45°$ and both equations (6.24) and (6.25) are independent of the attenuation factors and become, respectively,

$$\begin{aligned}
\sin 2\chi &= \frac{S_3}{S_0} = \frac{(2I_R(0°) - I(0°) - I(90°))}{(I(0°) + I(90°))}, \\
\tan 2\psi &= \frac{S_2}{S_1} = \frac{(I(0°) - I(90°))}{(I(0°) + I(90°) - 2I(45°))}.
\end{aligned}$$

By insisting that the quarter-wave-plate has isotropic attenuation the Stokes vectors given by equations (6.20), (6.21), and (6.22) are now those for circular polarisation and that the polariser—quarter-wave-plate combination functions as a circular polariser.

In summary, we can use the circular polariser method to obtain Stokes parameters and hence the ellipticity and orientation of the polarisation ellipse for a beam of light even when the quarter-wave-plate of the circular polariser combination has anisotropic attenuation. We follow the original plan for constructing the circular polariser and making intensity measurements. In order to obtain accurate values for the ellipticity and orientation of the polarisation ellipse for the beam we must first determine γ for the quarter-wave-plate from equation (6.26) using the measurement methods of Section (6.5) to obtain p_x and p_y and then use equations (6.24) and (6.25).

6.8 Null-Intensity Method using a Variable-Wave-Plate and an Analyser

The previous methods all required the use of a stable linear detector because the intensity measurements were used in obtaining the polarisation characteristics of the incident beam. This method requires that the detector only determine when there is a minimum in intensity or when there is no intensity at all. A schematic diagram of the apparatus is shown in Figure 6.3.

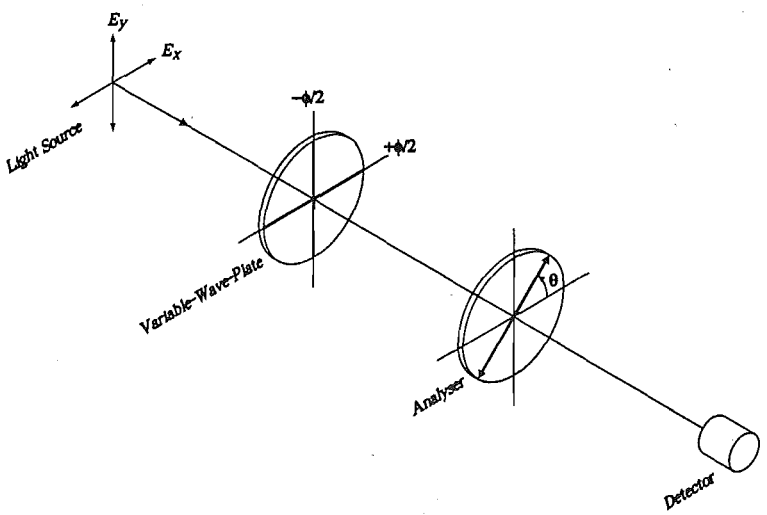

Figure 6.3: Polarisation characteristics determined from the introduced phase-shift by the variable-wave-plate and the analyser orientation.

The orientation of the variable-wave-plate is fixed with its fast axis parallel to the OX-axis. The linear polariser is in a rotatable mount which is calibrated to measure the orientation of the polariser. The detector need not be particularly linear but should have a good null-detection capability.

To obtain a measurement the phase of the variable-wave-plate is adjusted until a minimum is found in the intensity of light falling on the detector. The polariser is then rotated until the intensity at the detector falls even further towards zero. Theoretically, as the polariser is rotated there should be some point at which the intensity drops exactly to zero, however, in practice it is often necessary to readjust both the variable-wave-plate and polariser to achieve the best possible null.

In order to make the analysis easier we use the alternative form of the Stokes vector[22, pp41 - 42] for the beam entering the apparatus i.e.

$$S = I_0 \left(1, \cos 2\alpha, \sin 2\alpha \cos\delta, \sin 2\alpha \sin\delta\right)^T,$$

where $I_0 = \frac{1}{2}\sqrt{\varepsilon_0/\mu_0}\left({E_{0x}}^2 + {E_{0y}}^2\right)$, $\tan\alpha = E_{0y}/E_{0x}$, $\delta = \delta_y - \delta_x$ and the components of the electric field for the beam are $E_x(t) = E_{0x}(t)\cos\left[\omega t + \delta_x(t)\right]$ and $E_y(t) = E_{0y}(t)\cos\left[\omega t + \delta_y(t)\right]$. The Stokes vector for the light falling on the detector, S', is given by

$$S' = P_\theta W^{p,\gamma}_{0°,\phi} S = \frac{p^2 {p_p}^2 I_0}{4}\begin{pmatrix} K \\ K\cos 2\theta \\ K\sin 2\theta \\ L \end{pmatrix},$$

where

$$\begin{aligned} K &= \left(1 + \cos 2\alpha\left(\cos 2\gamma + \cos 2\theta\right) + \cos 2\theta\cos 2\gamma + \sin 2\alpha \sin 2\gamma \sin 2\theta \cos\left(\delta - \phi\right)\right), \\ L &= \sin 2\gamma \sin 2\alpha \sin(\delta - \phi). \end{aligned}$$

The intensity of the beam falling on the detector is given by the first component of S', that is,

$$I_0' = \frac{p^2 {p_p}^2 I_0}{4}\left(1 + \cos 2\alpha\left(\cos 2\gamma + \cos 2\theta\right) + \cos 2\theta\cos 2\gamma + \sin 2\alpha\sin 2\gamma\sin 2\theta\cos\left(\delta - \phi\right)\right). \tag{6.27}$$

To derive the equations giving the ellipticity and orientation of the polarisation ellipse we shall follow, mathematically, the steps taken in practice to get to a null. First, the phase-shift, ϕ, is adjusted until there is a minimum in intensity of the beam on the detector. Mathematically this is equivalent to $\partial I_0'/\partial\phi = 0$. From differentiation of equation (6.27) we get $\sin 2\alpha \sin 2\gamma \sin 2\theta \sin\left(\delta - \phi\right) = 0$. Since it is ϕ which is to be set so that I_0' is a minimum we have

$$\delta = n\pi + \phi, \tag{6.28}$$

where $n = 0, 1, 2, \cdots$. We can now replace $\cos\left(\delta - \phi\right)$ with $\cos n\pi$ in equation (6.27). The two possible values which $\cos n\pi$ can take are 1 for n even (or zero) and -1 for n odd. If the ellipticity and the orientation of the polarisation ellipse are calculated for both cases the results are the same. As a representative we shall follow the calculation through for n odd. Equation (6.27) can be therefore be rewritten as

$$I_0' = A\left[1 + \cos\left(2\alpha + B\right)\right], \tag{6.29}$$

where A$= 1 + \cos 2\gamma \cos 2\theta$ and $B = \tan^{-1}\left[(\sin 2\gamma \sin 2\theta) / (\cos 2\gamma + \cos 2\theta)\right]$.

The next step in the null-intensity method is to rotate the polariser until $I_0^{'} = 0$. Variable-wave-plates require transmission along both axes hence A is not zero. This means that the factor in the square brackets on the right-hand-side of equation (6.29) is zero. Hence we get $\cos(2\alpha + B) = -1$ or

$$2\alpha = (2m + 1)\,\pi - B, \tag{6.30}$$

where $m = 0, 1, 2, \cdots$. Born and Wolf[18, Chapter 1] give relationships between α, δ and χ, ψ, namely,

$$\tan 2\psi = \tan 2\alpha \cos\delta \tag{6.31}$$

$$\sin 2\chi = \sin 2\alpha \sin\delta. \tag{6.32}$$

Substitution of equations (6.28) and (6.30) into equations (6.31) and (6.32) gives

$$\tan 2\psi = \frac{\sin 2\gamma \sin 2\theta \cos\phi}{\cos 2\gamma + \cos 2\theta}, \quad \sin 2\chi = \frac{-\sin 2\gamma \sin 2\theta \sin\phi}{1 + \cos 2\gamma \cos 2\theta}. \tag{6.33}$$

One can verify that these equations revert into those given by Collett[22, p102] $\tan 2\psi = \tan 2\theta \cos\phi$, $\sin 2\chi = \sin 2\theta \sin\phi$ for the case where the variable-wave-plate is ideal and therefore has isotropic attenuation, i.e. $\gamma = \pi/4$, and where $\phi \rightarrow -\phi$ to account for Collett's use of retardance instead of a normal phase-shift. The ellipticity and orientation of the polarisation ellipse can be found from equations (6.33) (see the definitions at the end of Section 6.6).

6.9 Intensity Measurement Method using Fourier Analysis, a Rotating Quarter-Wave-Plate and an Analyser

The experimental set up is shown in Figure 6.4.

The incident beam first encounters a quarter-wave-plate mounted on a rotator and measurements of the intensity are taken at equiangular intervals so as to complete a full rotation. The transmitted beam passes through an analyser whose transmission axis is parallel to the OX-axis. Finally the beam falls on the detector. If the Stokes vector of the incident beam is $S = (S_0, S_1, S_2, S_3)$ then that for the beam falling on the detector is given by

$$S^{'} = P_{0^\circ} W^{p,\gamma}_{\theta,90^\circ} S = H \begin{pmatrix} 1 \\ 1 \\ 0 \\ 0 \end{pmatrix}$$

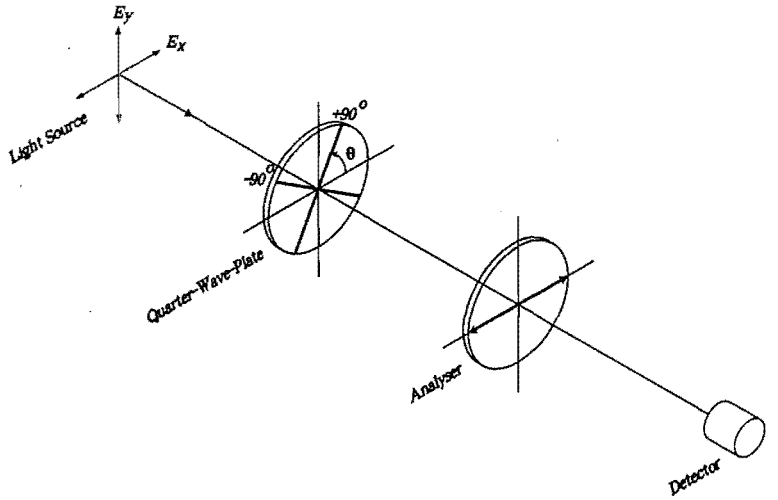

Figure 6.4: Polarisation characteristics obtained from the intensity measurements of the beam which passes through a quarter-wave-plate which is stepped in orientation and then an analyser.

where

$$H = \frac{{p_p}^2 p^2}{4} \left[\left(1 + \cos 2\gamma \cos 2\theta\right) S_0 + \cos 2\theta \left(\cos 2\theta + \cos 2\gamma\right) S_1 + \sin 2\theta \left(\cos 2\theta + \cos 2\gamma\right) S_2 - \sin 2\theta \sin 2\gamma S_3 \right].$$

The intensity can be written in the form of the truncated Fourier series as

$$I_0 = \frac{{p_p}^2 p^2}{4} \left[\left[S_0 + (S_1/2)\right] + \left[(S_0 + S_1)\cos 2\gamma\right] \cos 2\theta - \left[S_3 \sin 2\gamma - S_2 \cos 2\gamma\right] \sin 2\theta + \left[S_1/2\right] \cos 4\theta + \left[S_2/2\right] \sin 4\theta \right].$$

This can also be written as

$$I\left(\theta\right) = \frac{1}{2}\left[A + B^{'} \cos 2\theta + B \sin 2\theta + C \cos 4\theta + D \sin 4\theta\right], \tag{6.34}$$

where

$$A = \frac{{p_p}^2 p^2}{2}\left(S_0 + \frac{S_1}{2}\right), \tag{6.35}$$

$$B^{'} = \frac{{p_p}^2 p^2 \left(S_0 + S_1\right)\cos 2\gamma}{2} \tag{6.36}$$

$$B = \frac{{p_p}^2 p^2 \left(S_2 \cos 2\gamma - S_3 \sin 2\gamma\right)}{2}, \tag{6.37}$$

$$C = \frac{{p_p}^2 p^2 S_1}{4}, \tag{6.38}$$

$$D = \frac{{p_p}^2 p^2 S_2}{4}. \tag{6.39}$$

By Fourier analysis[17] the coefficients of this equation are given by

$$A = \frac{1}{\pi}\int_0^{2\pi} I\left(\theta\right) d\theta, \tag{6.40}$$

$$B' = \frac{2}{\pi}\int_0^{2\pi} I(\theta)\cos 2\theta d\theta \tag{6.41}$$

$$B = \frac{2}{\pi}\int_0^{2\pi} I(\theta)\sin 2\theta d\theta, \tag{6.42}$$

$$C = \frac{2}{\pi}\int_0^{2\pi} I(\theta)\cos 4\theta d\theta, \tag{6.43}$$

$$D = \frac{2}{\pi}\int_0^{2\pi} I(\theta)\sin 4\theta d\theta. \tag{6.44}$$

Solving equations (6.35), (6.37), (6.38) and (6.39) for the Stokes parameters gives

$$S_0 = \frac{2(A-C)}{{p_p}^2 p^2}, \tag{6.45}$$

$$S_1 = \frac{4C}{{p_p}^2 p^2}, \tag{6.46}$$

$$S_2 = \frac{4D}{{p_p}^2 p^2}, \tag{6.47}$$

$$S_3 = \frac{2}{{p_p}^2 p^2 \sin 2\gamma}\left[2D\cos 2\gamma - B\right]. \tag{6.48}$$

Equation (6.36) has been ignored because it is not essential for determining the Stokes parameters and its presence is entirely due to the anisotropic attenuation of the quarter-wave-plate.

In practice the measurements of the intensity are taken at N equal angular intervals as the quarter-wave-plate rotates a full turn. We now use the methods of discrete Fourier analysis to find the Stokes parameters. Equation (6.34) becomes

$$I(n\theta_s) = \frac{1}{2}\left[A + B'\cos 2n\theta_s + B\sin 2n\theta_s + C\cos 4n\theta_s + D\sin 4n\theta_s\right],$$

where $\theta_s = 2\pi/N$, being the angular step size. From the theory of discrete Fourier transforms[8] the coefficients A, B', B, C and D are given by

$$A = \frac{2}{N}\sum_{n=1}^{N} I(n\theta_s),$$

$$B' = \frac{4}{N}\sum_{n=1}^{N} I(n\theta_s)\cos 2n\theta_s,$$

$$B = \frac{4}{N}\sum_{n=1}^{N} I(n\theta_s)\sin 2n\theta_s,$$

$$C = \frac{4}{N}\sum_{n=1}^{N} I(n\theta_s)\cos 4n\theta_s,$$

$$D = \frac{4}{N}\sum_{n=1}^{N} I(n\theta_s)\sin 4n\theta_s.$$

The values for these coefficients can be substituted in equations (6.45) - (6.48) to get the Stokes parameters. From the general theory of polarised light we can find the ellipticity and orientation of the polarisation ellipse from

$$\begin{aligned} \sin 2\chi &= \frac{S_3}{S_0} = \frac{2D\cos 2\gamma - B}{(A-C)\sin 2\gamma}, \\ \tan 2\psi &= \frac{S_2}{S_1} = \frac{D}{C}. \end{aligned}$$

6.10 Null-Intensity Method using a Quarter-Wave-Plate and an Analyser

A correctly oriented quarter-wave-plate will transform a beam of elliptically polarised light into a linearly polarised one. An analyser whose transmission axis is orthogonal to the direction of the electric field vector of the beam transmitted by the quarter-wave-plate will extinguish it. From the orientation of both the fast-axis of the quarter-wave-plate and the transmission axis of the analyser one can determine the polarisation state of the incoming beam. A schematic diagram of the apparatus is shown in Figure (6.5).

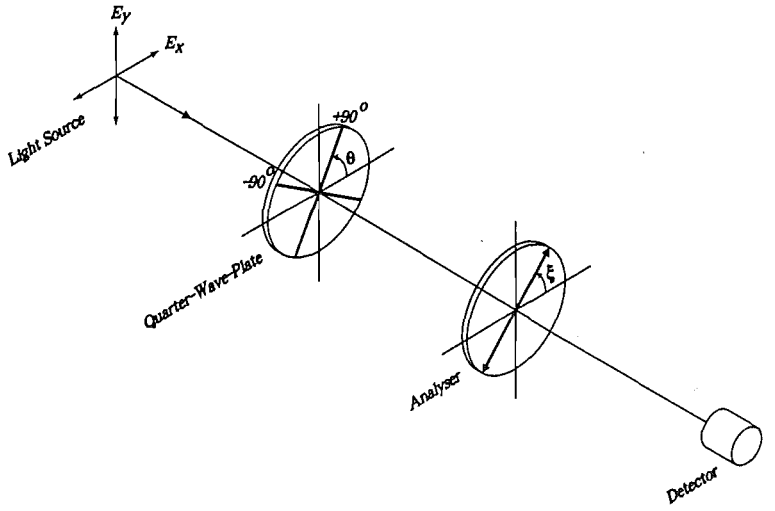

Figure 6.5: Polarisation characteristics determined from the orientation of a quarter-wave-plate and an analyser at extinction.

Let us assume that an arbitrary elliptically polarised beam input is represented by the Stokes vector, given in the alternative form[22, p102], as

$$S = I_0 \begin{bmatrix} 1 \\ \cos 2\alpha \\ \sin 2\alpha \cos\delta \\ \sin 2\alpha \sin\delta \end{bmatrix} \tag{6.49}$$

We shall also assume that the input beam, whose **k** vector is parallel to the OZ-axis, is transformed into a linearly polarised one when the fast axis of the quarter-wave-

plate is at an angle, θ, to the OX-axis. The Stokes vector of the beam transmitted by the quarter-wave-plate is given by

$$S'' = W^{p,\gamma}_{\theta,90^\circ} S = \frac{I_0 p^2}{2} \begin{bmatrix} 1 + \cos 2\gamma \left[\cos 2\alpha \cos 2\theta + \sin 2\alpha \sin 2\theta \cos \delta\right] \\ A \cos 2\theta - B \sin 2\theta \\ A \sin 2\theta + B \cos 2\theta \\ \sin 2\gamma \left[\cos 2\alpha \sin 2\theta - \cos 2\theta \sin 2\alpha \cos \delta\right] \end{bmatrix}, \tag{6.50}$$

where

$$A = \cos 2\gamma + \cos 2\alpha \cos 2\theta + \sin 2\theta \sin 2\alpha \cos \delta, \tag{6.51}$$

$$B = \sin 2\alpha \sin 2\gamma \sin \delta. \tag{6.52}$$

and where $W^{p,\gamma}_{\theta,90^\circ}$ is the matrix representing the quarter-wave-plate; being the matrix given by equation (6.8) with $\phi = 90^\circ$ appropriate to a quarter-wave-plate.

Since the polarisation of the transmitted beam is linear the fourth component of S'' is zero, that is, when $\cos 2\alpha \sin 2\theta - \cos 2\theta \sin 2\alpha \cos \delta$ or

$$\tan 2\theta = \tan 2\alpha \cos \delta. \tag{6.53}$$

From the general theory of polarised light[18, Chapter 1] the orientation, ψ, of the major axis of the polarisation ellipse to the OX-axis is given by the equation

$$\tan 2\psi = \tan 2\alpha \cos \delta. \tag{6.54}$$

By comparing equations (6.53) and (6.54) we have $2\psi = 2\theta + n\pi$ or

$$\psi = \theta + n\pi/2, \tag{6.55}$$

where $n = 0, 1$. Expression (6.55) shows that the fast-axis of the quarter-wave-plate is aligned with either the major or minor axis of the polarisation ellipse. The production of linearly polarised light from the quarter-wave-plate can be explained as follows. When the fast-axis of the quarter-wave-plate is aligned with either the major or minor axis of the polarisation ellipse then the 90° phase-shift between the fast and slow axes of the quarter-wave-plate adds to or subtracts from the 90° phase-shift between the components of the beam, depending on its handedness. In either case the transmitted beam is linearly polarised. We shall see later how to determine which of the axes of the polarisation ellipse is parallel with the fast-axis of the quarter-wave-plate.

For the apparatus illustrated in Figure (6.5) it is easy to find the polarisation characteristics of the input beam if the quarter-wave-plate is ideal. Attenuation in a real quarter-wave-plate has the effect of changing the direction and magnitude of the linearly polarised beam that would be transmitted by an ideal quarter-wave-plate. If the attenuation parameters p, γ, for a real quarter-wave-plate are known then the direction of the polarisation vector of a beam transmitted by an ideal quarter-wave-plate can be calculated from the direction of the polarisation vector of the beam transmitted by the real quarter-wave-plate. Hence the method for determining

the polarisation characteristics for a beam using an ideal quarter-wave-plate can be adapted for use with a real one.

Let us assume that the angle ξ is that which the transmission axis of the analyser makes with the OX-axis, assuming that the transmitted beam has been extinguished. Further, let us assume the angles θ and ξ are restricted so that $0 \leq \theta < 180°$ and $0 \leq \xi < 180°$. The angle $\beta^{'}$ which the polarisation vector of the linearly polarised beam transmitted by the real quarter-wave-plate makes with the OX-axis is given by

$$\beta^{'} = \xi \pm 90°, \tag{6.56}$$

where the sign is chosen so that $0 \leq \beta^{'} < 180°$. If the incident beam has intensity, I_0, then the Stokes vector of this beam is given by

$$S^{''} = qI_0 \begin{pmatrix} 1 \\ \cos 2\beta^{'} \\ \sin 2\beta^{'} \\ 0 \end{pmatrix}, \tag{6.57}$$

where q is a constant accounting for the attenuation in the beam intensity, and $I_0 = \sqrt{\varepsilon_0/\mu_0}\,({E_{0x}}^2 + {E_{0y}}^2)/2$. The Stokes vector of the linearly polarised beam transmitted by an ideal quarter-wave-plate placed in the same input beam is

$$S^{'} = I_0 \begin{pmatrix} 1 \\ \cos 2\beta \\ \sin 2\beta \\ 0 \end{pmatrix}. \tag{6.58}$$

Now the beam whose Stokes vector is $S^{''}$ is the same as the one represented by $S^{'}$ although anisotropically attenuated by the losses in the real quarter-wave-plate. Hence

$$S^{''} = D_{p,\gamma} S^{'}, \tag{6.59}$$

where $D_{p,\gamma}$ is the matrix given by (6.7) representing the attenuation and p and γ are the associated attenuation parameters. Substitution of (6.57), (6.58) and (6.7) in equation (6.59) gives

$$qI_0 \begin{bmatrix} 1 \\ \cos 2\left(\beta^{'} - \theta\right) \\ \sin 2\left(\beta^{'} - \theta\right) \\ 0 \end{bmatrix} = \frac{p^2 I_0}{2} \begin{bmatrix} 1 + \cos 2\gamma \cos 2\left(\beta - \theta\right) \\ \cos 2\gamma + \cos 2\left(\beta - \theta\right) \\ \sin 2\gamma \sin 2\left(\beta - \theta\right) \\ 0 \end{bmatrix}.$$

The ratio of the second and third components give

$$\frac{2\tan\left(\beta^{'} - \theta\right)}{1 - \tan^2\left(\beta^{'} - \theta\right)} = \frac{2\tan\gamma\tan\left(\beta - \theta\right)}{1 - \tan^2\gamma\tan^2\left(\beta - \theta\right)}$$

and we can identify

$$\beta - \theta = \tan^{-1}\left\{\frac{\tan\left(\beta' - \theta\right)}{\tan\gamma}\right\}. \qquad (6.60)$$

Hence the angle, $\beta - \theta$, between the fast-axis of the ideal quarter-wave-plate and the direction of the polarisation vector transmitted by it have been found in terms of the angle, $\beta' - \theta$, between the fast-axis of the real quarter-wave-plate and the polarisation vector of the beam transmitted by it and the attenuation parameter γ.

If we now assume that an ideal quarter-wave-plate is placed in the incident elliptically polarised beam and that it, together with the analyser, are being used to analyse the polarisation of the incident beam. The only information required to calculate the ellipticity and orientation of the polarisation ellipse are the angle, θ, between the fast-axis of the ideal (or real) quarter-wave-plate and the OX-axis and the angle, $\beta - \theta$ just found above.

Figure (6.6) shows the four types of polarisation ellipse possible for the elliptically polarised beam classified according to the handedness of the polarisation and which of the first two quadrants the major axis of the polarisation ellipse lies in.

On each diagram the line through the origin label **FA** shows the direction of the fast-axis of the quarter-wave-plate, the vector labelled **OE** shows the direction and amplitude of the electric field vector of the linearly polarised beam transmitted by the ideal quarter-wave-plate and the arrow on the ellipse shows the handedness of the polarisation. It can be seen that for left-handed polarisation $\beta - \theta < 0$ or $\beta - \theta > 90°$ and for right-handed polarisation $0 < \beta - \theta < 90°$. The caption associated with each part of the diagram shows how the angles in the diagram are related to the ellipticity angle, χ, and the orientation, ψ, of the (major axis of the) polarisation ellipse, bearing in mind that $\chi < 0$ for right-handed polarisation and $\chi > 0$ for polarisation of the opposite handedness.

6.11 Null-Modulation Intensity Method using a Variable-Wave-Plate and a Rotating Analyser

In 1937, C. V. Kent and J. Lawson proposed a new method for measuring the ellipticity and the orientation of the polarisation ellipse[43] which takes advantage of the best operating conditions for the photomultiplier tube, namely, full illumination. The input elliptically polarised beam is transformed by a variable-wave-plate whose phase-shift and orientation is adjusted so that the beam transmitted is circularly polarised. Circular polarisation is detected when the beam transformed by a spinning analyser remains unmodulated in intensity.

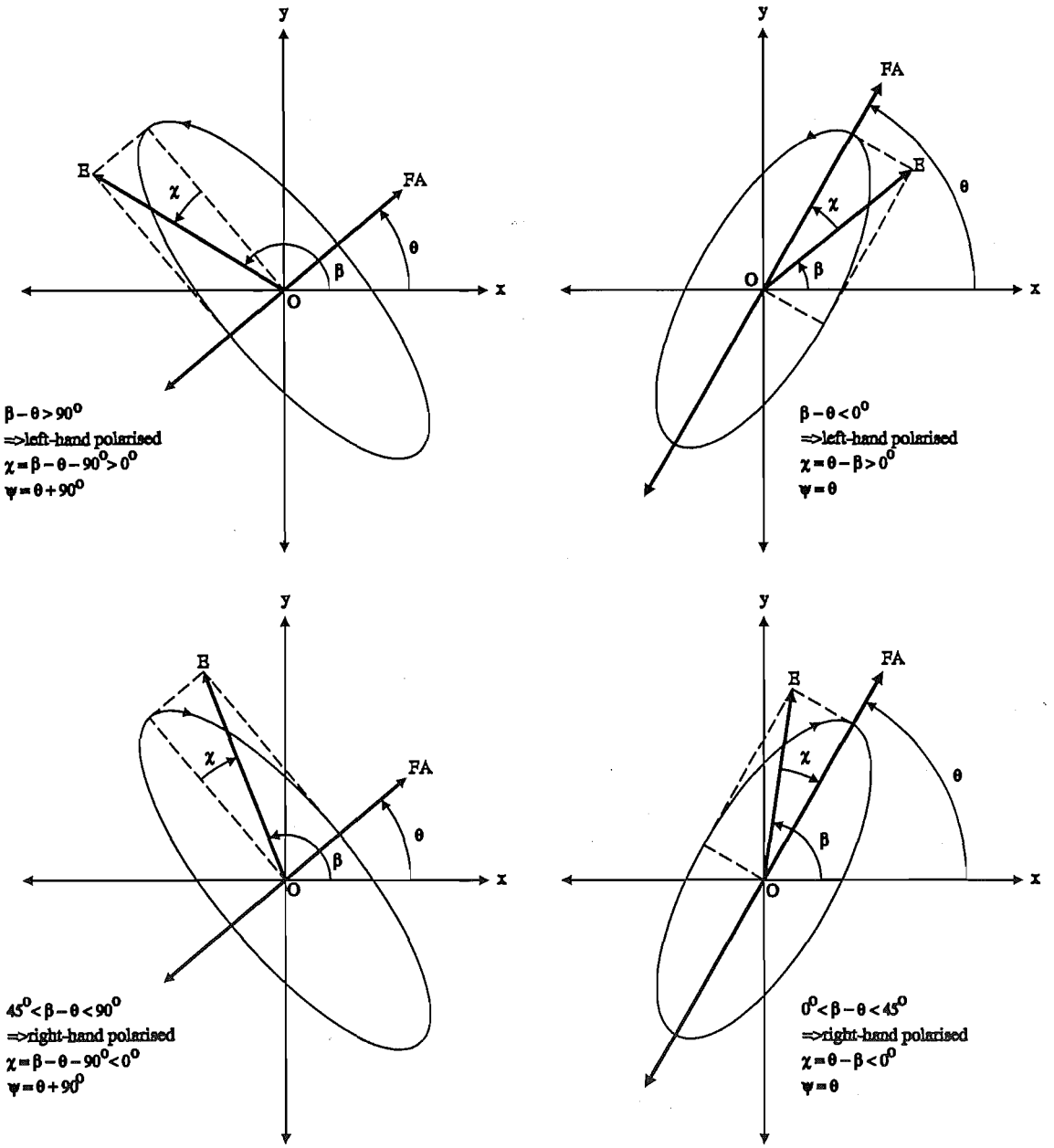

Figure 6.6: The four types of input beam polarisation ellipse possible. Vector OE shows the direction of the linearly polarised beam transmitted by the ideal quarter-wave-plate where its fast-axis is labelled FA.

Figure (6.7) shows a schematic diagram of the apparatus for measuring polarisation with this method.

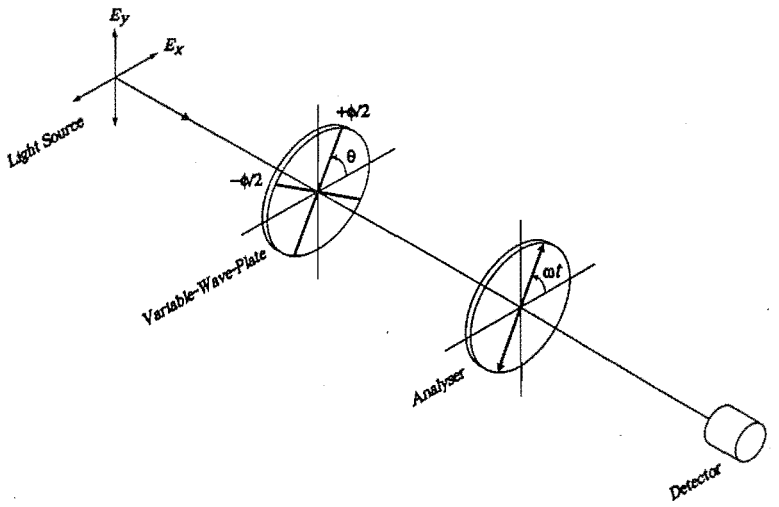

Figure 6.7: Polarisation characteristics determined by introducing a known phase-shift using a variable-wave-plate at a known orientation to generate a circularly polarised beam. Circular polarisation is detected by constant intensity in the beam transmitted by the rotating analyser.

The incident beam show **k**-vector is parallel to the OZ-axis of a cartesian system of axes has arbitrary elliptical polarisation represented here by the alternative form of the Stokes vector $S = I_0\,(1, \cos 2\alpha, \sin 2\alpha\cos\delta, \sin 2\alpha\sin\delta)^T$[22, p102], where $I_0 = \frac{1}{2}\sqrt{\varepsilon_0/\mu_0}\,({E_{0x}}^2 + {E_{0y}}^2)$, $\tan\alpha = E_{0y}/E_{0x}$, $\delta = \delta_y - \delta_x$ and the components of the electric field for the beam are $E_x(t) = E_{0x}(t)\cos[\omega t + \delta_x(t)]$ and $E_y(t) = E_{0y}(t)\cos[\omega t + \delta_y(t)]$.

Let us assume that the phase-shift, ϕ, and the angle, θ, which the fast-axis makes with the OX-axis of the variable-wave-plate have been adjusted so that the transmitted beam is circularly polarised. It is better to take a different approach to the usual straightforward one for analysing the problem further as it eliminates some tedious algebra. Since the output beam is circularly polarised we can represent this by the Stokes vector $S' = k\,(1, 0, 0, 1)^T$, where k is a constant. The Stokes vector, S', is the result of the input beam being transformed by the variable-wave-plate whose phase-shift and orientation have been appropriately adjusted hence we can write the vector equation

$$\frac{I_0 p^2}{2}\begin{bmatrix} 1 & 0 & 0 & 0 \\ 0 & \cos 2\theta & -\sin 2\theta & 0 \\ 0 & \sin 2\theta & \cos 2\theta & 0 \\ 0 & 0 & 0 & 1 \end{bmatrix}\begin{bmatrix} 1 & \cos 2\gamma & 0 & 0 \\ \cos 2\gamma & 1 & 0 & 0 \\ 0 & 0 & \sin 2\gamma\cos\phi & \sin 2\gamma\sin\phi \\ 0 & 0 & -\sin 2\gamma\sin\phi & \sin 2\gamma\cos\phi \end{bmatrix}\cdot$$
$$\begin{bmatrix} 1 & 0 & 0 & 0 \\ 0 & \cos 2\theta & \sin 2\theta & 0 \\ 0 & -\sin 2\theta & \cos 2\theta & 0 \\ 0 & 0 & 0 & 1 \end{bmatrix}\begin{pmatrix} 1 \\ \cos 2\alpha \\ \sin 2\alpha\cos\delta \\ \sin 2\alpha\sin\delta \end{pmatrix} = k\begin{pmatrix} 1 \\ 0 \\ 0 \\ 1 \end{pmatrix}.$$

By multiplying both sides of the equation by the inverse of the matrix appearing

on the extreme left, a new equation is generated. The process is repeated for each successive equation until we have

$$\frac{I_0 p^2}{2}\begin{pmatrix} 1 \\ \cos 2\alpha \\ \sin 2\alpha \cos\delta \\ \sin 2\alpha \sin\delta \end{pmatrix} = \frac{k}{\sin^2 2\gamma}\begin{pmatrix} 1 \\ \sin 2\gamma \sin 2\theta \sin\phi - \cos 2\gamma \cos 2\theta \\ -\sin 2\gamma \cos 2\theta \sin\phi - \cos 2\gamma \sin 2\theta \\ \sin 2\gamma \cos\phi \end{pmatrix}$$

The first components of the vector equation allow us to assign

$$k = \frac{I_0 p^2 \sin^2 2\gamma}{2}.$$

and so the next three components of the vector equation give

$$\cos 2\alpha = \sin 2\gamma \sin 2\theta \sin\phi - \cos 2\gamma \cos 2\theta, \tag{6.61}$$

$$\sin 2\alpha \cos\delta = -\sin 2\gamma \cos 2\theta \sin\phi - \cos 2\gamma \sin 2\theta, \tag{6.62}$$

$$\sin 2\alpha \sin\delta = \sin 2\gamma \cos\phi. \tag{6.63}$$

The parameters θ and ϕ are obtained from the settings of the variable-wave-plate, but the three unknowns α, δ and γ remain to be found. It might be thought that the three equations given would make this possible, however, the equations are not independent. The parameter, γ, defined in section 6.4, must be found from separate measurements.

If we divide (6.62) by (6.63) and (6.62) by (6.61) we obtain

$$\cos 2\alpha = -\left(\cos 2\gamma \cos 2\theta + \sin 2\gamma \sin 2\theta \sin\phi\right), \tag{6.64}$$

$$\cot\delta = \cos 2\theta \tan\phi - \cot 2\gamma \sin 2\theta \sec\phi, \tag{6.65}$$

$$\cos\delta = \frac{\cot 2\alpha \left(\cot 2\gamma \sin 2\theta - \cos 2\theta \sin\phi\right)}{\left(\cot 2\gamma \cos 2\theta + \sin 2\theta \sin\phi\right)}. \tag{6.66}$$

If a Soleil-Babinet is used as the variable-wave-plate it is a good approximation that $\gamma = \pi/4$ i.e. its attenuation is isotropic. This was the assumption that Kent and Lawson made in their analysis. Hence equations (6.61) and (6.62) become

$$\cos 2\alpha = \sin\phi \sin 2\theta, \tag{6.67}$$

$$\sin 2\alpha \cos\delta = -\sin\phi \cos 2\theta, \tag{6.68}$$

$$\sin 2\alpha \sin\delta = \cos\phi, \tag{6.69}$$

If we divide (6.68) by(6.69) and then (6.68) by (6.67) we obtain the equations

$$\cos 2\alpha = \sin\phi \sin 2\theta, \tag{6.70}$$

$$\cot\delta = \tan\phi \cos 2\theta, \tag{6.71}$$

$$\cos\delta = \cot 2\alpha \cot 2\theta. \tag{6.72}$$

By making the following change in notation

$$\begin{aligned} \alpha &\rightarrow \gamma, \\ \delta &\rightarrow \Delta, \\ o &\rightarrow \alpha, \\ \theta &\rightarrow \phi, \end{aligned}$$

and placing a $\pm$ sign in front of the right-hand side of equation (6.70) to account for their polarisation handedness choice for the beam exiting the wave-plate the equations (6.70), (6.71) and (6.72) become those given by Kent and Lawson.

It can be seen from equations (6.64), (6.65) and (6.66) that one does not require isotropic attenuation in the variable-wave-plate to still obtain the ellipticity and orientation of the polarisation ellipse. However, the variable, γ, will have to be obtained by separate measurements.

6.12 Intensity Measurement Method using Photoelastic Modulators

When mechanical stress is applied to a suitable transparent material (fused quartz, for example) the sample exhibits birefringence proportional to the resultant strain. If a rectangular bar is created from such material which will also support a longitudinal acoustic vibration then the periodic stress set up by the vibration will in turn induce a periodic change in birefringence. The block of material used in photoelastic modulators is designed to be acoustically resonant at a resonant frequency in the low ultrasonic range (20 kHz to 100 kHz), being determined by the speed of a longitudinal sound wave in the material and the length of the resonant cavity. By carefully varying the type, size and shape of optical material and coupling closely matched drive and control circuits a wide range of photoelastic modulators can be created.

In birefringent material ($n_x - n_y \neq 0$) the x- and y-components of a monochromatic beam of light passing through it propagate at different speeds. If a beam of light passes through a block of such material of thickness, T, and the components of the beam at the point of entry are in phase then at the point of exit there will be a phase difference, ϕ, between them given by

$$\phi = \frac{2\pi T\,(n_x - n_y)}{\lambda_l},$$

where n_x and n_y are, respectively, the refractive indices seen by the x- and y-components of the light beam; λ_l is the wavelength of the beam in vacuum. A device which induces a phase-shift between orthogonal components of a light beam travelling through it constitutes a wave-plate and because the birefringence periodically changes in the photoelastic modulator so does the phase-shift. The creation of the photoelastic modulator has enabled the polarisation characteristics of a light

beam to be measured successively every 10 μs. Previously the shortest interval between measurements was $\sim$ 1 ms [23]. The automating measurement has also been made easier with this device; Boyes *et al.*[19] show how this can be done using two photoelastic modulators, an analyser, a detector and some other electronics including three lock-in amplifiers and a computer to capture and process the data.

It must be pointed out that this device is only capable of making measurements to an accuracy of the order of 1%. Better results may be obtained with other methods, but at the sacrifice of the great speed of the photoelastic modulator.

Jasperson *et al.*[39] have constructed a photoelastic modulator and their work is briefly described below to illustrate the principles of operation of the device. Figure(6.8)

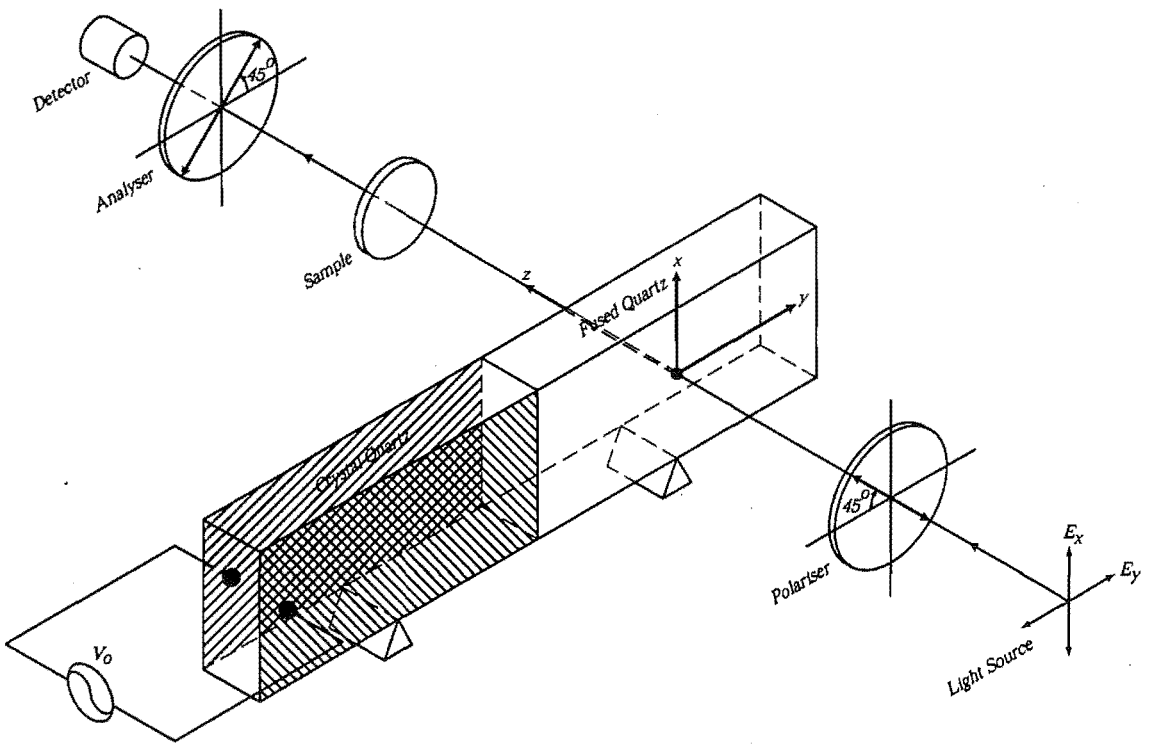

Figure 6.8: Strain birefringence in a sample measured using a photoelastic modulator.

shows a diagram of the photoelastic modulator they constructed. The set up shown in the diagram is that commonly used to measure strain and birefringence in a sample placed in the beam. A more complicated set up is required to measure Stokes parameters and the article by Boyer *et al.* mentioned above discusses just such a set up.

In Figure (6.8) the piezoelectric transducer glued to the left-hand end of the bar of fused quartz generates acoustic longitudinal waves which propagate parallel to the y-direction into the bar. The piezoelectric transducer is a 10 $\times$ 20 $\times$ 50 mm single crystal of quartz, $-18°$ X-cut, which resonates at 50 kHz. An alternating voltage

of this frequency applied between the conducting metal electrodes on the x-y faces induces strain in the crystal of quartz, alternately shortening and lengthening it. The bar of fused quartz glued to the transducer is set into a co-resonant vibration; being resonant at the same frequency. The bar is designed to resonate in its fundamental, simple extensional (longitudinal), mode, $l = \lambda_m/2$, where λ_m is the wavelength of sound in the material. The crystal quartz—fused quartz bars are supported on knife edges parallel to the z-axis at midpoint of their lengths, allowing them to freely resonate in their fundamental modes. The high-'Q' of the coupled resonant systems makes it possible to produce significant birefringence for a small voltage applied to the electrodes of the piezoelectric transducer.

In the cartesian system of axes, located at the center of the largest rectangular face of the fused quartz bar with the y-axis parallel to the longest edge (away from the piezoelectric transducer), the x-axis pointing up and the z-axis penetrating the bar, the extensional displacements along the bar caused by the resonant vibrations in it are described by $\delta = \delta_0 \sin(2\pi y/\lambda_m) \sin \omega t$, where δ_0 is a linear function of the maximum voltage applied to the electrodes of the piezoelectric transducer. The corresponding strain is proportional to $\partial\delta/\partial y$, i.e., to $\cos(2\pi y/\lambda_m)$, which is a maximum at the center of the bar. The birefringence $(n_x - n_y)$ is proportional to the strain and varies in time as $\sin(\omega t)$. Hence we may write

$$\phi = \phi_0 \cos\left(\frac{\pi y}{l}\right) \sin(\omega_m t) = \frac{GV_0}{\lambda_l} \sin(\omega_m t), \tag{6.73}$$

where $\phi_0 = GV_0/\lambda_l$ and G is a constant which is both independent of the voltage applied to the piezoelectric transducer and the wavelength of light used. The variable ϕ_0 denotes the maximum phase-shift applied to the beam during one period of the oscillation of the bar.

The Mueller matrix describing the optical behaviour of the photoelastic modulator is that for a variable-wave-plate, that is,

$$W_\phi^\gamma = \frac{p^2}{2} \begin{bmatrix} 1 & \cos 2\gamma & 0 & 0 \\ \cos 2\gamma & 1 & 0 & 0 \\ 0 & 0 & \sin 2\gamma \cos\phi & \sin 2\gamma \sin\phi \\ 0 & 0 & -\sin 2\gamma \sin\phi & \sin 2\gamma \cos\phi \end{bmatrix},$$

where p, γ and ϕ are the parameters defined in section (6.4). The losses in the real device are again taken care of by the attenuation parameters p and γ. The phase-shift, ϕ, is given by equation (6.73). Replacing ϕ by this equation in the matrix W_ϕ^γ results in terms involving the factors $\cos((GV_0/\lambda_l)\sin(\omega_m t))$ and $\sin((GV_0/\lambda_l)\sin(\omega_m t))$. We may expand both of these factors in terms of a series of Bessel functions[12] of the first kind as

$$\cos((GV_0/\lambda_l)\sin(\omega_m t)) = J_0\left(\frac{GV_0}{\lambda_l}\right) + 2\sum_{n=1}^{\infty} J_{2n}\left(\frac{GV_0}{\lambda_l}\right) \cos(2n\omega_m t),$$

$$\sin((GV_0/\lambda_l)\sin(\omega_m t)) = 2\sum_{n=0}^{\infty} J_{2n+1}\left(\frac{GV_0}{\lambda_l}\right) \sin[(2n+1)\omega_m t],$$

where $J_n(\beta)$ is a Bessel function of the first kind whose numerical value can be calculated from

$$J_n(\beta) = \sum_{m=0}^{\infty} \frac{(-1)^m (\beta/2)^{2m+n}}{m!\,(m+n)!}.$$

The investigation of the photoelastic modulator will not be taken further for two reasons. First, the output from the experimental ring laser was not expected to vary rapidly with time hence a fast measurement device was unnecessary, second, measurement of the birefringence and differential reflectance of the mirrors could easily involve measurements of light where the ellipticity was very small so the best accuracy would be required. It was still however necessary to investigate measurement of polarisation using the device to see if it was suitable and the findings have been included along with all the others.

There is a trend towards automation of experimental work where possible. There are a number of sound reasons why this is attractive. If experimental measurements are made independent of the operator then to a large extent, if the experimental apparatus has been designed correctly, this eliminates the possibility of operator error in taking measurements. If data is being recorded automatically by the same device as that which processes the data (a computer usually) then the possibility of transcription error in transferring data is also eliminated. Measurements taken directly by computer operated experiments are usually done more quickly and efficiently that those taken by a human operator.

The photoelastic modulator could easily be used for making the measurements of the polarisation characteristics of the internal beam of the ring laser. The $\sim 1\%$ accuracy might present a problem in measuring the defects of the ring mirrors. The main unattractive feature of using this device is that two photoelastic modulator heads and a lot of ancillary expensive electronics is required to measure the ellipticity and orientation of the polarisation ellipse for a beam. Since there is no call for great speed in taking measurements and there are easier and less costly options this device was not chosen.

Both the intensity measurement method using an oriented quarter-wave-plate and analyser and the intensity measurement method using a circular polariser do not easily lend themselves to automation. In each case it is difficult to automate the movement of one of the optical components. Although these methods could be implemented they were rejected on the grounds that there were easier methods for achieving the goal.

The null-intensity method using a variable-wave-plate and an analyser is a practical method for automation. The angular precision necessary for adjusting the phase-shift of the variable-wave-plate would be possible using a gearing arrangement on a stepper-motor with a similar arrangement used for orienting the analyser. This method was not chosen because another choice actually allowed two measurement methods to be employed using the same apparatus with the precision required and

the ease of use dictating which method was employed.

Null-modulation intensity method using a variable-wave-plate and a spinning analyser would be quite easy to implement if the variable-wave-plate remained fixed in phase and the range of the input beams phase was limited. If the wave-plate is required to vary then automation is no longer a simple proposition as the stepper-motor and gearing for phase adjustment would be required to rotate with the variable-wave-plate making a cumbersome and awkward mechanical problem to solve and for this reason this method was rejected.

Both the intensity measurement method using Fourier analysis using a stepped quarter-wave-plate and an analyser and the null-intensity method using again a quarter-wave-plate and an analyser were easy to automate and fulfilled all the requirements and could be implemented using the same combination of hardware. The Fourier analyser method was implemented with a photomultiplier set at a fixed voltage as the detector, a Glan-Thompson was used as the analyser set at a fixed orientation with a Soleil-Babinet whose phase-shift was fixed at 90° used as the angularly stepped quarter-wave-plate. The null-intensity polarimeter is described in its own chapter.

Chapter 7

Polarimeter Construction and Calibration

The polarimeter intended for analysing the beam exiting the back of one of the ring laser mirrors employs the intensity measurement method using Fourier analysis as described in Section (6.9). Figure (7.1) shows the construction of the polarimeter.

Two identical rotators were constructed. One was used to position a quarter-wave-plate, the other to rotate a Glan-Thompson polarising prism. Steel discs 250 mm in diameter and 8 mm thick with precision ground edges support the Glan-Thompson Prism and the quarter-wave-plate at their centres. Each disc is supported at the bottom on one side by a roller bearing. On the other side it is supported by a hardened steel shaft 4.762 mm in diameter which is driven by a stepper motor. At the top a loading bearing applies downward thrust on the disc so that good frictional contact is made between the hardened steel shaft and the disc. The stepper motor is driven by a microstepper controller card, supplied by the electronics workshop of the Department of Physics and Astronomy at the University of Canterbury, which delivers 10000 steps per revolution of the stepper motor.

To make measurements using the Fourier method the beam passes through both a quarter-wave-plate and a Glan-Thompson polarising prism on its path to the photocell measuring its intensity. A voltage proportional to the intensity is generated by converting the current generated by the cell into a voltage using a transimpedance amplifier. This signal is further boosted by a following amplifier stage. The output voltage is measured using an 8-bit A/D converter card also constructed by the electronics workshop of the Department of Physics and Astronomy. Control of the stepper motor and collection of the data is performed by a Pascal program on a 386 personal computer.

Although it was necessary for only the quarter-wave-plate to be accurately angularly positioned for measurements using the Fourier method, as mentioned at the end of chapter 6, it was my intention to design the apparatus so that it could also be used for the null-intensity method which requires accurate angular positioning of the analyser as well. For the measurement of the polarisation in the ring laser the accuracy of the Fourier method was thought to be sufficient hence angular position

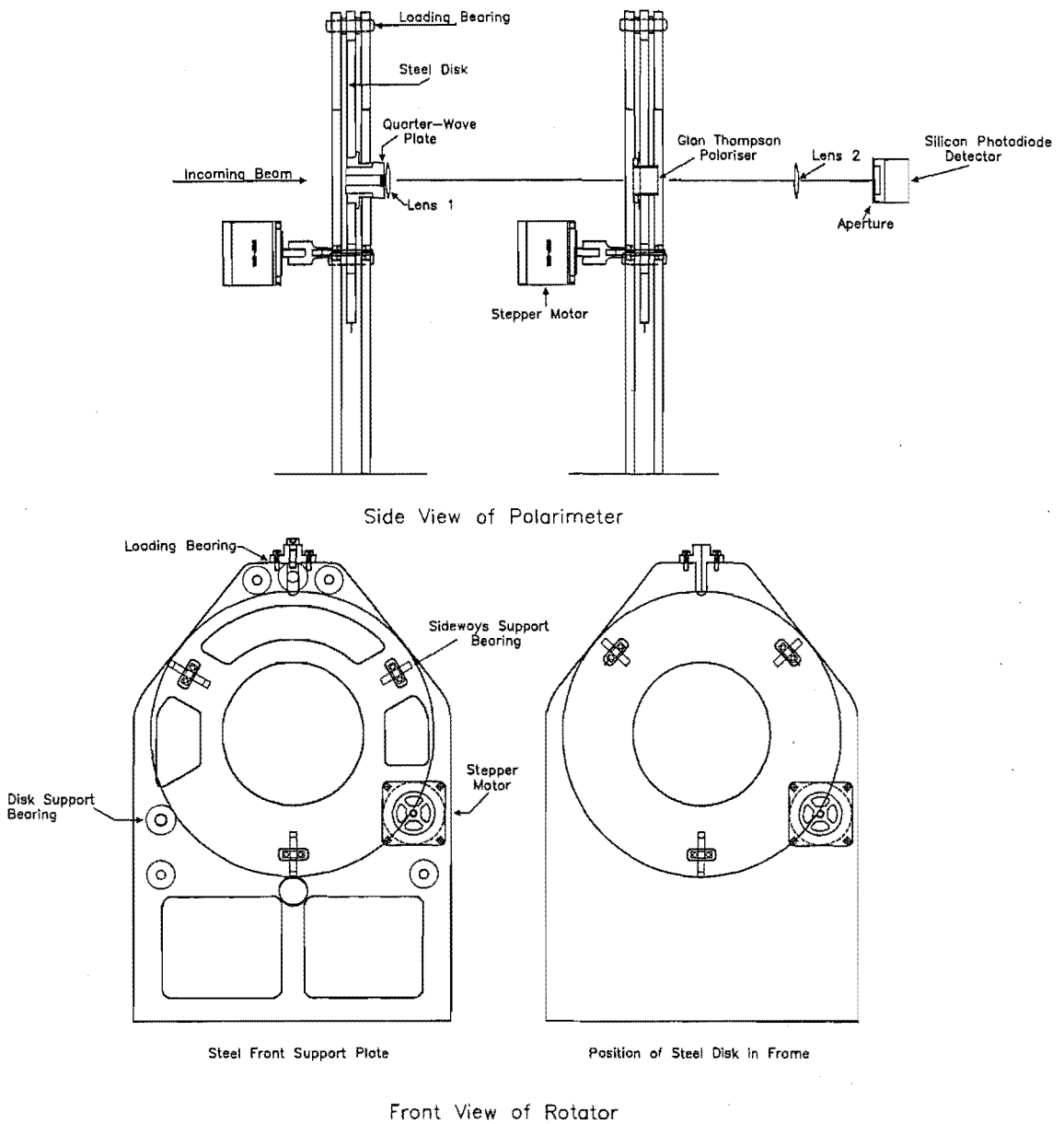

Figure 7.1: Construction of the polarimeter using a quarter-wave-plate and a Glan-Thompson polarising prism.

calibration was only performed on the rotator holding the quarter-wave-plate.

7.1 Calibration of the Polarimeter

To calibrate the angular position of the rotator the quarter-wave-plate was replaced, temporarily, by a Glan-Thompson analyser. An LHP111 Melles Griot laboratory laser was used to supply a polarised input beam normally incident on the Glan-Thompson in the rotator. Although the polarisation ratio of the laboratory laser is quoted as being 500:1 an additional Glan-Thompson polariser was placed in the beam to be sure that a good null would be obtained when the transmission axis of the analyser in the rotator was perpendicular to the direction of the electric field of the incident beam. The intensity of the beam exiting the Glan-Thompson in the rotator was measured using a silicon photodiode model 818-SL manufactured by Newport[61, p 13.21] together with the transimpedance amplifier and A/D converter as mentioned above.

The gain on the voltage amplifier was increased to the point where the readings taken by the 8-bit A/D converter were only zero at the points immediately adjacent to the null. The rotator was set to turn through ~ 5.5 revolutions or 3000000 steps with a reading taken every 1000 steps. With the gain on the voltage amplifier set so high only a small region around each of the nulls obtained readings within the limited range of the electronic circuitry.

To obtain the step numbers at which the intensity was null a computer program was written to optimise the constants I_0, I_{off}, k and n_{null} - being the incident intensity, an offset factor to account for scattered light into the detector and the uncompensated offset due to the finite step size of the A/D converter, a constant of proportionality to convert step number to an angle, and the step number at which the null occurs - in the modified Malus law relation $I = I_0[1 - \cos 2k(n - n_{null})] + I_{off}$, adapted for measurements around the null. Figures (7.2) and (7.3) show, respectively, the calculated curves fitting the data points around the nulls at the beginning and at the end of 5.5 rotations of the disk.

From the step numbers at the null positions and the number of revolutions of the disk between nulls it was calculated that the number of steps per rotation was 503580 ± 20.

For the purposes of calculating the polarisation characteristics of light using the Fourier method it was required that an integral numbers of measurements at equiangular intervals be chosen per revolution of the quarter-wave-plate. To make the number of measurements manageable in checking the calibration of the polarimeter I chose 463 measurements per revolution which means that the number of steps between each measurement is 1090 ($503580 = 462 \times 1090$); the extra measurement is at

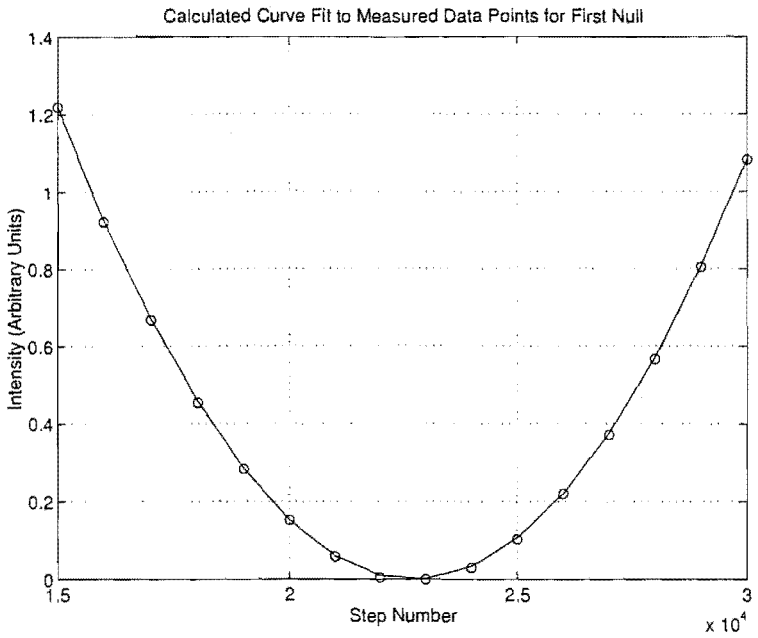

Figure 7.2: Curve optimised to fit the measured intensities at 1000 step intervals for the first null. The expression $I = I_0[1 - \cos 2k(n - n_{null})] + I_{off}$ is the Malus law relation adapted to fit around the null, accomodate the scattered light getting into the detector and the uncompensated offset introduced by the finite step size of the A/D converter. For the curve shown above $k = 1.2477 \times 10^{-5}$ rad/step, $I_0 = 65.994$ (arbitrary units), $I_{off} = -3.2419 \times 10^{-3}$ (arbitrary units) and $n_{null} = 22723 \pm 1$.

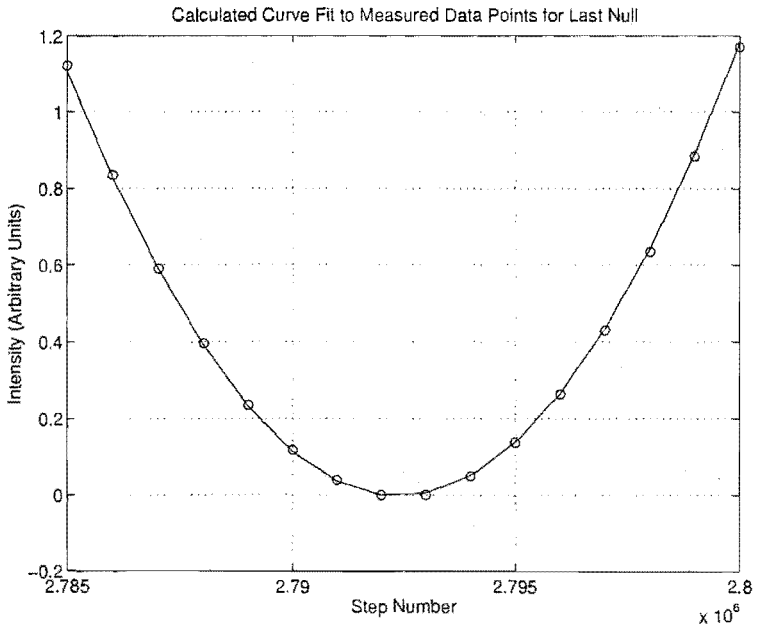

Figure 7.3: Curve optimised to fit the measured intensities at 1000 step intervals surrounding the last null, i.e. the null which occurs after 5.5 rotations of the disk. The expression $I = I_0[1 - \cos 2k(n - n_{null})] + I_{off}$ is the Malus law relation adapted to fit around the null, accomodate the scattered light getting into the detector and the uncompensated offset introduced by the finite step size of the A/D converter. For the curve shown above $k = 1.2477 \times 10^{-5}$ rad/step, $I_0 = 65.716$ (arbitrary units), $I_{off} = -3.0051 \times 10^{-3}$ (arbitrary units) and $n_{null} = 2792400 \pm 100$.

the same angular position as the first - a requirement of the boundary conditions for Fourier methods.

To calibrate the polarimeter and check how well it performed two experiments were devised. In the first a linearly polarised beam was prepared as above, that is, using the LHP111 Melles Griot laser and the Glan-Thompson polariser, where the orientation of the electric field of the incoming beam was inclined at $30°(\pm 0.2°)$ to the direction of the transmission axis of the polariser and the initial direction of the fast-axis of the quarter-wave-plate. Figure (7.4) shows the measured intensity as a function of the angle of the fast-axis (dotted line draw through the 463 data points by Matlab). The smooth curve is that obtained by calculating the intensity using the Stokes parameters obtained from the data using the Fourier intensity method and optimising the ellipticity to the order of 10^{-6} by adjusting the anisotropic attenuation factor for the quarter-wave-plate; it was expected that the ellipticity for a good Glan-Thompson polarising prism should be of this order.

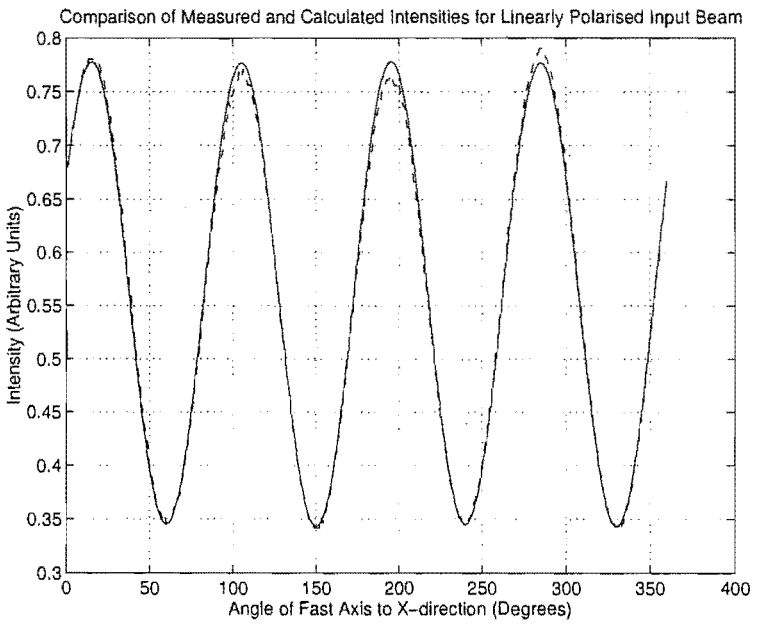

Figure 7.4: The beam intensity on the detector as a function of the angle of the fast-axis of the quarter-wave-plate for the Fourier intensity measurement method used on a linearly polarised beam whose electric field vector is inclined at 30° to the transmission axis of the analyser. The dotted curve is that drawn through measured data values by Matlab. The smooth curve is the intensity calculated from the Stokes parameters obtained from the measured data where the ellipticity was hand optimised to the order of 10^{-6} by adjusting the angle γ associated with the anisotropic attenuation of the quarter-wave-plate.

A Fast Fourier transform of the measured intensity was obtained using Matlab and the results are plotted as a bar-chart in Figure(7.5).

In Chapter (6) we calculated the ellipticity and orientation of the polarisation ellipse using the respective expressions

$$\sin 2\chi = S_3/S_0, \tag{7.1}$$

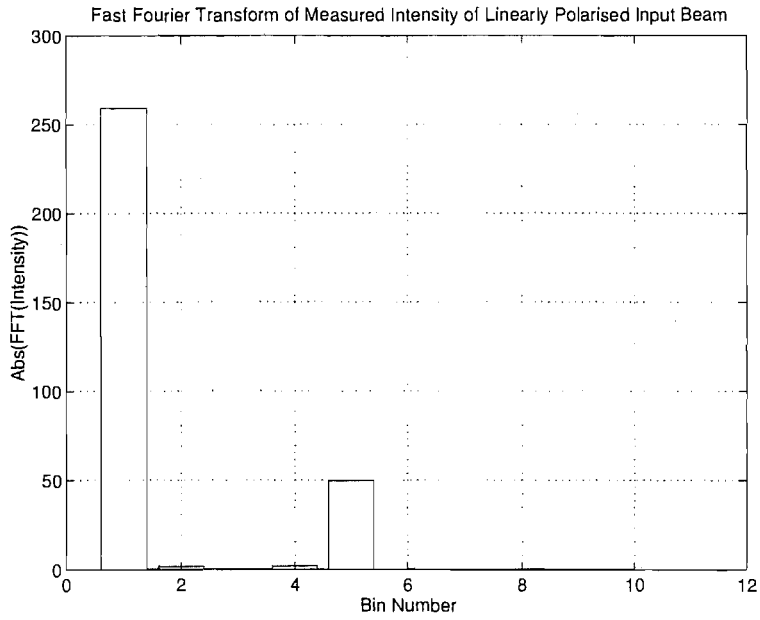

Figure 7.5: Fast Fourier Transform of the measured intensities of the linearly polarised beam whose electric field vector is inclined at 30° to the transmission axis of the analyser in the Fourier intensity measurement apparatus.

$$\tan 2\psi = S_2/S_1. \tag{7.2}$$

For these calculations we assumed that the source of light being measured had no unpolarised component. For a partially polarised beam of light the unpolarised component $S^{(u)}$ can be calculated from[22, p 51]

$$S^{(u)} = S_0 - S^{(p)}, \tag{7.3}$$

where the completely polarised component is given by

$$S^{(p)} = \sqrt{S_1{}^2 + S_2{}^2 + S_3{}^2}. \tag{7.4}$$

Hence for a beam with an unpolarised component the expression used to calculate the ellipticity becomes

$$\sin 2\chi = S_3/S^{(p)} \tag{7.5}$$

The values obtained for the Stokes parameters of the linearly polarised beam measured using the Fourier method above were calculated to be $S_0 = 0.907, S_1 = 0.428, S_2 = 0.753, S_3 = 5.53 \times 10^{-6}$. Hence the completely polarised component of the beam was calculated to be $S^{(p)} = 0.866$ with the unpolarised component being $S^{(u)} = 4.09 \times 10^{-2}$, representing 4.5% of the intensity of the incident beam on the detector. Uncompensated offset in the A/D converter would at most contribute 0.4% of the 4.5%. Hence it was assumed that at least 4.1% was attributed to an unpolarised component in the beam and to the movement of the beam falling on the

detector causing modulation of the output due to the nonuniformity of the response across the detector.

Because of the selective nature of the Fourier method, the scattered light and modulation of the output due to beam movement was not expected to affect the values of the Stokes parameters S_1. S_2 and S_3. Hence the ellipticity was calculated to be $3.19 \times 10^{-6}(\pm 10^{-8})$ and the orientation of the polarisation ellipse was $30.19°(\pm 0.02°)$, being within the uncertainty with which the orientation of the electric field of the input beam was set.

It was observed at the time of measurement that scattered light from the optical components in front of the detector produced a patch of light on the detector. A disk with a $\sim$ 2 mm diameter aperture was placed in front of the detector to limit the amount of scattered light falling on it. Another contributing factor to the performance of the polarimeter was the angular movement of the beam exiting the quarter-wave-plate in the rotating disk. This angular change in the direction of the beam translated to beam movement on the detector whose nonuniform response over the surface resulted in unwanted modulation in the output of the detector. The two lenses shown in Figure (7.1) largely removed this problem. The focal lengths of lenses 1 and 2 were, respectively, 75 mm and 250 mm. It was found that if lens 1 was placed as close to the quarter-wave-plate as possible and lens 2 placed at such a distance as to obtain a focus on the detector the effects of movement on the detector were controlled to the point where they could not be visually detected when the disk and quarter-wave-plate were quickly rotated by hand.

To check the performance of the polarimeter further a nominally circular beam was prepared by placing in the beam exiting an LHP111 Melles Griot laboratory laser, first, a Glan-Thompson polarising prism then a Soleil-Babinet Compensator (Melles Griot Product Number 04 SBC 001[57]), adjusted for a phase shift of $\pi/2$ and whose fast-axis was oriented at 135° to the transmission axis of a Glan-Thompson polariser. Figure (7.6) shows the intensity of light falling on the detector as a function of the orientation of the fast-axis of the quarter-wave-plate for both the measured data and the calculated values from the Stokes parameters obtained from the data.

The values for the Stokes parameters were calculated to be $S_0 = 0.803, S_1 = -3.45 \times 10^{-2}, S_2 = 3.86 \times 10^{-3}, S_3 = 0.787$. By using equations (7.4), (7.5) and (7.2) the ellipticity was calculated to be $0.96(\pm 0.4)$ and the orientation $176.81°(\pm 0.02°)$. The Fast Fourier transform of the intensity was also prepared for the measured data using Matlab and the results are plotted as a bar-chart in Figure(7.7).

A measurement of the ratio of the intensities transmitted by the Soleil-Babinet, adjusted for a phase shift of $\pi/2$, for a constant input beam of linearly polarised light whose electric field was oriented, respectively, in the fast-axis and slow axis directions yielded a value of 0.997. This would make the anisotropy in attenuation angle $\gamma = 44.958°$ and so the ellipticity of the light transmitted by the Soleil-Babinet

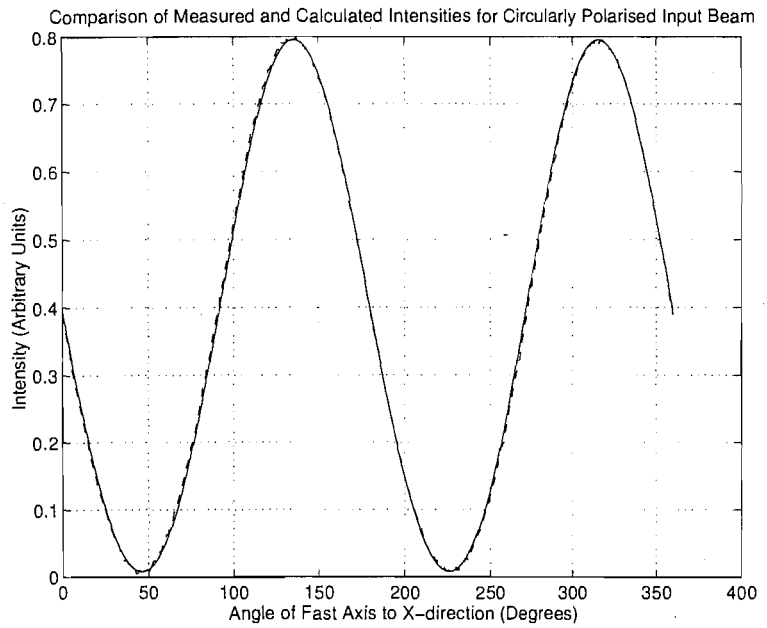

Figure 7.6: The beam intensity on the detector as a function of the angle of the fast-axis of the quarter-wave-plate for the Fourier intensity measurement method used on a nominally circularly polarised beam prepared from a linearly polarised beam by placing a quarter-wave-plate (an appropriately adjusted Soliel Babinet compensator) whose fast-axis was oriented at 135° to the transmission axis of the analyser. The dotted curve is that drawn through measured data values by Matlab. The smooth curve is the intensity calculated from the Stokes parameters obtained from the measured data where the angle $\gamma = 44.3903°$, associated with the anisotropic attenuation of the quarter-wave-plate, is the same as that obtained by optimisation in the case of the linearly polarised beam.

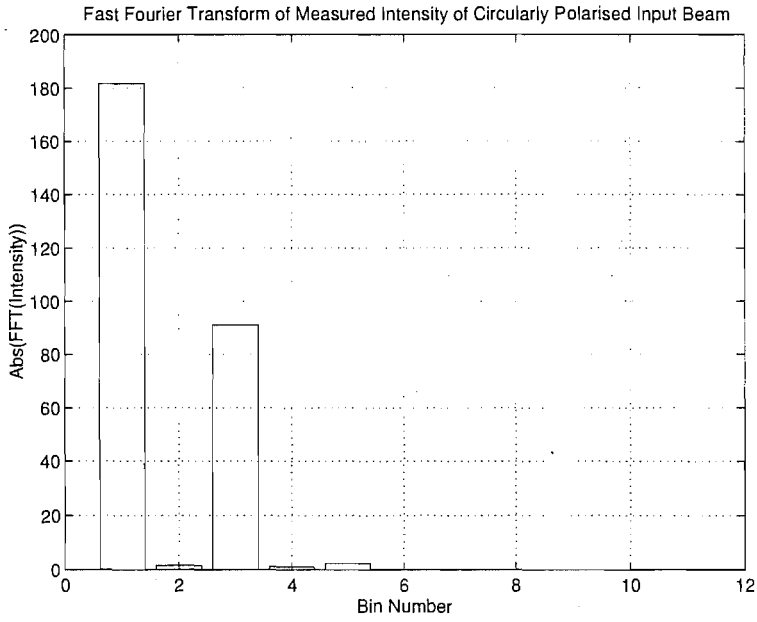

Figure 7.7: The Fast Fourier Transform of the measured intensity of the beam falling on the detector in a Fourier intensity measurement apparatus. The beam incident on the polarimeter is nominally circularly polarised and was created by placing in a linearly polarised beam, whose electric field vector is aligned with the analyser of the polarimeter, a Soliel Babinet compensator adjusted to produce a phase shift of $\pi/2$ and whose fast-axis is oriented at 135° to the transmission axis of the polarimeter.

compensator for the nominally circularly polarised beam in the second experiment above 0.9985. We see that this lies within the range of uncertainty of the experimental results. Hence at the present stage of development the polarimeter could find the ellipticity of the beam exiting the back of a mirror in a ring laser to an uncertainty of 4%.

Constraints have meant that the ring laser's polarisation dependence on aplanarity of the geometrical ray-path has not been measured.

References

[1] Miguel V Andres and Kenneth W H Foulds. Sensor applications of optical fibre resonant rings based on polarisation sensitive couplers. *SPIE*. 1011:235 – 239, 1988. Fibre Optic Sensors III.

[2] D A Andrews and King T A. Investigation of a multi-oscillator ring laser with magneto-optic bias. *J. Phys. D: Appl. Phys.*, 27:1815 – 1822. 1994.

[3] J A Arnaud. Nonorthogonal optical waveguides and resonators. *Bell Syst. Tech J.*, 49(9):2311 – 2348, 1970.

[4] J A Arnaud. Hamiltonian theory of beam mode propagation. In *Progress in Optics*, volume 11, pages 247 – 304. North-Holland Publishing Co., Amsterdam, The Netherlands, 1973.

[5] J A Arnaud. *Beam and Fiber Optics.* Academic Press, New York, 1976.

[6] J A Arnaud and H Kogelnik. Gaussian light beams with general astigmatism. *Appl. Opt.*, 8(8):1687 – 1693, 1969.

[7] Frederick Aronowitz. *Theory and operation of a travelling-wave laser.* Honeywell Systems and Research Division, 1969.

[8] H Baher. *Analog & Digital Signal Processing.* chapter 9. John Wiley & Sons, Chichester. New York, Brisbane, Toronto, Singapore, Reprinted 1991.

[9] R Becker. *Theory of Heat.* Springer-Verlag, Berlin, 2nd edition. 1967.

[10] Ernest E Bergmann. Optical resonators with paraxial modes. *Appl. Opt.*, 11(1):113 – 119, 1972.

[11] D A Berkowitz. Design of plane-mirror systems. *J. Opt. Soc. Am.*, 55:1464 – 1467, 1965.

[12] J. A. Betts. *Signal Processing, Modulation and Noise*, page 36. Hodder and Stoughton, London, (Reprinted with revisions) 1978.

[13] H. R. Bilger and G. E. Stedman. Stability of planar ring lasers with mirror misalignment. *Appl. Opt.*, 26:3710, 1987.

[14] H R Bilger, G E Stedman, and P V Wells. Geometrical dependence of polarisation in near-planar ring lasers. *Opt. Commun.*, 80(2):133 – 137, 1990.

[15] H R Bilger and W K Stowell. Light drag in a ring laser: An improved determination of the drag coefficient. *Phys. Rev. A*, 16(1):313 – 319, 1977.

[16] H R Bilger, P V Wells, and G E Stedman. Origins of fundamental limits for reflection losses at multilayer dielectric mirrors. *Appl. Opt.*, 33(31):7390 – 7396, 1994.

[17] Mary L Boas. *Mathematical Methods in the Physical Sciences*, chapter 6. John Wiley & Sons, Inc., New York, London, 1966.

[18] Max Born and Emil Wolf. *Principles of Optics: Electromagnetic Theory of Propagation, Interference and Diffraction of Light.* Pergamon Press, Oxford, 6th Corrected edition, Reprinted 1989.

[19] G. R. Boyer, B. F. Lamouroux, and B. S. Prade. Automatic measurement of the stokes vector of light. *Appl. Opt.*, 18(8):1217 – 1219, 1979.

[20] W W Chow, J Gea-Banacloche, L M Pedrotti, Virgil E Sanders, W Schleich, and M O Scully. The ring laser gyro. *Rev. Mod. Phys.*, 57(1):61 – 104, 1985.

[21] Weng W Chow, Jarel B Hambenne, Thomas J Hutchings, Virgil E Sanders, Murray Sargent III, and Marlan O Scully. Multioscillator laser gyros. *IEEE J. Quantum Electron.*, QE-16(9):918 – 936, 1980.

[22] Edward Collett. *Polarized Light: Fundamentals and Applications.* Marcel Dekker, Inc., New York, Basel, Hong Kong, 1993.

[23] Robert W. Collins and Kim Yeon-Taik. Ellipsometry for thin-film and surface analysis. *Anal. Chem.*, 62(17):887A – 900A, 1990.

[24] L Cooper and G E Stedman. Axion detection by ring lasers. *Phys. Lett. B*, 357:464 – 468, 1995.

[25] D C Cronemeyer. Electrical and optical properties of rutile single crystals. *Phys. Rev.*, 87(5):876 – 886, 1952.

[26] H De Lang. Derivation of the relationship between two weakly coupled nonlinear optical oscillators. *Appl. Phys. Lett.*, 9:205 – 207, 1966.

[27] H Demiryont, D B Kerwin, and J R Sites. Optical properties of ion-beam sputtered TiO_2 films. *Natl. Bur. Stand. Spec. Publ.*, 688:311 – 316, 1983.

[28] J R DeVore. Refractive indices of rutile and sphalerite. *J. Opt. Soc. Am.*, 41(6):416 – 419, 1951.

[29] M R Dickinson and King T A. Polarization frequency splitting in non-planar ring laser resonators. *J. mod. Opt.*, 34(8):1045 – 1055, 1987.

[30] T A Dorschner and I W Smith. Clear path four frequency resonators for ring laser gyros. *J. Opt. Soc. Amer.*, 68:1381, 1978.

[31] Terry A. Dorschner. Nonplanar rings for laser gyroscopes. *SPIE*, 412:192 – 202, 1983.

[32] J M Elson, J P Rahn, and J M Bennett. Relationship of the total integrated scattering from multilayer-coated optics to angle of incidence, polarization, correlation length, and roughness cross-correlation properties. *Appl. Opt.*, 22(20):3207 – 3219, 1983.

[33] T F Ewanizky. Ray transfer matrix approach to unstable resonator analysis. *Appl. Opt.*, 18:724, 1979.

[34] Mohammed Shuaib Ghausi. *Principles and Design of Linear Active Circuits.* McGraw-Hill Book Company, New York, 1965.

[35] G Herziger, W Holzapfel, and W Seelig. Verstärkung einer he-ne-gasentladung für die laserwellenlänge λ=6328 ae. *Z Phys.*, 189:385–400, 1966.

[36] Yoh Imai, Hideaki Koseki, and Yoshihiro Ohtsuka. Heterodyne fiber-optic gyroscope using orthogonally polarized two-frequency beams. *Appl. Opt.*, 25(15):2962 – 2965, 1987.

[37] E. F. Ishchenko and E. F. Reshetin. Sensitivity to misalignment of an optical resonator with a focusing element. *Opt. Spektrosk.*, 46(2):202 – 207, 1979.

[38] T Izawa and S Sudo. *Optical Fibres: Materials and Fabrication.* D Reidel Publishing Company, Dordrecht, The Netherlands, 1987.

[39] S. N. Jasperson and S. E. Schnatterly. An improved method for high reflectivity ellipsometry based on a new polarisation modulation technique. *Rev. Sci. Instrum.*, 40(6):761 – 767, 1969.

[40] W K Kahn and J T Nemit. Ray theory of astigmatic resonators and beam waveguides. In J Fox, editor, *Proc. Symp. Modern Optics*, pages 501 – 526. Polytechnic, New York, 1967.

[41] A Kalb. Neutral ion beam sputter deposition of high-quality optical films. *Optics News*, pages 13–17, 1986.

[42] G W C Kaye and T H Laby. *Tables of physical and chemical constants and some mathematical functions.* Longman, London, New York, 15th edition, 1986.

[43] C. V. Kent and James Lawson. A photoelectric method for the determination of the parameters of elliptically polarized light. *J. Opt. Soc. Am.*, 27:117–119, 1937.

[44] H Kogelnik and T Li. Laser beams and resonators. *Proc. IEEE*, 54:1312, 1966.

[45] H C Lefevre. Single-mode fibre fractional wave devices and polarisation controllers. *Electronics Lett.*, 16(20):778 – 780, 1980.

[46] John Lekner. *Theory of Reflection*, chapter 11. Martinus Nijhoff, Dordrecht, The Netherlands, 1987.

[47] David R Lide, editor. *CRC Handbook of Chemistry and Physics*, chapter 12, page 28. CRC Press, Boca Raton, Ann Arbor, Boston, 71st edition, 1990.

[48] R K Luneberg. *Mathematical Theory of Optics*, pages 240 – 243. University of California Press, Berkley, 1964. Sec. 36.

[49] M Macek and D T M Davis. Rotation rate sensing with travelling wave ring lasers. *Appl. Phys. Lett.*, 2:67 – 68, 1963.

[50] H A MacLeod. *Thin-Film Optical Filters*, chapter 2. Macmillan Publishing Company, New York, 2nd edition, 1986.

[51] H A MacLeod. New techniques revolutionize thin-film optical coatings. *Laser Focus World*, 28(11):111 – 119, 1992.

[52] Graham J. Martin. Non-planar gyros and magnetic biases. *SPIE*, 487:94 – 100, 1984.

[53] Arthur Mayer. Rotations and their algebra. *SIAM Rev.*, 3(2):77–122, 1960.

[54] Melles Griot, 1770 Kettering St., Irvine, CA92714, USA. *Optics Guide 5*, 1990. Page 13–3.

[55] Melles Griot, 1770 Kettering St., Irvine, CA92714, USA. *Optics Guide 5*, 1990. Page 4–24.

[56] Melles-Griot, 1770 Kettering St., Irvine, CA92714, USA. *Optics Guide 5*, 1990. Page 14–12.

[57] Melles Griot, 1770 Kettering St., Irvine, CA92714, USA. *Optics Guide 5*, 1990. Pages 14–33 - 14–34.

[58] Klaus D Mielenz and Karl F Nefflen. Gas mixtures and pressures for optimum output power of rf-excited helium-neon lasers at 632.8 nm. *Appl. Opt.*, 4(5):565–567, 1965.

[59] N D Milovsky and A M Tkachyov. Polarization instability of ring lasers. *Opt. Commun.*, 95:127 – 140, 1993.

[60] N F Mott and E A Davis. *Electronic Processes in Non-Crystalline Materials.* Clarendon Press, Oxford, 1971.

[61] Newport Corporation, 1791 Deere Avenue, Irvine, CA 92714, USA. *The 1994 Newport Catalogue*, 1994.

[62] Alan C Nilsson, Eric K Gustafson, and Robert L Byer. Eigenpolarization theory of monolithic nonplanar ring oscillators. *IEEE J. Quantum Electron.*, QE-25:767 – 790, 1989.

[63] R Olshansky. Propagation in glass optical waveguides. *Rev. Mod. Phys.*, 51(2):341 – 367, 1979.

[64] G Oster. The scattering of light and its application to chemistry. *Chem. Rev.*, 43:2319 – 2365, 1948.

[65] M M Popov. Resonators for lasers with rotated directions of principal curvatures. *Opt. Spectrosc.*, 25(2):314 – 316, 1968.

[66] M M Popov. Resonators for lasers with unfolded directions of principal curvatures. *Opt. Spectrosc.*, 25(3):394 – 400, 1968.

[67] E J Post. Interferometric path-length changes due to motion. *J. Opt. Soc. Am.*, 62(2):234 – 239, 1972.

[68] William H Press, Saul A Teukolsky, William T Vetterling, and Brian P Flannery. *Numerical Recipes in C: The Art of Scientific Computing.* Cambridge University Press, 2nd edition, 1992.

[69] H J Ross, B S Sherbourne, and G E Stedman. Selection rules for optical activity and linear birefringence bilinear in electric and magnetic fields. *J. Phys. B*, 22:459 – 473, 1989.

[70] A Roth. *Vacuum Technology*, page 190. Elsevier Science Publishers B. V., Amsterdam, 2nd revised edition, 1982.

[71] Hendrik Rothe, Angela Duparré, and Stefan Jacobs. Generic detrending of surface profiles. *Opt. Eng.*, 33(9):3023 – 3030, 1994.

[72] R Rujkorakarn, L S Hsu, and C Y She. Crystallisation of titania films by thermal heating. *Natl. Bur. Stand. Spec. Publ.*, 727:253 – 261, 1984.

[73] G Sagnac. L'éther lumineux démontré par l'effet du vent relatif d'éther dans un interféromtètre en rotation uniforme (The luminiferous ether demonstrated by the effect of the relative motion of the ether in an interferometer in uniform rotation). *Comptes Rendus de l'Académie des Sciences, Paris*, 157:708 –710, 1913.

[74] G A Sanders and S Ezekiel. Measurement of fresnel drag in moving media using a ring-resonator technique. *J. Opt. Soc. Am. B*, 5(3):674 – 678, 1988.

[75] Virgil E Sanders. Polarization characteristics of an anisotropic ring laser. *Opt. Commun.*, 29(2):227 – 229, 1979.

[76] Virgil E Sanders and Robert M Kiehn. Dual-polarized ring lasers. *IEEE J. Quantum Electron.*, QE-13(9):739 – 744, 1977.

[77] Schott Garsco Pty. Ltd., P O Box 174, Terrey Hills, New South Wales, Australia. *ZERODUR: glass ceramics*, 1982.

[78] Shinan-Chur Sheng. Optical-axis perturbation singularity in an out-of-plane ring resonator. *Opt. Lett.*, 19(10):683 – 685, 1994.

[79] Anthony E Siegman. *Lasers*, chapter 17. University Science Books, 1986.

[80] J R Sites, J S Postek, R S Robinson, T D Schemmel, and C Y She. Admixture of SiO_2 to suppress TiO_2 crystallization. *Natl. Bur. Stand. (U.S.) Spec. Publ.*, 752:332 – 335, 1986.

[81] H Statz, T A Dorschner, M Holtz, and I W Smith. *Laser Handbook*, volume 4, chapter 3. Elsevier, Amsterdam, 1985.

[82] G E Stedman. Polarisation dependence of natural and field-induced one-photon and multi-photon interactions. *Adv. Phys.*, 34(4):513 – 587, 1985.

[83] G E Stedman. Ring interferometric tests of classical and quantum gravity. *Contemp. Phys.*. 26(4):311 – 332, 1985.

[84] G E Stedman. On chiral or gyrotropic optical effects. *Phys. Lett. A*, 152(1,2):19 – 20. 1991.

[85] G E Stedman. Canterbury ring laser and tests for nonreciprocal phenomena. *Aust. J. Phys.*, 46:87 – 101, 1993.

[86] G E Stedman and H R Bilger. Ring laser, an ultrahigh resolution detector of optical nonreciprocities. *Digital Signal Proc.*, 2:105 – 109, 1992.

[87] A F Stewart and D J Gallant. Ultraviolet thin film coating characterization. *Natl. Bur. Stand. (U.S.) Spec. Publ.*, 727:272 – 284, 1984.

[88] George Gabriel Stokes. On the composition and resolution of streams of polarised light from different sources. *Trans. Camb. Phil. Soc.*,, 9:399, 1852. Reprinted in *Mathematical and Physical Papers*, Vol. 3, Cambridge University Press, London, 1901, p. 233.

[89] W K Stowell, F D Orazio, and R M Silva. Instrumentation of a variable angle scatterometer. *Natl. Bur. Stand. Spec. Publ.*. 638:205 - 222. 1981.

[90] David T Wei. Ion beam interference coating for ultralow optical loss. *Appl. Opt.*, 28(14):2813 – 2816, 1989.

[91] J R Wilkinson. Ring lasers. *Prog. Quant. Electr.*, 11:1 – 103, 1987.

[92] C Yelland, J Hong, M J Padgett, M H Dunn, and W Sibbett. A vector approach to the geometrical dependence of polarisation rotation in a non-planar cw Nd:YAG ring laser. *Opt. Commun.*, 109:451 – 456, 1994.

[93] H Zeeman. (drag in quartz). *Proc. R. Acad. Sci. (Amsterdam)*, 22:462, 512, 1920.

Appendix A

Polarisation

H R Bilger, G E Stedman, and P V Wells. Geometrical dependence of polarisation in near-planar ring lasers. *Opt. Commun.*, 80(2):133 - 137, 1990

Geometrical dependence of polarisation in near-planar ring lasers

H.R. Bilger
School of Electrical and Computer Engineering, Oklahoma State University, Stillwater, OK 74078-0321, USA

G.E. Stedman and P.V. Wells
Department of Physics, University of Canterbury, Christchurch 1, New-Zealand

Received 9 July 1990

The angular width β_0 of the transition between the linearly polarised eigenmodes of a planar ring laser and the circularly polarised modes of the nonplanar case depends on the anisotropies δ and χ of the mirror reflectance in amplitude and phase. With supercavity mirrors and with a novel technique for a 20-fold reduction in χ, β_0 can be reduced to picoradians. An optical lever incorporating this could have three orders of magnitude greater sensitivity than those presently used in various fundamental experiments.

1. Introduction

The accuracy of various fundamental experiments is dependent on that of an optical lever, in which the angular rotation or tilt of a mirror is sensed. As examples, we mention tests of the principles of equivalence [1], of novel theories of gravity [2], and of relativistic effects in the electrodynamics of moving dielectrics [3–5]. Current tiltmeters are sensitive to motions of the order of nanoradians [6]. We propose an optical lever in which the output of a nearly planar ring laser is compensated and where, given split-field polarization analysis, a sensitivity of the order of picoradians is possible.

Other applications in metrologic and related work may be imagined readily: a pendulum could be coupled mechanically to one laser mirror, making a linear transducer, with the feedback signal indicating a potential amplitude excursion. With reduction of the bandwidth, an unprecedented sensitivity for seismometry, for example, would be obtained.

This striking improvement may be associated partly with the active character of the device, and partly with a novel technique for optimization of the supercavity mirror coatings which is suggested and demonstrated here. The active character is reminiscent of Aladdin's lamp which gave on external rubbing a commensurate response from the bottled genie. The high potential sensitivity is characteristic of an active ring laser, as opposed to a passive resonator: the system actively converges on the eigenmode polarization consistent with the imposed geometry. The frequency shifts of a ring laser give a more sensitive measure of nonreciprocal optical path lengths than do the fringe shifts of a ring interferometer [7]. (Nevertheless, a system comprising a passive cavity tuned to an external laser has a frequency resolution comparable to that of a ring cavity with equivalent cavity losses [8]. The passive counterpart to the active system discussed here is therefore not excluded, though it would have considerably greater complexity.)

In a strictly planar active ring laser with non-gyrotropic mirrors, the eigenmodes are linearly polarised in the s (sagittal) and p (parallel) directions as shown below (the result for gyrotropic mirrors is less simple [9]). By contrast, the eigenmodes of a significantly nonplanar resonator (with more than three mirrors) are circularly rather than linearly polarised, because in one round trip, the plane of polarisation of an injected beam will rotate by an angle ρ whose magnitude is determined by the details of the beam geometry [10], in particular the fold angle β defining the degree of nonplanarity (fig. 1). As-

0030-4018/90/$03.50

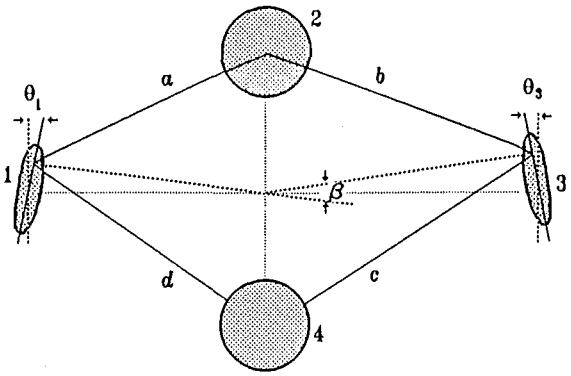

Fig. 1. The skew square ring used as our example. β is the dihedral angle defining the nonplanarity of the beam. It is determined by the angular misalignments θ_i of the mirrors, and in turn induces the polarization changes under discussion.

sociated interference properties have recently been discussed and verified experimentally in connection with the Berry phase [11]; incidentally, these authors describe the transition between planar and nonplanar interferometers as discontinuous, whereas our work demonstrates that the anisotropic reflection properties of actual mirrors will remove all such discontinuities.

We show that the eigenmode polarization of a resonator with real mirrors is very sensitive to small distortions from planarity. Such a device is a tiltmeter, or optical lever, since the nonplanarity depends solely on the angular misadjustments of the mirror with respect to tilt against the p plane [12]; in a skew square ring with sides l and with tilted flat mirrors 1, 3 and mirrors 2, 4 with finite radii of curvature, β is the sum $\theta_1+\theta_3$ of the angular misadjustments θ_i of the flat mirrors about the p axis (fig. 1).

The width and character of the polarization transition are determined by imperfections of the mirrors. Current multilayer dielectric coating techniques concentrate on minimizing amplitude losses. We show that linear reflective birefringence (differential s–p phase shift) limits the width of the transition for presently available supercavity mirrors, and that adjustment of the thickness of the topmost coating can reduce both birefringence and the transition width markedly. This method has been successfully demonstrated.

2. Mirror amplitude and phase imperfection

Let the amplitude reflectances for s and p polarization for each mirror be $r_s\exp(i\chi_s)$, $-r_p\exp(i\chi_p)$ respectively (the sign is included since the angle of incidence is less than the Brewster angle), and define the (real) imperfection parameters $\delta_s=1-r_s$, $\delta_p=1-r_p$ (in amplitude), χ_s, χ_p (in phase). We write power reflectance and transmission as $R_i=r_i^2$, $T_i=t_i^2$ for $i=s,p$; in the absence of loss, $(R_i+T_i=1)$. If s and p polarizations are treated differently only at the mirrors, the effects we discuss arise solely from the anisotropies δ $(\delta\equiv\delta_p-\delta_s)$ and χ $(\chi\equiv\chi_p-\chi_s)$ in these parameters. Reducing these anisotropies sharpens the transition, and improves the sensitivity of the device we propose.

Even for a lossless multilayer dielectric mirror, but with a finite number of layers and consequent nonzero transmission, δ is positive and typically 150 ppm or more. δ is constrained to be non-negative as a consequence of the form of the Fresnel reflection coefficients. Mirrors in our possession designed for 45° incidence consist of a $\lambda/4$ layer (at the HeNe wavelength, 633 nm) of TiO_2 on the Zerodur substrate, 11 pairs of TiO_2-SiO_2 $\lambda/4-\lambda/4$ layers, and a final $\lambda/2$ layer of SiO_2 for UV protection. These are measured to give $1-R_s=14.7\pm0.5$ ppm, $T_s=3.9\pm0.1$ ppm, $T_p=304\pm2$ ppm, and a scattering loss of 4 ± 3 ppm. Hence $\delta=150\pm1$ ppm, and $T_p/T_s=78\pm2$. With allowance for loss by extinction (estimated by difference as $\simeq7$ ppm) and by scattering as measured, these results are consistent with the theoretical predictions (see for example the analysis of McLeod [13], and taking the refractive index of TiO_2 as 2.33) of $1-R_s=4$ ppm, $T_p/T_s=89$; they also indicate that the imaginary parts of the material refractive indices quoted by Kalb [14] are overestimated for our mirrors by a factor ~6.

This anisotropy δ stabilizes the s direction of linear polarization relative to the p direction for a planar ring laser; the p component of any beam will be attenuated fractionally more than the s component on every round trip. The different round trip attenuation for s and p modes distinguishes the relevant quality factors ($Q=\omega_0E/P$ where E is the stored energy and P the power loss) so that a strictly planar ring will lase with linear (s) polarization. Competition between the rotational effect associated with

δ and the geometrical rotation ρ in the region $\beta<\delta$ leads to eigenmodes which are linearly polarized at a (β-dependent) angle ϕ to the s axis. Martin [15] briefly discussed this transition region in discussing the sensitivity of the ring laser gyro beat frequency to mechanical distortions and mirror imperfections. We ignore the effects of magnetic impurities and so the kinds of applications in which magnetic Kerr effects are deliberately incorporated [16].

The relatively ill-studied anisotropy χ in birefringence is always present, since coatings do not have their ideal thicknesses. It completely alters the above picture. In supermirror coating, reflectance is enhanced as desired by adding sufficient pairs of $\lambda/4$ layers. This does not guarantee a corresponding reduction in birefringence, since layer width need not be precisely controlled. A value $\chi\sim 0.1$ rad, corresponding to a 2% deviation from the ideal thickness of the top $\lambda/2$ layer, was measured on one such supercavity mirror. In this case $\chi\gg\delta$, and birefringence rather than reflection loss dictates the width ($\beta_0\sim\chi$) and nature of the polarization transition. The eigenmodes are now elliptical for all β not equal to zero, and become circular for $\beta\gg\chi$. We propose that the (β-dependent) s–p phase difference ϕ' in the output beam (differing from ϕ simply because of the anisotropy of transmission of the mirror) be monitored using a compensator followed by a split-field polarization analyser. For compensator, a $\lambda/4$ plate suffices in the limit $\delta/\chi\to 0$.

Our result gives mirror-coating specialists motivation to improve supermirror performance by lowering birefringence as well as transmission. We suggest that significant reduction of χ can be achieved by adjustment of the thickness of the topmost layer. In response to our suggestion, T. Louderback of Ojai Research (private communication) has etched a multilayer dielectric supercavity mirror to achieve a measured differential birefringence χ of 14 arc minutes (4×10^{-3} rad), with no detectable increase in scatter (the effect on δ, in increasing transmission, is minor). This is the level to which χ can be so reduced, since it corresponds to a change of thickness by one monolayer. The effects of birefringence so reduced are still an order of magnitude greater than those of reflectance loss ($\chi/\delta\sim 33$). It also follows that polarization switching, from linear to circular, could be achieved in a 4-mirror ring by a purely geometrical distortion which would be within the tolerance of mirror alignment for lasing. This obviates the use of quarter-wave plates and so the attendant degradation of cavity finesse for guaranteeing circular polarisation.

3. Derivation

As a simple example, we consider nonplanar effects in a skew square ring [10] whose mirrors are labelled 1, 2, 3, 4, and whose beams are labelled a (1–2), b(2–3), c (3–4), d (4–1). We associate the nonplanarity with bending of the optical circuit about the 2–4 axis; β is the fold or dihedral angle between the planes of ad and bc (fig. 1). The angle of apparent polarization rotation in each beam is then $\theta=\pm\beta/\sqrt{2}$, the signs alternating between adjacent beams. The polarization matrix for a single mirror and beam takes the form [10,11,17]

$$\begin{pmatrix} r_s\exp(\mathrm{i}\chi_s) & 0 \\ 0 & -r_p\exp(\mathrm{i}\chi_p)\end{pmatrix}\begin{pmatrix}\cos\theta & \sin\theta \\ -\sin\theta & \cos\theta\end{pmatrix}.$$

Iterating this four times, and considering only first order effects from δ_s, δ_p, χ_s, χ_p, β, we find a polarisation matrix for the ring of the form

$$\begin{pmatrix} 1-4\delta_s+4\mathrm{i}\chi_s & -2\sqrt{2}\,\beta \\ 2\sqrt{2}\,\beta & 1-4\delta_p+4\mathrm{i}\chi_p\end{pmatrix}.$$

The polarization eigenvector (e_1^s, e_1^p) then has the component ratio $e_1^p/e_1^s\equiv A$, where $A=(\gamma\pm\sqrt{\gamma^2-\beta^2})/\beta$; the amplitude $\beta_0\equiv\sqrt{(\delta^2+\chi^2)/2}$ of the complex number $\gamma\equiv(\delta-\mathrm{i}\chi)/\sqrt{2}$ is the scale parameter for the width of the transition. We take the solutions corresponding to s polarization at $\beta=0$ (fig. 2).

Solution for negligible birefringence ($\delta\gg\beta$, fig. 2(a); compare with fig. 8 of ref. [9]). When the angle β is less than the critical value $\beta_0=\delta/\sqrt{2}$, the eigenmode is linearly polarized at an angle $\phi=\tan^{-1}A=\frac{1}{2}\sin^{-1}\beta/\beta_0$. At the critical angle $\beta=\beta_0$, $\phi=\pi/4$. For $\beta>\beta_0$, the mode becomes elliptically polarized with axes at $\pm\pi/4$ and with a relative phase $\kappa\equiv\cos^{-1}(\beta_0/\beta)$ between its components, so having an eccentricity of $\sqrt{2\beta_0/(\beta+\beta_0)}$. The angle ϕ is a sensitive indicator of the nonplanarity of the beam.

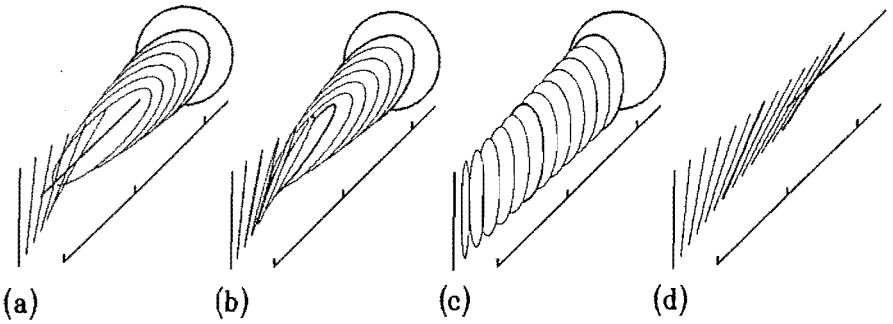

Fig. 2. Polarization mode status as a function of the relative nonplanarity β/β_0 where the ratio δ/χ of differential reflectance to differential birefringence has the values ∞, 10, 0.1 for (a), (b), (c), respectively. In (d), $\delta/\chi=0.1$ as for (c), but the ellipticity has been compensated by an s–p phase shift (approximately $\pi/2$). In each case β/β_0 ranges from 0 to 2 in 12 steps, and the limiting case ($\beta=\infty$) of circular polarization is included.

Since polarization analysis occurs outside the ring on transmitted light, the corresponding (small) angle ϕ' after transmission through the mirrors is related to ϕ by the ratio of p to s mirror transmission coefficients ($t_p/t_s \simeq 8.8$ for our mirrors).

Solution when birefringence dominates ($\chi \gg \delta$, fig. 2(c)). The scale parameter β_0 equals $\chi/\sqrt{2}$. $A=-i\tan(\psi/2)$, where $\psi \equiv \tan^{-1}\beta/\beta_0$. The linear mode of the strictly planar case becomes elliptical with s and p as major axes, fattening into the circular case when $\beta \gg \beta_0$. For $\beta=\beta_0$, the ratio of axes for the ellipse is $\sqrt{2}-1$. The ellipticity of the emergent light may be compensated by a $\lambda/4$ plate (fig. 2(d)). For small β, when $\phi=\beta/2\beta_0$, $\phi' \simeq 1500\beta$. The dependence of ϕ' on β is given in fig. 3 for various values of δ/χ.

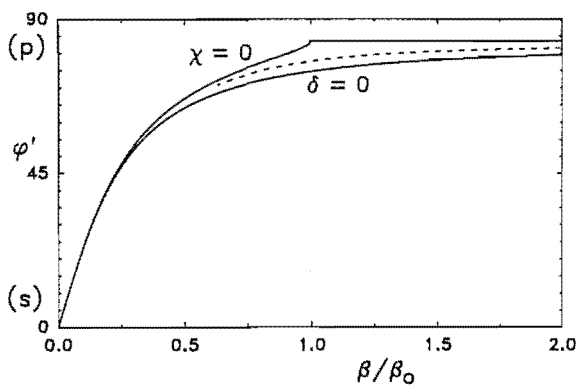

Fig. 3. Dependence on the relative nonplanarity β/β_0 of the angle ϕ' of the direction of linear polarization in the compensated ring output beam, for a transmittance ratio $t_p/t_s=8.8$ and for three choices of the ratio of differential birefringence and reflectance: $\chi=0$, $\delta/\chi=0.1$ (dashed line), $\delta=0$.

4. Limits to precision

The precision $\Delta\beta$ to which the fold angle may be measured now may be obtained from the precision $\xi=\Delta\phi'$ with which the angle ϕ' can be determined. Using a split-field analyzer whose halves have a relative rotation 2α, a misadjustment under joint rotation of ξ in the angular orientation of this analyzer will give a power difference $\sim\Delta P=\xi P\sin 2\alpha$ between detectors; $P\equiv T_p P_c/2$ and is the power through any port, while P_c is the total power circulating in the ring (we take $P_c\sim 1.0$ W). (More exactly, the factor T_p should be an average of T_p and T_s with a ϕ-dependent weighting).

We require that this difference be greater than optical quantum (shot) noise in each beam, and also greater than the noise equivalent power $N_d\sim 10^{-16}$ W of the detectors within the bandwidth (say 1 Hz) of a synchronous detection scheme. We show now that the first (quantum noise) condition is the limiting factor on the above estimates. Hence, a practical choice for α will be nearer 0° than 45° (the optimal figures for these respective limitations).

Over a time T ($T\simeq 10^2$ s) we count $N\sim PT(\sin^2\alpha)/2\hbar\omega$ photons in each detector, hence getting a noise equivalent power from the photon fluctuations of $\hbar\omega\sqrt{N_\gamma}/T$, and so a limiting preci-

sion ξ of angular polarization resolution due to optical quantum noise of $\sqrt{\hbar\omega/(8PT)} \sim 4\times10^{-9}$ rad. (The corresponding formula for detector-limited resolution is $\xi \simeq N_d/(P\sin\alpha) \sim 10^{-11}$ rad.) This translates into a sensitivity $\Delta\beta \sim \xi/1500 \sim 3$ picoradians, i.e. 0.15 nanodegrees or 0.6 microarcsecond.

The finite beam width (say 600 μm) in a laser is unlikely to affect the sensitivity of this device, just as the scale factor of laser gyros is defined by a mean point in the mode transverse power density [18] and is stable under different excitation conditions to within a few parts per million [10].

Acknowledgement

We acknowledge many useful comments about supermirror technology from Tony Louderback. One of us (HRB) acknowledges partial support from NSF grant INT-8900033 (United States/New Zealand Cooperative Effort in Ringlaser Construction) and from a Prince and Princess of Wales Award of the Royal Society of New Zealand.

References

[1] P.G. Roll, R. Krotkov and R.H. Dicke, Ann. Phys. (N.Y.) 26 (1964) 442.
[2] Wei-Tou Ni, Proc. 4th Marcel Grossmann Meeting on General Relativity, Rome, Italy, 1985 (North-Holland, Amsterdam, 1986) p. 1335.
[3] D.G. Lahoz and G.M. Graham, Can. J. Phys. 57 (1979) 667.
[4] R.V. Jones, Proc. Roy Soc. Lond. A 349 (1976) 423.
[5] M.P. Silverman, Europhys. Lett. 9 (1989) 95.
[6] A.C. Pinder and A.R. Palmer, J. Phys. E 5 (1982) 478; Report SRL-TR-76-0014, July 1976, Seiler Laboratory (U.S. Air Force Academy, Colorado Springs, CO.).
[7] G.E. Stedman, Contemp. Phys. 26 (1985) 311.
[8] J. Gea-Banacloche, Phys. Rev. A 35 (1987) 2518.
[9] M.P. Silverman, J. Opt. Soc. Am. A 3 (1986) 830.
[10] H. Statz, T.A. Dorschner, M. Holtz and I.W. Smith, Laser Handbook, Vol. 4, eds. M.L. Stitch and M. Bass (Elsevier, Amsterdam, 1985) ch. 3.
[11] H. Jiao, S.R. Wilkinson, R.Y. Chiao and H. Nathel, Phys. Rev. A 39 (1989) 3475.
[12] H.R. Bilger and G.E. Stedman, Appl. Optics 26 (1987) 3710.
[13] H.A. Macleod, Thin-film optical filters, 2nd Ed. (Macmillan, New York, 1986) ch. 2.
[14] A. Kalb, Optics News (August 1986) pp. 13–17.
[15] G.J. Martin, Proc. SPIE 487 (1987) 94.
[16] J.J. Krebs, W.G. Maisch, G.A. Prinz and D.W. Forester, IEEE Trans. Magn. MAG-16 (1984) 1179.
[17] W.W. Chow, J. Gea-Banacloche, L.M. Pedrotti, V.E. Sanders, W. Schleich and M.O. Scully, Rev. Mod. Phys. 57 (1985) 61.
[18] B. Prade and J.-Y. Vinet, Nuovo Cim. B 101 (1988) 323.

Appendix B

Nonreciprocal Phenomena

G E Stedman, H R Bilger, Li Ziyuan, M P Poulton, C H Rowe, I Vetharaniam, and P V Wells. Canterbury Ring Laser and Tests for Nonreciprocal Phenomena. *Aust. J. Phys.*, 46:87 - 101, 1993

Aust. J. Phys., 1993, **46**, 87–101

Canterbury Ring Laser and Tests for Nonreciprocal Phenomena*

G. E. Stedman, H. R. Bilger,[A] *Li Ziyuan, M. P. Poulton, C. H. Rowe, I. Vetharaniam and P. V. Wells*

Department of Physics, University of Canterbury, Christchurch 1, New Zealand.
[A] School of Electrical and Computer Engineering, Oklahoma State University, Stillwater, OK 74078–0321, U.S.A.

Abstract

An historic and simple experiment has been revitalised through the availability of supercavity mirrors and also through a heightened interest in interferometry as a test of physical theory. We describe our helium–neon ring laser, and present results demonstrating a fractional frequency resolution of $2{\cdot}1\times10^{-18}$ (1·0 mHz in 474 THz). The rotation of the earth unlocks the counterrotating beams. A new field of spectroscopy becomes possible, with possible applications to geophysical measurements such as seismic events and earth tides, improved measurements of Fresnel drag, detection of ultraweak nonlinear optical properties of matter, and also searches for preferred frame effects in gravitation and for pseudoscalar particles.

1. Introduction

A few years after the advent of the laser, Macek and Davis (1963) demonstrated the first ring laser, and also its unique potential as a rotation detector via the Sagnac effect. The optical lengths of the closed paths for the counterpropagating beams are made unequal by rotation of the whole device. In an active device the frequencies adapt to this, the corotating beam becoming more red and the counterrotating beam more blue (Heer 1964). Both beams take essentially the same path within the cavity, so that when the beams transmitted at any mirror interfere, the resulting beat frequency δf reflects only the difference in optical path length, and not any common-mode effects such as frequency jitter. The beat frequency depends on the angular frequency Ω of rotation with respect to the local inertial frame, the area $\mathbf{A}$ and perimeter P of the ring, and the optical wavelength λ (Post 1967; Anandan 1981; Chow *et al.* 1985; Stedman 1985*a*):

$$\delta f = \frac{4\mathbf{A}\,.\,\Omega}{\lambda P}. \tag{1}$$

Any nonreciprocal effect, i.e. one which distinguishes the optical path lengths of the counterpropagating beams, will give rise to a frequency shift, making the ring laser more versatile than merely a rotation sensor.

Macek and Davis (1963) (see also Macek *et al.* 1963, 1964) used a 1 m^2 square helium–neon ring laser at 1·15 μm to measure beat frequencies down to 5 kHz;

* Paper presented at the Tenth AIP Congress, University of Melbourne, February 1992.

0004-9506/93/010087$05.00

backscattering from the 16 beam interfaces (the Brewster windows on the four gain tubes) and the corner mirrors caused the two counterpropagating modes to lock at 2 kHz (for discussions of locking, see Aronowitz 1971, Statz *et al.* 1985). If we assume a Rayleigh or $1/\lambda^4$ variation of backscattering with wavelength, the equivalent locking threshold at 633 nm is 22 kHz.

In effect, we have repeated the Macek *et al.* experiment, and on a ring of similar shape and size. The key experimental differences are the use of supercavity mirrors, whose reflectances approach 99·999% — an ultimate, since it demands surface preparation which is smooth over atomic dimensions — and the complete absence of interfaces. This reduces the locking threshold to the point where the beat frequency induced by earth rotation (at 68 Hz) unlocks the ring without the need for any other biassing or dithering systems.

The development of supercavity mirrors has been vigorously driven by the potential for their application as ring gyros, now used for aviation inertial guidance systems in aircraft (e.g. the Airbus 320), and in various missiles (e.g. the Patriot system). An optical gyro with an area of the order of square decimetres has a sensitivity to rotation rates of order $10^{-4}\Omega_E$, where Ω_E is the earth rotation rate. Recently supercavity mirrors have been incorporated in such commercial items as the Newport SR-130 spectrum analyser. The scientific applications of the resolution enhancement inherent in these mirrors have not been fully explored.

2. Theoretical Aspects

(2a) Introduction

At the time of the Macek *et al.* experiment, only the application as a rotation sensor was demonstrated. This itself takes on a new interest with the increase in precision achieved over the intervening years. Some theoretical revitalisation is illustrated by the papers of Forder (1985), Scorgie (1990, 1991), Dieks and Nienhuis (1990) and Hendriks and Nienhuis (1990).

Less obvious physical effects could also generate a nonreciprocal effect in a ring laser (Macek *et al.* 1964; Bilger and Stowell 1977). There has been a renaissance of interest in interferometric tests of fundamental physical theory; the SQUID in the 1960s, the neutron interferometer in the 1970s and 1980s, and more recently atomic interferometry (Levi 1991) have spawned a variety of demonstrations and tests of quantum theory, relativity and related topics. These various interferometers are largely complementary, as discussed by Stedman (1985*a*, 1986) and Bilger *et al.* (1990), although atomic interferometry has much untapped potential (Clauser 1988; Levi 1991) and has demonstrated the Sagnac effect (Riehle *et al.* 1991; see Al'tshuler 1992). It is therefore appropriate to re-evaluate any unique potential that ring lasers may have as probes for old and new physics.

This potential rests partly in the geometry of the closed, as opposed to an open, interferometer, and partly in the unique characteristics of photons as the workhorse of the ring laser (Post 1972; Stedman *et al.* 1991), an electromagnetic system with the capability of detecting a parity-violating effect, in the sense that any frequency difference must be reversed by mirror reflection. Indeed effects which are detectable uniquely in a ring laser are not necessarily chiral (or gyrotropic, Stedman 1991) in the sense used in chemical physics; the relationship

depends on the configuration of the ring laser (Stedman 1992). There has been considerable interest over the last decade or so in setting experimental limits on possible parity-violating effects within relativity or gravitation theory on the one hand, and quantum field theory and particle theory on the other.

(2b) Rotation Sensing and Seismology

Since the earth rotation unlocks the Canterbury ring, it is a free device, sensing absolute rotation without the need of any external bias or dither (tricks whose absence prevented the first ring laser from showing the earth rotation, and which are otherwise universally applied for ring lasers). It becomes possible to sense seismic events and earth tides as they affect the observed earth rate, at a precision better than 10 ppm. A ring-laser-based seismometer would measure information on any rotational effects, associated for example with horizontal shear, in seismic waves which would complement that derived from the traditional linear accelerometers, and at comparable precision; the rotation detection sensitivity of 10^{-9} rad/s or 0·01 rad/yr demonstrated in this paper is quite enough for detecting microseisms according to the data of Giazotto (1989); see Robertson (1991). The cave in which our ring is due to be installed is built into an 11 million year old volcanic basalt, 131 km off the very active Indian–Pacific tectonic plate boundary.

In collaboration with Ojai Research, we have shown the possibility of using the polarisation state of a square ring laser to measure mirror tilt with an accuracy of the order of picoradians. This suggests a new technique for linear seismometry (Bilger *et al.* 1990).

According to general relativity, the local Lorentz frame itself can rotate with respect to the fixed stars, or be 'dragged', by a nearby rotating object such as the earth. This Lense-Thirring field exemplifies the gravitomagnetic effects in general relativity which so far have been tested only indirectly (Nordtvedt 1988). An experiment to detect this frame dragging, based on mechanical gyros, is due to be put into orbit by the Space Shuttle in 1996. Scully *et al.* (1981) have considered the possibility of their detection by a land-based experiment using a ring laser. Since such effects arise at $10^{-10}\Omega_E$, rather than the 10^{-5}–$10^{-7}\Omega_E$ sensitivity of the present ring, rings of a larger area/perimeter ratio are required.

(2c) Acceleration in Dispersive Media

Equation (1) for the response of a ring laser to rotation is sufficiently general to hold under linear and angular acceleration to very high precision. However, there has been some interest recently in examining the validity of (1), especially in the presence of dispersive dielectric media, under rotational and linear acceleration (Post 1972; Kuriyagawa and Mori 1979; Takahashi 1985; Fabri and Picasso 1989; Scorgie 1990, 1991; Kowalski *et al.* 1992). We mention also the increasing development of fibre optic gyro systems, e.g. Dennis *et al* (1991); however we consider the lack of solid material in our basic ring to be a potential advantage in reducing field- and stress-induced biases, as well as error and noise sources.

(2d) Fresnel Drag and Special Relativity

A popular application of ring laser precision is in tests of special relativistic effects in the dragging of the speed of light in moving media. The classic

experiments of Zeeman (1920) have now been considerably improved by Bilger and Stowell (1977) and by Sanders and Ezekiel (1988), although in each case the analysis and comparison with theory has left something to be desired. In the former case there is a residual small discrepancy between the theoretical estimate and the experimental value. In the latter case some questionable assumptions in the theory need examination, for example the use of the refractive index of the sample with respect to air in lieu of that in vacuo, and various problems of nonreciprocity of beam path in view of the use of nonperpendicular moving medium boundaries. The presence of counterrotating beams which may physically coincide makes the ring laser an ideal instrument for Fizeau-type drag experiments, with greatly increased precision and accuracy. Further experiments of this type would be one obvious test for a ring laser with increased precision.

(2e) Tests of Preferred-frame Theories

Ring interferometry *per se* has a long history in tests of relativity, going back at least to the 1851 experiments of Fizeau on Fresnel drag, but still has a confused status. Stedman (1972, 1973) and Anderson and Stedman (1977, 1992) pointed out some misconceptions arising from a neglect of the logically distinct role of ring interferometry in the kinematical development of special relativity. Tests of relativity have often been motivated at this kinematic level. The test theory of Mansouri and Sexl (1977) has been widely used to motivate Michelson–Morley-like and other experiments with linear lasers (see for example Riis *et al.* 1988; Will 1992*a*,*b*), albeit still in a form which is flawed by the claim of permitting one-way measurements (Vetharaniam and Stedman 1991, 1992). In the same vein one might well motivate searches for violations of special relativity in the conjugate ring geometry (Post 1972; Stedman *et al.* 1991) by postulating a parity-violating preferred-frame test theory.

For example, let us suppose that a boost, induced by the rotation of the earth carrying the ring laser into a new frame which is approximately inertial, generates a gravitomagnetic field $\mathbf{h}$ ($h_i = g_{0i}$) which is proportional to the velocity $\mathbf{v}$ relative to the preferred frame. It is customary but not necessary to identify the preferred frame as that in which the microwave background is isotropic. Let the proportionality constant be a parameter σ:

$$\nabla \times \mathbf{h} = \sigma \mathbf{v} . \tag{2}$$

From equation (1) in its general relativistic form (Post 1967; Anandan 1981), as applied to the earth-rotation-induced beat frequency in the Canterbury ring laser, we would have a (sidereal) diurnal variation in the beat frequency given by $\delta f = \delta[2f_0 \mathbf{A} \cdot \nabla \times \mathbf{h}/P] = 2f_0 A \sigma v \delta(\cos\theta)/P$, where $\delta(\cos\theta)$ is the maximum diurnal change in the projection $\cos\theta$ of the direction of the ring area $\hat{\mathbf{A}}$ on the direction $\hat{\mathbf{v}}$ of the velocity with respect to the preferred frame, on the assumption that the magnitude v of this velocity is much greater than its diurnal variation. We take the magnitude and declination of the preferred frame velocity from Narlikar *et al.* (1991) as $v \approx 6\times10^5$ m s^{-1} and $\delta \approx -26°$ so that, at the latitude of Christchurch ($\lambda \approx -43°.5$), $\delta(\cos\theta) = \cos(\lambda - \delta) - \cos(\pi - \lambda - \delta) = 1{\cdot}30$. Hence $\delta f/\sigma \approx 1{\cdot}6 \times 10^{20}$ m^2 s^{-2} and an experiment searching for a variation in the

Canterbury ring laser beat frequency with the Fourier period of one sidereal day and amplitude $\Delta\omega$ would give an estimate of σ as

$$\sigma \approx P\delta f/2{\cdot}6 f_0 A v; \qquad \sigma(\mathrm{s/m^2}) \sim 6 \times 10^{-21} \delta f\ (\mathrm{Hz})\,. \tag{3}$$

Equation (3) shows that at a beat frequency precision of 1 mHz we may set a bound on σ to an accuracy of the order of 10^{-23} s/m^2.

Why might we do such a test? While a purely kinematic postulate of such a gross assumption in flat spacetime and in the absence of matter has little appeal, the Mansouri–Sexl (1977) test theory was equally kinematic in motivation, but has still proved useful. One could argue, as did Okun (1988), on the possibility of testing the exclusion principle (whose possible violation, as Okun was concerned to show, is even less credible), that 'in fundamental physics if something can be tested it should be tested.' Franklin (1986) has emphasised, and recent stirring events in condensed matter verify, that novel experiments do not require a supporting theory; physics is an experimental science. Telegdi (1990) has emphasised such points in the context of a warm tribute to the skill of Michelson and Gale (1925) in their historic interferometric measurement of the Sagnac effect from earth rotation.

However, most physicists prefer to have a dynamic model, for example a Lorentz-invariance-violating term in the Lagrangian underpinning any test theory to motivate an experiment. The kinematic approach of Mansouri and Sexl (1977) for linear tests of special relativity has often been replaced (Will 1992*b*) with the dynamic model of the $TH\epsilon\mu$ theory. In this the assumption is made that Lorentz invariance may be broken by differentiating the speed of light and the limiting speed of matter. This still permits an elegant classical Lagrangian formulation and most importantly a quantised form which enables the use of high-precision atomic spectroscopy to place more accurate bounds on the parameters (Will 1992*b*).

Parity-violating models of gravitation have been of renewed interest (Gibbons 1992). Possible effects from a gravitational anomaly have been discussed by Dolgov *et al.* (1988, 1990). Ni (1977) has proposed, and Ritter *et al.* (1990) have tested, an alternative and parity-violating gravity theory in which a postulated constitutive tensor density, dependent in part on a scalar function of the gravitational fields, gives rise to anomalous torques on electromagnetically interacting and polarised bodies. The possible effects of spacetime torsion have been discussed by a number of authors such as Hojman *et al.* (1980) who showed that with torsion, gravitational theories admit a parity-violating term in the action. Hehl *et al.* (1976, 1992) considered the Einstein–Cartan theory of gravity whose non-zero torsion tensor is proportional to the antisymmetric part of the connection, and which gives rise to a non-propagating torsion inside matter. Hojman *et al.* (1978, 1979) developed a theory using Cartan's torsion tensor but departed from the Einstein–Cartan theory by modifying the concepts of gauge invariance and minimal coupling, thus obtaining a propagating torsion even within a vacuum. Propagating torsion was also discussed by Hammond (1990). Moffat (1989, 1990) considered the physical consequences of his nonsymmetric gravitation theory in which the fundamental geometric object is the nonsymmetric connection compatible with a complex, nonsymmetric metric. Others (Mashhoon 1975, 1988, 1989; Gabriel *et al.* 1991)

have discussed the electromagnetic effects of gravitational coupling to the rotation of the earth.

Dynamic support for an effect related to that of equation (2) was illustrated within the parametrised post-Newtonian (PPN) formalism by Scully *et al.* (1981). A variation in the apparent earth rotation rate with the period of one sidereal day could be interpreted in terms of a nonvanishing value for the preferred-frame PPN parameter α, which vanishes in general relativity. Presently α is bounded to vanish to 1 part in 10^4 (Will 1992*b*).

Other derivations of equation (2) from the rather more drastic parity-violating modifications referenced above can be expected to yield models that will also justify a search for bounds on the parameter σ.

(2f) Small Material Nonreciprocities

Nonreciprocal physical effects giving absolute phase shifts of 10^{-10} rad between counterrotating beams should be detectable (Stedman 1985; Ross *et al.* 1989; Stedman 1992). This would allow sensitive tests of nonlinear optical effects in gases associated with the chiral effects of electric and magnetic fields. Field-induced magnetic linear dichroism in gases is one obvious candidate. In chemical physics, absolute measurements of such parameters are often very difficult, and the determinations of the hyperpolarisabilities of helium by Buckingham and Dunmur (1968) and the quadrupole moment of CO_2 by Buckingham and Disch (1963) (see also Buckingham 1968) have stood unimproved for many years. Such devices as the ring laser give hope of new results in these directions. Finally, rotation could itself make an atomic gas optically active at a very low level (Silverman 1989; Stedman 1990).

(2g) Anomalous Interaction with Pseudoscalars

The anomaly or triangle diagram occurring in the quantum electrodynamics of pseudoscalar particles has been the focus of an extended literature. Since it is concerned with a parity-violating effect, a ring laser detection system has some relevance.

There has been speculation that even within QED, triangle diagrams provide physically detectable effects (Stedman and Bilger 1987). We are now convinced that such speculation is not well founded (Ross and Stedman 1988; we may note in passing that the work of Maiani *et al.* 1986 is not thereby compromised as Ross and Stedman suggested, since their ϕ does not correspond to measurement of optical activity). However, as discussed above, a novel experiment is worth doing whether or not theorists are sufficiently inventive to get a plausible test theory to justify it.

One can search for upper bounds on electric and/or magnetic field-induced optical properties of the vacuum. The Canterbury ring could set sensitive bounds on such effects. Like the above-mentioned special relativity test, these are particularly clean experiments, requiring no medium and consequently no degradation of cavity finesse. In many respects the vacuum behaves as a nonlinear medium for quantum optical experiments. It can be squeezed, in that some field amplitude fluctuations can be reduced below the levels suggested by the

uncertainty principle, at the expense of others. According to QED, the most well-tested of all physical theories, the vacuum is predicted to permit nonlinear processes such as light–light scattering, but at levels below detection by our present ring, although Ni *et al.* (1991) have proposed an interferometric technique for achieving the required sensitivity of 10^{-25} in a refractive index measurement.

The triangle diagram has noncontroversial application when the anomaly is external, and the pseudoscalar particle exists in nature, as for example in the analysis of $\pi^0 \rightarrow \gamma\gamma$ decay. Various candidates for new neutral pseudoscalar particles have been proposed, including the axion (e.g. Sikivie 1992), the arion and the majoron (Fischler 1991). In principle, these if they exist will interact by the axial anomaly or triangle diagram to couple with two photons. Searches have been conducted for axions, in which one photon is that of a magnetic field, and an optical effect is sought to reveal the otherwise invisible particle. The coupling strength is set through the mass of the pseudoscalar. If (as for Hagmann *et al.* 1990) a tunable microwave cavity were included in the ring laser optical path, it would be possible in principle to detect the effects of circularly polarised 633 nm photons created through the anomaly coupling with incoming pseudoscalars. The microwave magnetic field tunability of say 4 GHz is admittedly only a few ppm of the laser photon energy, 2·0 eV, an energy range which nevertheless is not covered by present axion searches (Sikivie 1992).

3. Canterbury Ring Design and Performance

(3a) Noise Limits

The fundamental limits on the resolution attainable with a ring laser are determined by quantum noise (Dorschner *et al.* 1980; Hellwig 1975) and $1/f$ noise. The transition between these two noise sources is clearly evident in the earlier work of Bilger and Sayeh (1983), and when $1/f$ noise takes over, further time averaging does not improve the data. However, both of these are reduced by a factor of order $1/P^n$, where P is the perimeter and $n \sim 2$–3, by using larger rings through the increasing finesse and the decreasing solid angle in backscatter. When this is done, as in our present ring, $1/f$ noise is essentially eliminated in that the ultimate resolution is restricted by other considerations such as laser stability. Methods such as quantum nondemolition measurement, which extend the resolution of optical systems to break the barrier imposed by quantum noise, are not of prime interest in this application at least at this stage; our strategy is to lower, rather than breach, the standard quantum noise limit itself. The introduction of squeezed light, say by introducing a nonlinear optical element into the cavity, while an exciting theoretical possibility, could in practice risk the very quality of cavity finesse that led to the lowering of the standard quantum limit. Our success in this direction, without resorting to squeezing etc., again illustrates that the potential of the ring laser for precision measurements is still quite underdeveloped.

In confirmation of these comments, we write the power spectral density of the beat frequency fluctuations as $S_{\delta f} = h_0 + h_{-1}/f$, where f is the Fourier frequency. The coefficient for quantum noise is given by $h_0 = 2hf_0^3 3/P_0Q^2$ with the value $h_0 = 3 \times 10^{-6}$ Hz^2/Hz for a total optical power loss $P_0 = 0{\cdot}1\ \mu$W and the ideal cavity quality factor Q; f_0 is the laser frequency of 474 THz;

$h_{-1} = 8f_0^2/Q^4$ (this is an empirical relation, for which see Sayeh and Bilger 1987). With a measurement time T, the rms frequency fluctuation of the beat frequency is then

$$\Delta f_{rms} = [2hf_0^3/Q^2P_0T]^{\frac{1}{2}} . \tag{4}$$

The analysis leading to equation (4) assumes that the cw and ccw beams are uncorrelated; while methods for inducing and exploiting a correlation for noise reduction are now well discussed and physically demonstrated, there is no immediate prospect of using this in systems such as ours. With the above specifications and $T = 1$ h, a frequency fluctuation of 20 μHz can be achieved in principle, corresponding to a frequency resolution $\Delta f/f_0 = 4 \times 10^{-20}$. Other interferometric techniques have been proposed (Ni *et al.* 1991) which could improve on this figure, and which would correspond to the performance that we may expect of a ring laser with an area of say 50 m^2 (as in Scully *et al.* 1981). From this viewpoint, even the earlier ring lasers have already outclassed (Bilger and Sayeh 1986) other precision tools such as the Mössbauer effect (Pound and Snider 1965) and the maser (Vanier 1982).

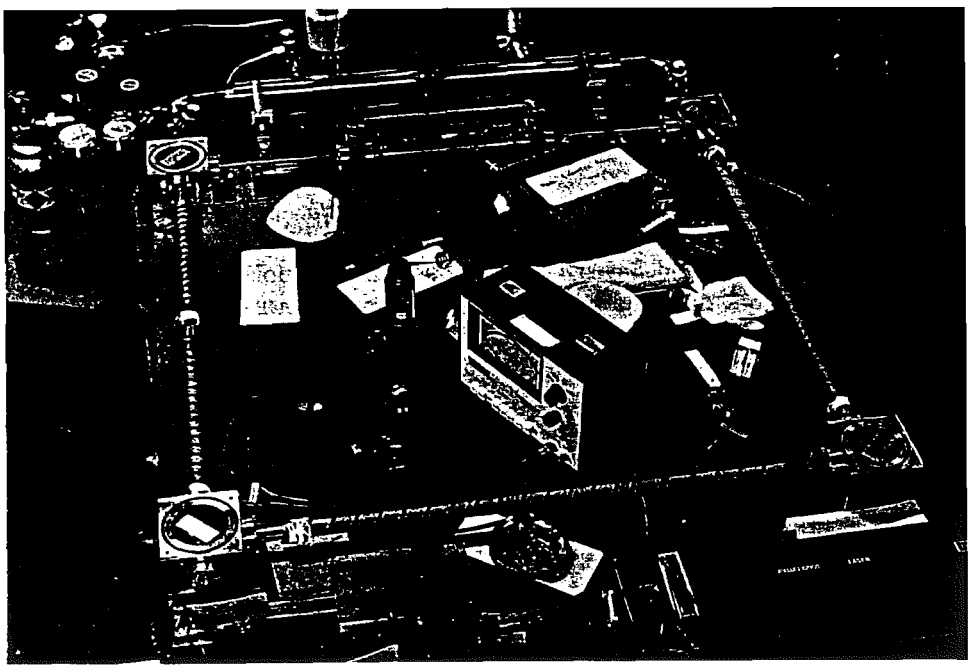

Fig. 1. The Canterbury ring laser. The RF excitation section is in the topmost leg, and the superinvar mirror mounts are visible through the glass lids of the corner boxes. The green helium–neon laser for alignment is in the foreground.

(3b) Construction

The Canterbury ring laser (Fig. 1) is designed to realise the potential of the recent advances. So that the cavity finesse is maximised, the beam paths are

entirely in the helium–neon gas; the Rayleigh scattering of neutral neon gas at 300 Pa has a negligible effect on the quality factor. Neither do the beams intersect any interface, although for some applications Brewster windows will be both necessary and tolerable. Supermirror coatings were generously provided by Ojai Research. Zerodur blanks were used which have 0·1 nm rms surface roughness (i.e. smoothness to atomic dimensions), achieved through ion beam milling with argon and nitrogen beams. Ultrahigh vacuum coated SiO_2/TiO_2 $\lambda/4$ layers give losses of 4 ppm due to scattering (TIS), 4 ppm from transmission, and absorption (by difference) of 7 ppm, approaching that of the bulk materials. The observed total reduction in reflection is then 15 ppm, corresponding to a reflectivity of 99·9985%. After extended use in our environment the total losses increased significantly.

The radio frequency excitation mechanism is novel, involving a magnetic coupling at 50 MHz. The laser gas is 7:1 He:Ne with a nominal total pressure of 2·3 Torr (300 Pa); however the latter can successfully be varied over an order of magnitude. A natural mixture of neon isotopes (Ne^{20}:Ne^{22} = 9:1) and natural helium is used at present.

For further mechanical and thermal stability the mirrors are mounted in superinvar holders resting on a 1×1 m^2 Zerodur plate, itself on a granite base. The stainless steel corner boxes avoid mechanical contact with the mirrors; their bottoms are open, and are sealed by Viton O-rings against the Zerodur plate.

A triangular ring was used in earlier lasers such as that of Bilger and Stowell (1977). We have used a square ring primarily to optimise the parameter $G = A/PN$, where A is the area, P the perimeter and N the number of mirrors. From earlier equations, together with the dependence of Q on mirror losses, G is proportional to the signal/noise ratio of the system. Since there is an odd number of reflections, each of which reverses handedness of the beam, a triangular ring cannot be put in circularly polarised mode. A square ring could be put in circularly polarised mode, should applications require it, for example by introducing nonplanarity (Bilger *et al.* 1990), another impossibility with a triangle. The increase in angle of incidence means that backscatter is reduced; indeed, Lambert backscatter formally vanishes at 45° incidence. Together these measures help to avoid locking.

Partly to preserve the advantages sought from a simple open design with mechanical and thermal isolation for the mirrors, and partly on account of cost, no feedthroughs are installed at this stage in the corner boxes. Hence alignment to 20 arcsec in angle and 10 μm in position has to be achieved before adding vacuum sealed covers to the corner boxes, pumping down, gas handling and initiating the lasing. Mirror holders were machined to locate the poles to this precision. A green helium–neon laser beam was overlaid with that of a standard red laser to preserve alignments under a sequence of operations where the mirrors were rotated from retroreflecting configurations, in which tilt about a horizontal axis was adjusted and from which mirrors were rotated about a vertical axis to reach the final positions. The output interferometer was mounted on top of the glass cover for one corner box. Its components were aligned to overlay the emergent beams to a precision of 0·3 mrad.

This device will shortly be taken to an underground cavern giving further thermal and mechanical stability. The results reported here are therefore only preliminary.

(3c) Results

The Canterbury ring generates a nominal beat frequency δf of 68·826 Hz, given the latitude of 43° 29′ South, (vacuum) wavelength $\lambda = 633{\cdot}0$ nm, perimeter $P = 3477{\cdot}1 \pm 0{\cdot}1$ mm (measured from the free spectral range of 86·218 MHz determined from the beat frequency between neighbouring longitudinal modes) and area $A = 0{\cdot}748$ m^2 (given with lesser accuracy from the two sides of 898 mm, 837 mm). Since the gain curve for natural neon has a width of order 1 GHz, several longitudinal modes could readily be excited, and of course the intermediate transverse modes. A fused silica tube of length 30 cm and 4 mm internal diameter served both as RF-excited amplifier and as an aperture. Our design aimed to achieve single mode operation by reducing the gain so that (thanks to the variation of gain with wavelength) all longitudinal modes except one would be starved. In principle this required output power reduction to the manageable level of 30 nW. In practice, we were pleasantly surprised at the ease at which such gain control achieved single mode excitation of the ring. Typical RF powers for single mode excitation were 5–7 W, and output beam powers were then indeed of the order of 30 nW. For higher excitation power, say 30 W, output beam powers reached 2 μW, which corresponds (since mirror transmission is 4 ppm) to a circulating power of 0·5 W. Although high circulating powers reduce quantum shot noise, they induce nonlinear effects in mirror media, and as noted by Chow *et al.* (1985) multimode rings give new branches in the beat-frequency–rotation-rate plot. Mode structure was monitored with a Newport SR-130 scanning Fabry–Perot.

The ringdown decay time of the ring was measured to be approximately $\tau = 15$ μs by monitoring lasing output as the RF is turned off using a digital storage oscilloscope. This translates into a quality factor $Q = \omega\tau = 4{\cdot}5 \times 10^{10}$, noticeably below the ideal. The causes of this long-term contamination of mirror coatings have been identified, and within our limited budget we are working towards their elimination.

The interference fringes on detection were processed by a Strobes Acquisition-PC data collection system (equivalent to Rapid Systems R380), which permitted runs of 16·384 s with a 2 ms sampling time. A spectrum obtained is given in Fig. 2.

While the 50 Hz signal from mechanical motion induced at the frequency of the New Zealand mains power supply, together with its harmonics, is conspicuous, the spectrum is dominated by the line associated with earth rotation in the region 67–78 Hz. Even the subsidiary features of the spectrum are sharp; the mechanical resonances of the ring support system (at 15 and 19 Hz for example), which appear at those frequencies and as sidebands to the main features, reflect their relatively high mechanical quality factor (measured to be 34 ± 1). Indeed in our current site on the sixth level of a multi-storey building facing the prevailing wind, data of the quality of Fig. 2 can only be obtained under relatively wind-free conditions and late at night, when other uses of the building are minimal.

The earth-rotation-induced signal is almost as sharp as the mains frequency line. Its width is dominated by the windowing resolution of up to 160 mHz (Fig. 3). However, a careful analysis (Stedman and Bilger 1992) has shown that the net optical line width of the beat frequency may be extracted by deconvolution, and by using the second and third harmonics of the earth-rotation-induced signal

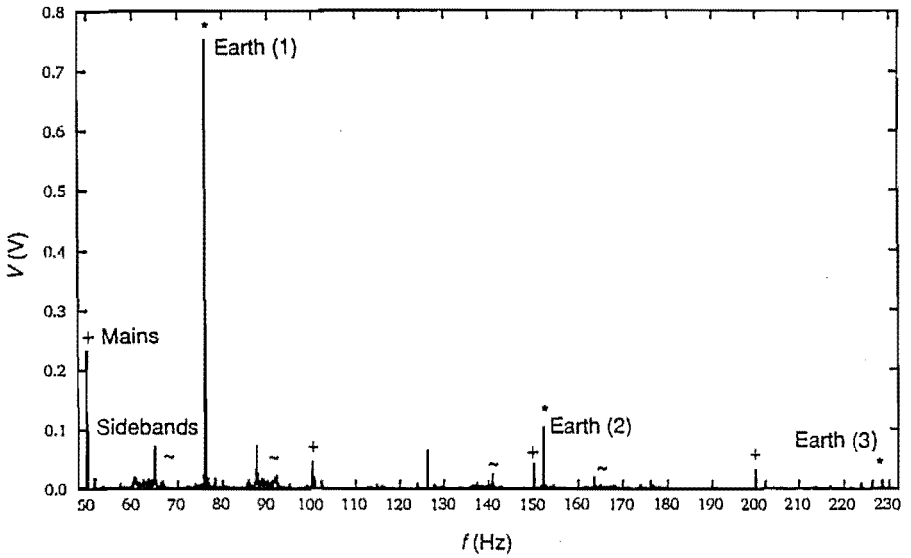

Fig. 2. A spectrum from the Canterbury ring. The beat signal from earth rotation, together with its two higher harmonics, are marked by an asterisk. Sidebands arising from the mechanical resonance of the support are marked by a tilde, and mechanical rotation from the AC mains with its harmonics by a plus sign.

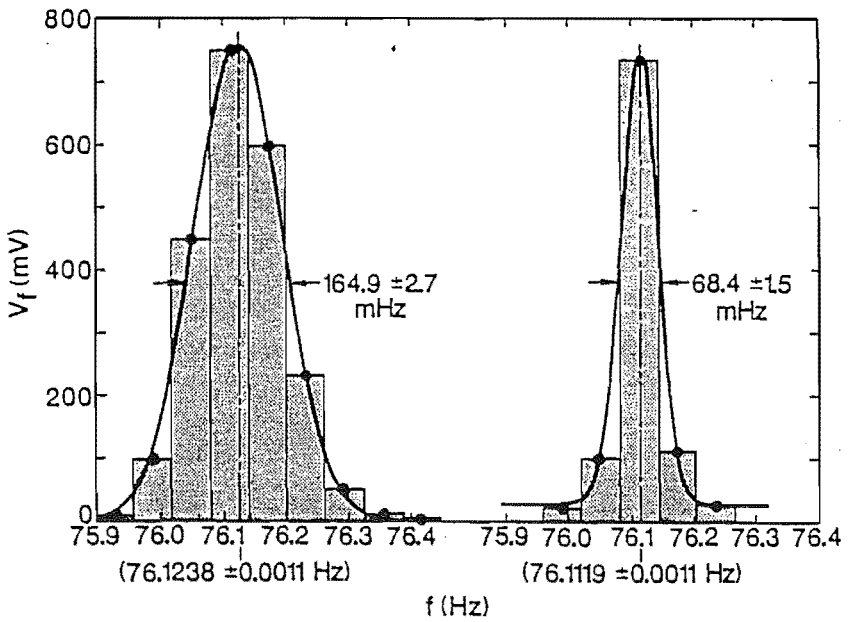

Fig. 3. The effect of windowing on the raw data for the fundamental earth rotation line in Fig. 2; on the left is a Nuttall window (Stedman and Bilger 1992), and on the right a square window corresponding to the time gate of 16·384 s.

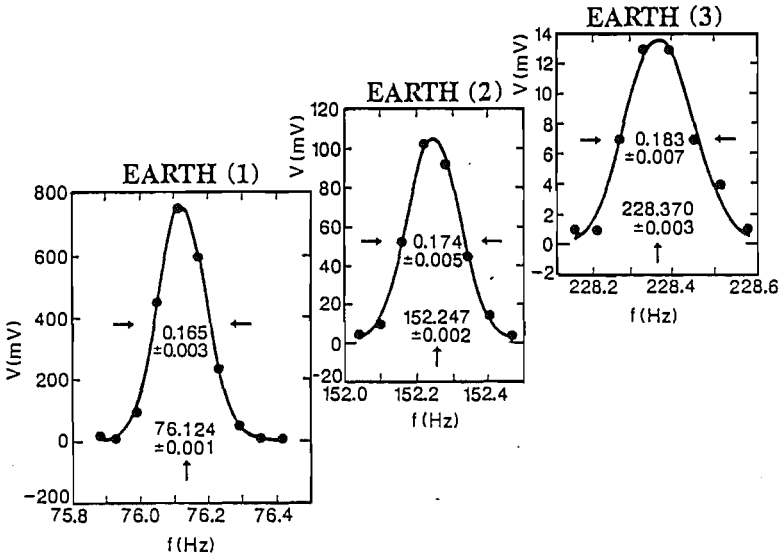

Fig. 4. A comparison of the widths of the raw data for all harmonics in Fig. 2. The fitted curve is a convolution of the known window function and a net laser line shape function, whose width is thus determined consistently to be 33 mHz. As noted in Fig. 3 and in the text, the line positions may thus be determined to 1·0 mHz, or $2{\cdot}1\times10^{-18}$ of the laser frequency.

(Fig. 4) it is possible to check the consistency of this procedure, and obtain at present a laser beat frequency full width at half maximum (FWHM) of $32{\cdot}7\pm1{\cdot}7$ mHz for the runs of 16·384 s duration. This is an order of magnitude larger than the expected quantum noise limit. Most importantly, the line profile can be fitted to a Gaussian and the position of the centre of the line obtained to a precision of 1·0 mHz; this estimate also was reduced by a comparison of harmonics. This justifies our claim for a fractional frequency resolution capability of $2{\cdot}1\times10^{-18}$. The earth-rotation-induced line position in our as yet unstabilised ring drifts typically by several hertz in a few minutes. Such drift during the sampling time explains the difference between the observed line width and the quantum noise limit. Shorter sampling times lead to wider windows, and to no improvement in resolution; at this stage our maximum data collection time is (fortuitously) optimal.

We attribute this drift to the well-known effects of the susceptibility variation over the composite neon gain curve when the path length, and with it the resonance frequency, varies, compounded by saturation effects (Aronowitz 1971; Sargent *et al.* 1974; Siegman 1986). Thermal expansion effects even in Zerodur would induce shifts of the cavity modes within the gain curve by several per cent of the free spectral range per Celsius degree, and the counterpropagating waves sample the gain curve at different frequencies. The difference in optical path length for these modes itself depends on the position within the gain curve. We are therefore deferring the proposed test of relativity suggested earlier in this paper until present work on stabilising the cavity modes within the gain curve via feedback is completed. The forthcoming transfer to the cavern will also markedly help reduce drifts and mechanical interference.

The cavity parameters appropriate for the original mirrors and for the results given above are given in Table 1, together with comparative figures for the Newport SR-130 supercavity.

Table 1. Ring parameters

We give the performance limit obtainable in principle given supercavity mirror parameters as measured by the manufacturer, the performance actually attained in our environment, and for comparison the corresponding figures for the Newport SR-130 scanning Fabry–Perot supercavity (Li *et al.* 1990). In all cavities, the quality factor is $Q = f_0/\Delta f_{\frac{1}{2}} = \omega\tau$, where $f_0 = \omega/2\pi = 474$ THz; the finesse is $F = S/\Delta f_{\frac{1}{2}} = Q\lambda/P$, where the free spectral range (FSR) is $S = c/P$, P is the round trip length and $\Delta f_{\frac{1}{2}}$ is the power FWHM of the cavity response. In a Fabry–Perot, $TF = \pi$ where the mirror power transmittance $T = 1 - R$, and $\Delta f_{\frac{1}{2}} = cT/\pi P$; in a four-mirror ring, $TF = \pi/2$ and $\Delta f_{\frac{1}{2}} = 2cT/\pi P$. The nonreciprocal refractive index and rotational velocity limits are estimated as in Stedman *et al.* (1987)

	Ring laser		Fabry–Perot
	Design	Achieved	SR-130
Perimeter P (mm)	3477·1		50·6
FSR S (GHz)	0·086218		6·0
Cavity finesse F	~200 000	30 000	85 000
FWHM $\Delta f_{\frac{1}{2}}$ (kHz)	~0·5	10·6	70
Quality factor Q	$\sim 10^{12}$	4×10^{10}	7×10^{9}
Resolution δf	~20 μHz	1·0 mHz	70 kHz
averaging time	1 h	16 s	
relative $\delta\nu/\nu$	$\sim 4\times10^{-20}$	$2\cdot1\times10^{-18}$	
rotation (rad/s)	10^{-10}		
refractive index	10^{-20}		

At this stage we estimate the beat frequency to be stable to the order of Hz over a time scale of hours, and that σ in equation (3) vanishes to a precision of the order of 10^{-19} s/m^2. It is hoped to improve this bound significantly in the future. This interferometric determination of the earth rotation rate already makes an interesting comparison with the historic interferometric measurements of Michelson and Gale (1925) using light and Werner *et al.* (1979) using neutrons.

Acknowledgments

We are most grateful to Tony Louderback of Ojai Research, Ojai, California, for providing the supercavity mirror coatings and for much advice; also Professors B.G. Wybourne for enthusiastic support and F.V. Kowalski for discussions and for substantial help in the construction of the ring, notably the output beam interferometer. H.R.B. acknowledges partial support by the US National Science Foundation under the US–NZ Cooperative Science scheme, the Royal Society of New Zealand by a Prince and Princess of Wales Science Award, and the University of Canterbury by two Erskine Fellowship awards. G.E.S. thanks Professors A. D. Buckingham, P. West and Dr B. Rosenstein for discussions and correspondence.

References

Al'tshuler, V. (1992). *Phys. Today* **45** (Feb.), 13.
Anandan, J. (1981). *Phys. Rev.* D **24**, 338.
Anderson, R., and Stedman, G. E. (1977). *Found. Phys.* **7**, 29.
Anderson, R., and Stedman, G. E. (1992). *Found. Phys. Lett.* **5**, 199.

Aronowitz, F. (1971). *In* 'Laser Applications' (Ed. M. Ross) **1**, pp. 133, 169 (Academic: New York).
Bilger, H. R., and Sayeh, M. R. (1983). *In* 'Noise in Physical Systems and $1/f$ Noise' (Eds M. Savelli *et al.*), pp. 325–8 (Elsevier: Amsterdam).
Bilger, H. R., and Sayeh, M. R. (1986). *In* 'Noise in Physical Systems and $1/f$ Noise' (Eds A. d'Amico and P. Mazzetti), pp. 293–6 (Elsevier: Amsterdam).
Bilger, H. R., and Stowell, W. K. (1977). *Phys. Rev.* A **16**, 313.
Bilger, H. R., Stedman, G. E., and Wells, P. V. (1990). *Opt. Commun.* **80**, 133.
Buckingham, A. D. (1968). *J. Chem. Phys.* **48**, 3827.
Buckingham, A. D., and Disch, R. L. (1963). *Proc. R. Soc. London* **273**, 275.
Buckingham, A. D., and Dunmur, D. A. (1968). *Trans. Farad. Soc.* **64**, 1776.
Chow, W. W., Gea-Banacloche, J., Pedrotti, L. M., Sanders, V. E., Schleich, W., and Scully, M. O. (1985). *Rev. Mod. Phys.* **57**, 61.
Clauser, J. F. (1988). *Physica* B **151**, 262.
Dennis, M. L., Diels, J.-C., and Lai, M. (1991). *Opt. Lett.* **16**, 529.
Dieks, D., and Nienhuis, G. (1990). *Am. J. Phys.* **58**, 650.
Dolgov, A. D., Kriplovich, I. B., and Zakharov, V. I. (1988). *Nucl. Phys.* B **309**, 591.
Dolgov, A. D., Kriplovich, I. B., Vainshtein, A. I., and Zakharov, V. I. (1990). *Nucl. Phys.* B **315**, 138.
Dorschner, T. A., Haus, H. A., Holtz, M., Smith, I. W., and Statz, H. (1980). *IEEE J. Quant. Electr.* QE-**16**, 1376.
Fabri, E., and Picasso, L. E. (1989). *Phys. Rev.* A **39**, 4641.
Fischler, W. (1991). *Phys. Lett.* B **266**, 408.
Forder, P. W. (1985). *J. Phys.* A **18**, 3343.
Franklin, A. (1986). 'The Neglect of Experiment' (Cambridge Univ. Press).
Gabriel, M. D., Haugan, M. P., Mann, R. B., and Palmer, J. H. (1991). *Phys. Rev. Lett.* **67**, 2123.
Giazotto, A. (1989). *Phys. Reports* **182**, 365.
Gibbons, G. W. (1992). Comments on long range parity violating forces. DAMPT R-91/17.
Hagmann, C., Sikivie, P., Sullivan, M. S., and Tanner, D. B. (1990). *Phys. Rev.* D **42**, 1297.
Hammond, R. T. (1990). *Gen. Rel. Gravitat.* **20**, 813.
Heer, C. V. (1964). *Phys. Rev.* **134**, A799.
Hehl, F. W., Lemke, J., and Mielke, E. W. (1992). *In* 'Bad Honnef Lectures' (Eds J. Debrus and A. C. Hirshfeld) (Springer: Berlin).
Hehl, F. W., von der Hyde, P., Kerlick, G. D., and Nester, J. M. (1976). *Rev. Mod. Phys.* **8**, 393.
Hellwig, H. W. (1975). *Proc. IEEE* **63**, 212.
Hendriks, B. H. W., and Nienhuis, G. (1990). *Quant. Optics* **2**, 13.
Hojman, R., Mukku, C., and Sayed, W. H. (1980). *Phys. Rev.* D **22**, 1915.
Hojman, S., Rosenbaum, M., Ryan, M. P., and Shepley, L. C. (1978). *Phys. Rev.* D **17**, 3141.
Hojman, S., Rosenbaum, M., and Ryan, M. P. (1979). *Phys. Rev.* D **19**, 430.
Kowalski, F. V., Murray, J., and Head, A. (1992). Interaction of light with an accelerating dielectric (submitted for publication).
Kuriyagawa, A., and Mori, S. (1979). *Phys. Rev.* D **20**, 1290.
Levi, B. G. (1991). *Phys. Today* **44** (July), 17.
Li, Z., Bennett, R. G. T., and Stedman, G. E. (1991). *Opt. Commun.* **86**, 51.
Macek, W. M., and Davis, D. T. M. Jr. (1963). *Appl. Phys. Lett.* **2**, 67.
Macek, W. M., Davis, D. T. M., Jr., Olthius, R. W., Schneider, J. R., and White, G. R. (1963). 'Symposium on Optical Masers', p. 199 (Polytechnic Press: New York).
Macek, W. M., Schneider, J. R., and Salamon, R. M. (1964). *J. Appl. Phys.* **35**, 2556.
Maiani, L., Petronzio, R., and Zavattini, E. (1986). *Phys. Lett.* B **175**, 359.
Mansouri, R., and Sexl, R. U. (1977). *Gen. Rel. Gravitat.* **8**, 497, 505, 819.
Mashhoon, B. (1975). *Phys. Rev.* D **11**, 2679.
Mashhoon, B. (1988). *Phys. Rev. Lett.* **61**, 2639.
Mashhoon, B. (1989). *Phys. Lett.* A **139**, 103.
Michelson, A. A., and Gale, H. G. (1925). *Astrophys. J.* **61**, 140.
Moffat, J. W. (1989). *Phys. Rev.* D **39**, 474.

Moffat, J. W. (1990). Review of the nonsymmetric gravitation theory, Lectures given at the Summer Institute on Gravitation, Banff, Alberta
Narlikar, J. V., Pecker, J. C., and Vigier, J. P. (1991). *Phys. Lett.* A **154**, 203.
Ni, W.-T. (1977). *Phys. Rev. Lett.* **38**, 301.
Ni, W. T., Tsubono, K., Mio, N., Narihara, K., Chen, S-C., King, S-K., and Pan, S-S. (1991). *Mod. Phys. Lett.* A **6**, 3671.
Nordtvedt, K. (1988). *Phys. Rev. Lett.* **61**, 2647.
Okun, L. B. (1988). *Comments Nucl. Part. Phys.* **19**, 99.
Post, E. J. (1967). *Rev. Mod. Phys.* **39**, 475.
Post, E. J. (1972). *J. Opt. Soc. Am.* **62**, 234.
Pound, R. V., and Snider, J. L., (1965). *Phys. Rev.* **140**, B788.
Riehle, F., Kisters, Th., Witte, A., and Helmcke, J. M. (1991). *Phys. Rev. Lett.* **67**, 177.
Riis, E., Andersen, L.-U. A., Bjerre, N., Poulsen, O., Lee, S. A., and Hall, J. H. (1988). *Phys. Rev. Lett.* **60**, 842.
Ritter, R. C., Goldblum, C. E., Ni, W.-T., Gillies, G. C., and Speaker, C. G. (1990). *Phys. Rev.* D **42**, 977.
Robertson, D. S. (1991). *Rev. Mod. Phys.* **63**, 899.
Ross, H. J., and Stedman, G. E. (1988). *Phys. Lett.* A **132**, 229.
Ross, H. J., Sherborne, B. S., and Stedman, G. E. (1989). *J. Phys.* B **22**, 459.
Sanders, G. A., and Ezekiel, S. (1988). *J. Opt. Soc. Am.* B **5**, 674.
Sargent, M. III, Scully, M. O., and Lamb, W. E. Jr. (1974). 'Laser Physics', Ch. 10 (Addison–Wesley: New York).
Sayeh, M. R., and Bilger, H. R. (1985) *Phys. Rev. Lett.* **55**, 700.
Scorgie, G. C. (1990). *J. Phys.* A **23**, 5169.
Scorgie, G. C. (1991). *Eur. J. Phys.* **12**, 64.
Scully, M. O., Zubairy, M. S., and Haugan, M. P. (1981). *Phys. Rev.* A **24**, 2009.
Siegman, A. E. (1986). 'Lasers', pp. 1193ff (University Science Books: Mill Valley).
Sikivie, R. (1992). Axion searches. UFIFT-HEP-91-29.
Silverman, M. P. (1989). *Europhys. Lett.* **9**, 95.
Statz, H., Dorschner, T. A., Holtz, M., and Smith, I. W. (1985). *In* 'Laser Handbook', Vol. 4 (Eds M. L. Stitch and M. Bass), p. 229 (North Holland: Amsterdam).
Stedman, G. E. (1972). *Am. J. Phys.* **40**, 782.
Stedman, G. E. (1973). *Am. J. Phys.* **41**, 1300.
Stedman, G. E. (1985*a*). *Contemp. Phys.* **26**, 311.
Stedman, G. E. (1985*b*). *Adv. Phys.* **34**, 513.
Stedman, G. E. (1986). *In* 'Quantum Optics IV' (Eds J. D. Harvey and D. F. Walls), pp. 259–66 (Springer: Berlin).
Stedman, G. E. (1990). *Phys. World* **3**, 23.
Stedman, G. E. (1991). *Phys. Lett.* A **152**, 19.
Stedman, G. E. (1993). *In* 'Modern Nonlinear Optics, Part 2' (Eds S. Kielich and M. W. Evans) (Wiley: New York).
Stedman, G. E., and Bilger, H. R. (1987). *Phys. Lett.* A **122**, 289.
Stedman, G. E., and Bilger, H. R. (1992). *Digital Signal Proc.* **2**, 105.
Stedman, G. E., Bilger, H. R., and Kowalski, F. V. (1991). *Aust. & N.Z. Physicist* **28**, 16.
Takahashi, Y. (1985). *Phys. Lett.* A **113**, 5.
Telegdi, V. L. (1990). Mind over matter: the intellectual content of experimental physics. CALTECH ERN-90-09.
Vanier, J. (1982). *Metrologia* **18**, 173.
Vetharaniam, I., and Stedman, G. E. (1991). *Found. Phys. Lett.* **4**, 275.
Vetharaniam, I., and Stedman, G. E. (1992). Significance of precision tests of special relativity (submitted for publication).
Werner, S. A., Staudenmann, J-L., and Colella, R. (1979). *Phys. Rev. Lett.* **42**, 1103.
Will, C. M. (1992*a*). *Phys. Rev.* A **45**, 403.
Will, C. M. (1992*b*). The confrontation between general relativity and experiment: a 1992 update. *Int. J. Mod. Phys.* A (to be published).
Zeeman, H. (1920). *Proc. R. Acad. Sci. (Amsterdam)* **22**, 462, 512.

Manuscript received 30 March, accepted 25 June 1992

Appendix C

Losses

H R Bilger, P V Wells. and G E Stedman. Origins of fundamental limits for reflection losses at multilayer dielectric mirrors. *Appl. Opt.*, 33(31):7390 - 7396, 1994

Origins of fundamental limits for reflection losses at multilayer dielectric mirrors

H. R. Bilger, P. V. Wells, and G. E. Stedman

Fundamental limits on reflection losses are set by internal material losses associated with the Urbach tail near a band gap and by thermodynamic density fluctuations in fabrication. In materials such as SiO_2 and TiO_2, these limits are of the order of parts in 10^9. The current quality of supercavity mirrors, in contrast to that of optical fibers, is still far from these limits because of purely technological limitations in surface preparation and in the reduction of impurity levels. Overcoming these would greatly benefit, for example, Fabry–Perot interferometers, ring lasers, and gravitational wave detectors.

1. Introduction

Multilayer dielectric mirrors are currently made at visible wavelengths with radiant reflectances of $R > 0.999999$ (six 9's), corresponding to a total power loss $1 - R$ of less than 1 part in 10^6 (ppm), as measured by a ring-down technique; the latter is capable of mirror reflectance analyses to well below the level of 1 ppm.[1,2]

Supermirror quality is indexed by scattering, transmission, and absorption losses, S, T, A. Transmission losses T are self-explanatory and are controlled by design of the multilayer system, at this time at the ppm level. Scattering S corresponds to nonspecular reflection as measured in a scatterometer and is defined by a dimensionless parameter TIS (meaning total integrated scattering).[3] All remaining losses are lumped into absorption A; multiple internal or bulk scattering may partly be detected in a scatterometer and so included in S, with the remainder appearing in A. Hence $R + S + T + A = 1$. Dramatic decreases in S and A over the last few decades, from parts per thousand to ppm, have made possible a new generation of revolutionary high-precision instruments in which the total loss $1 - R$ is a few ppm. The decrease in the total loss is 1 order of magnitude per 6 years during the period 1973–1989.[4] This raises the question as to whether fundamental limits have yet been reached. Further reduction in the total loss will have a correspondingly dramatic effect.

For example, high-resolution Fabry–Perot interferometers have a frequency resolution that is proportional to their finesse, F; this in turn is inversely proportional to $(1 - R)$. Finesses have already increased from $F \sim 30$ or so[5] to $F > 60{,}000$.[6] Another example is that of ring-laser gyroscopes, whose accuracy $\Delta\omega$ is limited by the quality factor, Q, of the cavity (itself related to the cavity finesse) through the relation[7] $\Delta\omega \propto Q^{-2}$. Values of $Q \sim 4 \times 10^{10}$ have been obtained, and values of $Q \sim 1 \times 10^{12}$ (corresponding to mirror losses less than 10 ppm) are being attempted in large ring lasers.[7–9] Finally, gravitational wave detectors and, more generally, high-power laser devices would benefit from further reduction in mirror loss.[10,11] Proposed gravitational wave detectors utilizing Michelson interferometers with recycled beams are designed for circulating cw beam powers of up to 100 kW.

We discuss scattering S in Section 2, distinguishing the role of surface and bulk scattering; we discuss the relative importance of transmission T and absorption A in Section 3. In so compartmentalizing our discussion, we assume the separability and the linear superposability of the various mechanisms for loss. These include scatter from bulk material (volume scattering) or from surfaces, transmission, and absorption, both in each bulk material component and in cases in which there are deviations from stoichiometric composition as the component materials are blended. The smaller the various loss contributions are, the more nearly additive they are likely to be, and so the separations we make become increasingly valid. We prove the separability of T, A in Section 3,

H. R. Bilger is with the School of Electrical and Computer Engineering, Oklahoma State University, Stillwater, Oklahoma 74078-0321; P. V. Wells and G. E. Stedman are with the Department of Physics and Astronomy, University of Canterbury, Private Bag 4800, Christchurch, New Zealand.

Received 8 February 1993; revised manuscript received 31 March 1994.

0003-6935/94/317390-07$06.00/0.

using the matrix analysis of thin films to derive the Koppelmann limit[12] of absorption as well as the Abelès limit[13] for lossless material, assuming only small overall losses.

The absolute and even the relative importance of each of these individual loss mechanisms in mirrors that are truly state of the art (as distinct from that described in the literature) is at best proprietary unpublished information, probably unknown in the absence of very detailed materials studies, and certainly under continuous change. For these reasons we do not attempt to define or balance the importance of the various contributions to loss or to prescribe a strategy to adjust such a balance, but rather focus on the quest of the fundamental limit for each mechanism. We conclude that the fundamental limits are those met in minimizing A. We emphasize the existence of such limits, inherent in all materials conceived at present as candidates for mirror films. The prediction made here for this fundamental limit, 1 part in 10^9 (ppb), naturally reflects the choice of those materials (SiO_2 and TiO_2) universally used at this time, but it is not expected to change significantly for other materials. Residual band-gap effects on absorption are treated in Section 4, and bulk scattering from irreducible volume density fluctuations are treated in Section 5.

2. Scattering as Measured by Total Integrated Scattering

We concentrate here on scattering from surface effects, and we assume the linear superposability of loss contributions from the scatter from bulk material and from surfaces. However, one might first ask whether existing technology gives any support for such a subdivision. Recently published summaries of the state-of-the-art[14–18] technologies indicate that in the case of ion-beam-sputtered mirrors such as our present mirrors, an amorphous bulk structure both of SiO_2 and TiO_2 is favored by high-energy particle deposition on a cold substrate,[4] leading to an absence of grains and grain boundaries and so to greatly reduced volume scattering in comparison with that of the columnar microcrystallite structures arising in older coating techniques.[14] Although the admixture of SiO_2 and TiO_2 can minimize devitrification, degradation of the composition can also greatly reduce the effects of surface nonflatness, apparently without contributing significantly to A. The choice of a low index of refraction $\lambda/2$ top layer may be of help in reducing scattering.[15] Together such effects reduce losses within the layers toward the value set by absorption in the bulk material (Section 3). Less recent discussions[19,20] of fundamental absorption mechanisms near the band edge (see Section 4) indicate, for example, that for then-current mirrors and in the absence of grains, Rayleigh scattering is essentially a surface property. The mirrors considered by all these authors are not to be confused with contemporary mirrors, much less future ones, and the cited research is becoming increasingly dated. Some mirrors, M, in our possession have a total (ring-down) measured loss of $1 - R \lesssim 4$ ppm; under good conditions, the beam spots on our ring-laser mirrors are almost invisible in the dark, and when intracavity circulating beam powers are ~ 1 W, indicative of values $S \sim 1$ ppm. Mirrors with total losses of 1 ppm are planned for in current designs of gravitational wave detectors. For these reasons we focus on the quest for fundamental limits.

A yardstick for surface smoothness is given by the simple equation[3]

$$\sigma = \frac{\lambda}{4\pi}\sqrt{\mathrm{TIS}}. \tag{1}$$

Here the measured TIS is expressed formally as a rms roughness parameter, σ, which, it should be noted, becomes meaningless for surfaces with surface roughness well below the lattice constant; Stewart and Gallant[21] derive from their scatterometer data a rms roughness of $\sigma = 0.05$ nm for a well-prepared silicon surface, whereas the lattice constant of silicon is 0.54 nm. Roughnesses of $\sigma = 0.0188$ nm have been achieved in SiO_2.[22] One mirror, M, as mentioned above had a measured surface roughness σ of 0.0166 nm.[23]

Equation (1) presupposes a random Gaussian distribution of surface roughness; as Elson *et al.*[3] have shown, the validity of Eq. (1) can be extended by the addition of lateral covariance functions, which is for the inclusion of nonrandom, or correlated, surface features. However, with improved techniques for generating good surfaces that may include cleaved surfaces, the scattering from multidielectric stacks with subatomic roughness is expected to yield structured and nonrandom scattering more akin to a diffraction pattern from a regular two-dimensional molecular grating. Local potential changes on the atomic scale have their maximum effect at the surface, and for the purposes of evaluating S, one might reasonably regard the bulk material as homogeneous and isotropic. Because the lattice spacing is very much less than the distance between scattering centers, interference effects should ensure that negligible nonspecular scattering is obtained from a surface layer that is suitably optimized, and that in particular is a regular two-dimensional lattice. Theoretical confirmation of this expectation will require an extension of the theory of reflection at rough surfaces, which usually is restricted to a Fresnel–Huygens–Kirchhoff approach. The latter involves boundary conditions that imply that the linear dimensions of diffracting apertures are small compared with the wavelength.[24] Currently available surface scans universally indicate that the principal contribution to nonspecular scattering is that of isolated individual scattering centers. With the advent of scanning tunneling microscopic techniques, considerable progress should be possible in this area. The design of such surfaces, with or without antiscattering layers,[15] should be based on the expected diffraction patterns of two-dimensional lattices scattering at

the surface. For future substrates we anticipate a decrease of the density of such isolated scattering centers to negligible magnitudes; the scattered power off the resulting surfaces should then be negligible even at the ppb level.

It is shown below that the complex index of refraction of the substrate does not enter into the expression of reflectance in a properly designed absorption-limited multilayer dielectric mirror. Hence the substrate material should be chosen only to give the lowest scattering. It may be emphasized here that much empirical information on scattering points to the fact that the overall scattering, at all interfaces including the top (air) interface, is closely correlated with the topological features of the substrate, simply because any surface defects are reproduced on all superimposed layers through to the final vacuum–dielectric interface.[25,26]

Surface effects, such as scattering losses along interface boundaries caused by the density fluctuations of two blending species and their stoichiometric differences, might be argued to play a much more important role in mirror coatings as opposed to optical fibers, and so might be expected to distinguish their fundamental limits, disallowing the parallel we draw. However, the use of a graded refractive index is a critical feature of both systems and over similar linear dimensions, and itself raises related issues concerning stoichiometry, homogeneity, extra absorption losses, and vitrification in the transition regions. The success of optical fiber technology in approaching the fundamental loss limits of the bulk materials therefore is evidence that such concerns are not insurmountable at the ppb level, and it is relevant to our interest in the ppb loss regime in the context of surface effects as well as of volume effects. Rayleigh scattering from bulk density fluctuations is considered in Section 5.

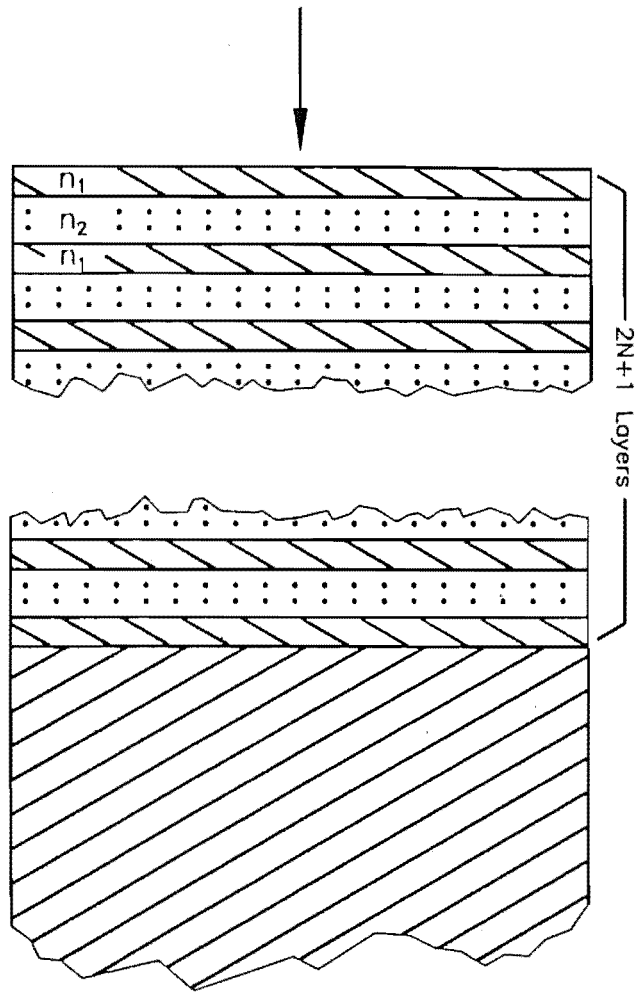

Fig. 1. Schematic of multilayer dielectric mirror, with $2N + 1$ layers of alternating high–low complex index of refraction, $n^* = n - jk$, where k is the extinction coefficient. The presumed plane wave enters at normal incidence.

3. Transmission and Absorption Analysis

We show that it is feasible to reduce transmission losses T below absorption losses A, which themselves are capable of considerable reduction, using a standard matrix analysis.[27,28] We define the complex index of refraction of the rth layer, n_r^*, as $n_r - jk_r$, where n_r is the real index of refraction and k_r is the extinction coefficient; also phase $\delta_r = (2\pi n_r^* l_r/\lambda_0)\cos\beta_r$, where l_r is the physical thickness and β_r is the angle of the refracted beam of the rth layer; λ_0 is the vacuum wavelength. We shall specialize by considering a particular multidielectric stack (Fig. 1). The matrix

$$\begin{bmatrix} \cos\delta_r & j\sin\delta_r/\eta_r \\ j\eta_r\sin\delta_r & \cos\delta_r \end{bmatrix} \tag{2}$$

represents the action of the rth layer on the stratified electromagnetic field amplitudes. Note that $\eta_r = n_r^*\cos\beta_r$ for the case we consider below, that of polarization in the s direction; $\eta_r = n_r^*/\cos\beta_r$ for the p direction. All layers are taken as $\lambda/4$ layers: $\mathrm{Re}(\delta_r) = \pi/2$, and we assume normal incidence. After expansion of the matrix elements to lowest order in k_H, k_L, we obtain the simplified matrix for layer r of

$$j\begin{vmatrix} \pi k_r/2n_r & 1/n_r \\ n_r & \pi k_r/2n_r \end{vmatrix}. \tag{3}$$

The customary alternating structure is used. On top of substrate S is deposited a high-index material (of H type), then a low-index material (L), and so on. We take the last layer in the stack, interfacing with the vacuum (say), to be of H type, now ignoring the effect of the customary UV protection ($\lambda/2$) layer; because the latter is of L type it tends to have minimal scattering and merely facilitates the impedance matching to the vacuum at the dielectric boundary.

We show in Eq. (5) that losses T, A through transmission and absorption become additive in the limit of small absorption,[12] i.e., $k_r \ll n_r$. This limit is in any case a necessary condition for good mirrors. This enables us to treat each source of loss separately, assuming the other is absent, and to expand all terms

to lowest order in k_r. We neglect the extinction of the last H layer and the substrate. This is not a serious assumption, because the major contribution to the overall absorption stems from the first few layers only; the field diminishes rapidly toward the substrate. The final mirror matrix is the product of those for N pairs of layers of type HL, the matrix for the last layer H, and that for the substrate. To first order in the extinction coefficients, this has the form:

$$\frac{(-1)^N j}{x^{N-1} y n_H}\begin{bmatrix} x^{2N-1}y & \epsilon_1 z \\ \epsilon_2 z & y/x \end{bmatrix}\begin{bmatrix} \tfrac{1}{2}\pi k_H & 1 \\ n_H{}^2 & \tfrac{1}{2}\pi k_H \end{bmatrix}\begin{bmatrix} 1 \\ n_S \end{bmatrix}$$

$$\simeq \frac{(-1)^N j}{x^{N-1} y n_H}\begin{bmatrix} n_S x^{N-1} y + \epsilon_1 n_H{}^2 y \\ n_H{}^2 y/x + \epsilon_2 n_S z \end{bmatrix} \equiv \begin{bmatrix} a \\ b \end{bmatrix}. \quad (4)$$

In this equation $x = n_L/n_H$ (note that $x < 1$), $y \equiv 1 - x^2$, $z \equiv 1 - x^{2N}$, $\epsilon_1 = \pi|(k_H + k_L)/2|/|n_H n_L| = \pi k_{av}/n_g{}^2 \ll 1$, with k_{av} being the average extinction coefficient in the stack and n_g^2 being the mean square refractive index, and $\epsilon_2 = \pi|(n_H/n_L)k_L + (n_L/n_H)k_H|$; note that $\epsilon_2 \ll 1$. The power reflectance back into the vacuum is then given as usual by $R = |(a - b)/(a + b)|^2$. Note that $z \to 1$ with a relatively few layers, so that we can apply this simplification in the column matrix of Eq. (4). It is also useful and appropriate to neglect the small term $\epsilon_2 n_S z$ in the vector element b, because $n_H{}^2 y \gg \epsilon_2 n_S x$. A similar approach is not possible for the column matrix element, a, because for large N both terms become small.

Because we are only concerned with high-reflectance mirrors in which transmission and absorption are small, we have $a \ll b$, and the loss of reflectance is then given in first order by

$$1 - R = 4a/b = P + Q, \quad (5)$$

where $P \equiv 4 n_S n_L{}^{2N} n_H{}^{-2(N+1)}$, $Q \equiv 2\pi(k_H + k_L)/(n_H{}^2 - n_L{}^2)$. In the limit $N \to \infty$, only Q survives; from its dependence on absorption parameters k_H, k_L, Q clearly corresponds to absorption loss A in this model. This gives the so-called Koppelmann limit,[12] $1 - R = Q$. In the limit of negligible absorption $(k_H + k_L) \to 0$, only P survives, giving the so-called Abelès limit.[13] For $N \to \infty$, this limit implies perfect reflectance in the absence of A and S, and this first term corresponds to T in this model. The additive form for Eq. (5) justifies our earlier assumptions on the additivity of such contributions to T, A.

The strategy for lowering T so that A dominates is obviously to increase the number of layers in Eq. (5) until T becomes negligible in comparison. This is achieved when $P \ll Q$. As an example, for SiO_2–TiO_2 layers and a Zerodur substrate, with $n_S = 1.54$, $n_H = 2.33$, $n_L = 1.46$, and $k_H + k_L = 1 \times 10^{-6}$, we would require $N > 16$ pairs, i.e., 33 layers to achieve the Koppelmann limit. In practice much larger stacks have been designed for specific filter purposes.[29]

Note that the substrate property, n_S, enters only in the transmission term P, not in the absorption term, Q; power is mainly absorbed in the first few layers on top of the stack. The substrate refractive index, n_S, does not affect the losses in the Koppelmann limit, and the associated extinction coefficient, k_s, if small (so that the approximations in the above derivation are justified), never affects the losses. We are therefore free to choose the substrate material purely for the quality of its surface topology (plus other, nonoptical, properties that may be desirable, e.g., heat diffusivity, mechanical resonances, impurity diffusion, vacuum compatibility), and that only in order to ensure that the quality of the top surface is not degraded.

The derivation of absorption term Q in Eq. (5) can be simplified if one supposes the field distribution in the layers to be as in the lossless case, and if one adds the losses *ad hoc*.[26] The presentation given here has the advantage of not assuming any field distribution *a priori*. It lets us determine the layer structure necessary to achieve a transmission loss much less than absorption, $T \ll A$, and also the extent to which the substrate properties enter in reflectance R. Suggestions[30] that one can achieve reflectances beyond the Koppelmann limit at the expense of varying the layer thickness give a very small return for the effort if extinction coefficients $k \leq 10^{-6}$ are considered.

We conclude that transmission T can be suppressed, given a finite amount of absorption, by adding enough layers to the stack. A transmission loss of 1 ppb would require an increase ($\sim 50\%$) in the number of layers over that appropriate for 1 ppm, i.e., ~ 50 layers; this is quite feasible in practice. Therefore, we turn now to a discussion of the more fundamental limitations: processes that lead to irreducible contributions to absorption term A.

4. Absorption in the Vicinity of a Band Gap

The empirical relation, Urbach's rule that $\alpha = A \exp(\sigma\hbar(\omega - \omega_0)/k_B T)$, has been observed to hold. Note that α, the absorption near a band edge, is related to extinction coefficient k by $\alpha = 4\pi k/\lambda$; k_B is Boltzmann's constant, T is the temperature, and A, σ, ω_0 are fitted to the data.

Present estimates of k for TiO_2 (the k_H of Section 3) would suggest that it is this extinction that gives the fundamental limit on absorption A and hence on reflectance R for multilayer mirrors. However, this estimate of k itself has been quite dramatically reduced, at roughly 1 order of magnitude per 2 years over the last 10 years (Fig. 2). We may compare this with the research of Wei,[4] who documented an order of magnitude of mirror improvement per 6 years over the last 20 years. We examine the fundamental mechanisms contributing to k in TiO_2, and we conclude that further and dramatic reductions in its measured value are feasible.

Suitable dielectric film materials are insulators near room temperature, exhibiting a large band gap of several electron volts, typically in the UV range.

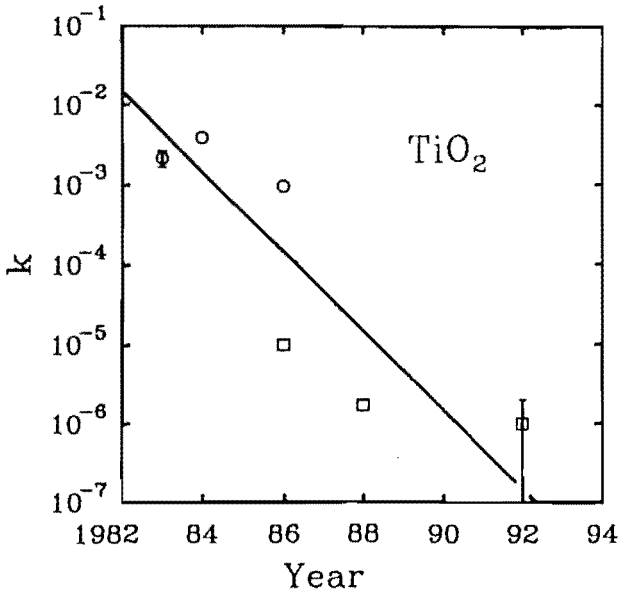

Fig. 2. Progress through recent decades in lowering extinction coefficient k for thin films of TiO_2 as evaluated from data, mostly in the literature, on finished mirrors. Circles denote data taken at 500 nm: 1983, Ref. 31; 1984, Ref. 32; 1986, Ref. 33. Squares denote data taken at 633 nm: 1986, Ref. 34; 1988, our estimate by difference from measurements of R, S, T on a 1988 set of supermirrors: Ref. 35; 1992, as for our 1988 measurements, but using more recent supermirrors (unpublished). Here k is either taken directly from the literature cited above or is evaluated from R after subtraction of TIS and transmission losses. The line has a slope of $-\frac{1}{2}$ and indicates 1 order of magnitude improvement per 2-yr period.

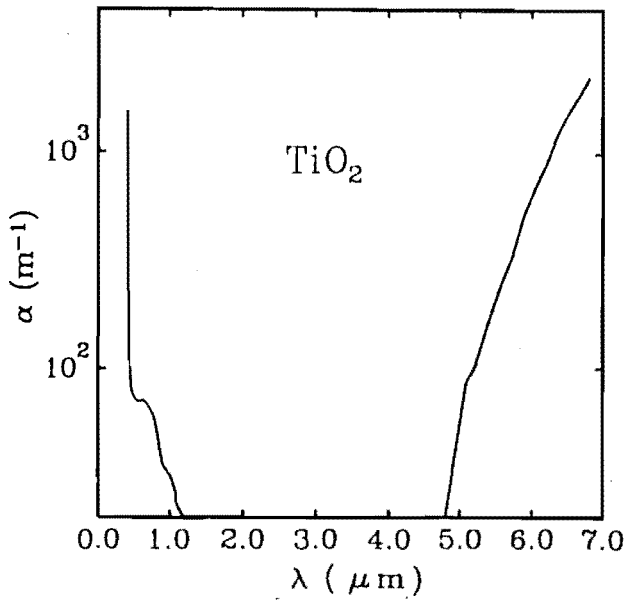

Fig. 3. Plot of absorption coefficient α of a slab of bulk TiO_2 after subtraction of the surface reflection (after Cronemeyer[37]).

We concentrate here on the H (high-refractive-index) material, because we expect more absorption for such materials according to the Kramers–Kronig relations. TiO_2, as an example, behaves in this classic fashion,[36] possessing a band gap of 3.05 eV (neglecting fine details of the anisotropic band structure of the various crystal formations). This places the nominal limit of transparency at 407 nm. In the visible the absorption is at present impurity limited, and in the far IR, atomic (phonon) resonances make the material opaque again (Fig. 3).[37] These features make the material suitable in the visible. The Urbach tail from the UV absorption in the visible region[37–39] is the most obvious limitation on the loss. An equivalent tail from the phonon absorption spectrum need not be considered for insulators such as TiO_2, in which the atomic resonance absorption starts at $\lambda \geq 5\ \mu m$.

The available data are somewhat contradictory. DeVore[40] proposed a single oscillator model for the index of refraction of TiO_2 from the band gap to $\lambda = 15\ \mu m$; the corresponding extinction coefficient would then vary with an inverse power law according to the Kramers–Kronig relations. This is clearly not the case for the direct measurements of Cronemeyer.[37] We use the latter. The extrapolated Urbach tail (Fig. 4) gives then $k = 7 \times 10^{-12}$ at $\lambda = 500$ nm. This value is similar to the cleanest fused silica. After decades of effort in optical fibers for communications, a loss of only $\bar{\alpha} = 0.15$ dB/km has been achieved for fused silica (at $\lambda = 1.55\ \mu m$), corresponding to $k = (\lambda/4\pi)(\ln 10)\bar{\alpha} \times 10^{-4} = 4 \times 10^{-12}$.[41] This figure includes Rayleigh scattering from density fluctuations (see Section 5) and residual phonon absorption as well as the Urbach tail in silica. Cronemeyer's data are for crystalline material. The Urbach rule is empirical, and its underlying mechanisms are not

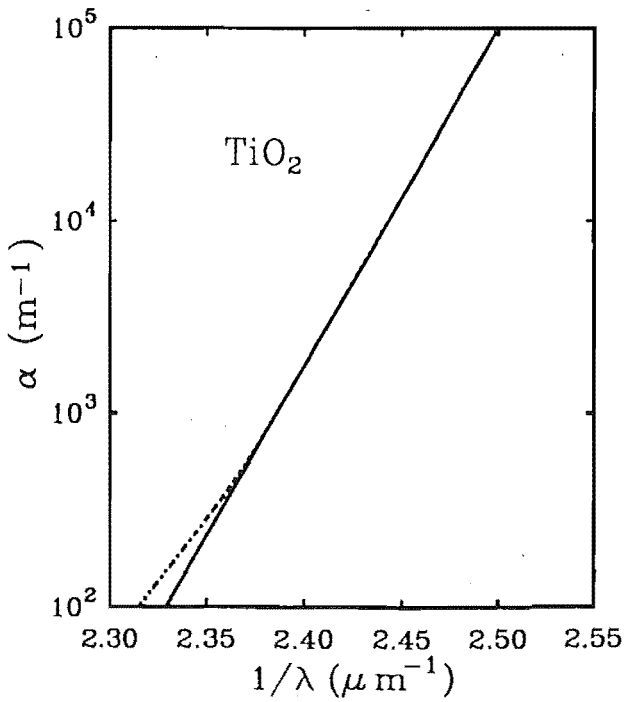

Fig. 4. Urbach tail for TiO_2 in the visible (400–430 nm), after Cronemeyer.[37] The deviation from linearity is attributed to impurities; a linear fit to this tail (solid line) gives on extrapolation to 500 nm an extinction coefficient of less than 10^{-11}.

unique. In crystalline solids many band-edge tails reveal exciton peaks at cryogenic temperatures, but in amorphous solids their excitonic character becomes more questionable. The semilog slope of the Urbach tail can decrease when a material becomes more amorphous.[20] Available direct measurements of absorption in TiO_2 in the visible give values for the extinction coefficient that are several orders of magnitude above this extrapolated value,[6,34] presumably because of impurity scattering, as was the case in SiO_2 before the removal of impurities, mainly paramagnetic ions.[42] An equivalent purification effort for TiO_2 would greatly enhance the potential of this material for multilayer dielectric mirror coatings. Equally, the now-standard use of SiO_2 as a material for the low-index material L in a multilayer dielectric stack itself no longer presents any fundamental obstacle to the attainment of reflectance losses well below 1 ppm. The experience with optical fibers shows that many of the problems have already been solved for SiO_2. It is an extrapolation from current measurements to suggest that TiO_2 will be as amenable as SiO_2 to high purification, but the above evidence does not support a significant distinction between TiO_2 and SiO_2 in this regard. This extrapolation deserves to be investigated.

5. Rayleigh Scattering from Density Variations in the Layer Volume

Another irreducible loss process is due to bulk Rayleigh scattering from density variations. This process may be attributed more to absorption A than to the experimentally determined TIS. In any case, because this process is incoherent, it removes power from the coherent beam. In order to reduce volume scattering, crystallization of the layer material is avoided by the use of ion-beam-sputtering techniques, and by adding a few percent of SiO_2 into the TiO_2 film.[4,33] The density fluctuations are then thermodynamically determined and this dominates the Rayleigh scattering.[14,19,43]

The mean square density fluctuations $\langle \delta\rho^2/\rho^2 \rangle$ are given by Oster[44] and Becker[45] as $\langle \delta\rho^2/\rho^2 \rangle = k_B T_f \bar{k}/V$, where T_f is the absolute temperature at which the fluctuations are established, $\bar{k}$ is the bulk compressibility, and V is the layer volume. The extinction coefficient caused by this scattering process is then[40] $k_r = 2\pi^2(n_r^2 - 1)^2 k_B T_f \bar{k}/3\lambda_0^3$. Comparing this Rayleigh limit between SiO_2 and TiO_2, we note that the respective parameters are all of similar magnitude ($T_f \sim 1800$–$2000K$, $n \sim 1.5$–2.3, $\bar{k} \sim 2.7$–1.5×10^{-11} Pa^{-1}, $\lambda_0 = 500$ nm). Hence we expect approximately the same limits for TiO_2 as for SiO_2 whose extinction coefficient $k_r = 1.0 \times 10^{-10}$, incidentally a factor of 10 better than pure water at its maximum transparency at 500 nm.[46] This extinction limit is approximately 4 orders of magnitude lower than that currently achieved (Fig. 2). Related thermodynamic fluctuations in the interface positions may also limit mirror performance through induced nonspecular reflection[24]; because of the close connection, we expect this to contribute at a similar level to the Rayleigh scattering discussed above.

6. Conclusions

Present supermirrors represent substantial improvements over past mirrors. With the recent improvement in deposition techniques, adding a sufficient number of layers to suppress the effect of transmission on the limit for reflectance appears not to be a technological problem. The state of the art of surface scattering that is now achieving overall losses in the single ppm range can be assumed to be capable of substantial improvement. Bulk scattering and residual volume absorption in the layers will then present the ultimate limitation, because both are irreducible. They are estimated to produce limits of extinction coefficients in the range $k_r \sim 10^{-10}$ and thus total reflectance loss in the ppb range.

It is therefore conceivable that with improvements in material technology and in the art of mirror making, the total reflection losses of multilayer dielectric mirrors can be lowered to the ppb range. Supercavity mirror technology should thus mature toward the level already achieved in the current development of optical fibers. The fundamental limits on extinction lengths arise from the same mechanisms in each case, and extinction lengths in optical fibers now approach 100 km, corresponding to an extinction coefficient of $k_r \sim 10^{-12}$. Given such considerations and the associated possibility of raising the design of surfaces from an art to a science, we suggest that it is reasonable to anticipate building on the success of the past 20 years toward the production of supermirrors with both their scattering S and their absorption A very much reduced from the present ppm range, well into the ppb range.

We acknowledge helpful comments on practical aspects of the manufacture of supercavity mirrors from A. W. Louderback of Ojai Research Corporation. H. R. Bilger acknowledges partial support of the National Science Foundation under the U.S.A.–New Zealand Cooperative Science Program. Other acknowledgements are included in the references.

References and Notes

1. A. O'Keefe and D. A. G. Deacon, "Cavity ring-down optical spectrometer for absorption measurements using pulsed laser sources," Rev. Sci. Instrum. **59**, 2544–2551 (1988).
2. D. Z. Anderson, J. C. Frisch, and C. S. Masser, "Mirror reflectometer based on optical cavity decay time," Appl. Opt. **23**, 1238–1245 (1984).
3. J. M. Elson, J. P. Rahn, and J. M. Bennett, "Relationship of the total integrated scattering from multilayer-coated optics to angle of incidence, polarization, correlation length, and roughness cross-correlation properties," Appl. Opt. **22**, 3207–3219 (1983).
4. D. T. Wei, "Ion beam interference coating for ultralow optical losses," Appl. Opt. **28**, 2813–2816 (1989).
5. M. Born, *Optik* (Springer-Verlag, Berlin, 1933).
6. Z. Li, R. G. T. Bennett, and G. E. Stedman, "Swept-frequency induced cavity ringing," Opt. Commun. **86**, pp. 51–57 (1991).
7. H. R. Bilger, G. E. Stedman, M. P. Poulton, C. H. Rowe, Z. Li and P. V. Wells, "Ring laser for precision measurement of

nonreciprocal phenomena," IEEE Trans. Instrum. Meas. **42**, 407–411 (1993).
8. G. E. Stedman, H. R. Bilger, Li Ziyuan, M. P. Poulton, C. H. Rowe, I. Vetharaniam, and P. V. Wells, "Canterbury ring laser and tests for nonreciprocal phenomena," Aust. J. Phys. **46**, 87–101 (1993).
9. R. Anderson, H. R. Bilger and G. E. Stedman, "The 'Sagnac' effect: a century of earth-rotated interferometers," Am. J. Phys. **62** (to be published).
10. J. Ehlers and G. Schäfer, eds., *Relativistic Gravity Research with Emphasis on Experiments and Observations*, Vol. 410 of Lecture Notes in Physics (Springer-Verlag, Berlin, 1992), pp. 185–260; W. Winkler, K. Danzmann, A Rüdiger, and R. Schilling, "Heating by optical absorption and the performance of interferometric gravitational-wave detectors," Phys. Rev. A **44**, 7022–7036 (1991).
11. C. A. Klein, "Thermally induced optical distortion in high-energy laser systems," Opt. Eng. **18**, 591–601 (1979).
12. G. Koppelmann, "Zur Theorie der Wechselschichten aus schwachabsorbierenden Substanzen und ihre Verwendung als Interferometerspiegel," Ann. Phys. (Leipzig) **7**, 388–396 (1960).
13. M. Born and E. Wolf, *Principles of Optics*, 6th ed. (Pergamon, Oxford, 1989), Chap. 1.
14. H. A. Macleod, "New techniques revolutionise thin-film optical coatings," Laser Focus World **28**(11), 116–119 (1992).
15. C. Amra, G. Albrand, and P. Roche, "Theory and application of antiscattering single layers: antiscattering antireflection coatings," Appl. Opt. **25**, 2695–2702 (1986).
16. C. Amra, "From light scattering to the microstructure of thin-film multilayers," Appl. Opt. **32**, 5481–5491 (1993).
17. C. Amra, C. Grezes-Besset and L. Bruel, "Comparison of surface and bulk scattering in optical multilayers," Appl. Opt. **32**, 5492–5502 (1993).
18. S. E. Watkins, J. P. Black, and B. J. Pond, "Optical scatter characteristics of high-reflectance dielectric coatings and fused-silica substrates," Appl. Opt. **32**, 5511–5518 (1993).
19. J. E. Midwinter, *Optical Fibers for Transmission* (Wiley, New York, 1979), Secs. 8.3.1 and 8.4.
20. N. F. Mott and E. A. Davis, *Electronic Processes in Non-Crystalline Materials*, 2nd ed. (Clarendon, Oxford, 1979), Fig. 6.45.
21. A. F. Stewart and D. J. Gallant, "Ultraviolet thin film coating characterization," Natl. Bur. Stand. (U.S.) Spec. Publ. **727**, 272–284 (1984).
22. We are grateful to K. Danzmann, Garching, Germany, for communicating this.
23. We are grateful to R. Rodloff, Deutsche Gesellschaft für Luft-und-Raumfahrt, Universität Braunschweig, for this measurement.
24. J. Lekner, *Theory of Reflection* (Nijhoff, Dordrecht, The Netherlands, 1987), Chap. 11.
25. W. K. Stowell, F. D. Orazio, and R. M. Silva, "Instrumentation of a variable angle scatterometer," (Natl. Bur. Stand. Spec. Publ. **638**, 205–222 (1981).
26. H. E. Bennett and D. K. Burge, "Simple expressions for predicting the effect of volume and interface absorption and of scattering in high-reflectance or antireflectance multilayer coatings," J. Opt. Soc. Am. **70**, 268–275 (1980).
27. H. A. Macleod, *Thin-Film Optical Filters*, 2nd ed. (Macmillan, New York, 1986).
28. P. Rouard, "Etudes des propriétés optiques des lames métalliques très minces," Ann. Phys. (Paris) **7**, 291–384 (1937).
29. V. R. Costich, "Multilayer dielectric coatings", in *Handbook of Lasers*, R. J. Pressley, ed. (Chemical Rubber Co., Cleveland, Ohio, 1971), pp. 155–170.
30. C. K. Carniglia and J. H. Apfel, "Maximum reflectance of multilayer dielectric mirrors in the presence of slight absorption," J. Opt. Soc. Am. **70**, 523–533 (1980).
31. H. Demiryont, D. B. Kerwin and J. R. Sites, "Optical properties of ion-beam sputtered TiO_2 films," Natl. Bur. Stand. Spec. Publ. **688**, 311–316 (1983).
32. R. Rujkorakarn, L. S. Hsu, and C. Y. She, "Crystallisation of titania films by thermal heating," Natl. Bur. Stand. Spec. Publ. **727**, 253–261 (1984).
33. J. R. Sites, J. S. Postek, R. S. Robinson, T. D. Schemmel, and C. Y. She, "Admixture of SiO_2 to suppress TiO_2 crystallization," Natl. Bur. Stand. (U.S.) Spec. Publ. **752**, 332–335 (1986).
34. A. Kalb, "Neutral ion beam sputter deposition of high-quality optical films," Opt. News 13–17 (Aug. 1986).
35. H. R. Bilger, P. V. Wells and G. E. Stedman, "Geometric dependence of polarisation in near-planar ring lasers," Opt. Commun. **80**, 133–137 (1990).
36. O. Madelung, Landolt-Börnstein, *Zahlenwerte und Funktionen aus Naturwissenschaften und Technik*, New Series III/17g (Springer-Verlag, Berlin, 1984), Sect. 9.15.2.1, Titanium oxides, pp. 133–166, 413–445.
37. D. C. Cronemeyer, "Electrical and optical properties of rutile single crystals," Phys. Rev. **87**, 876–886 (1952).
38. F. Urbach, "The long-wavelength edge of photographic sensitivity and of the electronic absorption of solids," Phys. Rev. **92**, 1324 (1953).
39. J. D. Dow and D. Redfield, "Toward a unified theory of Urbach's rule and exponential absorption edge," Phys. Rev. B **5**, 594–610 (1972).
40. J. R. DeVore, "Refractive indices of rutile and sphalerite," J. Opt. Soc. Am. **41**, 416–419 (1951).
41. T. Izawa and S. Sudo, *Optical Fibers: Materials and Fabrication* (Reidel, Dordrecht, The Netherlands, 1987).
42. R. Olshansky, "Propagation in glass optical waveguides," Rev. Mod. Phys. **51**, 341–367 (1979).
43. A. Einstein, "Theorie der Opaleszenz von homogenen Flüssigkeiten und Flüssigkeitsgemischen in der Nähe des kritischen Zustandes," Ann. Phys. (Leipzig), **33**, 1275–1298 (1910).
44. G. Oster, "The scattering of light and its application to chemistry," Chem. Rev. **43**, 2319–2365 (1948).
45. R. Becker, *Theory of Heat*, 2nd ed. (Springer-Verlag, Berlin, 1967).
46. G. M. Hale and M. R. Querry, "Optical constants of water in the 200 nm to 200 μm wavelength region," Appl. Opt. **12**, 555–563 (1973).